Comportement de l'Hydrogène lors des processus mantelliques

Carole Denis

Collège Doctoral du Languedoc-Roussillon

THÈSE

Pour obtenir le grade de

Docteur

Délivré par **Université de Montpellier**

Préparée au sein de l'école doctorale Sibaghe
Et de l'unité de recherche Géosciences Montpellier

Spécialité : **Géosciences**

Présentée par **Carole Denis**

COMPORTEMENT DE L'HYDROGÈNE LORS DES PROCESSUS MANTELLIQUES

Soutenue le 4 décembre 2015 devant le jury composé de

Olivier ALARD, DR, CNRS – GM, Montpellier	Co-directeur
Nathalie BOLFAN-CASANOVA, CR, CNRS – LMV, Clermont F^{d}	Rapporteur
Hélène BUREAU, CR, IMPMC, Paris	Examinateur
Étienne DELOULE, DR, CNRS – CRPG, Nancy	Rapporteur
Sylvie DEMOUCHY, CR, CNRS – GM, Montpellier	Co-directrice
Marguerite GODARD, DR, CNRS – GM, Montpellier	Pdt du jury
Michel GRÉGOIRE, DR, CNRS – GET, Toulouse	Examinateur

UNIVERSITÉ MONTPELLIER

GÉOSCIENCES MONTPELLIER
ÉCOLE DOCTORALE SIBAGHE

THÈSE

présentée par

Carole DENIS

en vue de l'obtention du
Doctorat de l'Université de Montpellier
Spécialité : Géosciences

COMPORTEMENT DE L'HYDROGENE LORS DES PROCESSUS MANTELLIQUES

soutenue le 4 décembre 2015, devant le jury compose de :

ALARD Olivier	Directeur de Recherche (CNRS – Géosciences Montpellier)	Co-directeur de thèse
BOLFAN-CASANOVA Nathalie	Chargée de recherche (CNRS – LMV, Clermont Ferrand)	Rapporteur
BUREAU Hélène	Chargée de recherche (IMPMC, Paris)	Examinateur
DELOULE Etienne	Directeur de recherche (CNRS – CRPG, Nancy)	Rapporteur
DEMOUCHY Sylvie	Directrice de Recherche (CNRS – Géosciences Montpellier)	Co-directrice de thèse
GODARD Marguerite	Directrice de Recherche (CNRS – Géosciences Montpellier)	Examinatrice
GRÉGOIRE Michel	Directeur de recherche (CNRS – GET, Toulouse)	Examinateur

To see a World in a Grain of Sand
And a Heaven in a Wild Flower
Hold Infinity in the palm of your hand
And Eternity in an hour

William Blake, *Auguries of innocence*.

REMERCIEMENTS

Sylvie et Olivier, différents mais complémentaires, c'est difficile pour un simple merci d'exprimer ma gratitude d'avoir su me supporter (dans tous les sens du terme) pendant ces 3 ans, et de m'avoir montré deux façons de vivre la recherche, entre l'organisation absolue de la pro-deadline et l'effervescence de l'anti-deadline. Sylvie, je te remercierai jamais assez pour m'avoir acceptée en stage en M2 à l'époque ; de m'avoir montré les bons côtés de la recherche, d'avoir tenté de me faire sortir de mon « côté obscur », merci pour les nounours en guimauve et les baby carottes ! Olivier, merci de m'avoir donné ma chance avec cette thèse, désolée pour le carbone, je le laisse pour le prochain !

Je remercie les membres de mon jury, Nathalie Bolfan-Casanova, Hélène Bureau, Étienne Deloule, Marguerite Godard et Michel Grégoire pour avoir accepté de lire et juger mon travail.

Ce projet n'aurait pas été possible sans le laboratoire Géosciences et l'équipe Manteau Interface qui m'ont accueillis. Je remercie tout particulièrement Alain, Dodo et Fabrice pour le temps qu'ils m'ont accordé, outre l'aide évidente qu'ils m'ont apportée, leur humour et leur bonne humeur égayait toujours ma journée. Un GRAND merci à Fleurice pour ses conseils judicieux, astucieux et raisonnables et surtout pour son écoute ! Je remercie aussi David Maurin, pour sa patience, son expertise en spectro infrarouge, et sa gentillesse. Je remercie Christophe et Doriane, toujours disponibles et efficaces. Je dois aussi un grand merci à Marie-France, pour son sourire et sa bienveillance !

Je tiens à remercier mes collègues de couloir successifs pour avoir su conserver cette bonne ambiance au fil des années, merci donc à Céline, toujours là pour moi, dans les succès comme dans les échecs et les manques d'inspiration, mais aussi à Cristiane, Sofia, Carlotta, Valentin, René, Hicham, Camille et Julie. Merci à tous les autres thésards, ATER et Postdoc d'ici et d'ailleurs pour y avoir participé pendant ces 3 années inoubliables : Greg, Nori, Roberto, Gustavo, Claudia, Gian Luca, Rémi, Ariana, Vanessa, Bianca, Sasha, Antoine, Sébastian, Hélène, Sébastien, Kate, Ousman, Steve, Karoly, Valentin et tous les autres !

Merci à mes amis de longue date, géologues ou non, d'avoir continué de m'accompagner lors de mes péripéties lointaines. Un grand merci à Charlotte M.d.C., Morgane B., Margaux B., Marjorie H., Louis D., Floe F., Alex F., Bilou P., Pierrot E., Lelyen C., Sylvain V., Manue C., Claire L., Romain L., Jé V., Mélanie C., Baz J., Vincent T., Aurélie G., Josy B., Marlène A., Charlène D. et Florent M. Jamais trop loin, jamais trop peu, l'amitié est au-dessus de ça. Merci à ceux qui m'ont recueillie à Montpellier, qui m'ont fait apprécier la ville, son soleil et ses bars. Merci à Pierre-Alex P., Juju D., Alex B., Elise, Kévin B., Grand, Cécile V., Julie S. et Popo C. pour les moments de détente autour des bières, du rock et des barbeuc ! C'est donc pourquoi ma gratitude va aussi à la Belgique et à l'Allemagne pour avoir étanché ma soif et à Fred Pizza pour avoir calmé ma faim. Merci à mes colocs Jérém et Nounours pour avoir partagé mes fluctuations de stress et de participations aux tâches ménagères ;p. Merci à mes courageux relecteurs non géologues, fouineurs de fautes dort aux graphes et de types O' : Charlotte M.d.C., Pierre-Alex P. et Alex D. !

Merci Pépé, Mémé, Maman, Papa, Antoine, Mickaël, Aurélien, Anne-So, Gaga, Martine, Myriam et Elyane de m'avoir toujours encouragé à réaliser mes rêves. Merci de m'avoir soutenu et d'avoir tenté de comprendre ce qui occupe mes journées loin de vous, ou du moins d'avoir retenu les mots clefs !

Enfin certains ont droit à un second merci, Antoine et Charlotte, toujours là pour moi, pour me conseiller, pour me faire rire, pour me ramener sur Terre et m'envoyer dans les étoiles, pourvu que ça dure !

COMPORTEMENT DE L'HYDROGÈNE LORS DES PROCESSUS MANTELLIQUES

Carole M.M. DENIS

Géosciences Montpellier, Université Montpellier, Place E. Bataillon, 34095 Montpellier.

Ces travaux de thèse apportent de nouvelles contraintes sur la concentration et le comportement de l'H dans le manteau lithosphérique. Ils reposent sur l'étude pétro-géochimique de trois séries de xénolites de péridotites à spinelle, associant les concentrations en élément majeurs et en traces y compris l'H dans les minéraux dits anhydres (les NAMs, ici, olivine, pyroxènes) et hydratés (amphibole).

Les effets de la remontée des xénolites dans du magma hôte sur les concentrations en H des NAMs ont été étudiés sur une série de xénolites de péridotite du champ volcanique d'Eifel (Allemagne). Une variation intracristalline de concentration en H a été identifiée dans l'olivine et non dans les pyroxènes coexistant. Ces profils de concentration en H peuvent être utilisés pour estimer des vitesses de remontées des magmas. Dans le cas des volcans étudiés, ces vitesses sont estimées entre 3.5 et 12 $m.s^{-1}$. Ces résultats suggèrent que les pyroxènes sont de meilleurs proxy que l'olivine pour quantifier la concentration mantellique de l'H.

Les xénolites de Ray Pic (Massif Central, France) ont permis de discuter de l'effet de la fusion partielle et du métasomatisme à grande échelle sur les concentrations en H des NAMs. Les concentrations en H des minéraux ne suggèrent pas de lien clair avec le métasomatisme subit, qu'il soit modal (amphibole) ou cryptique (métasomatisme par de faibles fractions de liquides enrichis en volatils et éléments incompatibles). Cependant, en comparant les concentrations en H avec un marqueur de la fusion partielle (Yb du cpx), l'H semble avoir un comportement similaire à une MREE (*e.g.*, Sm ; D(cpx/liquide) ~0.29).

L'interaction peridotite-basalte hôte a été étudiée et montre, dans le cas des olivines, des variations chimiques couplées entre éléments majeurs et les concentrations en H en fonction de leur proximité au filon. Plus l'olivine se rééquilibre avec le liquide moins elle contient d'H. Bien que partiellement rééquilibrés avec la lave hôte, les pyroxènes ne montrent pas le même comportement. Enfin, des xénolites composites (filons et veines traversant/jouxtant une péridotite) ont permis l'étude à l'échelle millimétrique à pluri-centimétrique du comportement de l'H lors du métasomatisme d'éponte. Chaque échantillon présente des concentrations en H homogènes pour chacune des phases minérales. Cependant plus les filons contiennent d'amphibole moins il y a d'H dans les NAMs. D'autre part, une nouvelle fois, la corrélation positive entre les concentrations en H des NAMs et le Sm(cpx) en tant que marqueur de métasomatisme suggère que l'H se comporte comme une MREE.

En conclusion, les minéraux des spl-harzburgites contiennent en moyenne un peu plus d'H que ceux des spl-lherzolites. Les concentrations en H des olivines sont sensibles à la dévolatilisation lors de la remontée dans le système magmatique et le rééquilibrage avec le magma. Au contraire, les concentrations en H des pyroxènes, spécialement l'opx, sont très homogènes suggérant que les concentrations mantelliques sont préservées. La présence d'amphibole n'implique pas un enrichissement en H des NAMs coexistant. Le comportement de l'H lors de la fusion partielle et du métasomatisme reste complexe ; nos données suggèrent que l'H suit les MREE tel que le Sm.

Mots clefs : péridotites, métasomatisme, fusion, pyroxénites, hydrogène, minéraux anhydres.

HYDROGEN BEHAVIOUR DURING MANTLE PROCESSES.

Carole M.M. DENIS

Géosciences Montpellier, Université Montpellier, Place E. Bataillon, 34095 Montpellier, France.

This thesis provides new constrains on H concentrations and H behaviour in the lithospheric mantle and is based on a petro-geochemical study on three spinel-peridotite xenoliths series with major and traces elements analyses, including H in nominally anhydrous minerals (NAMs, olivine and pyroxenes) as well as hydrous minerals (amphibole).

Ascent effects through a magmatic system on H concentration of NAMs are studied for a xenoliths series from the Eifel volcanic field (Germany). Intracrystalline variations in H concentration are observed in olivine but not in the coexisting pyroxenes. Such H concentration profiles are used to calculate the rate of magma ascent. For the studied volcanoes, the calculated rate of magma ascent is between 3.5 and 12 $m.s^{-1}$. Such H concentration variations imply a devolatilisation affecting only olivine, whereas the pyroxenes are homogeneous and then can be used as a reliable proxy for mantle H concentrations.

Ray Pic xenoliths (French Massif Central) belong to a mantle plume setting, implying the possibility to assess the effect of partial melting and large-scale metasomatism on H concentration of NAMs. The H concentrations determined do not suggest a strong link with the suffered metasomatism whether modal (occurrence of OH-bearing amphibole has no significant effect of H concentration of NAMs), nor cryptic (metasomatism by volatile rich melt/fluid has limited effect on the water content of NAMs). However, using H concentrations and a marker of the partial melting (Yb in cpx), H seems to behave as a MREE (*e.g.,* Sm, D(cpx/melt) ~ 0.29).

The interaction between a harzburgite and the host basalts has been studied in detail that, for olivines, chemical variations in major element as a function of olivine proximity to the vein, is coupled to H concentration of NAMs. More the olivines is close to equilibrium with the basalt, more H concentrations are low. However, for the pyroxenes such correlation is not observed.

Finally, three composite xenoliths (veins cross cutting a peridotite) have been studied to investigate at the mm- to cm-scale the effect of wall-rock metasomatism on the water content of NAMs to in the influence of small-scale metasomatism (pluri-centimetric). Each sample display homogeneous H concentration within each NAMs. However, H concentration is inversely correlated to modal content in amphiboles in the veins. Furthermore, H in NAMs correlate with Sm(cpx), which is a marker of metasomatism suggests again, that H behaves as a MREE.

To conclude, H concentrations in olivines are sensitive to degassing during magma ascent toward the surface and reequilibriate with magma. To the contrary, H concentration in pyroxenes, especially opx, are very homogeneous. Thus pyroxenes are more reliable indicator to assess water content of the mantle. The occurrence of amphibole does not imply that NAMs are enriched in water relative to amphibole free mineralogy. The behaviour of H during partial melting and metasomatism is complex. However, our data suggest that H broadly follows MREE.

Key words: peridotites; metasomatism; melting; pyroxenites; hydrogen; nominally anhydrous minerals.

TABLE DES MATIÈRES

Chapitre I : Introduction

Ce chapitre constitue un état de l'art sur deux processus permettant le transport de matière dans le manteau terrestre, à savoir la fusion et le métasomatisme. Cet état de l'art présente plus particulièrement le cas de l'hydrogène (H) dans le manteau terrestre.

I.1 Les enjeux et la problématique de l'eau dans la terre profonde.

L'eau liquide moléculaire H_2O, ou sous forme de glace, domine la surface de la Terre. Elle influe sur les processus superficiels d'érosion, de transport et de dépôts. Elle est une clef du climat et de la présence de vie sur Terre. L'exosphère (atmosphère et océans) s'est créée par dégazage de la terre primitive via le volcanisme. Cependant les laves actuelles contiennent toujours de l'eau (de l'ordre de 0,1 à 0,5 wt. % H_2O dite mantellique dans les basaltes de rides océaniques (MORB) ou de points chaud (OIB), Sobolev et Chaussidon, 1996). D'autre part, l'étude de xénolites mantelliques a montré que des espèces chimiques dérivées de l'eau étaient présentes sous différentes formes moins volumineuses que l'eau moléculaire dans la Terre profonde (Figure I.1). Des questions se posent toujours : combien y a-t-il d'eau dans le manteau ? Sous quelle forme ? Dans quels réservoirs ? Quels sont les échanges entre la surface et la terre profonde ? Quels sont les vecteurs de ces échanges ? La Terre est-elle en train de se déshydrater : le dégazage lié au volcanisme compense-t-il les apports en zone de subduction ? Combien d'eau est conservée dans le manteau après la déshydratation de la plaque subduite (Figure I.1) ?

La détermination du cycle profond de l'eau est un enjeu actuel puisque la présence d'H dans la structure cristalline des minéraux, même en très faible quantité de l'ordre de quelques ppm (part per million), affecte de manière drastique de nombreuses propriétés physico-chimiques de ces minéraux et donc de la roche mantellique. En effet, la présence d'H accroit les cinétiques de transport dans les minéraux, et donc accélère l'homogénéisation chimique dans le manteau (Bolfan-Casanova, 2005). Par exemple, la présence d'H dans le réseau cristallin joue sur la diffusion ionique. L'étude de l'interdiffusion Fe-Mg en milieu hydraté est un ordre de grandeur plus rapide qu'en milieu anhydre, (Wang *et al.,* 2004, Demouchy *et al.,* 2007). L'H dans un système va affecter les changements de phases qui vont alors s'effectuer à des profondeurs différentes, plus faibles (olivine-wadsleyite, *e.g.*, Wood, 1995) ou plus élevées (bridgmanite-ferropericlase, Litasov et Ohtani, 2007). Les discontinuités à 410 km et 650 km se retrouvent déplacées en contexte de subduction par exemple. La présence d'H abaisse la température de fusion (Aubaud *et al.* 2004 ; Hirth et Kohlstedt, 1996 ; Gaetani et Grove, 1998). Elle contrôle la vitesse de propagation des ondes sismiques (Jacobsen et Smyth, 2006) et augmente la conductivité électrique (Karato, 1990, Yoshino *et al.,* 2006 ; Poe, 2010). Enfin, la présence d'H pourrait affecter la rhéologie des minéraux, et permettre la diminution de la résistance à la déformation (Smyth *et al.,* 2005a, 2006 ; Smyth et Jacobsen, 2006 ; Mackwell *et al.,* 1985 ; Mei et Kohlstedt, 2000a, 2000b ; Demouchy *et al.,* 2013 ; Fei *et al.,* 2013). Les concentrations, et plus spécifiquement le comportement de l'H dans la lithosphère lors de processus tels que la fusion et le métasomatisme, sont donc des paramètres à ne pas éluder dans les modèles de dynamique terrestre globale.

I.2 Le Manteau Terrestre

Le manteau terrestre représente 80 % du volume de la terre, mais seule la partie superieure est directement échantillonnée sous forme de xénolites de péridotites lors de la remontée de magma (> 300 km, Haggerty et Sautter 1990 ; Sautter *et al.,* 1991). Néanmoins, les échantillons du manteau se présentent sous plusieurs formes, soit sous forme de massifs, soit sous forme de xénolites et/ou de xénocristaux, ou encore en inclusions conservées au cœur des minéraux de ces xénolites ou de diamants. Ces derniers représentent un échantillonnage particulier permettant d'accéder à de plus grandes profondeurs (*e.g.,* Pearson *et al.,* 2014 ; Novella *et al.,* 2015). Des massifs de roches mantelliques ont été mis à l'affleurement dans des zones orogéniques tels que les massifs pyrénéens (*e.g.,* Lherz), ou aux fonds des océans (péridotites abyssales), ou comme lambeaux de lithosphère océanique obductés sur les marges continentales (ophiolites d'Oman) et repris lors de phases orogéniques (*e.g.,* ophiolites Alpines : Chamrousse). Ces massifs, de taille métrique à plurikilométrique, permettent notamment l'observation de relations structurales entre les différents lithotypes et unités les constituants. Cependant, ces échantillons sont habituellement fortement serpentinisés. Les xénolites en enclaves dans les basaltes alcalins sont généralement peu ou pas serpentinisés mais de taille centi- à pluridéci-métrique. Ils ont aussi l'avantage d'avoir été remontés à la surface très rapidement lors d'éruptions volcaniques, ce qui n'est pas le cas des massifs orogéniques (mise en place au cours de plusieurs Ma, Bodinier et Godard, 2014). La rapidité de leur remontée ne permet pas un rééquilibrage minéralogique, ni chimique complet, (Pearson *et al.,* 2003) mais les données structurales sont alors perdues (*e.g,.* orientation de la linéation, des veines). Néanmoins, ces échantillons sont donc ce qui est le plus proche d'un échantillonnage *in situ*. Les travaux d'expérimentation, à hautes pressions et hautes températures, ou les modélisations numériques permettent d'aborder les domaines les plus profonds (> 10 GPa).

L'ensemble des propriétés physico-chimiques de l'assemblage minéralogique du manteau (*e.g.,* densité, température de fusion, propriétés plastiques) contrôle les transferts de matière et d'énergie entre la terre profonde et l'exosphère (océans et atmosphère) (Figure I.1) Une compréhension globale des rouages de cette machinerie terrestre permettrait le développement de modèles cherchant à évaluer les aléas liés à la tectonique des plaques et à l'exosphère (*e.g.,* le climat), mais aussi d'appréhender la géologie extraterrestre. Nous sommes encore loin de cet objectif. Les modèles existants de dynamique terrestre restent encore très simplifiés.

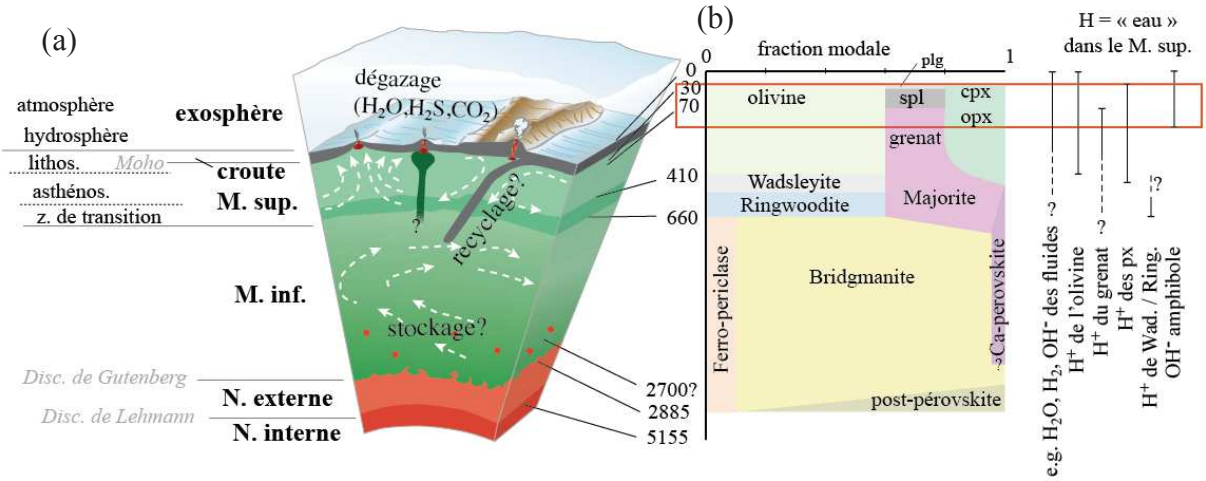

Figure I.1 – (a) Schéma présentant les échanges de matières entre les différentes couches constitutives de la Terre, (b) les minéraux majeurs, et les phases porteuses de l'H dans le manteau terrestre. L'encadré rouge délimite le manteau lithosphérique, provenance des xénolites de péridotite étudiés. Abréviations : Lithos. : lithosphère ; asthénos. : asthénosphère ; z. : zone ; Disc. : discontinuité ; M. sup. : manteau supérieur ; M. inf. : manteau inférieur ; N. : noyau ; plg : plagioclase ; spl : spinelle ; cpx : clinopyroxène ; opx : orthopyroxène ; px : pyroxène; Wad. : wadsleyite ; Ring. : ringwoodite. Modifié d'après Dasgupta (2013).

L'étude d'échantillons naturels permet de faire un lien entre les modèles globaux, les données expérimentales et la complexité du manteau naturel.

Les Massifs orogéniques, ophiolites et les xénolites de peridotites présentent deux grands types de lithologie : les péridotites (ol > 40 %) et les pyroxénites. Généralement, les péridotites dominent par rapport aux pyroxénites. Ces dernières représentent toutefois une lithologie importante car elles ont des propriétés physiques et pétrologiques bien différentes de celles des péridotites. On notera que les pyroxénites forment un pourcentage significatif des échantillons des massifs orogéniques alors qu'elles sont plus rares parmi les xénolites (Bodinier et Godard, 2014).

Dans les péridotites lithosphériques, on retrouve des minéraux silicatés : l'olivine, les pyroxènes (clinopyroxène et orthopyroxène), associés à une phase alumineuse dont la nature varie en fonction de la profondeur (le plagioclase jusqu'à ~ 30 km de profondeur, puis le spinelle (spl) jusqu'à ~ 70 km et enfin le grenat) en diverses proportions. Dans les plateformes continentales d'âges Protérozoïques à Phanérozoïques les péridotites échantillonnant la lithosphère subcontinentale les plus courantes sont équilibrées dans le faciès à spl. Les péridotites échantillonnant la partie mantellique de la lithosphère cratonique d'âge Archéenne sont, elles, équilibrées dans le faciès à grenat et à spinelle. La diversité des roches mantelliques accessibles est liée aux processus qu'elles ont subis avant et pendant leur extraction (péridotites, pyroxénites). Les enrichissements ou appauvrissements en certains éléments chimiques consécutifs à ces processus ont changé non seulement la composition

chimique de la roche mais peuvent aussi affecter sa texture (taille de grain, microstructure, fabrique) et sa composition modale. Les processus majeurs du manteau mis en cause en profondeur sont la fusion partielle de la roche (passage au-delà du point de fusion de certain minéraux) et le métasomatisme (modification de la composition de l'encaissant due à la percolation d'un liquide au travers de la roche). Ces processus dépendent de paramètres intrinsèques comme la composition chimique de la roche, les phases minérales présentes, la porosité réactive (et possible perméabilité). Des paramètres extrinsèques influencent aussi ces processus, comme la pression (P), la température (T), la présence de fluides et leur composition, l'état d'oxydation (fugacité en O_2, fO_2), la présence de volatils (*e.g.,* en H_2O (fH_2O), en CO_2 (fCO_2)), et les diffusivités ioniques. Cependant l'action conjuguée de chacun de ces paramètres n'est pas encore établie pour des systèmes naturels.

I.3 L'H dans le manteau

I.3.1 Réservoirs minéralogiques : Phases nominalement hydratées et anhydres de la péridotite à spinelle.

Dans le manteau lithosphérique, on retrouve l'H, élément incompatible et léger, sous forme H_2O, H_2, CH_4, OH^-, H^+ dans les fluides percolants. L'H est aussi présent dans les phases cristallines hydratées / hydroxylées, où un groupement hydroxyle, OH, fait partie intégrante de la structure cristalline, comme par exemple la pargasite : $NaCa_2(Mg,Fe^{2+})_4Al(Si_6Al_2)O_{22}(OH)_2$ (Figure I.2). D'autre part, les minéraux dit anhydres (*nominally anhydrous minerals*, NAMs du manteau) comme l'olivine, les pyroxènes et le grenat peuvent aussi contenir une faible quantité d'H dans leur réseau cristallin, avec des protons décorant des défauts ponctuels (*e.g.*, lacunes cationiques). Par convention, cet H est souvent exprimé avec des unités en poids d'oxydes (ppm wt. H_2O), donc d'eau. Ainsi on peut parler de concentration en eau bien qu'il s'agisse de simples protons fixés dans le réseau cristallin.

Cette particularité fait du manteau un réservoir d'eau non négligeable de la Terre (~ 2700 ± 1350 ppm wt. H_2O soit 10±5 fois la masse des océans, Marty, 2012).

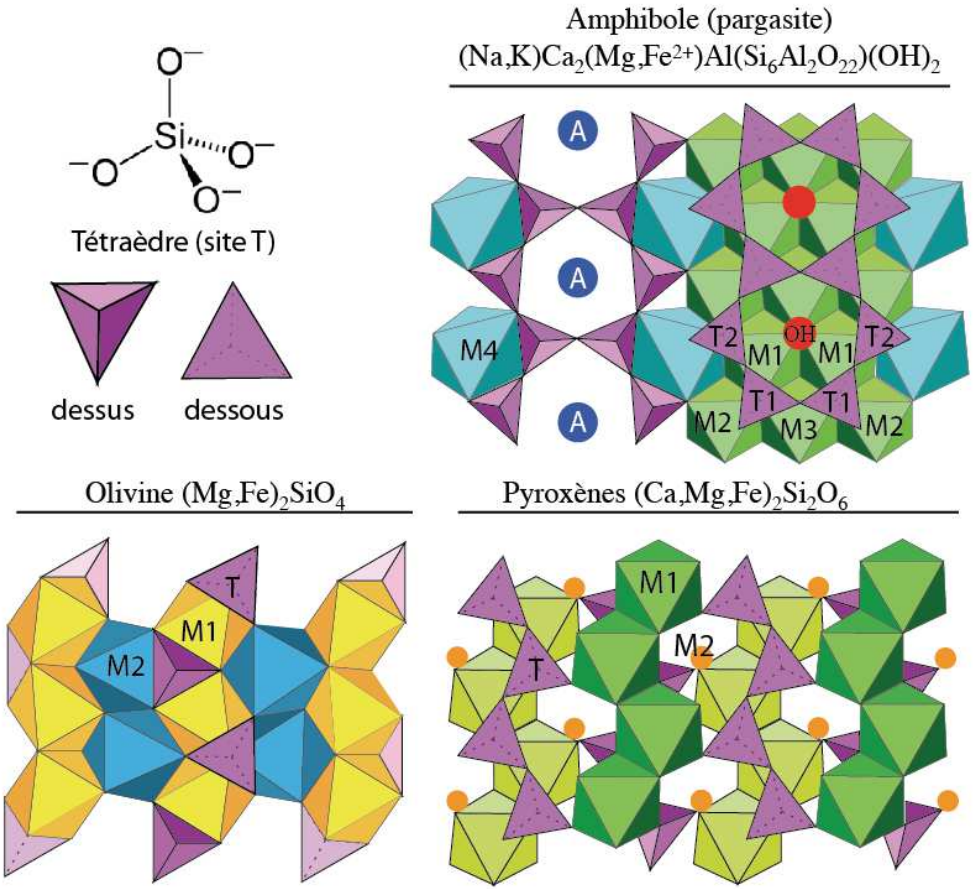

Figure I.2 – Exemples de structure cristalline d'un minéral hydraté (l'amphibole) et de NAMs (olivine et pyroxènes). D'après Pr Dutchs, Jackson *et al.,* 2013, Deer *et al.,* 1997 et Klein and Hurlbut, 1999.

I.3.2 Incorporation, solubilité et concentration mesurée de l'H dans les NAMs

Dans les péridotites à spinelle, l'H est incorporé dans les défauts ponctuels de l'olivine et des pyroxènes. Par contre, le spinelle mantellique (chromite) ne contient pas d'H dans sa structure (*e.g.,* Bromiley *et al.,* 2010) (Figure I.2). La structure cristalline des NAMs, ne permet pas l'incorporation d'un groupement OH^- indépendant et l'H y est incorporé sous forme de proton H^+ formant une liaison de van der Waals avec un atome d'oxygène de la structure cristalline (par partage d'électrons). L'H peut se placer dans un site tétraédrique T (Figure I.3) ou dans les sites métalliques (M1, M2). Pour permettre l'incorporation d'H des substitutions sont nécessaires afin de respecter les règles de Goldschmidt (Goldschmidt, 1937; Ringwood, 1955).

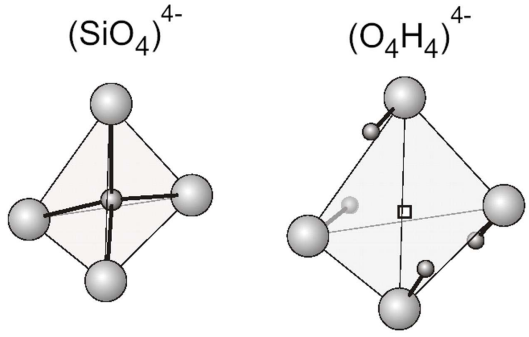

Figure I.3 – Structure d'un tétraèdre SiO_4, ainsi que d'un tétraèdre où un site vacant de silicium a permis l'incorporation de 4 H.

Les réactions d'incorporation de l'H dans le réseau cristallin dépendent de la position du H^+. Ces réactions sont écrites selon la notation de Kröger et Vink, 1956 qui permet de décrire les atomes en présence, leurs emplacements dans la structure (site atomique indiqué en indice) et la charge électrique résultante du site (•, ×, ′ comme exposant indiquant un excès de charge, une charge nulle et une charge manquante, respectivement, Annexe 1).

(i) Par réaction d'oxydo-réduction, l'H peut se mettre en position interstitielle :

$$\mathrm{Fe}_{\mathrm{Me}}^{\bullet} + \frac{1}{2}\mathrm{H}_2(\mathrm{gaz}) \rightarrow \mathrm{Fe}_{\mathrm{Me}}^{\times} + \mathrm{H}_{\mathrm{i}}^{\bullet} \quad \text{(I.1)}$$

(ii) L'H peut s'associer à un site métallique vacant (M1, M2, Figure I.2) :

$$2(\mathrm{H}_{\mathrm{i}}^{\bullet}) + \mathrm{V}_{\mathrm{Me}}'' \rightarrow 2\mathrm{H}_{\mathrm{Me}}^{\times} + V_i^{\times} \quad \text{tel que } \{2(\mathrm{OH})_{\mathrm{O}}^{\bullet} - \mathrm{V}_{\mathrm{Me}}''\}^{\times} \quad \text{(I.2)}$$

La création de ce site vacant peut, par exemple, être liée à la précipitation de MgO, telle que :

$$2(\mathrm{H_2O})_{(f)} + 2\left(\mathrm{Mg}_{\mathrm{Mg}}^{\times}\right) \leftrightarrows 2\mathrm{MgO}_{(s)} + 2(2\mathrm{H})_{\mathrm{Mg}}^{\mathrm{X}} \quad \text{avec } \left\{2(\mathrm{OH})_{\mathrm{O}}^{\bullet} - \mathrm{V}_{\mathrm{Mg}}''\right\}^{\times} \quad \text{(I.3)}$$

(iii) Des atomes d'H peuvent créer un défaut dit de type « hydrogrenat » impliquant 4 atomes d'H intégrant un site tétravalent :

$$2\mathrm{H_2(g)} + \mathrm{V}_{\mathrm{Si}}'''' \rightarrow \mathrm{H}_{\mathrm{Si}}^{\times} \quad \text{tel que } \{4(\mathrm{OH})_{\mathrm{O}}^{\bullet} - \mathrm{V}_{\mathrm{Si}}''''\}^{\times} \quad \text{(I.4)}$$

$$\mathrm{H}_{\mathrm{i}}^{\bullet} + \mathrm{Al}_{\mathrm{Si}}' \rightarrow (\mathrm{AlH})_{\mathrm{Si}}^{\times} \quad \text{avec } \{(\mathrm{OH})_{\mathrm{O}}^{\bullet} - \mathrm{Al}_{\mathrm{Si}}'\}^{\times} \quad \text{(I.5)}$$

Cependant, ces défauts peuvent exister sans être occupés par un ou plusieurs atomes d'H. Par conséquent, il faut distinguer la concentration d'H, soit la quantité d'H présent, et la solubilité en H, soit la quantité maximale d'H que le minéral peut contenir dans les différents sites atomiques afin d'arriver à saturation.

2.1 L'olivine

L'olivine (ol) est le minéral le plus abondant du manteau lithosphérique (40 à 80 % en volume). L'incorporation et la solubilité de l'H dans l'olivine ont été intensément étudiées afin de mieux contraindre la capacité de stockage en eau du manteau. La loi de solubilité de l'H dans l'olivine réalisée par Férot et Bolfan-Casanova (2012) montre qu'à 150 km de profondeur la solubilité est 2,4 fois plus importante qu'à 50 km (ca. 30 ppm wt. H_2O).

Cependant les analyses sur échantillons naturels restent globalement à 20 ppm wt. H_2O en dessous de cette courbe (Demouchy *et al.,* 2015, Figure 5.A). Cette différence de concentration pourrait impliquer soit que la valeur de solubilité, c'est à dire la saturation des sites atomiques de stockage, n'est pas atteinte, soit une perte non négligeable de l'H contenu dans l'olivine pendant sa remontée à la surface dans le magma. Ce dernier cas est possible mais pas omniprésent ; des profils de déshydration par diffusion ionique n'ont été observés que pour trois localités (Patagonie, Demouchy *et al.,* 2006, Mexico, Peslier et Luhr, 2006 et Hawaï, Peslier *et al.,* 2015).

2.2 L'orthopyroxène

Dans l'orthopyroxène (opx), minéral le plus abondant après l'olivine dans les péridotites du manteau sommital, les mécanismes d'échange et de stockage impliquant l'H et les cations trivalents comme l'Al^{3+}, le Fe^{3+}, le Cr^{3+} jouent un rôle important (Stalder, 2004 ; Stalder *et al.,* 2005). Les études expérimentales montrent que l'augmentation d'1 wt. % Al_2O_3 dans une enstatite à 1,5 GPa et 1100 °C fait passer la solubilité de l'H de 199 à 1100 ppm wt. H_2O (Rauch et Keppler, 2002). De plus, Mierdel *et al*. (2007) ont montré que le long d'un géotherme lithosphérique, l'enstatite dopée en Al (mais sans fer) peut incorporer beaucoup d'H dans sa structure (> 300 ppm wt. H_2O), mais qu'avec l'augmentation de la température et de la pression (la profondeur), la solubilité de H diminue drastiquement. Les auteurs suggèrent que ce comportement est dû au changement de partage de l'Al entre l'enstatite et la phase alumineuse (spinelle puis grenat) et de l'H associé. En comparaison, les concentrations en H dans l'orthopyroxene du manteau sommital varient de 20 à 450 ppm wt. H_2O (*e.g*., Ingrin et sckogby, 2000 ; Demouchy et Bolfan-Casanova, soumis).

2.3 Le clinopyroxène

Le clinopyroxène (cpx) de type diopside ($CaMgSi_2O_6$) est le minéral qui contient généralement le plus d'H dans la péridotite à spinelle. Comme pour l'opx, la présence d'aluminium tétraédrique Al^{3+}, augmente l'incorporation d'H sous forme de défauts associés (*i.e.*, $Al^{3+}+H^{+}\leftrightarrow Si^{4+}$ et $Al^{3+}+H^{+}\leftrightarrow 2Mg^{2+}$; Rauch et Keppler, 2002 ; Mierdel *et al.,* 2007), de même que la présence de Ca (Gavrilenko, 2008). Etant donné l'importance des cations trivalents comme l'Al^{3+} dans les réactions d'incorporation de l'H ; la présence en grand nombre dans le cpx d'éléments en traces trivalents sensibles au métasomatisme comme les terres rares (REE[1]) peut jouer un rôle déterminant dans la solubilité de l'H dans le cpx. En effet, les réactions d'incorporation des REE dans la structure cristalline peuvent créer des défauts associés hydratés (Van Orman *et al.,* 2001):

$$REE_2O_3 + 2CaO_{M2}^{\times} + Mg_{M1}^{\times} \leftrightarrows 2REE_{M2}^{\bullet} + V_{M1}'' + MgO(s) + 2CaO(s) \qquad (I.6)$$

[1] De l'anglais « Rare Earth Elements » qui sont les lanthanides de La à Lu.

$$REE_2O_3 + 3CaO_{M2}^{\times} \leftrightarrows 2REE_{M2}^{\bullet} + V_{M2}'' + 3CaO(s) \quad (I.7)$$

Les concentrations en H des clinopyroxènes des échantillons naturels de péridotites à spinelle vont de 5 à 1000 ppm wt. H_2O (Ingrin *et al.* 1989; Ingrin et Skogby, 2000 ; Skogby et Rossman, 1989; Skogby *et al.,* 1990 ; Skogby, 1994 ; Chen *et al.,* 2006; Demouchy et Bolfan-Casanova, soumis). Le diopside étant le NAMs le plus fusible de cette péridotite, il est un acteur principal du cycle profond de l'eau, tant en terme de stockage que de recyclage (Bell *et al.,* 2004 ; Bolfan-Casanova, 2005).

I.4 Mobilisation de la matière dans le manteau : la Fusion

I.4.1 La fusion : la théorie

Pour induire la fusion d'une roche, il faut que la température de fusion d'au moins un de ses minéraux constitutifs soit dépassée. Cela se fait soit par augmentation de la température, soit par décompression adiabatique, soit par ajout d'un fluide libre dans le système (plus ou moins riche en éléments incompatibles (comme les volatils), ou un mélange des trois possibilités (McKenzie, 2000) (Figure I.4).

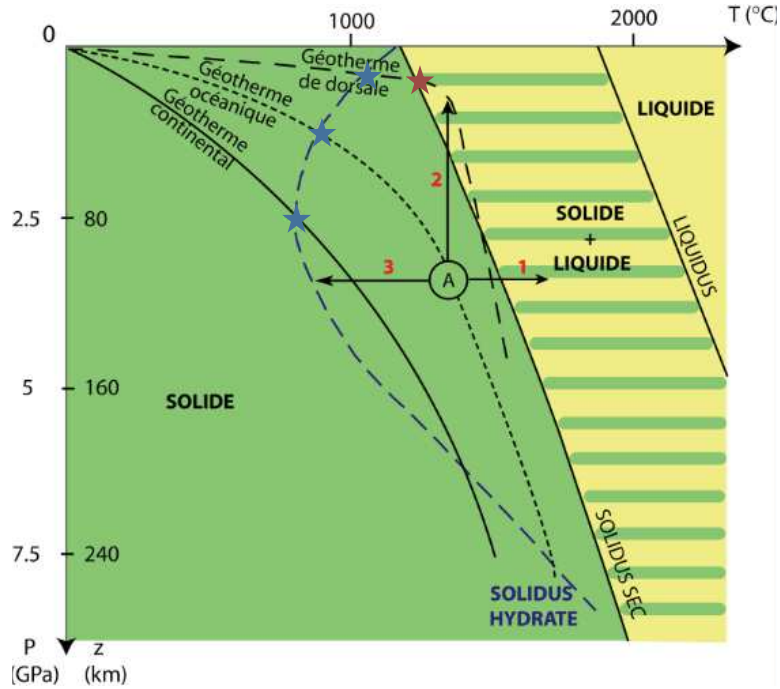

Figure I.4 – Température du système péridotitique (°C) en fonction de la profondeur (km) et de la pression (GPa). La fusion est possible lorsque le géotherme recoupe le solidus, à partir des étoiles bleues pour le solidus hydraté, et à partie de l'étoile rouge pour le solidus sec. (1) augmentation de la température. (2) décompression adiabatique. (3) évolution du solidus sec vers un solidus hydraté par l'apport de fluides. (Modifié d'après Caron *et al*, 1989).

Cette température de fusion est la température du solidus pour une pression donnée. Elle est fonction de l'assemblage minéralogique et de la composition chimique de chacune des

phases cristallines de la roche ainsi que des conditions (pression et température, présence de volatils) du milieu dans lequel se trouve cette roche. Dans le cas de la fusion des péridotites, un liquide est produit et un solide est résiduel : la fusion est donc partielle. Lors de la fusion de la péridotite, ce sont les minéraux les plus riches en éléments volatils (i.e. H, C, Cl, F, S) qui vont fondre les premiers, puis la phase alumineuse (spl, ou grenat) et le cpx, suivit de l'opx et enfin l'olivine qui est le minéral le moins fusible. Ainsi par différents degrés de fusion partielle, on peut passer d'une lherzolite à une harzburgite, voire à une dunite (P < 2 GPa ; Walter *et al.*, 1995). Dans le cas de la fusion d'un manteau anhydre à 2 GPa, la température de fusion du cpx, de l'opx et de l'olivine est respectivement de 1240 °C, 1295 °C et 1410 °C (Kushiro, 1969).

Différentes réactions sont mises en jeu lors de la fusion du manteau.

(i) En l'absence de fluide libre et de minéraux hydratés, les phases contenant le plus d'Al fondent, créant un liquide et un solide résiduel magnésien (Kinzler et Grove, 1992; Baker et Stolper, 1994) tel que :

$$Cpx + Opx + Gt \rightleftarrows Liquide + Ol \quad (I.8)$$

(ii) À 1,2 GPa, dans le champ de stabilité du spinelle, Kinzler et Grove (1992) montrent également que :

$$Cpx + Opx \rightleftarrows Liquide + Ol \quad (I.9)$$

(iii) Dans le champ de stabilité de l'amphibole, donc en présence de l'eau dans la structure cristallographique, l'amphibole fond avec les autres phases alumineuses :

$$Am + Opx + Sp/Gt \rightleftarrows Liquide + Ol \quad (I.10)$$

(iv) A plus haute pression ou température (pour une pargasite, P> 3GPa, T> 1050°C), l'amphibole se déstabilise selon les réactions suivantes (Holloway, 1973 ; Kinzler et Grove, 1992 ; La Tourette *et al.,* 1995) augmentant la concentration en H dans la phase liquide:

$$Am \rightleftarrows Cpx + Ol + spl + liquide \quad (I.11)$$

$$Am + Ol \rightleftarrows Cpx + Opx + Gt + H_2O \quad (I.12)$$

I.4.2 Les traceurs géochimiques de la fusion

Le rééquilibrage chimique se fait entre le liquide présent et le solide qui affecte chacun des minéraux de l'encaissant. En effet, le degré d'incompatibilité des éléments dans un minéral par rapport au fluide n'est pas le même. Par exemple, le Cr est moins incompatible que l'Al dans le spinelle, en conséquence le cr# (100×(Cr/Cr+Al)) du spinelle augmente. De la même façon le pourcentage de forstérite de l'olivine augmente ainsi que le mg# de l'opx. Au contraire la concentration en Al_2O_3 de l'opx diminue (Dick *et al.,* 1984). Les éléments en traces comme le Ti se retrouvent concentrés dans le liquide. Une roche qui a subi de la fusion présente des olivines moins titanifères que les olivines d'une roche fertile.

Les éléments les plus affectés sont les éléments les plus incompatibles comme les REE. Les spectres de REE de cpx de roche, ayant subie de la fusion se retrouvent appauvris en terres rares légères (LREE[2], qui sont les plus incompatibles). Ces spectres sont marqués par une diminution du rapport La/Sm par rapport à celui du manteau primitif. Si le degré de fusion est important, les concentrations en REE lourdes (HREE[3]) diminuent. Cependant, les observations pétrographiques, minéralogiques et géochimiques ne suivent pas toujours un simple modèle de fusion partielle connu, (Menzies, 1987). Pour cela, il faut intégrer aux modèles un autre processus : le métasomatisme.

I.4.3 La fusion : les modèles

Deux modèles extrêmes décrivent numériquement la fusion partielle : (1) la fusion à l'équilibre (*batch melting*) en système fermé et (2) la fusion fractionnée (*fractional melting*) en système ouvert.

L'équation reliant la concentration d'un élément dans le solide (Cs) et le taux de fusion (F) pour une fusion à l'équilibre non modale (Shaw, 1970) c'est-à-dire où les proportions relatives des minéraux évoluent avec la fusion est :

$$Cs = \frac{(D_0 - PF)c_0}{(1-F)(D_0 + F(1-P)} \quad (I.13)$$

La fusion fractionnée fait intervenir comme la fusion à l'équilibre, c_0 la concentration initiale de l'élément, et D le coefficient de partage de l'élément entre le solide et le fluide. Néanmoins elle prend en compte P un paramètre reliant la proportion de fusion des phases minérales (p_i) et les coefficients de partage ($D^{i\text{-}m}$) entre le minéral i et le fluide (m) telle que :

$$P = \sum_i p_i D^{i-m} \quad (I.14)$$

On obtient alors l'équation reliant la composition du solide Cs au taux de fusion F selon l'équation de fusion fractionnée (Shaw, 1970) telle que :

$$Cs = \frac{c_0}{1-F} \times \left(1 - \frac{PF}{D_0}\right)^{\left(\frac{1}{P}\right)} \quad (I.15)$$

Dans le premier cas (Equation (I.13)), le liquide n'est pas extrait, il se rééquilibre en permanence avec le solide résiduel (Gast, 1968 ; Shaw, 1970). Dans le second cas (Equation (I.15)), chaque liquide produit est extrait du système, seul le dernier liquide produit est en équilibre avec le solide résiduel (Allègre et Minster, 1978 ; Shaw, 1970). Des modèles plus réalistes de fusion continue (Langmuir *et al.,* 1977 ; Shaw, 2000) concilient les deux, en permettant l'extraction d'une partie du liquide tout au long de la fusion mais jamais dans sa totalité. Cette quantité de liquide extrait et de liquide coincé dépend de la viscosité du liquide, du type de source et du champ de contraintes.

---

[2] De l'anglais, « *Light rare Earth elements* »
[3] De l'anglais « *Heavy rare Earth elements* »

Pour de très faible taux de fusion (<1 %), les modèles de fusion à l'équilibre et de fusion fractionnée qu'ils soient exprimés sous forme modale ou non modale donnent des résultats très proches (Figure I.5). Norman (1998) simplifie ces modèles en ne considérant que la fusion du cpx. Les équations de la fusion à l'équilibre (équation (I.16)) et de la fusion fractionnée (équation (I.17)) permettent de calculer la concentration de l'élément considéré dans le résidu solide (C_{cpx}). Elles ne font intervenir que la proportion de cpx (X_{cpx}), la concentration initiale de cet élément (C_0), le coefficient de partage de cet élément entre le cpx et le liquide silicaté (D_{cpx}) et le degré de fusion partielle (F).

$$C_{cpx} = (D_{cpx} \times C_0)/(D_{cpx} \times X_{cpx} \times (1 - F) + F) \quad \text{(I.16)}$$

$$C_{cpx} = (C_0/X_{cpx}) \times (1 - F)^{[1/D_{cpx}X_{cpx}]-1} \quad \text{(I.17)}$$

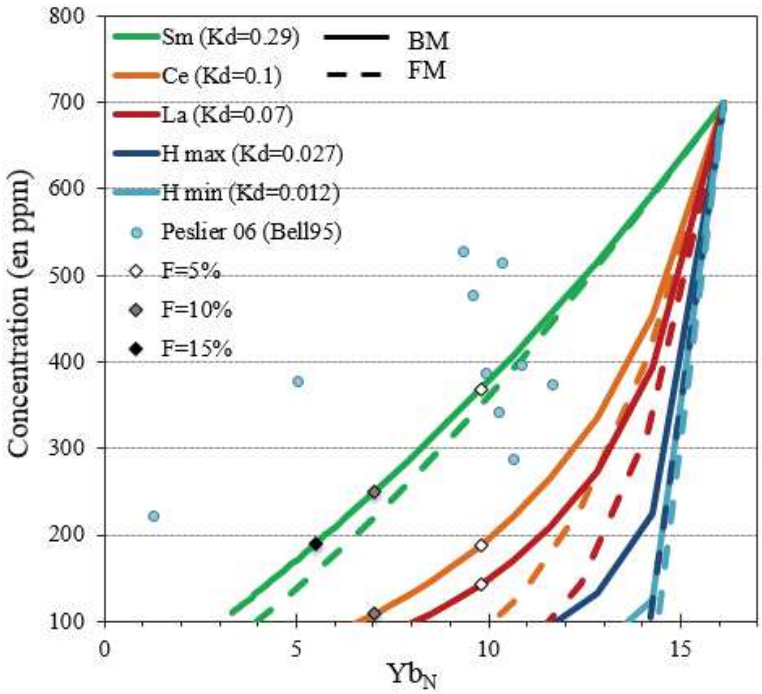

Figure I.5 – Comparaison des modèles de fusion à l'équilibre, fusion fractionné du modèle de Norman (1998). *i.e.*, concentrations des éléments calculées en fonction d'un marqueur de la fusion l'Yb_N (N pour normalisée aux valeurs des chondrites d'après Sun et McDonough, 1995). $Kd^{cpx/melt}$ Yb et Sm d'après Johnson *et al.*, 1998 ; $Kd^{cpx/melt}$ La et Ce d'après Adam et Green, 2006 ; $Kd^{cpx/melt}$ H minmum et maximum de la gamme d'après Tenner *et al.*, 2009; Novella *et al.*, 2014 ; Rosenthal *et al.*, 2015. Pour comparaison, les données de Peslier et Luhr., 2006 sur échantillons naturels sont représentés.

I.5 Transport de matière dans le manteau : extraction des liquides de fusion et métasomatisme.

La fusion débute aux joints de grains, un faible pourcentage de porosité se crée alors. Le liquide ayant une densité plus faible que le solide environnant, le liquide va migrer contre la gravité. Il va mouiller la roche et circuler dans le manteau. L'interaction entre ce fluide et la roche se traduit par un échange d'éléments chimiques. Ce processus par lequel la composition d'un minéral, d'une roche ou d'une portion de roche est altérée de façon généralisée est le métasomatisme. L'importance des interactions entre le fluide et la roche est liée à la quantité de fluide, au type de fluide en présence, et au mécanisme de circulation. Chacun de ces paramètres peut être défini entre deux types extrêmes. (Tableau I.1).

Tableau I.1 – Caractéristiques des pôles entre lesquels évoluent les liquides magmatiques.

Volume de liquide faible ou faible rapport magma/roche	Volume de liquide élevé ou rapport magma/roche élevé
Liquide riche en volatils (*e.g.*, liquide carbonaté)	Liquide silicaté (*e.g.,* liquide basaltique)
Viscosité faible	Viscosité élevée
Percolation au joint de grains	Fracturation hydraulique (*e.g.*, dyke)
Métasomatisme cryptique	Métasomatisme modal

I.5.1 Volume de fluide mis en jeu lors du métasomatisme

Le volume de fluide produit est conditionné par le taux de fusion de la péridotite. Ce taux dépend de la pression, de la température, de l'assemblage minéralogique de la péridotite ainsi que de la présence de fluide libre. Par conséquent, le taux de fusion est lié au contexte géodynamique. A l'archéen, la terre étant plus chaude, les péridotites atteignaient des domaines de fusion à des pressions plus importantes. Les taux de fusions archéens étaient très élevés (≥ 40 %), formant des laves magnésiennes de type komatiite. Actuellement, les géothermes sont beaucoup plus bas et ne permettent plus de tels taux de fusion élevés. En moyenne le taux de fusion est de 10 % pour les dorsales lentes, 25 % pour les dorsales rapides (*e.g.,* Niu et Batiza, 1997 et références associées). Ces processus permettent la mise en place de roches magmatiques de type basalte et gabbro. Le taux de fusion partielle dans le cas d'OIB (*ocean island basalt*) est variable. Lorsqu'il est faible, de l'ordre de 5 %, il en résulte des basaltes alcalins et des basanites (Hofmann et White, 1982 et références associées). Dans les zones de subduction, la fusion est complexe : la croûte océanique, les fluides et les minéraux hydratés dans le coin mantellique jouent un rôle majeur dans la fusion. On y retrouve des basaltes andésitiques jusqu'à des tholéites. De très faibles taux de fusion partielle sont invoqués (inférieurs à 0,5 %, Dalton et Presnall, 1998; Lee et Wyllie, 1998) pour expliquer l'origine de laves moins courantes et beaucoup plus riches en éléments très

incompatibles, de type laves carbonatées (carbonatites, néphélinites pauvres en silice) (Bell, 1998 ; Woolley et Kjarsgaard, 2008 ; Fischer *et al.,* 2009).

I.5.2 Les fluides

Dans le manteau terrestre, les fluides libres métasomatisants peuvent donc être très variables : carbonatés (*e.g.*, Dautria *et al.,* 1992, Yaxley *et al*., 1991), silicatés (*e.g.*, Cortolti *et al.,* 2000), aqueux. Ces fluides sont plus ou moins riches en éléments incompatibles comme les REE, les éléments lithophiles à large rayon ionique (LILE[4] : K, Rb, Cs, Sr, Ba), les éléments à fort potentiel ionique (HFSE[5] : Ti, Zr, Nb, Ta, Hf, Th, U), les espèces volatils (H_2O, CO_2, CO, CH_4, H_2, SO_2, H_2S, HCl, HBr, HI), les chlorures (NaCl, KCl, CaCl) et le S.

Ici le terme « fluide » permet de regrouper les liquides silicatés, les liquides non silicatés, les fluides supercritiques ainsi que les fractions vapeurs dont les limites de phases et les propriétés thermodynamiques (équation d'état) ne sont pas bien définies voire inconnues (*e.g.,* Yang *et al.,* 2014, Baptiste *et al.,* 2015). Cependant, les auteurs ont tendance à utiliser le terme « fluide » pour décrire une phase non-solide riche en espèces volatils dissoutes (*e.g.,* H_2O-CO_2), et le terme « liquide » (magma / melt) pour un liquide silicaté riche en solides dissous (*e.g,.* silicates).

I.5.3 Les modes de migration : échelles du métasomatisme

Deux modèles de circulations dans la roche s'opposent :

(1) le transport par fracturation hydraulique. Lorsque la pression de fluide est trop élevée dans le système, des fractures se créent en fonction des hétérogénéités pétrologiques et structurales de l'encaissant. Le fluide peut alors circuler de façon plus rapide, et sur de plus grandes distances. Ce mécanisme de transport est considéré comme le mécanisme dominant de transfert de fluides du manteau à la croûte (Spera, 1980 ; Nicolas, 1986).

(2) la migration de fluide par percolation aux joints de grains. Deux mécanismes induisent ce transport : les écoulements poreux réactifs (*e.g.,* Kelemen, 1990, McKenzie, 1984 ; Thompson et Connolly, 1990) et l'infiltration poreuse liée aux tensions de surface (Stevenson, 1986). Dans les deux cas, le mouvement est possible uniquement lorsque le liquide formé en joint de grains crée de la porosité interconnectée dans la péridotite encaissante. L'écoulement poreux est contrôlé par la loi de Darcy. La migration est contrôlée par un gradient hydraulique, tandis que dans l'infiltration poreuse, la migration est contrôlée par les tensions de surface. La connectivité du fluide interstitiel dépend des phases en présence. L'assemblage minéralogique joue donc un rôle majeur dans ce cas. Toramaru et Fuji (1986) montrent que les joints triples entre olivines sont plus favorables à la connectivité du fluide que les autres.

---

[4] De l'anglais « *large-ion lithophile elements* »
[5] De l'anglais « *High field strength elements* »

Cependant, la connectivité du fluide dépend en grande partie du type de fluide. Les fractions vapeur (fluides de faible densité) comme l'H_2O ou le CO_2 « purs » forment des angles dièdres avec les faces minérales trop grands pour permettre le développement d'un réseau (Figure I.6) (Watson et Brenan, 1987 ; Menzies et Dupuy, 1991). La fracturation est donc un mécanisme plus propice à leur migration (Pili *et al.,* 1997) surtout lorsqu'ils se retrouvent dissous dans des liquides silicatés (Bureau et Keppler, 1999). Au contraire, les liquides carbonatés et silicatés forment des angles dièdres inférieurs à 60°, ce qui permet l'inter-connectivité du fluide entre les grains (Figure I.6, Menzies et Dupuy, 1991). Plus le liquide contient d'éléments volatils, plus sa viscosité, sa densité (McKenzie, 1989) et la valeur de ses angles dièdres diminuent (Von Bargen et Waff, 1988), ainsi que sa température de solidus. Le processus de transport mis en jeu pourra évoluer jusqu'à un processus intermédiaire : *l'écoulement chenalisé* (Davies, 1999) qui est induit par le piégeage de fluides qui se connectent créant des chenaux de 0,001 à 100 mètres de large.

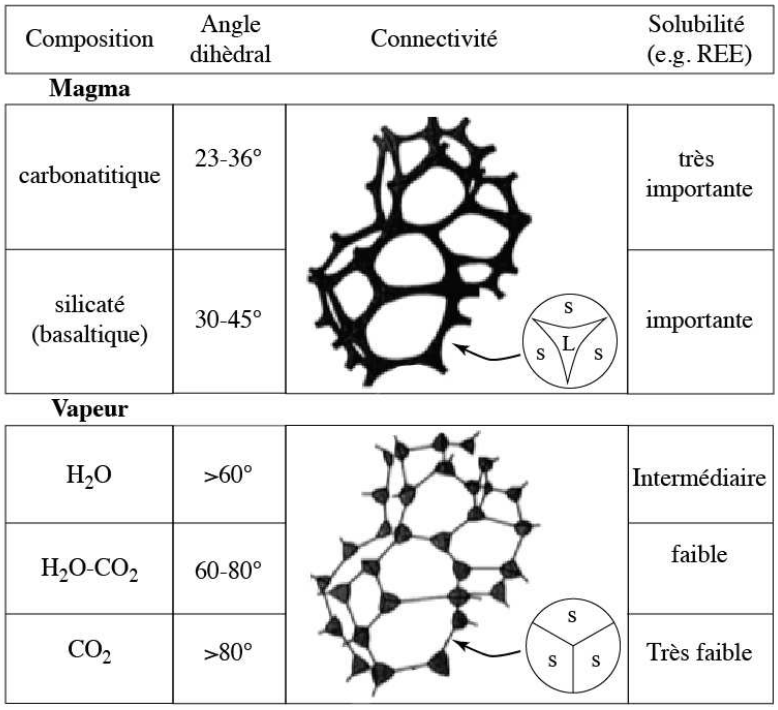

Figure I.6 – Connectivité des fluides dans les dunites en fonction de l'angle dièdre formé avec les faces cristallines. (d'après Menzies et Dupuy, 1991, Fig.3)

Le rééquilibrage, chimique et thermique, continu entre le liquide et la péridotite encaissante contrôle le degré de cristallisation du fluide et donc sa distance de migration. Ce rééquilibrage dépend des coefficients de partage fluide/roche mais aussi de la porosité, la perméabilité, le coefficient de diffusion ionique, la température, la pression et la vitesse de circulation du liquide dans les conduits (Bédart, 1989 ; Vasseur *et al.*, 1991).

I.5.4 Les différents métasomatismes

Trois types majeurs de métasomatismes ont été distingués :

- *le métasomatisme modal* (Harte, 1983 ; Dawson, 1984) qui implique la cristallisation de nouvelles phases minérales (*e.g.,* amphibole, micas, sulfures) aux dépens des minéraux préexistants (Aoki, 1975; Erlank *et al.*, 1987; Jones *et al.*, 1982; Haggerty, 1983 ; Bodinier *et al.,* 1990).
- *le métasomatisme crypto-modal* (« stealth metasomatism ») qui implique la cristallisation de minéraux néoformés d'une phase majeure d'une péridotite (*e.g.,* du clinopyroxène secondaire dans une lherzolite). Sous ce terme se retrouve le processus de refertilisation (*e.g.,* Arai, 1994 ; Bodinier et Godard, 2003; Beyer *et al.*, 2006) au cours duquel s'effectue la réaction suivante :

$$Ol + Opx + Fluide1 \rightleftarrows Cpx + Fluide2 \qquad (I.18)$$

- *le métasomatisme cryptique* (Dawson, 1984) qui implique des changements de composition des minéraux préexistants sans formation de nouvelles phases. Typiquement on observe un découplage entre éléments majeurs, en traces et les REE (Frey et Green, 1974 ; Frey et Prinz, 1978 ; Nixon *et al.*, 1981 ; Menzies, 1983) *i.e*., par exemple, un enrichissement en LREE dans les minéraux d'une harzburgite.

En contexte intra-plaque, deux types majeurs de fluides induisent du métasomatisme. On distingue le *métasomatisme silicaté* mafique riche en alcalins (± riche en Na, K, Rb, CO_2 ; Wulff-Pedersen *et al.*, 1996, 1999) et le *métasomatisme carbonatitique / carbonaté* (*e.g.,* Yaxley *et al.*, 1991 ; Ionov *et al.*, 1993 ; Coltorti *et al.*, 1999).

Dans le premier cas, le fluide percolant est un liquide silicaté produisant de forts enrichissements en éléments incompatibles par rapport aux modérément incompatibles. Ce type de percolation peut mener à un métasomatisme de type modal. Si les conditions intensives et la composition de la roche (présence de grenat) concordent, ce type de fluide peut mener à la cristallisation de phlogopite (mica magnésien) (Dawson, 2001 ; Van Achterbergh *et al.*, 2001). Dans le cas d'un métasomatisme silicaté, la péridotite s'enrichit progressivement en K, Na, Ca, Rb, Sr, Ba et en éléments en traces incompatibles (LREE et les HFSE) (Menzies *et al.,* 1987 ; Dawson, 2001 ; van Achterbergh *et al.,* 2001).

Dans le second cas, les fluides percolants sont carbonatitiques c'est-à-dire pauvre en Si et riche en Ca, Sr, U, Th et en CO_2 dissous. Ils sont caractérisés par de forts enrichissements en LREE et des appauvrissements en HFSE (± Nb). On retrouve des fractionnements « anormaux » entre des éléments de comportement généralement associé, aboutissant à des rapports Zr/Hf et Nb/Ta élevés (Dautria *et al.,* 1992 ; Ionov *et al.,* 2002) par rapport aux valeurs du manteau primitif (McDonough et Sun, 1995). Hamilton *et al.* (1989) présentent des coefficients de partages dans des conditions de péridotites à grenat permettant aux REE de rester coincées dans les carbonates tandis que l'Hf reste concentré dans la phase silicatée.

Des études expérimentales ont montré que les magmas carbonatitiques pourraient provenir de faibles taux de fusion partielle (< 0,5 %) de péridotites carbonatées à partir de ~ 2 GPa (~ 70 km) (*e.g.,* Dalton et Presnall, 1998 ; Lee et Wyllie, 1998 ; Gudfinnsson et Presnall, 2005).

Néanmoins, ces deux agents métasomatiques ne sont pas obligatoirement inconciliables (Menzies et Chazot, 1995). Par exemple, au cours de la cristallisation fractionnée d'un liquide silicaté, le fluide résiduel s'enrichit en éléments les plus incompatibles (comme les alcalins qui sont les éléments majeurs les plus incompatibles, et les éléments volatils). D'autre part, les interactions fluide/roche permettent une évolution chimique du fluide percolant lors de son trajet. Ce processus est lié à un fractionnement entre éléments comme proposé dans le modèle d'effet chromatographique. Cet *effet chromatographique* implique la mise en place de fronts de concentration d'éléments avançant à différentes vitesses dans le fluide (Navon et Stolper, 1987, Vernières *et al.,* 1997 ; Bodinier *et al.*, 1990 ; Vasseur *et al.,* 1991 ; Ionov *et al.*, 2002). Les fluides en haut et en bas de la colonne chromatographique n'ont alors plus la même composition chimique et donc plus les mêmes caractéristiques (*e.g.,* viscosité, densité, fO_2, fH_2O, fCO_2). Le fluide le plus éloigné de la source de l'agent métasomatique initial s'enrichit progressivement en éléments les plus incompatibles (Figure I.7; Navon et Stolper, 1987). Ce modèle permet d'expliquer de très grandes variations de rapports La/Ce, La/Nd observées sur les échantillons d'un même site. Les auteurs montrent l'évolution potentielle que peut suivre la composition chimique de la roche encaissante (Figure I.7). La péridotite en haut de la colonne de percolation garde une composition initiale jusqu'à ce qu'elle soit affectée par le 1er fluide au temps t = tc. Puis, comme les fronts d'éléments les plus incompatibles avancent plus rapidement dans la colonne, leurs concentrations dans la roche augmentent avant celles des autres. Ce processus fait naître le début d'une forme en « U » du spectre des REE. Dans le cas présenté en Figure I.7, la composition du fluide métasomatisant correspond au fluide extrait lors de 0,1 % de fusion à l'équilibre d'un manteau chondritique avec 65 % d'ol + spl, 22 % d'opx, 13 % de cpx. La percolation se fait, quant à elle, dans un encaissant correspondant au résidu d'une fusion à l'équilibre de 20 % d'un manteau chondritique similaire, alors composé de 74 % d'ol, 22 % l'opx, et 4 % de cpx. Les valeurs de Kd des éléments ont été calculées par les auteurs en utilisant les valeurs données par Frey *et al.* (1978) et sont indiquées dans la figure.

La présence de fluides permet un transport de matière beaucoup plus rapide que la diffusion à l'état solide, et donc un rééquilibrage par dissolution des phases préexistantes et la précipitation de produits. Par exemple, les veines de pyroxénites sont généralement interprétées comme le produit de la cristallisation d'un liquide silicaté en profondeur qui métasomatise la péridotite encaissante lors de la percolation.

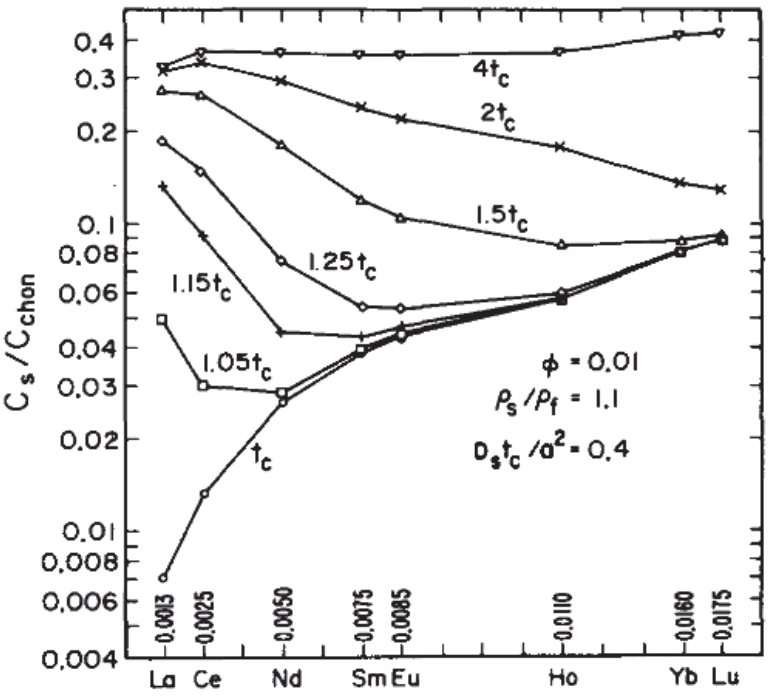

Figure I.7 – Evolution de spectres de REE d'une péridotite appauvrie en REE lors d'un métasomatisme impliquant un liquide silicaté enrichi en éléments incompatible (Navon et Stolper, 1987 ; Figure 4). La percolation commence au temps t. La première contamination de la roche en haut de la colonne se fait à $t=t_c$. La composition du liquide percolant évolue avec le temps ce qui se traduit par un changement de composition de la roche encaissante jusqu'à $t=4t_c$. La quantité de volume s'exprime en $L\phi$ avec L la hauteur de la colonne et ϕ la fraction de liquide présente dans la colonne par volume (= porosité).

I.6 Problématique de thèse

Le manteau pourrait être un réservoir d'eau non négligeable de la Terre (~ 2700 ± 1350 ppm wt. H_2O soit 10 ± 5 fois la masse des océans, Marty, 2012). Mais les échantillons naturels du manteau lithosphérique ont des concentrations beaucoup plus faibles et assez variables (sur roche totale : 10 à 160 ppm wt. H_2O (Demouchy et Bolfan-Casanova, soumis). En absence de minéraux hydratés (*e.g.*, amphibole), ce sont les pyroxènes qui contrôlent le budget de l'eau dans la roche (section I.3.2). Or la fusion et le métasomatisme affectent principalement les pyroxènes. Ces processus devraient donc contrôler le transport de l'H dans le manteau comme pour les autres éléments en traces. Que ce soit lors de la fusion, où les éléments les plus incompatibles rejoignent le fluide ou lors du métasomatisme, où les éléments se séparent par chromatographie, le comportement des éléments est dépendant de leur incompatibilité et donc de leurs coefficients de partage (Figure I.7).

La recherche des coefficients de partage de l'H en fonction de différents systèmes est un enjeu actuel. De nombreuses études expérimentales portent sur la solubilité, et le coefficient de partage de l'H entre minéraux et /ou liquides silicatés dans diverses conditions de pression, de température, en fonction d'un système chimique donné. Le TableauI.2 présente un résumé des travaux portant sur les coefficients de partages de l'H dans le manteau lithosphérique. Les différents résultats obtenus sont très variables ($Kd^{cpx/melt}$ de 0.012 à 0.027) plaçant l'H dans le cpx tel un LREE (Dixon *et al.,* 2002 ; Tenner *et al*., 2009, Novella *et al.,* 2014, Aubaud *et al*., 2004 ; Rosenthal *et al.*, 2015). Les valeurs de coefficients de partage expérimentaux de l'H pour l'olivine et l'opx place aussi l'H parmi les LREE ($Kd^{ol/melt}$ de 0.0003 à 0.0025 ; $Kd^{opx/melt}$ de 0.003 à 0.027).

Des précédentes études (*e.g*., Michael, 1995 ; Danyushevsky *et al.,* 2000 ; Dixon *et al.,* 2002 ; Bizimis et Peslier, 2015 ; Peslier *et al*. 2015) utilisent le ratio H_2O/Ce comme traceurs de la source mantellique et des processus magmatiques. L'utilisation de ce ratio dans ces études a pour hypothèse que l'H est légèrement moins compatible que le Ce (Dixon *et al.*, 2002). Or les données expérimentales ne permettent pas de conclure avec certitude sur le degré d'incompatibilité de l'H par rapport aux REE (Tableau I.2) et donc sur le comportement de l'H pendant les processus mantelliques tels que la fusion partielle et le métasomatisme.

Cette thèse se focalise sur les roches ultramafiques du faciès à spinelle du manteau sous continental, d'une part pour déterminer les concentrations en H, d'autre part pour étudier le comportement de l'H lors des processus magmatiques et mantelliques.

Ces études se basent sur une caractérisation pétro-géochimique de xénolites de péridotites. L'acquisition des données des concentrations en éléments majeurs, des éléments en traces dont l'H est présentée dans le chapitre « Méthodes analytiques et échantillons étudiés » (**chapitre 2**).

Pour répondre à la problématique de cette thèse, différents processus magmatiques et mantelliques ont été ciblés afin d'y étudier le comportement de l'H ainsi que les concentrations associées d'H dans la roche.

Avant de s'intéresser aux processus mantelliques, il faut s'assurer que les concentrations en H des NAMs des xénolites ne sont pas altérées au travers des systèmes magmatiques superficiels. Le **chapitre 3** porte sur la diffusion ionique de l'H dans des péridotites mantelliques transportées vers la surface par des laves. L'absence de variation de concentrations en H dans un minéral suggèrera que les concentrations sont mantelliques. Par contre, l'existence de profils de concentration intracristalline implique un changement des concentrations mantelliques initiales. Ce type d'observation peut permettre d'estimer les vitesses ascensionnelles des magmas.

Une série de xénolites de péridotite (± amphibole) du Ray Pic (Massif Central), ne présentant pas de variations intracristallines en H, a été sélectionnée afin de s'intéresser aux processus mantelliques. Le **chapitre 4** aborde le comportement de l'H lors des processus de fusion et de métasomatisme de grande échelle en contexte de point chaud. L'étude des concentrations en éléments en traces (*e.g.,* REE) permet de caractériser les processus subis par la roche. La comparaison avec les concentrations en H permet de définir le degré d'incompatibilité de l'H relativement aux REE, et donc le comportement de l'H pendant les processus mantelliques. Cette étude permet aussi d'aborder l'influence des minéraux hydratés sur les concentrations en H des NAMs.

Tableau I.2 – Travaux expérimentaux de détermination des coefficients de partage minéral / liquide silicaté et/ou minéral/minéral dans le manteau.

Autor	P (GPa)	T (°C)	System	Methods	D ol / melt	D opx / melt	D cpx / melt	D cpx / opx	D cpx / ol	D opx / ol
Aubaud *et al.* (2004)	1–2	1230–1380	70% basalt + 30% peridotite	SIMS	0 .0011–0 .0029	0 .013–0 .027	0 .019–0 .026	1.4	12.5	9.1
Tenner. *et al.* (2009)	3	1380	Modified MORB + 2 wt% H2O	SIMS	0.0006	0 .009–0 .019	0 .014–0 .021	1 .2–2	25	
Ardia *et al.* (2012)	5–8	1400–1500	Natural dry San Carlos olivine powder + hydrous peridotite with 1% H_2O	SIMS					16.6*	9.7*
Hauri *et al.* (2006)	1–4	1000–1380	synthetic peridotite + basalt	SIMS	0 .0013–0 .0021	0 .012–0 .034	0 .0069–0 .034	1.31	14.04	10.75
	1.6	1370		SIMS				1.42	9.22	6.47
	1.2	1185		SIMS				0.85	12.56	14.7
Grant *et al.* (2007)	1.5	1295-1320	albite – forsterite – H_2O	FTIR	0.0001	0.003				24
				FTIR	0.0001	0.003				27
Novella *et al.* (2014)	6	1400	oxides and hydroxides powders	NanoSIMS	0.004	0.0064	0.0032	0.5	0.8	1.6
Kovacs *et al.* (2012)	2.5	1000	olivine and pyroxenes interlayered	FTIR				2 .7 ± 1 .1		6 .7 ± 2
Sakurai *et al.* (2014)	1.5	1300	Natural ol + synthetic opx	FTIR						7 .2 -12 .6
	2	1300		FTIR						14 .9 -35 .8
	3	1300		FTIR						16 - 24 .7
Withers (2011)	3	1200	MgO – SiO_2 – FeO – H_2O	SIMS						1.05
	6	1200	MgO – SiO_2 – FeO – H_2O	SIMS						0.61
Koga *et al.* (2003)	1.8	1380	olivine (San Carlos) and opx (Kangan)	FTIR & SIMS						12 ± 2
Férot and Bolfan-Casanova (2012)	2.5	1175 – 1400	MgO – SiO_2 – Al_2O_3 – FeO – H_2O	FTIR						2
Rosenthal *et al.* (2015)	2.5	1400	(4wt% CO_2) olivine tholeiite	SIMS		0.0168	0.023	1.37		
	1.2	1300	(Green & Ringwood. 1967)	SIMS		0.0085	0.0122	1.44		

ol, olivine; opx, orthopyroxene; cpx, clinopyroxene; SIMS, Secondary Ion Mass Spectrometry; FTIR: Fourier Transform InfraRed spectroscopy

*D_{OH} from Ardia et al. (2012) are calculed with 3.4 and 6 wt % of Al_2O_3 for opx and cpx, respectively, after : $D_{H_2O}^{px/ol} = 2{,}63 \times C_{Al_2O_3}^{px} + 0{,}78$

Afin de mieux cerner le comportement de l'H durant les processus métasomatiques, dans le **Chapitre 5**, cinq xénolites composites (avec un filon) ont été étudiés, dans lesquels la péridotite jouxte l'agent métasomatique principal. Le choix des échantillons vise à englober une large gamme d'agents métasomatiques a priori facilement identifiables afin de suivre les processus de percolation/réaction en fonction de la distance par rapport au liquide métasomatique (*i.e.* veine de pyroxénite, d'amphibolite, patch basaltique). Les buts de cette étude sont (1) de déterminer les concentrations en H dans les veines métasomatiques, (2) de définir les relations entre les concentrations en H dans le filon et la péridotite adjacente ; (3) de préciser le degré d'incompatibilité de l'H relativement aux REE.

La conclusion (**Chapitre 6)** fait le bilan des concentrations en H dans le faciès à spinelle du manteau sous continental ainsi que les informations acquises sur échantillons naturels abordant le comportement de l'H lors des processus magmatiques et mantelliques. Ce bilan soulignera l'implication de ces résultats et les perspectives à cibler afin de compléter nos connaissances sur l'H dans le manteau lithosphérique.

Chapitre II : Méthodes analytiques et échantillons étudiés

Ce chapitre résume la préparation des échantillons nécessaires à chaque analyse utilisée lors de cette thèse ainsi que les modalités des différentes acquisitions de données qui ont permis de caractériser les échantillons.

II.1 Echantillonnage

Les roches étudiées sont toutes des péridotites à spinelle, ce qui confère aux xénolites une origine lithosphérique, entre 1-2 GPa (10 et 20 kb), soit de 30-40 à 60-70 km.

Chaque échantillon a été nettoyé des parties altérées à la scie, puis divisé. Une partie a été transformée en fine poudre (< 100 μm) dans un broyeur en agate pour les mesures des éléments majeurs et en traces sur roche totale. Une autre partie a été montée en lame épaisse (~100μm) pour les analyses de ces éléments dans les minéraux. Pour déterminer les concentrations en hydrogène, les minéraux doivent être polis sur 2 sections parallèles (double poli). Pour cela, ont été réalisés des lames épaisses (~ 500 μm) et/ou des grains séparés à double poli.

II.2 Microsonde électronique

Les teneurs en éléments majeurs de chacune des phases minérales pour chacun des échantillons ont été déterminées à l'aide d'une microsonde électronique CAMECA SX100 au laboratoire Microsonde Sud (UM). Cette microsonde est équipée de 5 spectromètres à dispersion d'onde (WDS) permettant une micro-analyse précise d'un grand nombre d'éléments.

Selon la phase minérale et les éléments voulus, différents réglages ont été utilisés. L'ensemble des conditions analytiques utilisées est reporté dans le Tableau II.1.

II.3 Spectrométrie de masse couplée à un plasma inductif (ICP-MS)

Pour préparer la solution à analyser, 100 mg de poudre d'échantillon sont pesés à l'aide d'une balance de précision (± 1 mg). Deux échantillons blancs et 2 standards (UB-N et JP1) sont également préparés. Une série d'attaques-acide ($HF + HNO_3 + HClO_4$) est effectuée afin de casser les liaisons atomiques et ainsi permettre leurs analyses quantitatives par spectromètre de masse. Chaque attaque est suivie d'une évaporation à une température de 150 °C durant 24 h. Les solutions sont réduites à l'état solide par évaporation, puis sont reprises avec de l'eau milliQ et de l'HNO_3 afin d'obtenir une solution limpide. Ces solutions sont ensuite diluées à 1:2000 pour éviter la sursaturation et permettre l'analyse avec le spectromètre de masse, sauf JP1 qui est dilué à 1:1000. Les blancs permettent de détecter d'éventuelles traces de contamination au cours de la série d'attaques ou pendant l'analyse. Les standards, analysés dans les mêmes conditions, renforcent la validité des analyses.

Tableau II.1 – Conditions analytiques utilisées à la microsonde électronique CAMECA SX100 du laboratoire de microsonde Sud (UM) sur les olivines, pyroxènes, spinelles, amphiboles, plagioclases et verres.

	Sillicate				AmF-10kV			
Faisceau	ponctuel / défocalisé (verre)				ponctuel			
Tension / Intensité	20keV / 10nA				10KeV / 20nA			
Conditions d'analyse	Cristal	Élement	Temps de comptage (s)	Standard	Cristal	Élement	Temps de comptage (s)	Standard
Spectromètre 1	TAP	Al	30	Al_2O_3	PC1	F	40	CaF_2
		Si	30	Wollastonite				
Spectromètre 2	LPET	Ca	30	Wollastonite	LPET	Cl	20	Chloroapatite
		K	30	Orthose		Ca	20	CaF_2
Spectromètre 3	LLIF	Ni	20	Nickel métal	LLIF	Fe	20	Fe_2O_3 (hématite)
		Fe	20	Fe_2O_3 (hématite)		Ti	20	TiO_2
		Mn	20	Manganèse métal				
Spectromètre 4	PET	Ti	30	TiO_2	PET	K	20	Orthose
		Cr	30	Cr_2O_3 (oxyde de chrome III)		Mn	20	Rhodochrosite
Spectromètre 5	TAP	Na	30	Albite	TAP	Al	20	Al_2O_3
		Mg	30	Forstérite		Si	20	Wollastonite

TAP : phtalate de thallium $C_8H_5O_4Tl$; LLIF : Fluore de lithium ; LPET / PET : pentaérythriol $C_5H_{12}O_4$; PC1 : cristal multicouche à W-Si.

Les teneurs des éléments en traces sur roche totale sont mesurées avec le spectromètre de masse Agilent 7700x (Laboratoire Géosciences Montpellier, plateforme AETE[6]) dont la sensibilité est de l'ordre de 200 Millions de coups par ppm sur ^{115}In. Les échantillons sont sous forme liquide, le taux de solide dissous est de 1/8000. Les standards internes choisis sont ^{115}In et ^{209}Bi. La mesure par ICP-MS peut être affectée par différentes interférences (*e.g.,* $^{138}Ba + {}^{16}O = {}^{154}Gd$). Pour corriger ces erreurs, on utilise les standards externes et les valeurs de référence Zr et Hf.

II.4 ICP-MS par ablation LASER

Les concentrations en éléments traces des minéraux ont été analysées sur lame épaisse ou sur minéraux séparés. Ces analyses concernaient les clinopyroxènes ainsi que, pour certains échantillons, des orthopyroxènes, des amphiboles et des olivines. Ces concentrations ont été analysées par un système d'ablation laser (Plateforme GeoLas Q+ dotée d'un laser Excimer CompEx102) couplé avec un ICP-MS (ThermoFinnigan Element XR) à Géosciences Montpellier. Toutes les analyses sont effectuées en atmosphère He pur, en utilisant comme standard externe le NIST 612 (50 ppm) et comme standard interne la concentration en CaO et SiO déterminés par la sonde électronique. Le temps d'analyse est de 4 min (3 min de blanc et 1 min d'analyse). La taille du faisceau est ajustée en fonction du minéral et de sa taille, 51 µm, 77 µm ou 102 µm avec une fluence de 10–12 $J.cm^2$ et une fréquence de 7 à 10 Hz. Toutes les données ont été traitées avec le logiciel GLITTER (Griffin *et al.,* 2008) en vérifiant que le volume de minéral analysé ne présente pas d'hétérogénéités.

[6] Analyse des Éléments en Traces dans l'Environnement

II.5 Diffraction des électrons rétrodiffusés (EBSD) sur un microscope électronique à balayage (MEB)

Chaque lame à double-poli a été caractérisée par MEB (Figure II.1). Puis, des cartes ou des analyses ponctuelles de l'orientation cristallographique des grains sont effectuées.

La diffraction des électrons rétrodiffusés (EBSD) dans un MEB est devenue la technique la plus répandue pour mesurer les orientations cristallographiques des phases cristallines dans les lames minces ou épaisses. Cette technique est basée sur la propriété ondulatoire des électrons et leur capacité à être diffractés par les plans cristallographiques d'un petit volume d'échantillon (quelques nm^3). Les électrons rétrodiffusés font scintiller un écran de phosphore et peuvent ainsi être détectés par une caméra CCD (Charge-Coupled Device). Le cliché de diffraction est constitué de lignes de Kikuchi (Figure II.1b). La géométrie de ces lignes, (intersections, espacements) permet de déterminer les paramètres de la maille cristalline et l'orientation cristallographique de la phase solide considérée.

L'orientation cristallographique des grains a été mesurée par EBSD soit avec le CamScan CrystalProbe X500FE, soit avec le FEI Quanta FEG 200 à Géosciences Montpellier (Figure II.1a). Dans le 1er cas, les conditions d'analyses sont de 15 kV, 3.5 nA avec une distance de travail de 25 mm et sous un vide faible (3-4 Pa d'azote dans la chambre) afin d'éviter la surcharge électrique des échantillons. Le faisceau incident d'électrons est incliné à 20° de la platine horizontale qui porte l'échantillon. Dans le 2nd cas, c'est l'échantillon qui est penché de 70°, les conditions d'analyses étaient de 17 kV avec la distance de travail est de 24 mm. L'image est alors traitée et indexée par le logiciel CHANNEL5 de Oxford Instruments HKL.

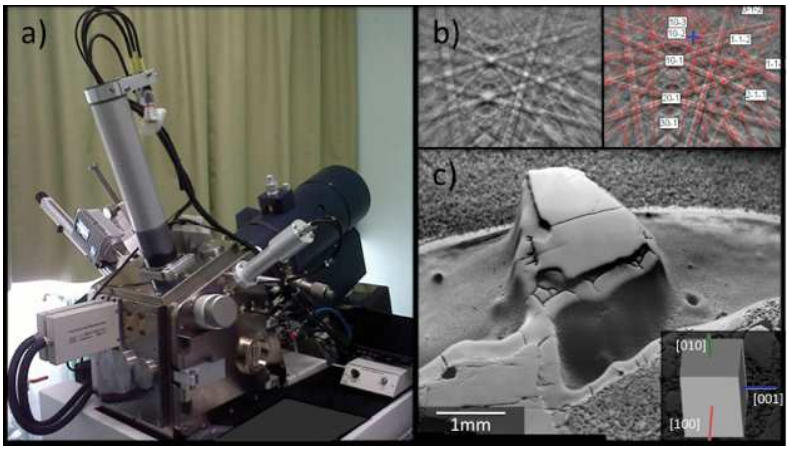

Figure II.1 – a) photo du CamScan CrystalProbe X500FE à Géosciences Montpellier ; b) à gauche un cliché de diffraction avec les bandes de Kikuchi ; à droite l'indexation des lignes de Kikuchi pour une olivine dans l'échantillon DW ; c) image en électrons rétrodiffusés d'un grain d'olivine (500 µm d'épaisseur) dans l'échantillon DW avec son orientation cristallographique calculée.

II.6 Spectroscopie infrarouge à transformée de Fourier (IRTF)

La spectroscopie IRTF est une méthode très sensible pour détecter la présence d'eau dans les minéraux. Cette technique permet à la fois de fournir une information sur la concentration en H mais également sur la position dans la structure cristalline des défauts ponctuels. Dans cette étude, la concentration en H des NAMs des échantillons est mesurée par spectroscopie IRTF.

II.6.1 Principe et Matériel

La spectroscopie IRTF est basée sur la propriété d'absorption des liaisons covalentes dans le solide ionique. Lorsque les liaisons sont excitées par le faisceau infrarouge, elles absorbent la radiation IR à des fréquences spécifiques pour lesquelles elles vibrent en fonction de niveaux d'énergie (modes vibratoires). Ces fréquences sont au premier ordre fonction de la force de la liaison ainsi que des atomes qui la forment. En conséquence, la fréquence des vibrations peut être associée à une liaison particulière.

Les spectres d'absorption des minéraux sont acquis à l'aide d'un spectromètre Bruker™ IFS66v, équipé d'un détecteur MCT (Mercure Cadmium Tellure) refroidi à l'azote liquide au laboratoire des colloïdes, verres et nanomatériaux (Université de Montpellier) (Figure II.2). Ce spectromètre est couplé à un microscope optique HYPERION équipé d'un objectif ×15 et d'un condensateur ×15. Ce dernier permet une visualisation précise de l'échantillon lors des acquisitions.

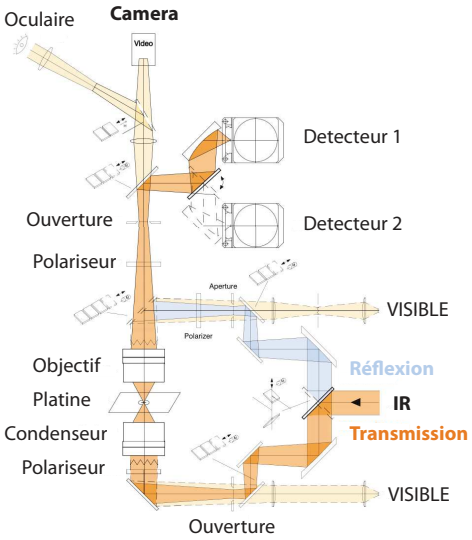

Figure II.2 – a) photo du Bruker™ IFS66v couplé au microscope Bruker™ HYPERION au laboratoire des colloïdes, verres et nanomatériaux (Université de Montpellier) ; b) schéma du chemin des faisceaux optiques de l'HYPERION (d'après la brochure Bruker™).

Les mesures peuvent être faites avec un faisceau IR polarisé ou non (Figure II.2 et Figure II.3). La polarisation du rayonnement IR est produite avec un polarisateur ZnSe placé entre la source IR et l'échantillon.

L'étude de l'H se fait dans l'IR moyen (4000-400 cm^{-1}) où les pics d'absorption des liaisons O-H sont visibles. Une fois le faisceau IR passé à travers l'échantillon, le détecteur forme un interferrogramme représentant la variation de l'intensité en fonction du temps. Cet interferrogramme va subir une transformée de Fourier qui permet de passer cette fonction non périodique en spectre de fréquences. Puis une suite de traitements est faite : une soustraction au spectre de base (spectre obtenu sans échantillon) reflétant le bruit de l'analyse, puis une correction de ligne de base et enfin une correction à l'épaisseur (normalisation à 1 cm d'épaisseur), aboutissant au spectre réel d'absorption d'une mesure ponctuelle dans le minéral.

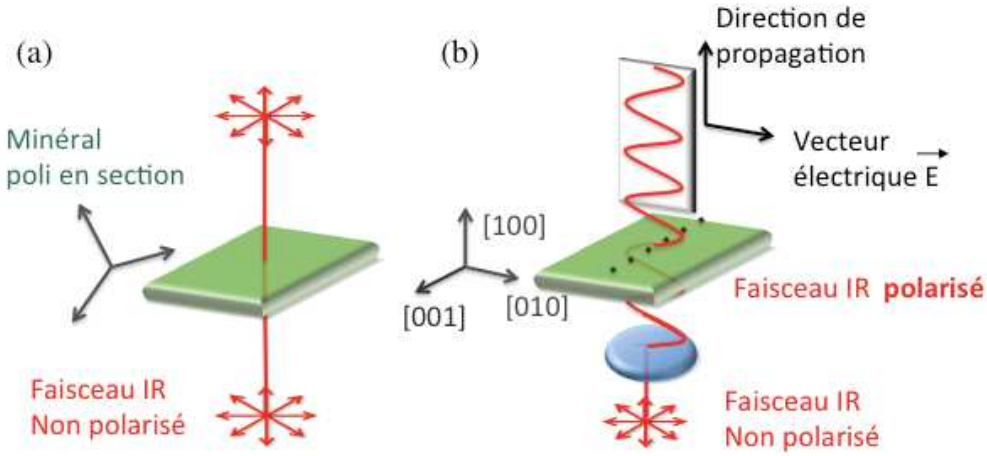

Figure II.3 – Schéma de principe d'une analyse en faisceau (a) non polarisé sur un minéral non orienté ; (b) polarisé sur un minéral orienté, avec $\vec{E}$ parallèle à [010].

II.6.2 Calcul de la concentration en H

Une fois le spectre d'absorbance (Abs) obtenu, la quantification de la concentration en H dans le minéral C_{H_2O} est basée sur la loi de Beer-Lambert, soit :

$$C_{H_2O} = \frac{Abs}{l \times \varepsilon} \qquad (II.1)$$

La C_{H_2O} est donc proportionnelle à l'absorbance Abs, l'épaisseur de l'échantillon l (cm) et au coefficient d'extinction molaire du minéral ε (cm^{-1}/ (mol/L)).

Plusieurs calibrations ont été proposées pour lier l'absorbance des minéraux obtenue par spectroscopie infrarouge à transformée de Fourier (IRTF) et la concentration en O-H du minéral. Différents problèmes surviennent lorsque l'on veut comparer les données de la littérature. Premièrement sur la calibration : laquelle a été utilisée ? Deuxièmement sur la

méthode : les analyses ont-elles été faites avec un faisceau IR polarisé ou non, sur des minéraux cristallographiquement orientés ou non ?

Pour l'olivine, trois calibrations sont couramment utilisées, la calibration de Bell *et al.,* 2003 (équation (2)), celle de Withers *et al.,* 2012 (équation (3)) et celle de Paterson, 1982 (équation (4)).

Bell *et al.,* 2003 $$C_{H_2O}(\text{ppm wt.}\,H_2O) = 0.188 \times Abs_{tot} \quad \text{(II.2)}$$

Withers *et al.,* 2012 $$C_{H_2O}\,(\text{ppm wt.}\,H_2O) = 0.119 \times Abs_{tot} \quad \text{(II.3)}$$

Paterson, 1982 $$C_{H_2O} = \frac{\chi_i}{150\xi}\int_{\upsilon_1}^{\upsilon_2}\frac{K(\upsilon)}{3780-\upsilon}\,d\upsilon \quad \text{(II.4)}$$

Abs_{tot} : absorbance totale (cm^{-1}),
χ_i : facteur de densité en fonction de la proportion de forsterite
ξ : facteur d'orientation, $\xi = 1/3$ pour des analyses IR non polarisé (sur cristaux non orientés),
$\xi = 1$ pour des analyses IR polarisé (sur cristaux orientés).
υ : la longueur d'onde (cm^{-1})
$\int K(\upsilon)\,d\upsilon$: l'intégral du coefficient d'absorption (= Abs_{tot}) en fonction de la longueur d'onde υ
υ_1-υ_2 : longueur d'onde délimitant le champ d'intégration du spectre d'absorption.

Pour les pyroxènes, deux calibrations sont utilisées : celle de Paterson, 1982 (équation (II.4)) et celle de Bell *et al.,* 1995 (équation (II.5)).

Bell *et al*. (1995) $$C_{H_2O} = \frac{1}{\xi I} \times \int_{\upsilon_1}^{\upsilon_2} K(\upsilon)d\upsilon \quad \text{(II.5)}$$

Avec I le coefficient d'absorption spécifique intégral, 7.09 ±0.32, et 14.84 ±0.59 pour le cpx et l'opx respectivement (1/ (ppm.cm²)).

Comme pour l'olivine, la calibration de Paterson (1982) permet de prendre en compte les variations de composition des pyroxènes. En comparaison, la calibration de Bell *et al.* (1995) a été basée sur l'analyse par manométrie d'un unique mégacristal de clinopyroxène et un unique cristal d'orthopyroxène mantellique. Ce cristal de clinopyroxène est une augite choisie pour sa taille indispensable aux analyses postérieures. Il a une composition très éloignée de celle d'une composition de diopside mantellique (13.26 wt% CaO contre 20 wt.% CaO pour un diopside moyen du manteau). Ces différences de compositions (*e.g.*, riche en FeO, pauvre en Al_2O_3) jouent sur la solubilité de l'H dans le clinopyroxène, c'est pourquoi la calibration de Bell *et al*., 1995 n'est pas adaptée au diopside mantellique, qui est le clinopyroxène le plus courant du manteau lithosphérique.

II.7 Autres méthodes analytiques

Les analyses des concentrations en H_2O des amphiboles ont été réalisées par H. Behrens au laboratoire de minéralogie à Hanovre (Allemagne) suivant la méthode de titrage de Karl Fisher décrite dans Behrens *et al.*, 1996.

Les analyses des concentrations en éléments majeurs en roche totale ont été réalisées par le service analytique de l'Instituto Andaluz de Ciencias de la Tierra (IACT, Grenade, Espagne) par spectrométrie de fluorescence X avec un spectromètre Bruker S4 Pioneer. Les conditions d'analyses pour le tube à rayon-X en Rh étaient de 160 kVet159 mA. L'intensité des rayons-X des échantillons a été comparée à 9 standards. Lors de ces analyses, l'état d'oxydation du fer a été ignoré. La perte au feu est calculée par le déficit de masse d'un gramme de poudre qui a été chauffé pendant une heure à 900°C. La perte au feu correspond à la perte massique des éléments volatils (OH, S, Cl, F).

Les concentrations en roche totale de Soufre et de Carbone ont été déterminées par analyseur élémentaire (service analytique, IACT, Espagne) suivant la méthode décrite dans Alt *et al.,* 2012.

La recherche de micro-phases carbonées/carbonatées, par microscope à cathodoluminescence au laboratoire Géosciences Montpellier, (Université de Montpellier) n'a pas donné de résultats exploitables.

Une étude approfondie de ces phases par cartographie Raman (réalisée par O. Beyssac, IMPMC, Paris) a montré que ces phases étaient secondaires et donc inutile pour l'étude des processus mantelliques.

Chapitre III : Diffusion ionique de l'H et vitesses de remontée magmatique

Ce chapitre détaille la diffusion ionique de l'H dans des péridotites mantelliques transportées vers la surface par des laves.

III.1 Introduction

Afin de quantifier l'H dans le manteau et d'identifier son comportement dans les processus mantelliques, il faut s'assurer que les concentrations en H des NAMs des xénolites ne sont pas altérées dans les systèmes magmatiques.

Les laves basaltiques contiennent une quantité importante d'eau, de 0.12 wt.% pour les MORB jusqu'à 8wt.% pour les basaltes de zone de subduction (*e.g.*, Sobolev et Chaussidon, 1996 ;Wallace et Anderson, 1998 ; Métrich et Wallace, 2008).

Mais le dégazage du magma lors de la remontée/décompression peut affecter la distribution de l'H dans les NAMs des xénolites de péridotite (*e.g.,* Demouchy *et al.*, 2006 ; Peslier et Luhr*,* 2006). Ces changements de conditions d'équilibre entrainent des variations des concentrations en H des NAMs du xénolite par diffusion ionique (*e.g.,* Pitzer et Sterner, 1994; Férot et Bolfan-Casanova, 2012).

L'H est un élément très incompatible dans les NAMs (Dixon *et al.*, 2002 ; Koga *et al.*, 2003 ; Aubaud *et al.*, 2004 ; Rosenthal *et al*., 2015). De plus, la diffusion de l'H dans l'olivine et les pyroxènes a été quantifiée par des études expérimentales à HP (0.2-1.5 GPa) et HT (800-1300 °C) donnant des coefficients de diffusion rapide de l'ordre de 10^{-10} à 10^{-12} $m^2.s^{-1}$ (Mackwell et Kohlstedt, 1990 ; Kohlstedt et Mackwell, 1999 ; Stalder et Skogby, 2003, Demouchy et Mackwell, 2006 ; Padron-Navarta *et al.*, 2014 ; Ingrin et Blanchard, 2006).

Par contre, seulement quelques études récentes sur échantillons montrent des concentrations en H dans des olivines de xénolite qui varient en fonction de la taille de grains (Demouchy *et al.*, 2006 ; Peslier *et al.*, 2006). Ces observations sont interprétées comme un changement des concentrations mantelliques initiales par diffusion ionique de l'H. En combinant la diffusion de l'H avec la profondeur estimée de la source des péridotites, on peut estimer la vitesse ascensionnelle minimum du magma hôte. Plusieurs études estiment que les vitesses d'ascension des xénolites dans les basaltes alcalins sont comprises entre 0.1 et 10 $m.s^{-1}$ (*e.g.*, Spera, 1984 ; Demouchy *et al.*, 2006 ; Peslier et Lhur, 2006). Cette étude vise à essayer d'estimer les vitesses de remontée des magmas de volcans du champ volcanique d'Eifel (Allemagne) et de tester les capacités de préservation des concentrations mantelliques d'H des NAMs.

III.2 Denis *et al. (*2013) Evidence of dehydration in peridotites from Eifel Volcanic Field and estimates of the rate of magma ascent

Journal of Volcanology and Geothermal Research 258 (2013) 85–99

Contents lists available at SciVerse ScienceDirect

Journal of Volcanology and Geothermal Research

journal homepage: www.elsevier.com/locate/jvolgeores

Evidence of dehydration in peridotites from Eifel Volcanic Field and estimates of the rate of magma ascent

Carole M.M. Denis [a,*], Sylvie Demouchy [a], Cliff S.J. Shaw [b]

[a] Geosciences Montpellier, University of Montpellier 2, Place E. Bataillon, Montpellier, France
[b] Department of Earth Sciences, University of New Brunswick, 2 Bailey Drive, Fredericton, Canada

ARTICLE INFO

Article history:
Received 19 December 2012
Accepted 11 April 2013
Available online 22 April 2013

Keywords:
Hydrogen
Olivine
Pyroxene
Eifel
Ascent rate
Ionic diffusion

ABSTRACT

We report major element compositions and water contents in upper mantle minerals from peridotites transported by silica undersaturated, mafic alkaline lavas from three volcanoes Rockeskyllerkopf, Dreiser Weiher, and Meerfelder Maar of the Eifel Volcanic Field (West Germany). The hydrogen concentrations (expressed in ppm wt. H_2O) obtained from unpolarized and polarized Fourier transform infrared (FTIR) spectroscopy give water contents for olivine, enstatite and diopside of ~6 ppm wt. H_2O, ~200 ppm wt. H_2O and ~285 ppm wt. H_2O, respectively. The hydrogen concentration in individual olivine grains is strongly heterogeneous whereas that in pyroxenes is homogeneous. Profiles measured across crystallographically oriented single-crystals of olivine using polarized infrared radiation reveal hydrogen depleted rims that are interpreted to be due to partial dehydration by ionic diffusion during the ascent of the xenolith to the surface. Using experimentally obtained diffusion coefficients for hydrogen in olivine at high temperature and high pressure, we estimate that the duration of the dehydration for the spinel-bearing xenoliths is limited to a few hours yielding rates of magma ascent from 3 ms^{-1} to 12 ms^{-1}. Our study suggests that the water contents of the upper mantle based solely on measurements of mantle-derived olivine, when concentration is not homogeneous, underestimate the true water content of the equilibrated uppermost mantle and that pyroxenes are a better proxy to constrain uppermost mantle water contents.

1. Introduction

'Water' occurs within two different forms in the deep Earth: as hydrous minerals such as serpentine, amphibole, and lawsonite in subduction zones, and as hydrogen trapped in atomic defects and bonded to silicate oxygen in nominally anhydrous minerals (NAMs). These NAMs, which may contain hundreds of parts per million hydrogen atoms, can be found in both the crust (e.g., quartz, Aines and Rossman, 1984; Rossman, 1988) and also in the Earth's mantle (e.g. olivine, pyroxenes and garnet, Beran and Putnis, 1983; Bell and Rossman, 1992). The NAMs represent an important deep reservoir and as such, are an important component of the deep water cycle. In order to understand this reservoir, hydrogen solubility (Bell and Rossman, 1992), also known as water storage capacity (Hirschmann et al., 2005) must be quantified. In addition, the hydrogen content of natural samples must be defined to better constrain both the nature of interactions between the atmosphere/hydrosphere and the mantle and the rates and mechanisms of degassing magma, whether past or present, during its passage through the mantle and crust.

Studies of basaltic lavas have shown that silicate melts (e.g. quenched glasses) may contain a significant amount of water; of the order of a few ppm wt. H_2O (Michael, 1988; Jambon and Zimmermann, 1990) in various forms (H_2O, H_2, OH^-). Crustal minerals such as quartz and feldspar may contain up to 1400 ppm wt. H_2O (Griggs and Blacic, 1965; Aines and Rossman, 1984; Johnson and Rossman, 2003) and mantle-derived minerals such as olivine, orthopyroxene, garnet and clinopyroxene may contain as much as several hundred ppm of water by weight (e.g., Miller et al., 1987; Rossman and Smyth, 1990; Bell and Rossman, 1992; Ingrin and Skogby, 2000; Peslier et al., 2002; Demouchy et al., 2006; Li et al., 2008). Several authors have suggested that Earth's mantle may contain hydrogen concentrations equivalent to 3 to 11 times the ocean mass (Smyth, 1987; Bolfan-Casanova, 2005; Marty, 2012).

Olivine is particularly important in understanding the water budget of the mantle since it is the most abundant phase in the upper mantle (60–80% in volume). Hydrogen (H) in olivine may occupy three different atomic sites: (1) a metallic site in the octahedron, (Mg^{2+}, Fe^{2+} or Fe^{3+}), and/or (2) a silicon site, replacing partially Si^{4+} in tetrahedron, and/or (3) an interstitial site (Kohlstedt et al., 1996; Karato, 2006).

In addition to its importance in the deep water cycle, the presence of H in NAMs significantly affects the physical and chemical properties of mantle minerals and thus of mantle rocks. For instance, the presence of H can decrease the strength and velocity of seismic waves and increase major element diffusivities and electrical conductivity in NAMs (Mackwell et al., 1985; Goldsmith, 1987; Karato, 1990; Costa and Chakraborty, 2004; Hier-Majumder et al., 2004; Jacobsen et al., 2004;

* Corresponding author. Tel.: +33 467144942; fax: +33 467 14 36 42.
E-mail address: caroledenis@gm.univ-montp2.fr (C.M.M. Denis).

0377-0273/$ – see front matter © 2013 Elsevier B.V. All rights reserved.
http://dx.doi.org/10.1016/j.jvolgeores.2013.04.010

Demouchy et al., 2007; Demouchy et al., 2012; Yoshino et al., 2012). Addition of hydrogen to NAMs also decreases the solidus temperature of the mantle, increasing the degree of partial melting, and thus changing the composition of the magma produced (Kushiro, 1972; Gaetani et al., 1993). Hydrogen incorporation in NAMs is strongly affected by pressure, water and oxygen fugacity, temperature and mineral composition (Bali et al., 2008; Férot and Bolfan-Casanova, 2012).

Despite the recent studies referred to above, the origin, concentration, and ultimate fate of hydrogen in mantle minerals is still poorly constrained. In particular, the mechanism of mantle degassing is a key factor in terrestrial mantle geodynamics and there is a significant need for improvement in our understanding of how magmatic systems interact with and help to drive degassing of NAMs.

During melting, hydrogen is partitioned into the melt phase from NAMs. Mantle xenoliths in the rising magma may lose hydrogen during chemical interactions with the undersaturated melt during decompression. Since this loss will be via diffusion, due to decreasing pressure and thus decreasing water fugacity (from 2 GPa to room pressure, Pitzer and Sterner, 1994; Férot and Bolfan-Casanova, 2012), hydrogen concentrations in minerals such as olivine and pyroxene may provide a valuable new indicator of deep magma ascent rates. It will extend the current range of compositions beyond that for which ascent estimates have been so far established e.g., Spera (1984), Hawkesworth et al. (2000), Tepley et al. (2000), Costa and Dungan (2005), Humphreys et al. (2008), MacKenzie and Canil (2008), and Hamada et al. (2011). Since this H diffusion will occur regardless of whether or not there is chemical interdiffusion of Fe and Mg between the minerals and melt e.g. Shaw and Klugel (2002), it is a particularly valuable recorder of the ascent of mantle xenoliths and their entraining magma.

We must also consider a complex system in which H loss by diffusion may be linked to the final water vapor exsolution from a volatile-rich melt (H_2O, but also potentially CO_2) transporting mantle xenoliths toward the surface. In this case the duration of dehydration may reflect transport only in the upper crustal section rather than the total ascent time from the source of the mantle xenoliths. In both cases, dehydration profiles provide a unique insight into magma transport and eruption.

Hydrogen is an incompatible element (Dixon et al., 2002; Koga et al., 2003; Aubaud et al., 2004; Bell et al., 2004), which diffuses extremely rapidly (Mackwell and Kohlstedt, 1990). The diffusivity of H in olivine and pyroxenes, constrained by experimental studies at high pressures and high temperatures, is of the order of 10^{-10} to 10^{-12} m^2 s^{-1} at 1100 °C (Kohlstedt and Mackwell, 1999; Stalder and Skogby, 2003; Demouchy and Mackwell, 2006) which is approximately six orders of magnitude faster than Fe–Mg interdiffusion in olivine (Chakraborty, 1997). Such rapid diffusivities imply that H concentrations in olivine in peridotite xenoliths will show significant variations over the hours to days that it takes for such xenoliths to reach surface (Demouchy, 2004; Demouchy et al., 2006) and that the observed H concentrations in mantle xenolith olivine are not representative of the concentration in the mantle source. Combining information on hydrogen diffusion with the depth to the source of xenoliths allows a calculation of the minimum ascent rate of magma. In cases where ascent is extremely rapid, i.e. a few hours or days, there may not be sufficient time to develop a measurable Fe–Mg interdiffusion profile in olivine. For such cases, the H diffusion approach allows a greater level of accuracy in quantification of ascent rates than is currently possible using major element zonation.

This study focuses on determining the concentration and distribution of hydrogen (H) in peridotite xenoliths from the Eifel Volcanic Field (Germany) to discuss the role of water in determining the rate of magma ascent. In addition, the effect of H on the electrical conductivity recorded under Eifel will be discussed.

2. Geological context

The Eifel Volcanic Field is part of the Central European Volcanic Province, which is associated with the development of Tertiary intracontinental rifts (Wilson and Downes, 1991). Quaternary volcanism in the Eifel accompanied the uplift of the Rhenish Massif beginning at 0.8 Ma; the last known eruption was at 11 ka (Zolitschka et al., 1995). Tomography studies as well as receiver function and seismic anisotropy analysis indicate abnormal seismic velocities between 50–60 km and 410 km depth which have been interpreted to result from a narrow thermal plume in the asthenosphere below the Eifel (Ritter et al., 2001; Keyser et al., 2002). In addition, the receiver function images show a thinning of the lithosphere placing the Moho between 25 and 28 km beneath the Eifel Volcanic Field (Budweg et al., 2006).

Eifel volcanism comprises 250 eruptive centers spread over 600 km^2 (Fig. 1). The average time between eruptions is 2875 years, assuming monogenetic volcanism; though Shaw et al. (2010) have shown that individual volcanic centers can have multiple events separated by tens to hundreds of thousands of years. Two distinct areas can be defined: the West and the East Eifel volcanic fields. Each domain was developed on both sides of the zone of maximum uplift. The volcanoes of the West Eifel sit atop the highest parts of the Rhenish Massif, while the lavas of the East Eifel were erupted in the Neuwied Basin. In each area the early eruptions are characterized by potassic basanites followed by more evolved and sodic lava (Mertes and Schmincke, 1985). Volcanoes are mainly cinder and tuff cones and maars with tuff rings whose formation is partially governed by magma–water interaction resulting in phreatomagmatic eruptions. The presence of gas fumaroles with carbon dioxide, sulfur and methane, as well as weak volcanic earthquakes show that magmatic activity in Eifel is nowadays dormant, but not ended (Schmincke, 2007).

The West Eifel field shows a clear trend NW–SE in both the distribution of volcanoes and age of volcanism (Schmincke et al., 1983). The volcanic activity of this field was developed initially near Ormont, and then volcanism has migrated to the SE after a stagnant period in the uplift of the Rhenish massif. The frequency of volcanic eruption has decreased during the last 100,000 years (Nowell et al., 2006).

The samples analyzed in this study are peridotite xenoliths brought up by three volcanoes in the West Eifel Volcanic Field: Meerfelder Maar, Dreiser Weiher, and Rockeskyllerkopf (Fig. 1). Dreiser Weiher is a maar where xenoliths are abundant in the tuff cone. The host lava is part of the sodi-potassic olivine nephelinite and basanite suite (Mertes and Schmincke, 1985). Meerfelder Maar is part of the largest group of maars and cinder cones in the extreme south of the West Eifel. Peridotite xenoliths were collected from tephra deposits in a quarry on the west side of Meerfelder Maar. Quartzofeldspathic xenoliths, rich in glass and vesicles are also found among the laminated deposits of scoria, together with clinopyroxenites (Shaw and Eyzaguirre, 2000), and glimmerite xenoliths with large grains (>5 mm) of phlogopite and amphibole. Based on magmatic cumulate xenoliths (mostly dunite), the magma reservoir of Meerfelder Maar was located at a depth of ~14 km (Shaw, 2003). Studies based on Fe–Mg interdiffusion in these magmatic olivines have shown that they recorded at depth a magma arrival between 1 and 3 years before the eruption. Two suites of mantle clinopyroxenites recorded two other events of a few days (1–8) and also only 3 h before the eruption (Shaw, 2003) based as well on Fe–Mg interdiffusion data. The last event is interpreted as recording the volcano eruption and it also represents the time required for xenolith transport from the peridotite source to the surface, it yields a rise rate of 4.2 ms^{-1} (Shaw, 2003).

Several studies of the evolution of the lithospheric mantle beneath the West Eifel used specimens from Dreiser Weiher and Meerfelder Maar. In the xenoliths studied, two distinct episodes of metasomatism have been identified: a Hercynian event that formed titanium-poor amphibole, phlogopite and clinopyroxene and a second event, dating from the Quaternary, which formed Ti-rich amphibole veins, clinopyroxene and phlogopite. In the case of xenoliths derived from greater depth, the second event resulted in development of clinopyroxenite veins (Witt-Eickschen and Kramm, 1998; Witt-Eickschen et al., 2003).

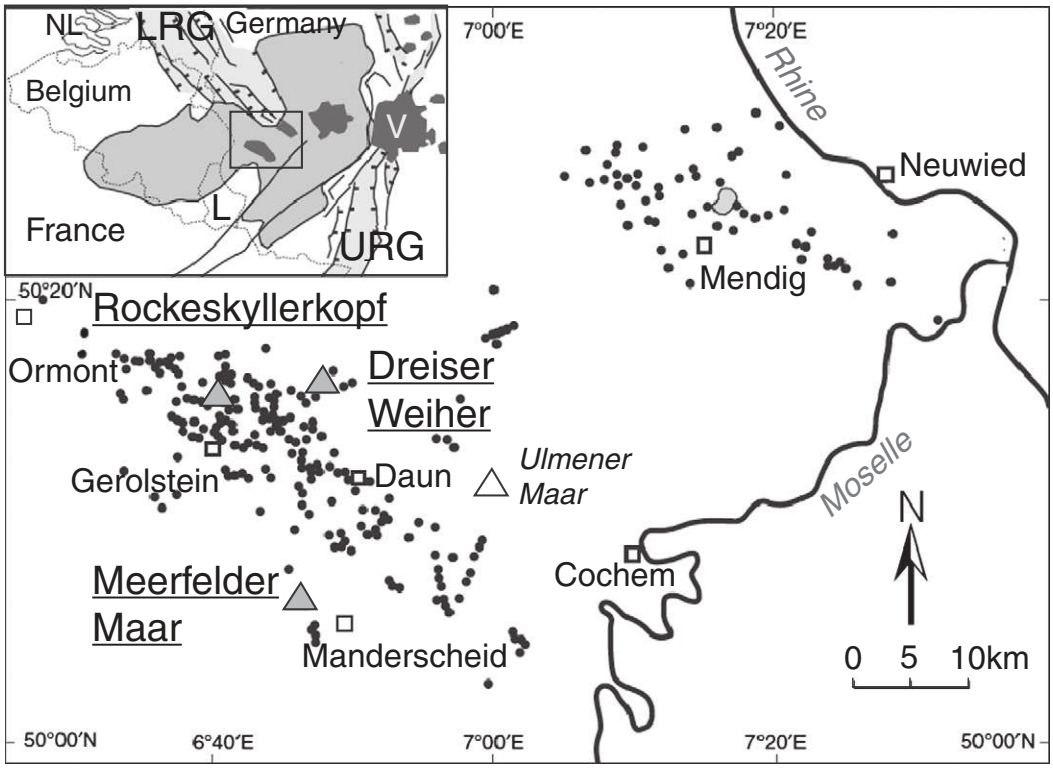

Fig. 1. Location and distribution of Tertiary and Quaternary volcanic centers (points) in the Eifel Volcanic Field. Studied xenolith locations (triangle) and major towns (square), Luxembourg (L), Netherlands (NL), tertiary volcanism (V), upper and lower Rhine grabens (respectively URG and LRG).
Modified after Preusser et al. (2011).

The Rockeskyllerkopf volcanic complex first erupted around 475 ka and last erupted about 360 ka (Shaw et al., 2010). Lavas are mainly basanites with only minor fractionation; though trace element data suggest mixing of magmas derived from two geochemically distinct sources (Shaw and Woodland, 2012). Peridotite xenoliths range from harzburgite and lherzolite to dunite and wehrlite, the latter being cut by veins of clinopyroxene and phlogopite. Zinngrebe and Foley (1995) and Shaw (2005) suggested that wehrlites at this and other West Eifel localities formed due to interaction between previously metasomatised lherzolitic to harzburgitic mantle and a large volume of percolating silica undersaturated alkaline magma. During this reaction, orthopyroxene was consumed and secondary olivine, phlogopite and clinopyroxene were precipitated. Veins formed during periodic events of overpressure when magma was concentrated in fractures rather than flowing along grain boundaries/intergranular spaces (Shaw, 2005).

3. Analytical techniques

To constrain the model parameters for ionic diffusion in a crystalline solid, we need to know the equilibrium temperature and the crystallographic orientation of compositional traverses through the grains. Equilibrium temperature is calculated using exchange geothermometers from Brey and Köhler (1990) and the host magma temperature is estimated using the MELTS thermodynamic model of Ghiorso and Sack (1995). Crystallographic orientations were obtained from electron backscatter diffraction (EBSD) after which the concentration and distribution of hydrogen was quantified by Fourier transform infrared spectroscopy (FTIR).

3.1. Sample preparation

For this study one xenolith from Dreiser Weiher (sample DW) and one from Rockeskyllerkopf (Ro) and four xenoliths (samples MMa, MMb, MMc, MME) from Meerfelder Maar were selected from the authors' collection. These samples were chosen as they contain fresh, coarse-grained forsterite-rich olivine. The samples were prepared as doubly polished thick sections (~500 μm of thickness) for FTIR. A final polishing with colloidal silica (siton) was done to remove the surface damaged by mechanical polishing to allow EBSD and SEM analyses without the need for a carbon coating. Grains separated from thick sections of MMa3 and MMc2, which have a grain size greater than 1 mm, were also mounted in epoxy plugs before polishing with siton. These samples were removed from their glass support by washing in pure acetone before FTIR analysis. Finally, after the analysis by FTIR, selected grains from samples MMa1, MMa2, MMb, MMc1 and MMe were embedded in epoxy plugs and carbon coated for additional EPMA analyses.

3.2. Chemical compositions

Major elements in each mineral phase for each sample were determined using a Cameca SX100 electron microprobe at Microsonde Sud facility, in Montpellier (France). The samples were analyzed with a 20 kV accelerating voltage and a 10 nA probe current in wavelength dispersive mode. A peak and a background counting time of 20 s was used for the analysis of Fe, Mn and Ni, and 30 s for the other elements. Standards used for calibration were Forsterite (Mg), Fe_2O_3 (Fe), Ni metal (Ni), Chromite (Cr), Al_2O_3 (Al), Wollastonite (Si, Ca), Albite (Na), TiO_2 (Ti), Orthoclase (K) and pure manganese (Mn).

3.3. Rock texture and crystallographic orientation

The texture of the samples was characterized and the crystallographic orientation of the olivine grains was determined by EBSD with the CamScan CrystalProbe X500FE SEM in Geosciences Montpellier (Fig. 2). The analytical conditions were 15 kV, 3.5 nA with a working distance of 25 mm and under a low vacuum (3–4 Pa of nitrogen) to avoid electrical overload of the samples. The incident electron beam

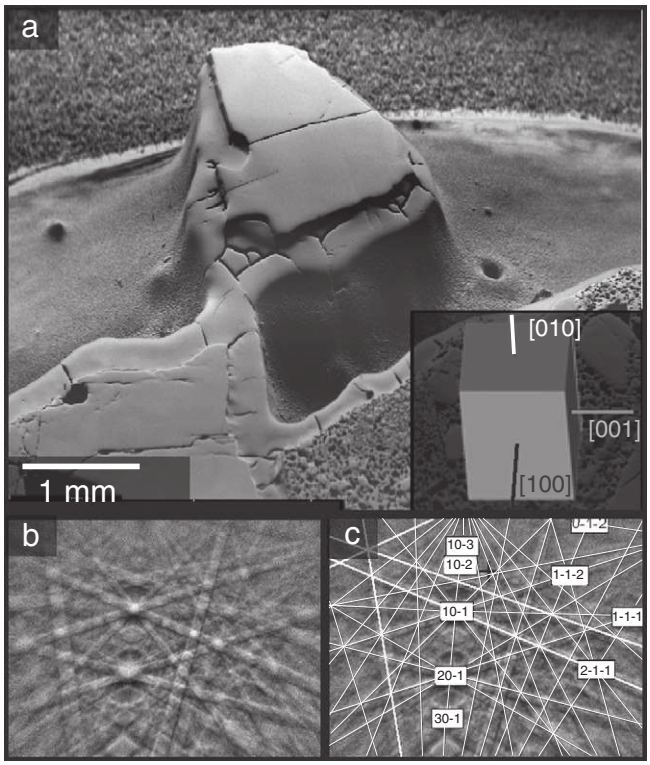

Fig. 2. a). Backscattered electron image of an olivine grain (500 μm thick) from sample DW with its crystallographic orientation calculated from Kikuchi bands. b) Diffraction pattern with Kikuchi bands. c) Indexed Kikuchi bands for this olivine.

was inclined at 20° to the horizontal sample holder. The electrons interact with a small sample volume (few nm^3) before being diffracted by the crystallographic planes of the mineral. Backscattered electrons are detected by a CCD camera. The diffraction pattern consists of Kikuchi lines (Fig. 2b–c). The geometry of these lines (intersection, spacing) determines the parameters of the crystal lattice and crystallographic orientation. This image is then processed and indexed by the Oxford Instruments HKL CHANNEL5 software. The EBSD analyses were used to choose grains for subsequent polarized FTIR analysis. Such grains should be as large as possible and should have one of the three crystallographic axes normal or near normal to the section plane. Of the approximately 380 large grains examined, only 38 had the correct orientation, of these only 20% were free of cracks and inclusions and thus suitable for FTIR analysis.

3.4. Infrared spectroscopy

The hydrogen concentration of the samples was measured in transmission mode by FTIR spectroscopy at the Laboratoire des Colloïdes, Verres et Nanomatériaux (LCVN) at Université de Montpellier 2, France. The unpolarized and polarized infrared spectra were acquired using a Bruker Vertex 70, equipped with an MCT detector (Mercury Cadmium Telluride) cooled with liquid nitrogen, coupled to a Bruker HYPERION (i.e., IR microscope). This allows accurate visualization of the sample prior and during acquisitions. A Globar light source and a Ge–KBr beam splitter were used to generate unpolarized mid-infrared radiation (between 4000 and 400 cm^{-1}). The polarization of the infrared beam is produced with a KRS-5 polarizer (Thallium Bromoiodide) placed between the mid-IR source and the sample. Measurements on olivine (ol), orthopyroxene (opx), and clinopyroxene (cpx) were performed with a square aperture of sizes ranging from 50 to 100 μm. For each measurement 200 scans were accumulated with a resolution of 4 cm^{-1}. The series of resulting interferograms was ratioed against the reference spectrum, i.e. the spectrum obtained without the sample in the beam path, which corrects for the background in the analysis, then treated with a correction of the baseline, and a correction of the sample thickness; all samples were normalized to a thickness of 1 cm. The background and the baseline correction were carried out using the OPUS software. From each spectrum, the quantification of the hydrogen concentration in the sample is based on the Beer–Lambert law (Beer, 1852). To accurately compare our results with previous studies; we used the calibration of Paterson (1982):

$$C_{OH} = \frac{\chi_i}{150\xi}\int \frac{k(\upsilon)}{3780-\upsilon}d\upsilon. \quad (1)$$

This empirical equation gives the hydrogen concentration (C_{OH}) as a function of factor χ_i, which is a function of the density of the mineral (χ_i ol = 2695 ppm wt. H_2O; χ_i opx 2812 ppm wt. H_2O; χ_i cpx = 2752 ppm wt. H_2O). ξ is the orientation factor, $\xi = 1/3$ for non-polarized IR analyses (non-oriented samples), $\xi = 1$ if the crystal is oriented crystallographically and if the source is polarized IR; $k(\upsilon)$, the absorption coefficient is a function of the wavenumber υ. The H concentration of the samples was calculated by integrating each spectrum between 3610 and 3150 cm^{-1} for olivine, 3670–2800 cm^{-1} for orthopyroxene and 3770–3000 cm^{-1} for clinopyroxene. This calibration allows a detection limit of about 1 ppm wt. H_2O (H concentration expressed as weight ppm of oxide) for a sample of 1 mm of thickness. The estimated error in the resulting H concentration is 30% (see details given in Paterson, 1982, page 26 and Rauch, 2000). The calibration from Paterson (1982), using unpolarized and polarized IR light is likely to underestimate the absolute hydrogen concentration for olivine, while the calibration from Bell et al. (2003) using polarized IR light applicable to oriented olivine only is likely to overestimate the absolute hydrogen concentration (Withers et al., 2012). We chose to use the calibration of Paterson (1982) since it allowed us to determine hydrogen concentrations for the largest number of analyses and also allows comparison between the concentrations from the different mineral phases (i.e., one common method for all phases) as well as comparison with previous studies. As demonstrated by Férot and Bolfan-Casanova (2012), a factor of 3 can be used to convert the concentrations reported here to values obtained with the method of Bell et al. (2003) (i.e., see their Fig. S1, Férot and Bolfan-Casanova, 2012) and a factor between 1.8 and 2 can be used to convert the concentrations reported here to values obtained with the recent calibration of Withers et al., 2012 (i.e., see their Fig. S1, Withers et al., 2012). However, the choice of the calibration has no consequences on the durations obtained, since we use the variation of OH concentration through one grain (i.e., the same correction applies to all spectra).

Since the hydrogen diffusion coefficient varies as a function of crystallographic orientation (Mackwell and Kohlstedt, 1990; Demouchy and Mackwell, 2006) to model diffusion, the measurements must be made on oriented grains and with polarized IR radiation. Average H concentrations were obtained from averaging several spectra (1–5) from each grain.

3.5. Hydrogen diffusion and models

The ionic diffusion coefficient depends mainly on the temperature of the system, but also of the mechanism of diffusion. Two mechanisms of H diffusion have been proposed for olivine (Mackwell and Kohlstedt, 1990; Demouchy and Mackwell, 2006). The first mechanism, called "proton–polaron diffusion" is a relatively rapid redox reaction involving a flux of polarons (marked h•) countered by a proton flux (i.e., a polaron is an electronic hole site formed in the valence band, Serway et al., 1997; in olivine, it corresponds to the Fe^{2+} to Fe^{3+} change of redox state). The second mechanism, "proton-vacancy" is a slower mechanism, which is controlled by the mobility of metal (Mg or Fe) vacancies. The first process dominates at low temperature (below 1000 °C) or over short time scales and can rapidly incorporate a limited amount of H in the

crystallographic structure; of the order of 4–5 ppm wt. H_2O at 1000 °C and 0.2 GPa in olivine Fo_{90}. The second process, which is dominant at temperatures > 1000 °C or over longer time scales allows hydrogen saturation at equilibrium (Demouchy and Mackwell, 2006).

Numerous studies have shown that the mechanism of hydrogen incorporation by diffusion in clinopyroxene is dominated by the "proton–polaron" mechanism (Skogby, 1994; Ingrin et al., 1995; Carpenter-Woods et al., 2000). In orthopyroxene, the same two diffusion mechanisms are also present but the diffusion rates are constrained by the oxidation state of iron in the crystal. In orthopyroxene with low ferric iron content (i.e., low Fe^{3+}/Fe_{tot}) hydrogen diffuses by the "proton–polaron" mechanism. Otherwise the diffusion is controlled by a much slower "proton-vacancies" mechanism (Stalder and Skogby, 2003). Hydrogen diffusion in pyroxene is in the same range at the same temperature as that of olivine (10^{-11}–10^{-9} m^2/s) i.e., hydrogen diffusion is very rapid in both phases (see Ingrin and Blanchard, 2006 and Farver, 2010 for a review). Most of the studies on diffusion mechanisms in pyroxenes have been done by hydrogen incorporation at high pressure. As a result, the mechanisms involved in the dehydration processes (under high pressure and with co-existing olivine) are poorly constrained and the role of each process cannot be quantified solely from natural mantle minerals. We assume here, as demonstrated recently by Gaetani et al., 2012, based on hydration and dehydration of water-bearing melt inclusion in olivine, that dehydration involves the same mechanisms as hydration.

For olivine, the diffusion coefficient is determined using the diffusion equations as a function of composition (olivine Fo_{90}), grain orientation, and the diffusion mechanism (Demouchy and Mackwell, 2006). The temperature dependent diffusion coefficient D is calculated from an Arrhenius relation:

$$D = D_0 e^{\left(\frac{-Q}{RT}\right)}. \quad (2)$$

Since the temperature of the system is well above 1000 °C for each sample (see below), we use the diffusion equations determined by Demouchy and Mackwell (2006) for the "proton-vacancy" mechanism:

$$D_{PV}[100],[0101] = 3.1 \times 10^{-5} \cdot \left[\left(-204,000\left(\pm 94 \times 10^{-3}\right)\right)/RT\right] \quad (3)$$

$$D_{PV}[001] = 3.9 \times 10^{-2} \cdot \exp\left[\left(-258,000\left(\pm 11 \times 10^{3}\right)\right)/RT\right] \quad (4)$$

where D_{PV} is the diffusion coefficient for the PV mechanism ($m^2\ s^{-1}$), Q is the activation energy ($J\ mol^{-1}$), R is the gas constant and T the temperature in K. In the discussion we present a sensitivity analysis of the effects of uncertainties in Q and T on the models of the diffusion profiles.

Different geometries of diffusion are possible. The first is diffusion in one dimension (1D) in a semi-finite solid surrounded by an infinite source or reservoir (outlet). This is quite similar, but not totally equivalent, to the model of isotropic diffusion in a sphere (Crank, 1975, pp. 32; Zhang, 2011, pp. 17). The main limitation of this first model is that it considers the diffusion in other directions in the measured profile as negligible so that the concentration plateau is taken to represent the initial content of the diffusing species. In this case, the concentration in the solid at any point x (m) along a crystallographic axis is described by:

$$C_{OH}(x) = C_0 \mathrm{erfc}\left(\frac{x}{2\sqrt{Dt}}\right) + \mathrm{erfc}\left(\frac{L-x}{2\sqrt{Dt}}\right) \quad (5)$$

where $C_{OH}(x)$ ($H/10^6Si$) is the concentration at time t (s) at position (x). $C_{OH}(x)$ is a function of the diffusion coefficient D ($m^2\ s^{-1}$), and L is the total grain length (m) along the given crystallographic axis.

A three dimensional model, based on the equations of Carslaw and Jaeger (1959, equations 5 to 7, p. 184), was also used. It takes into account diffusion in 3D within an anisotropic rectangular parallelepiped (Demouchy, 2004; Demouchy et al., 2006 GSA data repository item). This model takes into account the interactions of diffusion along the three different crystallographic directions, as well as a compositional plateau, which does not represent the initial content of the diffusing species (thus the system is no longer semi-infinite with respect to diffusion). The solution of the sum of fluxes is the product of the concentration. This model includes an approximation, as the model requires that the grain be a perfect rectangular parallelepiped. In the natural samples, evaluation of the width of the grain in each direction is difficult since the analyzed section might not include the center of the grain. Therefore, we used the apparent length and width of the grain.

In each model, the diffusion time t (s) is estimated by matching the calculated profile (1D and 3D) to the measured concentration profile. Temperature is taken as a constant during the ascent of the magma and the entrained xenoliths. The effect of changes in pressure on diffusion rate and therefore on the concentration profile is considered negligible. Our model does not currently account for any dependence of hydrogen diffusion on oxygen or water fugacity. Finally, in presenting ascent velocities, we assume that the magma and xenoliths were transported directly to surface, which means that we provide a minimum estimate of the rate of magma ascent and not absolute ascent rates.

4. Results

4.1. Mineralogy and petrology

The texture and the mineralogical composition of the samples are summarized in Fig. 3 and Table 1. The sample from Rockeskyllerkopf is a dunite with many veins containing clinopyroxene, spinel and phlogopite. The sample from Dreiser Weiher is a coarse-grained dunite, which has clusters of clinopyroxene and spinel. Some subgrain boundaries due to deformation are visible. The four samples from Meerfelder Maar show textural and compositional diversities: samples MMa, MMc and MMe are harzburgites; MMa and MMe are equigranular and coarse-grained whereas MMc is inequigranular. Sample MMb is a finer grained equigranular lherzolite.

4.2. Chemical composition

Representative analyses of each phase in the sample suite are presented in Table 2. The dunite sample from Rockeskyllerkopf contains the most iron-rich olivine with Fo from 84.4 to 87.2. The dunite from Dresier Weiher and the lherzolite from Meerfelder Maar contain slightly more magnesian olivine that ranges from Fo 86.2–88.2 (Fig. 4). The harzburgites from Meerfelder Maar have the most magnesian olivine; two (MMa and MMc) have Fo contents of 89.2–90.4, sample MMe has the smallest range of olivine composition and is the most magnesian at Fo 90.6–91.

Clinopyroxene is aluminian chromium diopside containing 0.9 to 1.2 wt.% Na_2O with the exception of the sample from Rockeskyllerkopf, which contains less than 0.5 wt.% Na_2O. This sample also has the highest TiO_2 and CaO and lowest Cr_2O_3 content of the seven analyzed samples. Orthopyroxene, which occurs only in the samples from Meerfelder Maar is aluminian chromian enstatite with 4 to 5 wt.% Al_2O_3

The spinel is chromite with cr# = 100 * [Cr * 100 / (Cr + Al)] between 29.7 and 33.7 for MMc and MMa while cr# is >40 for Ro and below 12 for MMb.

Microprobe traverses show that the Fo content of olivine does not vary in the Meerfelder Maar and Dreiser Weiher samples. However, the Rockeskyllerkopf sample shows distinct core to rim variation (Fig. 5a), which has been interpreted by Shaw (2005) to be due to

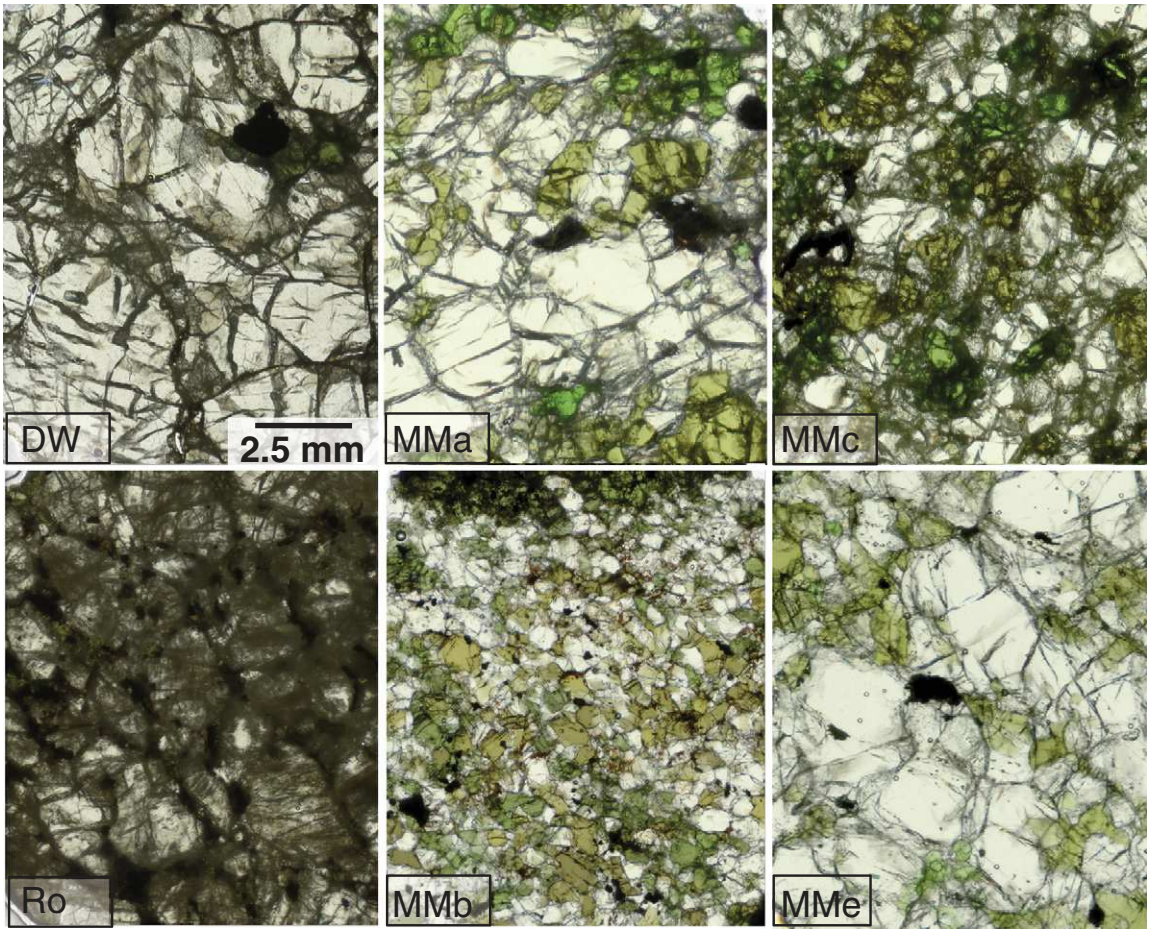

Fig. 3. Eifel spinel-peridotite xenoliths from Earth's upper mantle. Transmitted light microphotographs with mineral assemblage: olivine (white), diopside (bright green), orthopyroxene (brownish green), and spinel (opaque). The scale is the same for each microphotograph.

interdiffusion with an infiltrating melt. A profile was analyzed in a large olivine crystal in the lava matrix of MMb (Fig. 5b). It also shows compositional zonation consistent with inter-diffusion of Fe–Mg between olivine and the surrounding melt with Fo varying from 90 at the center of the grain to 86 at the edge. In addition, NiO also shows zonation from 0.4 NiO wt.% at the center to 0.1 NiO wt.% at the edge, and no significant variation in CaO was detected.

Table 1
Modal composition, texture and location of xenoliths. (Meerfelder M.: Meerfelder Maar; Harz.: harzburgite; Lherz.: Lherzolite; ol: olivine; cpx: clinopyroxene; opx: orthopyroxene; sp: spinel).

Location	Sample	ol	cpx	opx	sp	Rock type	Texture
%							
Meerfelder M.	MMa1	60	5	33	2	Harz.	Coarse-grained to
Meerfelder M.	MMa2	63	7	27	3	Harz.	equigranular
Meerfelder M.	MMa3	68	10	20	2	Lherz.	
Meerfelder M.	MMb	49	28	21	3	Lherz	Equigranular
Meerfelder M.	MMc1	73	3	17	1	Harz.	Equigranular to coarse-grained
Meerfelder M.	MMc2	62	5	31	2	Harz.	Equigranular to coarse-grained
Meerfelder M.	MMe	74	4	20	2	Harz.	Equigranular to coarse-grained
Rockeskyllerkopf	Ro	>80	5	0	3	Dunite	Coarse-grained with veins
Dreiser Weiher	DW	97	2	0	0	Dunite	Coarse-grained

4.3. Geothermometry

Equilibrium temperatures of MMa, MMb, MMc and MMe are calculated using the thermometer of Brey and Köhler (1990) based on the partitioning of Na between opx and cpx. The temperature is 1125 °C (±50) for MMb to 1181 °C (±50) for MMc. Our DW sample does not contain opx; the equilibrium temperature used is 1200 °C (±50) as reported by Witt-Eickschen and Kramm (1998) for this locality and similar xenoliths of peridotite. In the latter study, the temperature was calculated using the geothermometer of Brey and Köhler, 1990 in combination with a second geothermometer based on the partitioning of Ca between olivine and cpx (Brey and Köhler, 1990).

The temperature of the magma can be estimated using MELTS (Ghiorso and Sack, 1995) since we know the composition of the lavas that carried the xenoliths to surface and that they contain 10–30% clinopyroxene phenocrysts (e.g. Mertes and Schmincke, 1985; Shaw and Eyzaguirre, 2000; Shaw et al., 2010; Shaw and Woodland, 2012). The MELTS results indicate temperatures between 1250 and 1200 °C, at 0.5 GPa, for a clinopyroxene phenocryst content between 5 and 35%. This is in general agreement with the equilibration temperatures for the xenoliths in the lithospheric mantle. Since we do not have data on the concentration of water in the co-existing melt, we cannot estimate the potential decrease of the equilibrium temperature due to water in the system.

4.4. Concentration and distribution of hydrogen

Water concentrations were obtained for 56 olivine, 15 clinopyroxene and 19 orthopyroxene grains. The olivine spectra show three groups of

Table 2
Major element composition of xenolith minerals from electron microanalyses.

Sample	DW		Ro			MMa1			MMa2			MMa3			MMb			MMc1			MMc2			MMe		
Phase	ol	cpx	ol	cpx	phl	ol	cpx	opx	sp	ol	cpx	opx	ol	cpx	opx	ol	cpx	opx	sp	ol	cpx	opx	ol	cpx	opx	sp
SiO_2	40.71	51.19	40.29	50.42	37.55	41.21	51.99	54.78	0.19	41.20	52.10	54.76	41.84	52.57	55.16	40.15	50.13	52.89	0.20	40.95	51.66	54.43	40.80	54.57	40.72	52.04	54.59	0.18
TiO_2	0.03	0.69	0.00	1.17	3.92	0.04	0.31	0.08	0.48	0.00	0.26	0.09	0.01	0.28	0.12	0.04	0.86	0.30	0.41	0.01	0.30	0.14	0.01	0.11	0.03	0.21	0.09	0.23
Al_2O_3	0.09	5.47	0.01	4.81	16.49	0.06	5.24	4.53	37.53	0.04	5.03	4.65	0.05	7.18	6.01	0.06	7.71	5.82	54.81	0.04	7.11	4.21	0.06	4.32	0.05	5.24	4.54	41.42
Cr_2O_3	0.07	1.44	0.02	0.38	0.63	24.45	0.05	1.33	0.92	28.77	0.02	1.28	0.88	0.03	0.99	0.67	0.05	0.65	0.47	10.25	0.05	0.97	0.90	0.07	0.86	0.04	1.29	0.78	25.81
FeO	11.23	4.34	13.58	4.66	6.76	34.82	9.56	3.63	6.08	15.09	9.76	3.49	6.15	9.57	3.63	6.07	11.31	4.09	7.36	13.70	9.72	3.51	6.07	9.88	6.18	8.79	3.07	5.59	13.26
MnO	0.18	0.10	0.22	0.08	0.04	0.30	0.14	0.11	0.14	0.19	0.14	0.12	0.14	0.15	0.14	0.14	0.16	0.10	0.15	0.12	0.12	0.10	0.14	0.13	0.14	0.12	0.08	0.15	0.18
MgO	47.28	16.56	45.19	14.94	19.87	12.63	48.25	17.17	17.53	48.26	17.16	31.76	47.65	15.71	30.25	47.00	15.36	30.87	19.91	48.55	15.52	30.04	48.04	30.01	49.04	16.80	32.30	18.37
CaO	0.16	18.42	0.22	22.80	0.01	0.02	0.12	18.52	1.44	–	0.13	18.47	1.42	0.13	18.22	1.32	0.12	18.46	1.11	0.01	0.14	17.90	1.43	0.14	1.40	0.11	19.42	1.20	0.00
Na_2O	0.03	1.05	0.00	0.49	0.53	–	0.00	0.92	0.10	–	0.01	0.87	0.09	0.02	1.19	0.16	0.00	1.25	0.11	–	–	1.21	0.12	0.01	0.10	0.00	0.91	0.09	0.00
K_2O	0.00	0.00	0.01	–	10.35	–	0.01	0.01	–	–	0.00	0.02	0.00	0.01	0.01	0.00	0.00	0.00	0.01	–	–	0.00	0.00	–	0.00	0.00	0.01	0.01	0.01
NiO	0.31	0.07	0.33	0.01	0.17	0.33	0.35	0.05	0.10	0.25	0.34	0.08	0.10	0.38	0.09	0.10	0.29	0.04	0.10	0.35	0.33	0.07	0.10	0.34	0.10	0.38	0.04	0.12	0.30
Total	100.09	99.33	99.86	99.77	96.31	98.14	99.79	99.28	100.03	99.89	98.87	100.05	99.84	100.00	100.00	99.17	98.65	99.18	99.76	99.92	98.36	97.56	99.48	97.79	99.28	99.12	99.45	99.78
Mg#[a]	0.88	0.87	0.85	0.85		0.49	0.90	0.89	0.90	0.72	0.90	0.90	0.90	0.89	0.90	0.88	0.88	0.88	0.76	0.90	0.89	0.90	0.90	0.90	0.91	0.91	0.91	0.75

[a] Mg# = Mg / (Mg + Fe), for olivine %Fo = Mg# × 100.

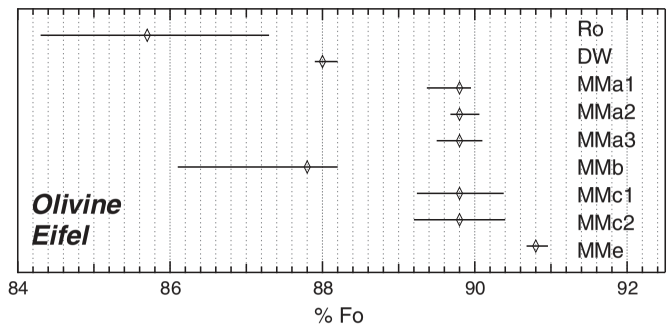

Fig. 4. Forsterite content expressed as %Fo (i.e., %Fo = Mg / (Mg + Fe) × 100) for xenoliths from Rockeskyllerkopf (Ro), Dreiser Weiher (DW), and Meerfelder Maar (MM).

absorption bands: Group 1 (G1): from 3598 to 3420 cm^{-1}, Group 2 (G2): from 3420 to 3280 cm^{-1}, Group 3 (G3): from 3280 to 3195 cm^{-1} (Fig. 6). The band at 3571 cm^{-1} has, in the vast majority of cases, the highest absorbance and is always present. The Group 2 and 3 bands at 3355 and 3226 cm^{-1} are not present in every spectrum and when they are present their absorbance is variable. The absorption spectra of orthopyroxene and clinopyroxene each show three major

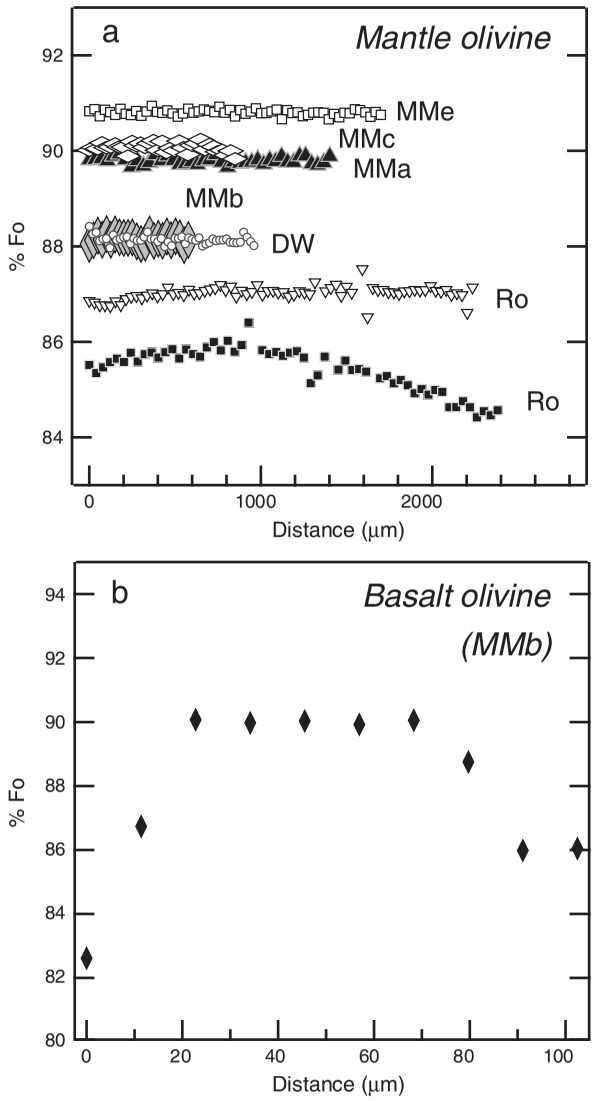

Fig. 5. Forsterite contents across olivine grains. a) Longest %Fo profile vs distance obtained for mantle-derived olivine from each thin section. b) %Fo profile vs distance obtained in an olivine phenocryst in the basalt crust of MMb sample.

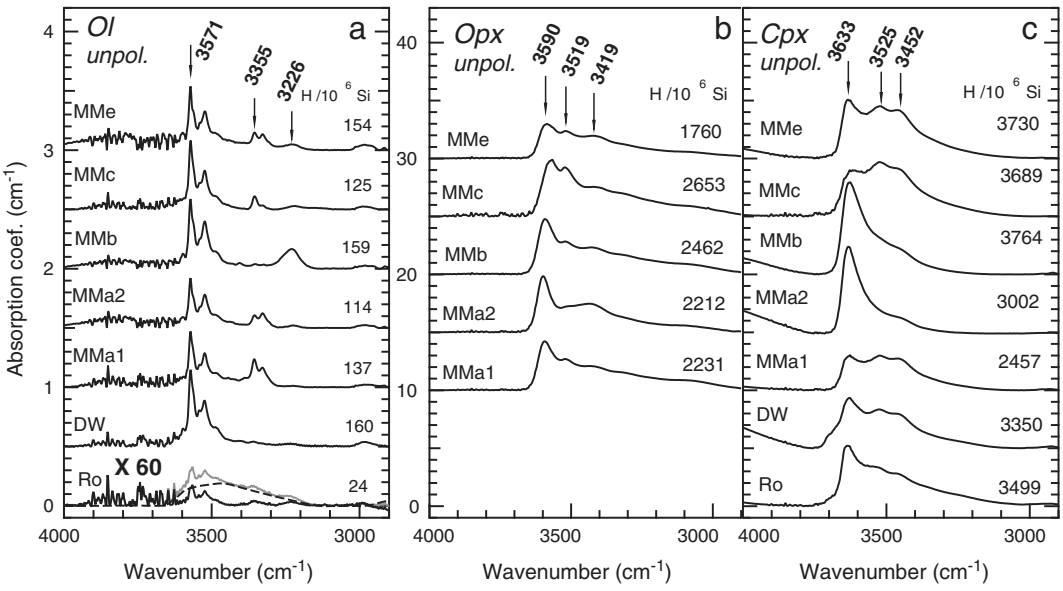

Fig. 6. Representative infrared spectra of each mineral. The spectrum for Ro olivine is multiplied by 60 for readability, and it shows evidence of contamination (gray curve), i.e., a spectrum affected by the OH not from the olivine crystal structure (e.g., hydrous mineral species located in the intergranular space or in inclusion). Contamination results in a broad absorption band (dashed curve). The later spectrum can be subtracted from the original to obtain a corrected spectrum (black curve). Spectra are normalized to a thickness of 1 cm.

absorption bands at 3590, 3519, and 3419 cm^{-1} and 3633, 3525 and 3452 cm^{-1} respectively (Fig. 6).

The polarized analyses on oriented olivine grains highlight the anisotropy of OH group distribution in the crystal structure (Fig. 7). The G1 absorption band is very developed parallel to the [100] axis, while the G2 band is less well developed and the G3 band is poorly developed or absent (Fig. 7). In contrast, in spectra collected on olivine parallel to the [010] axis, all absorption bands are very poorly developed; both the G1 and G 3 bands are absent and the G2 band is just discernible. Parallel to [001], G1 and G 3 bands are just discernable and the G2 band is absent. Such variation in polarized spectra with orientation is typical of olivine from peridotite xenoliths.

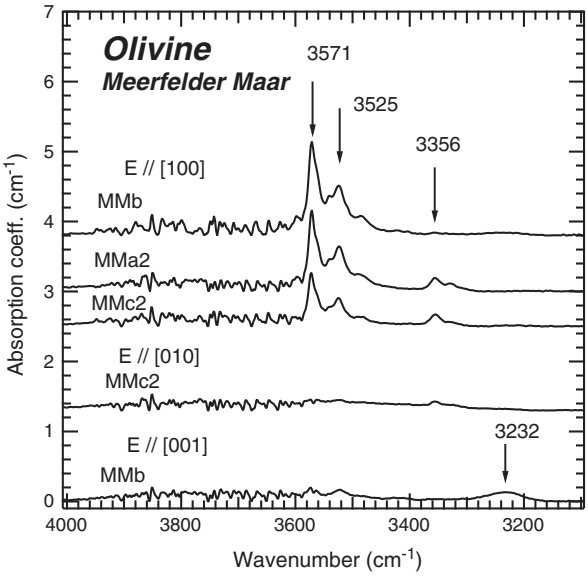

Fig. 7. Polarized infrared spectra of olivine representative of each crystallographic axis. Spectra are normalized to a thickness of 1 cm.

4.4.1. Hydrogen concentration

The range and average concentrations of hydrogen in minerals in ppm wt. H_2O is reported in Table 3. The concentrations in the Meerfelder Maar olivine range from 3.3 to 11 ppm. Olivine in the Dreiser Weiher sample contains around 5 ppm wt. H_2O and the olivine in the Rockeskyllerkopf sample contains less than 3 ppm. Clinopyroxenes are almost homogeneous compared to olivine (within the error bars), and contain between 210 and 353 ppm wt. H_2O. The orthopyroxene in the Meerfelder Maar samples also has small variation (almost homogeneous) with concentrations between 153 and 260 ppm wt. H_2O. These small variations can also may be due to pleochroism in clinopyroxene since they were analyzed with unpolarized IR radiation. In addition, contrary to olivine, no significant variation between center and edge in pyroxene grains was observed as illustrated in Fig. 1S (Supplementary material).

If we consider the hydrogen content of orthopyroxene to be at equilibrium, based on the small variation in the grains analyzed we can calculate the expected hydrogen concentrations in both clinopyroxene and olivine using the partition coefficient data of Aubaud et al. (2004). Aubaud et al. (2004) have used SIMS on selected glasses and minerals, which have also been measured for hydrogen with FTIR spectroscopy and the calibrations of Ohlhorst et al. (2001) as well as by continuous flow mass spectrometry following the methods of Eiler and Kitchen (2001). The study by Aubaud et al. (2004) is so far the best data available for the pressure and temperature conditions of equilibrium for the mantle specimens from Eifel.

The calculations show that for a pressure of 1–2 GPa and temperature of 1230 to 1380 °C, the equilibrium hydrogen content of clinopyroxene is close to the FTIR analysis results (Fig. 8b); however, the equilibrium hydrogen content in olivine is much higher at equilibrium (22–25 ppm wt. H_2O) than actually observed (2–15 ppm wt. H_2O). This suggests that there has been significant loss of hydrogen from the olivine grains.

The distribution of hydrogen content against the maximum apparent length of each olivine grain section (Fig. 8a) shows that for the samples from Meerfelder Maar there is a weak correlation between hydrogen content and the maximum length of each grain section. For the samples from Rockeskyllerkopf this correlation is absent, while for olivines from Dreiser Weiher there is only a weak negative correlation.

Table 3
Hydrogen concentration in xenolith minerals in ppm wt. H_2O. ('Range' gives minimum concentration to maximum concentration; 'Average' gives average concentration from (*n*) measurement).

Sample	Olivine		Clinopyroxene		Orthopyroxene	
	Range (ppm)	Average (ppm)	Range (ppm)	Average (ppm)	Range (ppm)	Average (ppm)
DW	3–7	5 (*4*)	98–289	193 (*2*)	–	–
Ro	2–3	3 (*4*)	301	301 (*1*)	–	–
MMa	5–11	8 (*16*)	212–259	232 (*3*)	157–194	181 (*3*)
MMb	4–11	6 (*7*)	210–353	295 (*7*)	192–218	204 (*9*)
MMc	3–9	6 (*14*)	318	318 (*1*)	173–231	202 (*6*)
MMe	4–6	5 (*11*)	321	321 (*1*)	153–260	203 (*3*)

To convert in H/10^6Si, please follow: For olivine Fo90: 1 ppm wt. H_2O = 16.35 H/10^6Si; for opx: 1 ppm wt. H_2O = 11.49 H/10^6Si; for cpx: 1 ppm wt. H_2O = 11.61 H/10^6 Si.

4.4.2. Hydrogen distribution within individual olivine grains

The spectra taken at points along the [001] axis of olivine show higher absorbance in the three bands and thus higher concentration at the center compared to the edge of the grains (Figs. 9 and 10). In the case of the grain from Dreiser Weiher the concentration decreases by about 66% from core to rim. In sample MMc the decrease is almost 50%, while in MMa and MMb the decrease in concentration toward the border is only 33%.

5. Discussion

5.1. Distribution and concentration of hydrogen

The average concentrations of H in the mantle-derived lherzolites and harzburgites from Meerfelder Maar are ~6 ppm wt. H_2O for olivine, ~226 ppm wt. H_2O for orthopyroxene and ~310 ppm wt. H_2O for clinopyroxene (all values have ~30% of uncertainties). These concentrations are in agreement with water contents reported from spinel-bearing peridotites from a variety of other locations in which concentrations of 1–13, 70–199 and 158–530 ppm wt. H_2O were reported for olivine, orthopyroxene and clinopyroxene respectively (Bell and Rossman, 1992; Demouchy, 2004; Peslier and Luhr, 2006; Chaufaud et al., 2011). However, the water contents are lower than concentrations reported for xenolithic garnet-bearing peridotites (Demouchy et al., 2006; Peslier et al., 2008) and for xenoliths and xenocrysts carried to the surface in volatile-rich host magmas such as kimberlite (Peslier et al., 2008; Kamenetsky et al., 2009; Baptiste et al., 2012).

The variation in hydrogen contents at the centers of olivines as a function of the maximal (apparent) grain size (Fig. 8a) on one hand, and the low hydrogen concentration observed when compared to the calculated equilibrium concentration from partitioning (assuming that orthopyroxene is at equilibrium) on the other hand, are both strongly suggestive of dehydration of olivine by ionic diffusion. The decrease in hydrogen concentration along crystallographic axes (e.g. Fig. 9) is interpreted to be due to dehydration of the olivine during its ascent in a water-undersaturated magma. For the samples with distinct hydrogen variation within grains we can rule out hydrogen variation due to growth in a water poor magma as the grains are otherwise compositionally homogeneous (Fig. 5).

The low water contents and zoned olivine from Rockeskyllerkopf suggest a different petrogenesis for the veined wehrlite. There are two possible interpretations. First, the low Fo content and the presence of veins, the high TiO_2, CaO and low Na_2O in clinopyroxene and the low cr# and mg# of spinel may be due to interaction of lithospheric mantle with percolating melts. Witt-Eickschen and Kramm (1998) and Shaw (2005) have suggested that there was an episode of melt infiltration in the mantle prior to the entrainment of mantle xenoliths. This infiltration event caused diffusive exchange and metasomatic growth of new minerals such as clinopyroxene. Since the melt was likely undersaturated in water, this could also have been responsible for the loss of water from olivine. Alternatively, the dunite from Rockeskyllerkopf could be a dry magmatic cumulate.

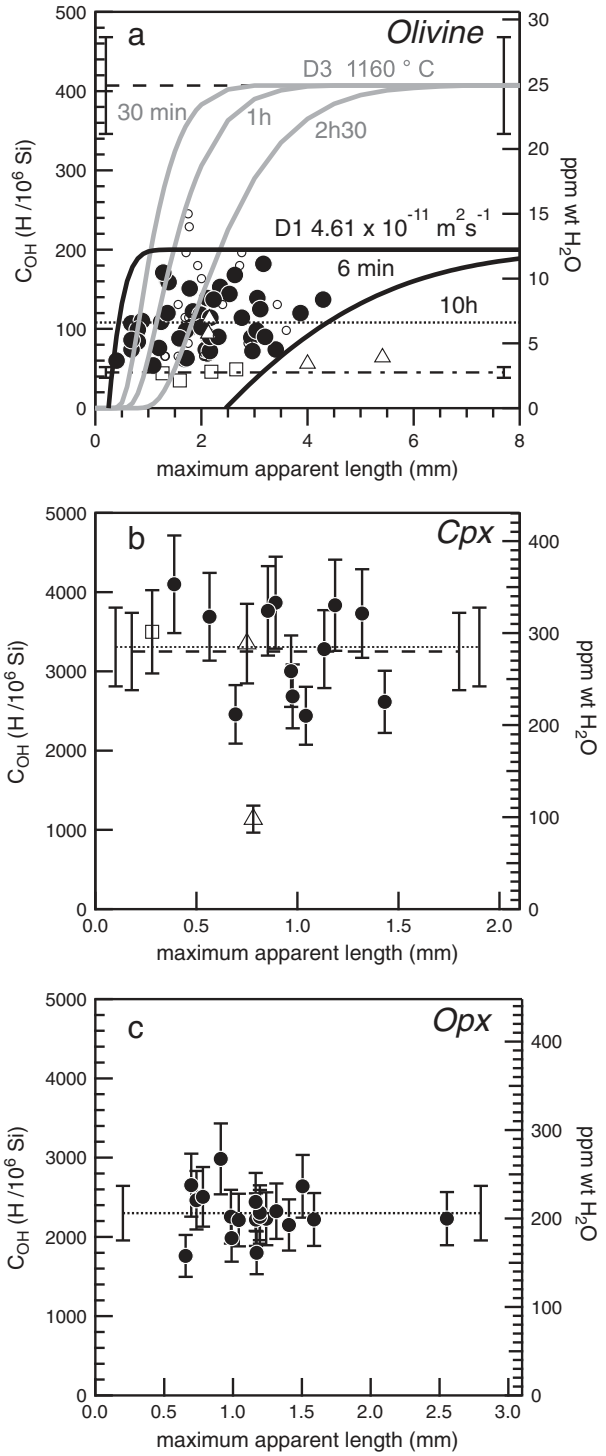

Fig. 8. C_{OH} as a function of the maximum apparent length (mm) of the grain. Each datum point corresponds to one FTIR spectrum. C_{OH} have 30% of uncertainties, and the error bar on the hydrogen concentration in olivine is not shown for clarity. Circles: MM squares: Ro; triangle: DW. The dotted line is the average hydrogen concentration. The dashed line is the expected initial H concentration in MM grains derived from partition coefficient of H,Kd olivine/opx = 0.11 (Aubaud et al., 2004). a) In the case of olivine, the dot-dashed line is based on the almost flat distribution of the data from Ro. The gray curves represent the variation of hydrogen concentration at grain centers as a function of the grain size from the 3D diffusion model with an initial concentration of 25 ppm H_2O wt. (360 H/10^6 Si), and for various durations. The black curves are from the 1D diffusion model for an initial concentration of 12 ppm H_2O wt. (200 H/10^6 Si), for various durations. See Section 4.4.1 for details.

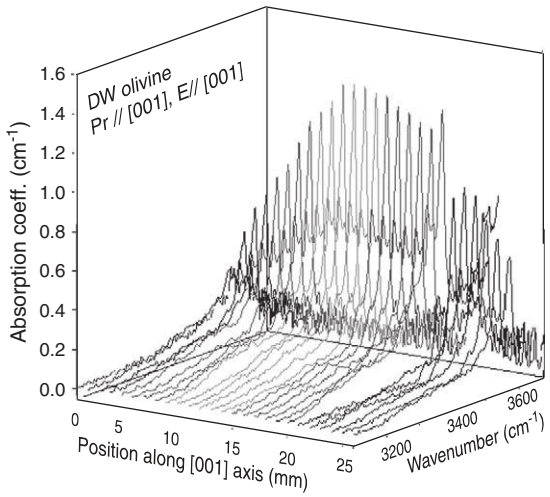

Fig. 9. IR profiles in 3D (x = distance in mm, y = wavenumber, cm^{-1} and y = absorbance). Olivine from DW, E vector//[001] and profile//[001]. Spectra are normalized to a thickness of 1 cm.

In contrast to the heterogeneity of olivine, the homogeneity of the H concentrations measured in orthopyroxene from Meerfelder Maar is interpreted as representing an equilibrium concentration for MM xenoliths. There are four ways in which this could have occurred: (1) the H concentration in orthopyroxene reflects mantle equilibrium, and thus the initial H concentration in the mantle source; (2) the hydrogen concentration in orthopyroxene and clinopyroxene is the result of complete reequilibration with the host magma occurring during ascent (syn-transport equilibrium along an unknown depth path); (3) the observed hydrogen contents represent complete reequilibration with the magma during a period of stagnation in a magma chamber (pre-eruptive equilibrium); and (4) the hydrogen concentration in orthopyroxene and clinopyroxene is the consequence of a late metasomatic event in the mantle lithosphere.

Regardless of which interpretation of the Rockeskyllerkopf dunite we choose, the water content of the olivine is the result of direct crystallization of olivine from a water-poor magma or dehydration due to interdiffusion of mantle olivine with a water-poor magma.

The rate of hydrogen diffusion in pyroxene is very fast; published rates are similar to those for olivine (e.g. at 1200 °C, 2×10^{-11} m^2 s^{-1} in orthopyroxene for the [001] axis, as reported by Carpenter (2000) and 3×10^{-9} m^2 s^{-1} in clinopyroxene as reported by Carpenter Woods et al. (2000)). Thus if there was complete reequilibration of all phases with a water-poor magma we would expect to see diffusion profiles in the pyroxenes as well; but to date none have been observed (on our samples or in other studies). Therefore, one can question the relevance of the experimental diffusion data from pyroxene when applied to natural systems. Our study points toward a strong effect of composition on the H diffusion coefficient in both orthopyroxene and clinopyroxene. Although it suggests that pyroxenes are a better proxy for upper mantle estimation of water content than olivine.

By combining the H concentrations (Table 3) and modal mineralogy (Table 1) for each xenolith, we obtained a bulk average lithospheric mantle concentration of ~90 ppm wt. H_2O for the Meerfelder Maar samples; compared to 54 and 16 ppm wt. H_2O for Dreiser Weiher and Rockeskyllerkopf respectively. When orthopyroxene is present in the samples, as it is the case at Meerfelder Maar, it is the major reservoir for the H in the shallow mantle. In the other two samples, clinopyroxene is the main reservoir for hydrogen. This contrasts the proposal that olivine is the main hydrogen reservoir as previously made by Mierdel et al. (2007) based on experimental data and by Chaufaud et al. (2011) based on analyses of mantle xenoliths from Massif Central (France).

The studied samples allow us to constrain more fully the behavior and the distribution of hydrogen within mantle xenoliths and to analyze the behavior of H in olivine as the xenoliths are transported to

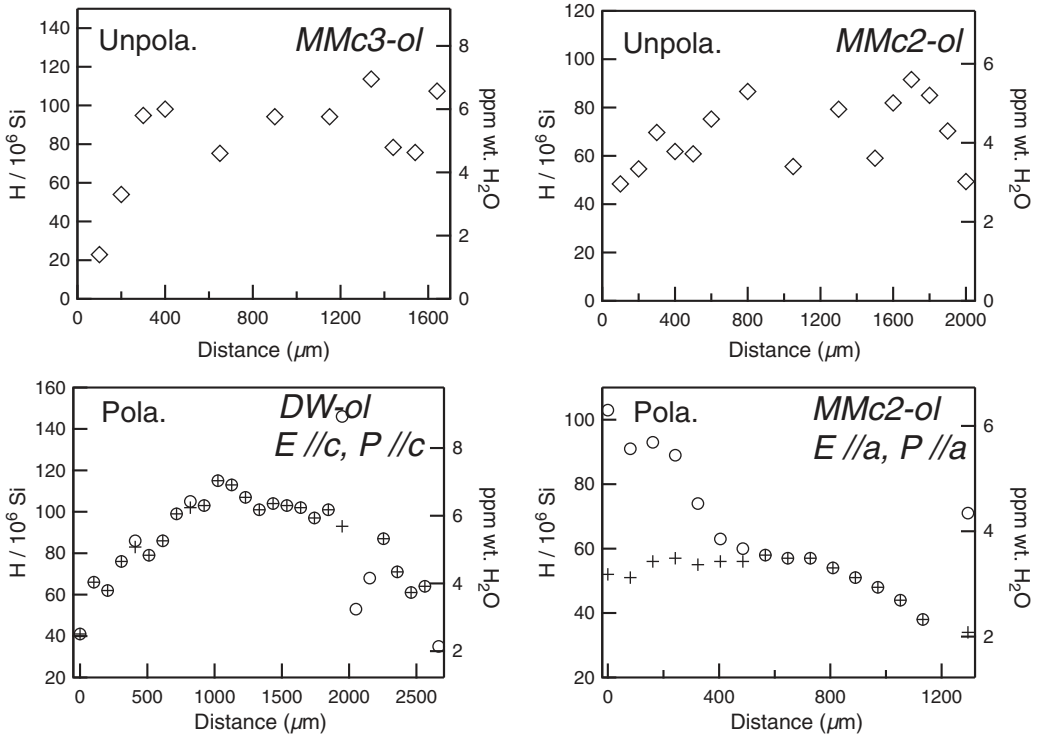

Fig. 10. Hydrogen concentration ($H/10^6$ Si and ppm wt. H_2O) as a function of the distance along the grain of olivine (in μm): the circles represent the concentration of the absorption spectrum from raw data; crosses correspond to the concentration calculated from the absorption spectrum corrected (without contamination or edge effects). Unpola.: unpolarized IR radiation; Pola.: Polarized IR radiation. The error on the hydrogen concentration is about 30%, the error bars are not shown for clarity.

the surface. There are two key observations; first the hydrogen content of the olivine does not vary across the xenoliths, i.e. concentrations are the same in grains from the center of the xenolith or near the edge. Second, there is no variation in the H concentration profiles in olivine based on their position in the xenolith. These observations suggest that during transport, hydrogen was partitioned from olivine into intergranular space and/or along grain boundaries that opened up during decompression. Given the magnitude of the hydrogen loss, the partition coefficient must been significantly less than 1 $\left(K_D^{GB/solid}(OH) \ll 1\right)$ as previously suggested by Hiraga et al. (2003), Suzuki and Mishin (2005), Hiraga et al. (2007) and Demouchy (2010) and sketched in Fig. 11.

5.2. Modeling of dehydration by diffusion

Hydrogen concentration profiles along a crystallographic axis in olivine (Figs. 9 and 10) show that there is a distinct compositional variation. Small edge effects or contamination were observed in only a few grains and corrections were applied to remove these (e.g., boundaries effect from underlying olivine and/or contamination by hydrous material, see Fig. 6 for Ro sample). The hydrogen distribution shows that the crystals are not at equilibrium and profiles are consistent with ionic diffusion of H. We have used two different diffusion models. In the 1D model (Eq. (5)), the initial concentration ($C_{OH}i$) in the grain is dictated by the concentration level of the plateau in the profile (i.e., the maximum observed concentration is taken as the initial concentration). We consider the magma as an infinite sink for H (McMillan, 1994), thus the final concentration of H found at the grain edge should be either zero ($C_{OH}f = 0$) or at its equilibrium value with the H-poor silicate liquid; also likely to be close to zero. The first FTIR measurement in each profile was acquired 50 μm from the edge of the grain. Thus we cannot quantify the minimum concentration at the extreme grain limit. In the models, an assumption of $C_{OH}f = 0$ results in very short diffusion times: 3 min for sample MMa and 1 h and 40 min for sample MMc. These diffusion times are much faster than expected from other estimates of xenolith transport. If they were correct, they would give ascent rates of between 30 and 1000 km/h!

The assumption that the initial concentration in the grain is represented by the core composition is not supported by the experimentally determined partitioning of hydrogen between olivine and orthopyroxene. The experimentally measured partition coefficient is $Kd^{ol/opx} = 0.11$ (Aubaud et al., 2004); however, our data give $Kd^{ol/opx}$ of 0.02 to 0.05 suggesting that the hydrogen content of the cores of the olivine grains does not represent the equilibrium content and that the cores have been affected by diffusive hydrogen loss. If we take the temperatures calculated from the geothermometry and assume a pressure of 1.6 GPa, based on the geotherm for the Eifel region determined by Garcia-Castellanos et al. (2000), the partition coefficient data of Aubaud et al. (2004) give: $K_{D_H}^{ol/opx} = 0.11 \pm 0.01$ and $K_{D_H}^{cpx/opx} = 1.4 \pm 0.3$ for 1–2 GPa and 1230–1380 °C. Using these values we obtain equilibrium concentration of 280 ppm wt. H_2O in clinopyroxene which is closed to the measured value. For olivine, we calculate an initial water content of 22–25 ppm wt. H_2O; i.e. two to four times more than the analyzed maximum. The pressure and temperature under which Aubaud et al. (2004) determined the partition coefficients were slightly higher than those of the xenoliths; therefore the calculated hydrogen concentrations for clinopyroxene and olivine might be slightly overestimated. Nevertheless, this approach suggests that the simple 1D approach described above it not valid and that the diffusion times calculated are much too short.

Since there has been a significant decrease in the concentration of H in olivine from the initial concentration, we must account for this and for the anisotropy of hydrogen diffusion in the olivine since there will be significant differences in concentration as a function of crystallographic orientation. To account for this anisotropy we use the 3D model from Carslaw and Jaeger (1959). The results of this model are reported in Table 4 and examples are shown in Fig. 12. The diffusion durations obtained are very similar for the Meerfelder Maar samples (~1 h for all axes, not just the [001] axis. The profiles for the sample from Dreiser Weiher give a longer diffusion time of 3 h and 40 min. These observations lead to two conclusions: (1) the diffusion duration from the 3D model does not exceed a few hours, and (2) the unreasonably short durations derived from the 1D model are no longer obtained.

A ±50 °C uncertainty on temperature leads to a doubling or halving of the diffusion time (Fig. 12). The large uncertainty on the activation energy (Demouchy and Mackwell, 2006) leads to very different diffusion times. For activation energies of minus one standard

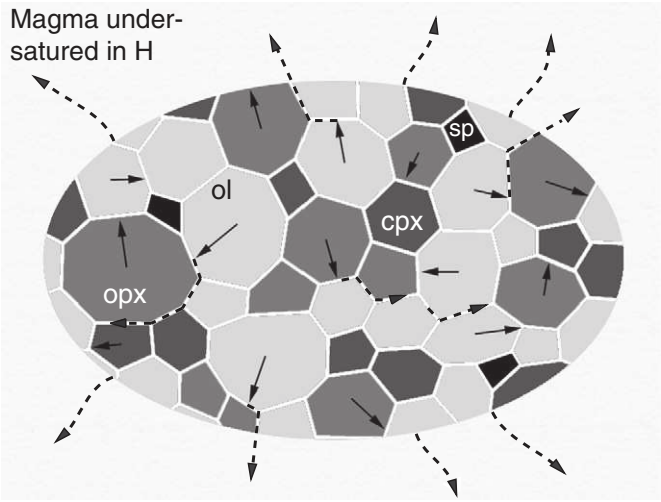

Fig. 11. Schematic diagram illustrating the mobility of H in a mantle xenolith transported by magma; dashed arrow: diffusion of H along the inter-granular space/interface to the magma, solid black arrow: diffusion of H from a crystalline solid to the intergranular space/interface.

Table 4
Hydrogen diffusion coefficients (calculated from Demouchy and Mackwell, 2006) used in this study and results from the 3D model for each sample. See text for details.

Proton-vacancy diffusion					
Sample	D [100]	D [010]	D [001]	Time (s)	
	$m^2\ s^{-1}$			t_{max}	t_{min}
DW 1200 °C	**5.43×10^{-12}**	**5.43×10^{-12}**	**8.30×10^{-11}**	**13,500**	**12,960**
T − 50 °C	3.02×10^{-12}	3.02×10^{-12}	3.96×10^{-11}	27,720	23,400
T + 50 °C	9.38×10^{-12}	9.38×10^{-12}	1.66×10^{-10}	6480	6120
Q − 1σ	1.57×10^{-08}	1.57×10^{-08}	3.95×10^{-10}	46.8	48.6
Q + 1σ	1.07×10^{-15}	1.07×10^{-15}	1.56×10^{-11}	72,000	54,000
MMa 1176 °C	**4.12×10^{-12}**	**4.12×10^{-12}**	**5.86×10^{-11}**	**4320**	**4428**
T − 50 °C	2.25×10^{-12}	2.25×10^{-12}	2.73×10^{-11}	9000	9720
T + 50 °C	7.24×10^{-12}	7.24×10^{-12}	1.20×10^{-10}	2160	
Q − 1σ	1.37×10^{-08}	1.37×10^{-08}	2.89×10^{-10}	10.08	
Q + 1σ	6.95×10^{-16}	6.95×10^{-16}	1.06×10^{-11}	25,200	
MMb 1121 °C	**2.11×10^{-12}**	**2.11×10^{-12}**	**2.52×10^{-11}**	**3600**	
T − 50 °C	1.10×10^{-12}	1.10×10^{-12}	1.10×10^{-11}	8280	
T + 50 °C	3.88×10^{-12}	3.88×10^{-12}	5.44×10^{-11}	1648.8	
Q − 1σ	9.76×10^{-09}	9.76×10^{-09}	1.36×10^{-10}	9	8.28
Q + 1σ	2.44×10^{-16}	2.44×10^{-16}	4.11×10^{-12}	21,600	
MMc 1181 °C	**4.36×10^{-12}**	**4.36×10^{-12}**	**6.31×10^{-11}**	**4104**	**4176**
T − 50 °C	2.39×10^{-12}	2.39×10^{-12}	2.95×10^{-11}	9000	8640
T + 50 °C	7.65×10^{-12}	7.65×10^{-12}	1.28×10^{-10}	1980	2088
Q − 1σ	1.41×10^{-08}	1.41×10^{-08}	3.09×10^{-10}	12.6	11.88
Q + 1σ	7.62×10^{-16}	7.62×10^{-16}	1.15×10^{-11}	22,320	

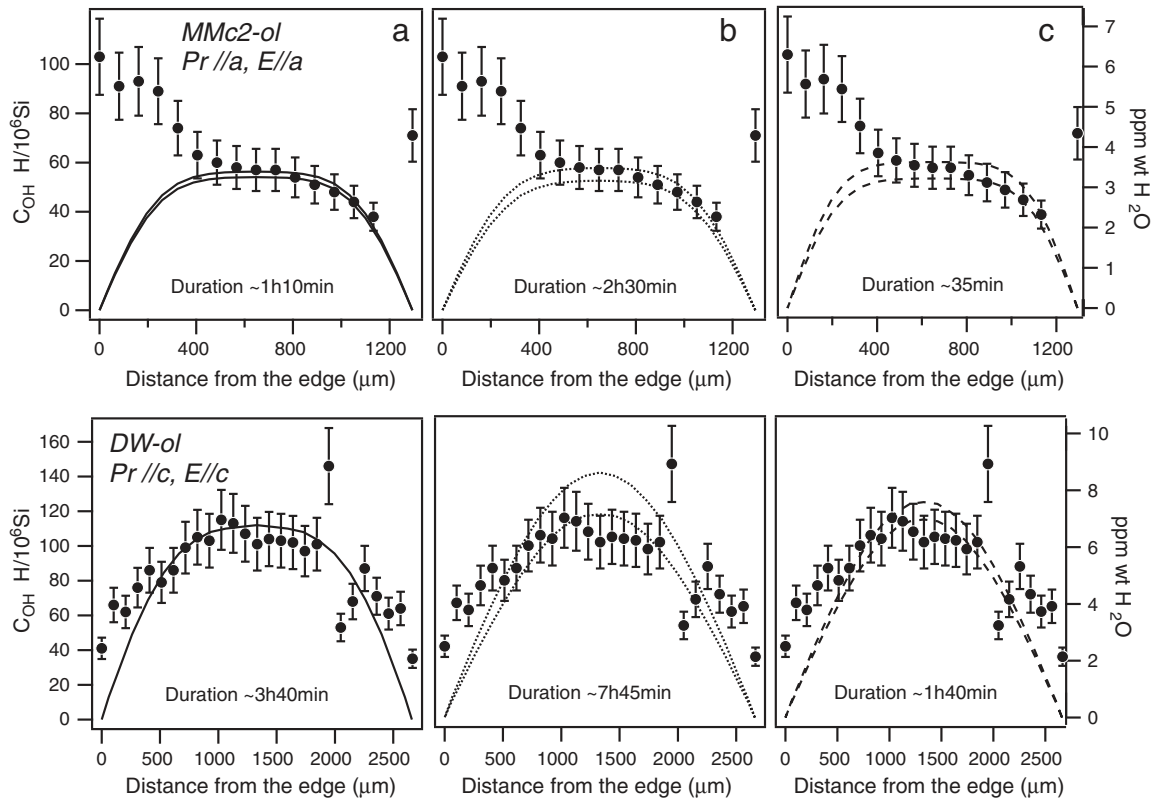

Fig. 12. Representative profiles of H concentration in MMc olivine and DW olivine and calculated with the 3D model. a) Solid curves show the two best results. b) Dotted curves: −50 °C. c). Dashed curves: +50 °C temperature.

deviation, the diffusion times are extremely short ≪1 min. For activation energies of plus one standard deviation, the diffusion times are 5 to 6 times slower than in the case of the average diffusion coefficient. The olivine from Rockeskyllerkopf cannot be used as an ascent 'recorder' since they lack compositional variation in hydrogen.

5.3. Rates of ascent rate and implications for the understanding of magmatic systems

With the durations obtained from the 3D diffusion model and the estimate of the magma chamber depth (14 km, Shaw, 2005) or of the mantle source (45–50 km), the ascent rates of host magmas were calculated (Table 5). The average speed obtained for magmatic ascent from a magma chamber at 14 km is ~3.4 m s^{-1}, while the values determined for transport from the mantle source are ~12 m s^{-1}. These results are in general agreement with those obtained for Shaw (2003, 2009) who showed the Fe–Mg interdiffusion profiles in olivine a transport rate of approximately 4 m s^{-1} for the final eruptive event. Some wehrlite xenoliths from Meerfelder Maar record xenolith – magma contact times of up to 8 years – we would expect these olivine grains to have similar hydrogen contents to those from Rockeskyllerkopf since they would have been immersed in water undersaturated magma long enough to have lost most of their hydrogen.

Our results are well within the range of ascent rates estimated using other methods (Table 6). Together with Fe–Mg interdiffusion, modeling of hydrogen loss during ascent is an effective tool for examining the ascent of mantle xenolith-bearing magmas. Fe–Mg interdiffusion is effective in defining longer periods of diffusion (Shaw, 2003; Costa and Dungan, 2005) whereas the faster diffusion rates for hydrogen make it an effective marker for studying the rapid ascent of xenoliths (as well as for volcanic products, see Lloyd et al., 2012).

Finally, if the H loss by diffusion in olivine is linked to events just before the vesiculation and final water vapor exsolution from a water-rich melt (H_2O, with or without CO_2), the duration of dehydration recorded by olivine only permits an estimate of the velocity of the melt in the crustal section below the vesiculation and fragmentation front. However, since we do not know the water content of the melt and its evolution as a function of depth, we cannot determine the depth of the vapor exsolution and thus an ascent rate. Nevertheless, this very late process must have been very fast since olivines are not fully dehydrated and interestingly, if such a process operated it has affected only olivine and not the pyroxenes.

5.4. Implications for electrical conductivity of the mantle beneath Eifel

Karato (1990) suggested that the presence of hydrogen in mantle silicates should increase their electrical conductivity. Our data show that the mantle olivine below the Eifel has a non-negligible water content, thus one would expect that there will be an effect on the electrical conductivity of the uppermost mantle in this region. The electrical conductivity can be calculated using the Nernst–Einstein relation (Karato, 1990) and H concentrations in olivine. Since olivine is the dominant and interconnected mineral phase (see Pommier and le Trong, 2011 for a review and software), it will control the electrical conductivity of the polymineralic aggregates. The equation links σ the electrical conductivity (S m^{-1}) with D the diffusivity (m^2 s^{-1}), C_{OH} the concentration of H (H m^{-3}) and T the temperature (K):

$$\sigma = f D c q^2 / kT \quad (6)$$

where f is a numerical (correlation) factor approximately equal to unity, q is the electrical charge of the charge species (C), and k is Boltzmann's constant.

The calculation yields resistivity (i.e., in Ωm, thus the inverse electrical conductivity) of 141, 586 and 3514 Ωm for H concentration of 25, 6 and 1 ppm wt. H_2O, respectively. Leibecker et al. (2002)

Table 5
Estimates of rates of magma ascent from two sources of depth (D1: mantle source, D2: magmatic chamber, which yield two different ascent rates, V1 based on D1 and V2 based on D2). See text for details.

Proton-vacancy diffusion								
Sample	Time (s)		Depth (km)		V1 (m s^{-1})		V2 (m s^{-1})	
	t_{max}	t_{min}	D1 Mantle	D2 Mag	$V1_{max}$	$V1_{min}$	$V2_{max}$	$V2_{min}$
DW 1200°C	**13,500**	**12,960**	**52**	**14**	**3.9**	**4**	**1**	**1.1**
T − 50 °C	27,720	23,400	52	14	1.9	2.2	0.5	0.6
T + 50 °C	6480	6120	52	14	8	8.5	2.2	2.3
Q − 1σ	46.8	48.6	52	14	1111	1070	299	288
Q + 1σ	72,000	54,000	52	14	0.7	1	0.2	0.3
MMa 1176 °C	**4320**	**4428**	**50**	**14**	**11.6**	**11.3**	**3.2**	**3.2**
T − 50 °C	9000	9720	50	14	5.6	5.1	1.6	1.4
T + 50 °C	2160		50	14	23.1		6.5	
Q − 1σ	10.08		50	14	4960		1389	
Q + 1σ	25,200		50	14	2		0.6	
MMb 1121 °C	**3600**		**45**	**14**	**12.5**		**3.9**	
T − 50 °C	8280		45	14	5.4		1.7	
T + 50 °C	1648.8		45	14	27.3		8.5	
Q − 1σ	9	8.28	45	14	5000	5435	1556	1691
Q + 1σ	21,600		45	14	2.1		0.6	
MMc 1181 °C	**4104**	**4176**	**50**	**14**	**12.2**	**12**	**3.4**	**3.4**
T − 50 °C	9000	8640	50	14	5.6	5.8	1.6	1.6
T + 50 °C	1980	2088	50	14	25.3	24	7.1	6.7
Q − 1σ	12.6	11.88	50	14	3968	4209	1111	1179
Q + 1σ	22,320		50	14	2.2		0.6	

identified a layer at a depth between 22 and 90 km beneath Eifel with a resistivity of 250 Ωm, which would correspond to 14 ppm wt. H_2O in olivine. This is in reasonable agreement with our results with or without dehydration occurring in olivine. The directional dependence of conductivity noted by Leibecker et al. (2002) may be due to localized addition of hydrogen to olivine during various metasomatic episodes. It is already known that the mineralogical, major and trace element contents of xenolith minerals varies as a function of the degree and type of metasomatism (O'Reilly and Griffin, 2013) and we would expect similar variations for the hydrogen concentration in NAMs.

6. Conclusions

The concentration of H in olivine, orthopyroxene and clinopyroxene from peridotite xenoliths from the West Eifel Volcanic Field obtained by FTIR shows that all three phases contain small amounts of hydrogen (on average 6, 200 and 285 ppm wt. H_2O respectively). Olivines from mantle-derived peridotite from Meerfelder Maar and Dreiser Weiher show evidence of dehydration by ionic diffusion and the measured concentrations do not reflect the concentrations that existed prior to entrainment. Olivine in the dunite xenolith from Rockeskyllerkopf, is either dehydrated due to a longer contact time with water undersaturated magma or it may represent a magmatic cumulate. Three-dimensional diffusion models provide an estimate of the duration of H diffusion in olivine and can be extrapolated to a rate of magma ascent of ~12 ms^{-1} if the source is in the mantle (at 50 km depth), but other depths of dehydration initiation were also considered. The diffusion of H in olivine during ascent toward the surface is suitable marker of the rate of ascent of xenoliths and when used in conjunction with Fe–Mg interdiffusion gives a unique time window into the dynamics of ascent of xenolith-bearing magmas. The H in pyroxenes cannot be used as a marker of magma ascent but they are a more reliable marker of the concentration of H of the mantle source at depth. The study also calls for further H diffusion experiments at low pressure and high temperature within pyroxenes in compositional systems relevant to uppermost peridotitic mantle. Finally, the use of electrical conductivity as a proxy for 'water content' in the uppermost mantle requires the establishment of a precise experimental resistivity calibration that takes into account the low H content, the bulk chemistry, mineralogy and pressure/temperature variation in the uppermost mantle.

Supplementary data to this article can be found online at http://dx.doi.org/10.1016/j.jvolgeores.2013.04.010.

Table 6
Rates of magma ascent from this study and previous studies based on various approaches and methods.

Method	V (m s^{-1})	Source	Reference
H diff. in mantle olivine	~12–3	14–52 km	This study
H diff. in mantle olivine	6 ± 3	60–70 km	Demouchy et al. (2006)
H diff. in mantle olivine	0.2–0.5	32–40 km	Peslier and Luhr (2006)
H diff. in glass inclusion	37–64	4–8 km	Humphreys et al. (2008)
Numerical model	~4	7.2 km	Carey et al. (1995)
H diff. in plagioclase	~0.03	10 km	Hamada et al. (2011)
Zoned magnetite crystals	>0.017	5–6 km	Rutherford and Devine (2003)
Numerical model	2.9–16.8	100 km	Sparks et al. (2006)
CO_2 and H_2O diff in melt incl.	0.05–0.35	180 MPa	Liu et al. (2007)
Numerical model	~5–8	180 MPa	Papale et al. (1998)
Migration of tremor hypocenters	0.03 1.7		Klein et al. (1987)
Dissolution rate of garnet and theoretical models of magma flow	6		Sparks et al. (2006)

Acknowledgments

The authors thank O. Alard and R. Dohmen for constructive discussions and C. Nevado and D. Delmas for providing high-quality polishing of sections for EBSD and FTIR measurements. Electron microprobe analyses were carried out with the help of B. Boyer and C. Merlet at 'Microsconde SUD'. FTIR analyses were performed with the assistance of D. Maurin from the Laboratoire Charles Coulomb at Université Montpellier 2, France. The EBSD-SEM national facilities (F. Barou) in Montpellier are supported by the Institut National de Sciences de l'Univers (INSU), the Centre National de la Recherche Scientifique (CNRS, France) and the Conseil Régional Languedoc-Roussillon.

References

Aines, R.D., Rossman, G.R., 1984. Water in minerals? A peak in the infrared. Journal of Geophysical Research 89, 4059–4071.

Aubaud, C., Hauri, E.H., Hirschmann, M.M., 2004. Hydrogen partition coefficients between nominally anhydrous minerals and basaltic melts. Geophysical Research Letters 31, 1–4. http://dx.doi.org/10.1029/2004GL021341.

Bali, E., Bolfan-Casanova, N., Koga, K., 2008. Pressure and temperature dependence of H solubility in forsterite: an implication to water activity in the Earth interior. Earth and Planetary Science Letters 268, 354–363.

Baptiste, V., Tommasi, A., Demouchy, S., 2012. Deformation and hydration of the lithospheric mantle beneath the Kaapvaal craton, South Africa. Lithos 149, 31–50. http://dx.doi.org/10.1016/j.lithos.2012.05.001 (Sp. Issue "Formation, reactivation and destruction of cratons").

Beer, A., 1852. Bestimmung der Absorption des rothen Lichts in farbigen Flüssigkeiten. Annalen der Physik und Chemie 86, 78–88.

Bell, D., Rossman, G., 1992. Water in Earth's mantle: the role of nominally anhydrous minerals. Science 255, 1391–1397.

Bell, D.R., Rossman, G.R., Maldener, J., Endisch, D., Rauch, F., 2003. Hydroxide in olivine: a quantitative determination of the absolute amount and calibration of the IR spectrum. Journal of Geophysical Research 108, 2105. http://dx.doi.org/10.1029/2001JB000679.

Bell, D.R., Rossman, G.R., Moore, R.O., 2004. Abundance and partitioning of OH in a high-pressure magmatic system: megacrysts from the Monastery kimberlite. The South African Journal of Petrology 45 (8), 1539–1564.

Beran, A., Putnis, A., 1983. A model of the OH position in olivine, derived from infrared-spectroscopic investigations. Physics and Chemistry of Minerals 9, 57–60.

Bolfan-Casanova, N., 2005. Water in the Earth's mantle. Mineralogical Magazine 69, 229–257.

Brey, G., Köhler, T., 1990. Geothermobarometry in four-phase lherzolites II. New thermobarometers and practical assessment of existing thermobarometers. Journal of Petrology 31, 1353–1378.

Budweg, M., Bock, G., Weber, M., 2006. The Eifel Plume — imaged with converted seismic waves. Geophysical Journal International 166, 579–589.

Carey, S., Gardner, J., Sigurdsson, H., 1995. The intensity and magnitude of Holocene Plinian eruptions from Mount St-Helens volcano. Journal of Volcanology and Geothermal Research 66 (1–4), 185–202.

Carpenter, S.J., 2000. The Kinetics of Hydrogen Diffusion in Single-Crystal Orthopyroxene. Ph.D. Thesis Pennsylvania State University 410.

Carpenter Woods, S., Mackwell, S.J., Dyar, D., 2000. Hydrogen in diopside: diffusion profiles. American Mineralogist 85, 480–487.

Carslaw, H.S., Jaeger, J.C., 1959. Conduction of Heat in Solids, second edition. Oxford University Press 184.

Chakraborty, S., 1997. Rates and mechanisms of Fe–Mg interdiffusion in olivine at 980 °–1300 °C. Journal of Geophysical Research 102, 12317–12331. http://dx.doi.org/10.1029/97JB00208.

Chaufaud, J., Alard, O., Demouchy, S., Dautria, J.-M., O'Reilly, S.Y., 2011. Water Behaviour During Mantle Melt Percolation-Reaction: A Case Study from the Borée Peridotite Xenoliths (Massif Central, France). 5-9/12 AGU Fall Meet. 2011 Suppl., Abstract DI21A-2061.

Costa, F., Chakraborty, S., 2004. Decadal time gaps between mafic intrusion and silicic eruption obtained from chemical zoning patterns in olivine. Earth and Planetary Science Letters 227 (3–4), 517–530.

Costa, F., Dungan, M., 2005. Short time scales of magmatic assimilation from diffusion modeling of multiple elements in olivine. Geology 33, 837–840.

Crank, J., 1975. The Mathematics of Diffusion. Oxford University Press (p. 32 et p. 151).

Demouchy, S., 2010. Hydrogen diffusion in spinel grain boundaries and consequences for chemical homogenization in hydrous peridotites. Contributions to Mineralogy and Petrology 160, 887–898. http://dx.doi.org/10.1007/s00410-010-0512-4.

Demouchy, S., Mackwell, S., 2006. Mechanisms of hydrogen incorporation and diffusion in iron-bearing olivine. Physics and Chemistry of Minerals 33, 347–355.

Demouchy, S., 2004. Thermodynamics and kinetics of hydrogen incorporation in olivine and wadsleyite. Bayerisches Geoinstitut, Universitaet Bayreuth, Bayreuth, p. 163.

Demouchy, S., Jacobsen, S.D., Gaillard, F., Stern, C.R., 2006. Rapid magma ascent recorded by water diffusion profiles in mantle olivine. Geology 34, 429–432.

Demouchy, S., Mackwell, S.J., Kohlstedt, D.L., 2007. Influence of hydrogen on Fe–Mg interdiffusion in (Mg,Fe)O and implications for Earth's lower mantle. Contributions to Mineralogy and Petrology 154, 279–289.

Demouchy, S., Tommasi, A., Barou, F., Mainprice, D., Cordier, P., 2012. Deformation of olivine in torsion under hydrous conditions. Physics of the Earth and Planetary Interiors 203–203, 56–70. http://dx.doi.org/10.1016/j.pepi.2012.05.001.

Dixon, J.E., Leist, L., Langmuir, C., Schilling, J.G., 2002. Recycled dehydrated lithosphere observed in plume-influenced mid-ocean-ridge basalt. Nature 420 (6914), 385–389.

Eiler, J.M., Kitchen, N., 2001. Hydrogen-isotope analysis of nanomole (picoliter) quantities of H_2O. Geochimica et Cosmochimica Acta 65 (24), 4467–4479.

Farver, J.R., 2010. Oxygen and hydrogen diffusion in minerals. Diffusion in Minerals and Melts 72, 447–507.

Férot, A., Bolfan-Casanova, N., 2012. Water storage capacity in olivine and pyroxene to 14 GPa: implications for the water content of the Earth's upper mantle and nature of seismic discontinuities. Earth and Planetary Science Letters 349–350, 218–230.

Gaetani, G.A., Grove, T.L., Bryan, W.B., 1993. The influence of water on the petrogenesis of subduction-related igneous rocks. Nature 365 (6444), 332–334. http://dx.doi.org/10.1038/365332a0.

Gaetani, G.A., O'Leary, J.A., Shimizu, N., Bucholz, C.E., Newville, M., 2012. Rapid reequilibration of H_2O and oxygen fugacity in olivine-hosted melt inclusions. Geology 40, 915–918. http://dx.doi.org/10.1130/G32992.1.

Garcia-Castellanos, D., Cloetingh, S., van Balen, R.T., 2000. Modelling the Middle Pleistocene uplift in the Ardennes–Rhenish Massif: thermo-mechanical weakening under the Eifel? Global and Planetary Change 27, 39–52.

Ghiorso, M.S., Sack, R.O., 1995. Chemical mass-transfer in magmatic processes. 4. A revised and internally consistent thermodynamic model for the interpolation and extrapolation of liquid–solid equilibria in magmatic systems at elevated-temperatures and pressures. Contributions to Mineralogy and Petrology 119, 197–212. http://dx.doi.org/10.1007/BF00307281.

Goldsmith, J.R., 1987. Al/Si interdiffusion in albite: effect of pressure and the role of hydrogen. Contributions to Mineralogy and Petrology 95, 311–321.

Griggs, D.T., Blacic, J.D., 1965. Quartz: anomalous weakness of synthetic crystals. Science 147, 292–295.

Hamada, M., Kawamoto, T., Takahashi, E., Fujii, T., 2011. Polybaric degassing of island arc low-K tholeiitic basalt magma recorded by OH concentrations in Ca-rich plagioclase. Earth and Planetary Science Letters 308, 259–266.

Hawkesworth, C.J., Blake, S., Evans, P., Hughes, R., Macdonald, R., Thomas, L.E., Turner, S.P., Zellmer, G., 2000. Time scales of crystal fractionation in magma chambers — integrating physical, isotopic and geochemical perspectives. Journal of Petrology 41, 991–1006.

Hier-Majumder, S., Anderson, I.M., Kohlstedt, D.L., 2004. Influence of protons on Fe–Mg interdiffusion in olivine. Journal of Geophysical Research 110. http://dx.doi.org/10.1029/2004JB003292.

Hiraga, T., Anderson, I.M., Kohlstedt, D.L., 2003. Chemistry of grain boundaries in mantle rocks. American Mineralogist 88, 1015–1019.

Hiraga, T., Hirschmann, M.M., Kohlstedt, D.L., 2007. Equilibrium interface segregation in the diopside–forsterite system 2: Applications of interface enrichment to mantle geochemistry. Geochimica et Cosmochimica Acta 71, 1281–1289.

Hirschmann, M.M., Aubaud, C., Withers, A.C., 2005. Storage capacity of H_2O in nominally anhydrous minerals in the upper mantle. EPSL 236 (1–2), 167–181.

Humphreys, M., Menand, T., Blundy, J.D., Klimm, K., 2008. Magma ascent rates in explosive eruptions: constraints from H_2O diffusion in melt inclusions. Earth and Planetary Science Letters 270, 25–40.

Ingrin, J., Blanchard, M., 2006. Diffusion of hydrogen in minerals. In: Keppler, H., Smyth, J.R. (Eds.), Water in Nominally Anhydrous Minerals. Review in Mineralogy and Geochemistry: American Mineralogical Society Geochemical Society, Chantilly (Vir.), 62, pp. 291–320.

Ingrin, J., Skogby, H., 2000. Hydrogen in nominally anhydrous upper-mantle minerals: concentration levels and implications. European Journal of Mineralogy 12 (3), 543–570.

Ingrin, J., Hercule, S., Charton, T., 1995. Diffusion of hydrogen in diopside: results of dehydration experiments. Journal of Geophysical Research 100, 15,489–15,499.

Jacobsen, S.D., Smyth, J.R., Spetzler, H.A., Frost, D.J., 2004. Sound velocities and elastic constant of iron-bearing hydrous ringwoodite. Physics of the Earth and Planetary Interiors 143–144, 47–56.

Jambon, A., Zimmermann, J.L., 1990. Water in oceanic basalts: evidence for dehydration of recycled crust. Earth and Planetary Science Letters 101, 323–331.

Johnson, E.A., Rossman, G.R., 2003. The concentration and speciation of hydrogen in feldspars using FTIR and H-1 MAS NMR spectroscopy. American Mineralogist 88 (5–6), 901–911.

Kamenetsky, V.S., Maas, R., Kamenetsky, M.B., Paton, C., Phillips, D., Golovin, A.V., Gornova, M.A., 2009. Chlorine from the mantle: magmatic halides in the Udachnaya-East kimberlite, Siberia. Earth and Planetary Science Letters 285, 96–104.

Karato, S.-I., 1990. The role of hydrogen diffusivity in the electrical conductivity of the upper mantle. Nature 347, 272–273.

Karato, S.-I., 2006. Remote sensing of hydrogen in the earth's mantle. Mineralogy and Geochemistry 62, 343–375.

Keyser, M., Ritter, J.R.R., Jordaneyser, M., 2002. 3D shear-wave velocity structure of the Eifel plume, Germany. Earth and Planetary Science Letters 203, 59–82.

Klein, F.W., Koyanagi, R.Y., Nakata, J.S., Tanigawa, W.R., 1987. The seismicity of Kilauea's magma system. In: Decker, R.W., Wright, P.H., Staufer, T.L. (Eds.), Volcanism in Hawaii: U.S. Geol Survey Prof Paper 1350, pp. 1019–1185.

Koga, K., Hauri, E., Hirschmann, M.M., Bell, D., 2003. Hydrogen concentration analyses using SIMS and FTIR: comparison and calibration for nominally anhydrous minerals. Geochemistry, Geophysics, Geosystems 4 (2). http://dx.doi.org/10.1029/2002GC000378.

Kohlstedt, D.L., Mackwell, S.J., 1999. Solubility and diffusion of "water" in silicate minerals. In: Wright, K., Catlow, R. (Eds.), Microscopic Properties and Processes in Minerals. Kluwer Academic Publishers, Dordrecht, pp. 539–559.

Kohlstedt, D.L., Keppler, H., Rubie, D.C., 1996. Solubility of water in the α, β and γ phases of $(Mg,Fe)_2SiO_4$. Contributions to Mineralogy and Petrology 123, 345–357.

Kushiro, I., 1972. Effect of water on the composition of magmas formed at high pressures. Journal of Petrology 13, 311–334.

Leibecker, J., Gatzemeier, A., Honig, M., 2002. Evidence of electrical anisotropic structures in the lower crust and the upper mantle beneath the Rhenish Shield. Earth and Planetary Science Letters 202 (2), 289–302. http://dx.doi.org/10.1016/S0012-821X(02)00783-5.

Li, Z.X.A., Lee, C.-T.A., Peslier, A., Lenardic, A., Mackwell, S.J., 2008. Water contents in mantle xenoliths from the Colorado Plateau and vicinity: implications for the mantle rheology and hydration-induced thinning of continental lithosphere. Journal of Geophysical Research 113. http://dx.doi.org/10.1029/2007JB005540.

Liu, Y., Anderson, A.T., Wilson, C.J.N., 2007. Melt pockets in phenocrysts and decompression rates of silicic magmas before fragmentation. Journal of Geophysical Research 112, B06204. http://dx.doi.org/10.1029/2006JB004500.

Lloyd, A.S., Plank, T., Ruprecht, P., Hauri, E.H., Rose, W., 2012. Volatile loss from melt inclusions in pyroclasts of differing sizes. Contributions to Mineralogy and Petrology. http://dx.doi.org/10.1007/s00410-012-0800-2.

MacKenzie, J.M., Canil, D., 2008. Volatile heavy metal mobility in silicate liquids: implications for volcanic degassing and eruption prediction. Earth and Planetary Science Letters 269 (3–4), 488.
Mackwell, S.J., Kohlstedt, D.L., 1990. Diffusion of hydrogen in olivine — implication for water in the mantle. Journal of Geophysical Research 95 (B4), 5079–5088. http://dx.doi.org/10.1029/JB095iB04p05079.
Mackwell, S.J., Kohlstedt, D.L., Paterson, M.S., 1985. The role of water in the deformation of olivine single crystals. Journal of Geophysical Research 90, 11319–11333.
Marty, B., 2012. The origins and concentrations of water, carbon, nitrogen and noble gases on Earth. Earth and Planetary Science Letters 313–314, 56–66.
McMillan, P.F., 1994. Review in mineralogy: water solubility and speciation models. In: Caroll, M.R., Holloway, J.R. (Eds.), Volatiles in Magmas. Review in Mineralogy American Mineralogical Society, Washington D.C., pp. 131–156.
Mertes, H., Schmincke, H.U., 1985. Mafic potassic laves of the quaternary west Eifel volcanic field. 1. Major and trace-elements. Contributions to Mineralogy and Petrology 89 (4), 330–345. http://dx.doi.org/10.1007/BF00381555.
Michael, P.J., 1988. The concentration, behavior and storage of H_2O in the suboceanic upper mantle: implications for mantle metasomatism. Geochimica et Cosmochimica Acta 52 (2), 555–566.
Mierdel, K., Keppler, H., Smyth, J.R., Langenhorst, F., 2007. Water solubility in aluminous orthopyroxene and the origin of Earth's asthenosphere. Science 315, 364–368.
Miller, G.H., Rossman, G.R., Harlow, G.E., 1987. The natural occurrence of hydroxide in olivine. Physics and Chemistry of Minerals 14, 461–472.
Nowell, D.A.G., Jones, M.C., Pyle, D.M., 2006. Episodic Quaternary volcanism in France and Germany. Journal of Quaternary Science 21, 645–675. http://dx.doi.org/10.1002/jqs.1005.
Ohlhorst, S., Behrens, H., Holtz, F., 2001. Compositional dependence of molar absorptivities of near-infrared OH^- and H_2O bands in rhyolitic to basaltic glasses. Chemical Geology 174 (1–3), 5–20.
O'Reilly, S.Y., Griffin, W.L., 2013. Mantle metasomatism. In: Harlov, D., Austrheim, H. (Eds.), Metasomatism and the Chemical Transformation of Rock, the Role of Fluids in Terrestrial and Extraterrestrial Processes. : Lecture Notes in Earth System Sciences. Springer, Berlin, Heidelberg, pp. 471–533.
Papale, P., Neri, A., Macedonio, G., 1998. The role of magma composition and water content in explosive eruptions — 1. Conduit ascent dynamics. Journal of Volcanology and Geothermal Research 87 (1–4), 75–93.
Paterson, M.S., 1982. The determination of hydroxyl by infrared absorption in quartz, silicate glasses and similar materials. Bulletin de Mineralogie 105, 20–29.
Peslier, A.H., Luhr, J.F., 2006. Hydrogen loss from olivines in mantle xenoliths from Simcoe (USA) and Mexico: mafic alkalic magma ascent rates and water budget of the sub-continental lithosphere. EPSL 242 (3–4), 302–319.
Peslier, A., Luhr, J.F., Post, J., 2002. Low water contents in pyroxenes from spinel-peridotites of the oxidized, sub-arc mantle wedge. Earth and Planetary Science Letters 201, 69–86.
Peslier, A.H., Woodland, A.B., Wolff, J.A., 2008. Fast kimberlite ascent rates estimated from hydrogen diffusion profiles in xenolithic mantle olivines from southern Africa. Geochimica et Cosmochimica Acta 72, 2711–2722.
Pitzer, K.S., Sterner, S.M., 1994. Equations of state valid continuously from zero to extreme pressures for H_2O and CO_2. The Journal of Chemical Physics 101, 3111–3116.
Pommier, A., Le Trong, E., 2011. SIGMELTS: a web portal for electrical conductivity calculations in geosciences. Computers and Geosciences 37, 1450–1459.
Preusser, F., Rufer, D., Schreurs, G., 2011. Direct dating of Quaternary phreatic maar eruptions by luminescence methods. Geology 39 (12), 1135–1138.
Rauch, M., 2000. Der Einbau von Wasser in Pyroxene. Bayreuth Universität, Bayreuth (141 pp.).
Ritter, J.R.R., Jordan, M., Christensen, U.R., 2001. A mantle plume below the Eifel volcanic fields, Germany. Earth and Planetary Science Letters 186, 7–14.
Rossman, G.R., 1988. Vibrational spectroscopy of hydrous species. Reviews in Mineralogy 18, 193–206.
Rossman, G., Smyth, J., 1990. Hydroxyl contents of accessory minerals in mantle eclogites and related rocks. American Mineralogist 75, 775–780.
Rutherford, M.J., Devine, J.D., 2003. Magmatic conditions and magma ascent as indicated by hornblende phase equilibria and reactions in the 1995–2002 Soufriere Hills magma. Journal of Petrology 44 (8), 1433–1454.
Schmincke, H.U., 2007. Volcanism. Springer, Berlin–Heidelberg 324.
Schmincke, H.U., Lorenz, V., Seck, H.A., 1983. The Quaternary Eifel volcanic fields. In: Fuchs, K. (Ed.), Plateau Uplift. Springer, Berlin, pp. 139–151.
Serway, R.A., Moses, C.J., Moyer, C.A., 1997. Moderns Physics2nd ed. Saunders College 580.
Shaw, C.S.J., 2003. The temporal evolution of three magmatic systems in the West Eifel volcanic field, Germany. Journal of Volcanology and Geothermal Research 131, 213–240.
Shaw, C.S.J., 2005. Regional variations in the mineralogy of metasomatic assemblages in mantle xenoliths from the West Eifel volcanic field, Germany. Journal of Petrology 46, 945–972.
Shaw, C.S.J., 2009. Caught in the act — the first few hours of xenolith assimilation preserved in lavas of the Rockeskyllerkopf volcano, West Eifel, Germany. Lithos 112, 511–523.
Shaw, C.S.J., Eyzaguirre, J., 2000. Origin of megacrysts in the mafic alkaline lavas of the West Eifel volcanic field, Germany. Lithos 50, 75–95.
Shaw, C.S.J., Klugel, A., 2002. The pressure and temperature conditions and timing of glass formation in mantle-derived xenoliths from Baarley, West Eifel, Germany: the case for amphibole breakdown, lava infiltration and mineral-melt reaction. Mineralogy and Petrology 74 (2–4), 163–187. http://dx.doi.org/10.1007/s007100200003.
Shaw, C.S.J., Woodland, A.B., 2012. The role of magma mixing in the petrogenesis of mafic alkaline lavas, Rockeskyllerkopf Volcanic Complex, West Eifel, Germany. Bulletin of Volcanology 74, 359–376.
Shaw, C.S.J., Woodland, A.B., Hopp, J., Trenholm, N.D., 2010. Structure and evolution of the Rockeskyllerkopf Volcanic Complex, West Eifel Volcanic Field, Germany. Bulletin of Volcanology 72, 971–990. http://dx.doi.org/10.1007/s00445-010-0380-9.
Skogby, H., 1994. OH incorporation in synthetic clinopyroxene. American Mineralogist 79, 240–249.
Smyth, J.R., 1987. β-Mg_2SiO_4: a potential host for water in the mantle? American Mineralogist 72, 1051–1055.
Sparks, R.S.J., Baker, L., Brown, R.J., Field, M., Schumacher, J., Stripp, G., Walters, A., 2006. Dynamical constraints on kimberlitic volcanism. Journal of Volcanology and Geothermal Research 155, 18–48.
Spera, F.J., 1984. Carbon dioxide in petrogenesis: III. Role of volatiles in the ascent of alkaline magma with special reference to xenolith-bearing mafic lavas. Contributions to Mineralogy and Petrology 88, 217–232. http://dx.doi.org/10.1007/BF00380167.
Stalder, R., Skogby, H., 2003. Hydrogen diffusion in natural and synthetic orthopyroxene. Physics and Chemistry of Minerals 30, 12–19.
Suzuki, A., Mishin, Y., 2005. Atomic mechanism of grain boundary diffusion: low versus high temperatures. Journal of Mathematical Sciences 40, 3155–3161.
Tepley III, F.J., Davidson, J.P., Tilling, R.I., Arth, J.G., 2000. Magma mixing, recharge, and eruption histories recorded in plagioclase phenocrysts from El Chichón Volcano, Mexico. Journal of Petrology 41, 1397–1411.
Wilson, M., Downes, 1991. Tertiary Quaternary extension-related alkaline magmatism in western and central-Europe. Journal of Petrology 32 (4), 811–849.
Withers, A.C., Bureau, H., Raepsaet, C., Hirschmann, M.M., 2012. Calibration of infrared spectroscopy by elastic recoil detection analysis of H in synthetic olivine. Chemical Geology 334, 92–98.
Witt-Eickschen, G., Kramm, U., 1998. Evidence for the multiple stage evolution of the subcontinental lithospheric mantle beneath the Eifel (Germany) from pyroxenite and composite pyroxenite/peridotite xenoliths. Contributions to Mineralogy and Petrology 131 (2–3), 258–272. http://dx.doi.org/10.1007/s004100050392.
Witt-Eickschen, G., Seck, H.A., Mezger, K., 2003. Lithospheric mantle evolution beneath the Eifel (Germany): constraints from Sr–Nd–Pb isotopes and trace element abundances in spinel peridotite and pyroxenite xenoliths. Journal of Petrology 44 (6), 1077–1095. http://dx.doi.org/10.1093/petrology/44.6.1077.
Yoshino, T., Shimojuku, A., Shan, S., Guo, X., Yamazaki, D., Ito, E., Higo, Y., Funakoshi, K., 2012. Effect of temperature, pressure and iron content on the electrical conductivity of olivine and its high-pressure polymorphs. Journal of Geophysical Research 117, B08205.
Zhang, Y., 2011. Diffusion in minerals and melt: theoretical background. In: Zhang, Y., Cherniak, D.J. (Eds.), Diffusion in Minerals and Melts. : Review in Mineralogy and Geochemistry, vol. 72. American Mineralogical & Society Geochemical Society, Chantilly (Vir.), pp. 5–59.
Zinngrebe, E., Foley, S.F., 1995. Metasomatism in mantle xenoliths from Gees, West Eifel, Germany — evidence for the genesis of calc-alkaline glasses and metasomatic Ca-enrichment. Contributions to Mineralogy and Petrology 122, 79–96.
Zolitschka, B., Negendank, J.F.W., Lottermoser, B.G., 1995. Sedimentological proof and dating of the early Holocene volcanic-eruption of Ulmener Maar (Vulkaneifel, Germany). Geologische Rundschau 8, 213–219.

Chapitre IV : Transport de l'H lors de processus mantelliques de grande échelle : fusion partielle et métasomatisme

Ce chapitre détaille le comportement de l'H lors des processus de fusion et de métasomatisme dans un contexte de point chaud en prenant comme sujet d'étude une série de xénolites de péridotite du Ray Pic (Massif Central).

IV.1 Introduction

Le chapitre précèdent a permis d'observer que les concentrations en H des olivines peuvent être affectées par la remontée magmatique alors que les concentrations en H très homogènes des pyroxènes suggèrent une signature mantellique intacte. Une série de xénolites de péridotite (± amphibole) du Ray Pic (Massif Central Français) ne présentant pas de variations intracristallines en H a été sélectionnée afin de s'intéresser aux processus mantelliques.

Cette série d'échantillons provient d'un contexte de point chaud, impliquant des processus de fusion et de métasomatisme de grande échelle. Elle est donc un objet clé pour contraindre le comportement de l'H dans le manteau. La caractérisation des processus subis par la roche (*e.g.*, taux de fusion, métasomatisme modal/cryptique) est basée sur les concentrations en éléments en traces (*e.g.*, REE). Le type de métasomatisme est déterminé par l'abondance et le fractionnement des éléments incompatibles tels que les terres rares.

Les principales conclusions des précédentes études (Zangana *et al.,* 1997 ; 1999) sont que le manteau sous le Ray Pic est hétérogène en termes de minéralogie, de chimie des éléments majeurs ainsi qu'en éléments en traces. Les auteurs suggèrent que ces hétérogénéités sont dues à la surimposition d'évènements métasomatiques sur un protolithe variablement appauvri par de faibles taux de fusion partielle.

D'autre élément en traces jouent un rôle important dans les fluides métasomatisant, tel que l'H puisque des minéraux hydratés comme l'amphibole peuvent précipiter (Bodinier *et al.*, 2004). Cependant l'H peut aussi être incorporé dans les NAMs et se comporterait comme un élément incompatible avec un coefficient de partage proche de celui du La et du Ce (Dixon *et al*., 2002) ou même plus incompatible (*e.g.*, Novella *et al*., 2014 ; O'Leary *et al*., 2010). Le comportement de l'H reste controversé durant les processus mantelliques. La comparaison avec les concentrations en H permet de définir le degré d'incompatibilité de l'H par rapport aux REE, donc le comportement de l'H pendant les processus mantelliques. L'originalité de cette étude est de s'intéresser au comportement de l'H notamment en présence de minéraux hydratés (*i.e.,* amphibole).

IV.2 Denis *et al.* (2015) Water content and hydrogen behaviour during metasomatism in the uppermost mantle beneath Ray Pic volcano (Massif Central, France)

Lithos 236–237 (2015) 256–274

Contents lists available at ScienceDirect

Lithos

journal homepage: www.elsevier.com/locate/lithos

Water content and hydrogen behaviour during metasomatism in the uppermost mantle beneath Ray Pic volcano (Massif Central, France)

Carole M.M. Denis *, Olivier Alard, Sylvie Demouchy

Geosciences Montpellier, University of Montpellier, place E. Bataillon, Montpellier, France

ARTICLE INFO

Article history:
Received 25 May 2015
Accepted 19 August 2015
Available online 2 September 2015

Keywords:
Hydrogen
Peridotite
Mantle
Melting
Metasomatism
Amphibole

ABSTRACT

To understand the deep cycle of water, upper mantle water content and distribution between nominally anhydrous minerals (NAMs) and hydrous minerals (e.g., amphibole) must be constrained. We need then to understand H behaviour during mantle melting and metasomatism. Major, minor and trace element compositions including water contents were obtained on ten xenoliths of spinel-bearing peridotites from the Ray Pic locality, in the Southern part of the Massif Central (France). The sample suite investigated here is composed of rather fertile lherzolites (89.4 ≤ Fo ≤ 90.8%; 11.3 ≤ cr# in spinel ≤ 21.1%; 0.942 ≤ $[Yb]_{cpx}$ ≤ 1.90 ppm; cpx: clinopyroxene), which can be best explained by batch melting, with degree of melting between 3 and 10%. These xenoliths contain up to 8% modal amphibole. Three groups are defined as a function of the amphibole modal abundance (above or below 1%) and equilibrium temperature (above or below 1000 °C). Results show no clear positive correlation between modal metasomatism (amphibole) and incompatible element enrichment in cpx. Trace element compositions in cpx show strong enrichments of the most incompatible elements (e.g., $(La/Sm)_{PM}$ as high as 15.7; PM: normalised to primitive mantle values), but strong negative anomalies of the high field strength elements (e.g., $(Th/Nb)_{PM}$ as high as ~680). Such trace element fractionations are usually ascribed to the so-called carbonatitic metasomatism involving the percolation of small volume melts which are enriched in volatiles. The hydrogen concentrations in cpx range from 203 to 330 ppm wt. H_2O, in orthopyroxene from 66 to 160 ppm wt. H_2O and in olivine from 2 to 6 ppm wt. H_2O. These values are within the common concentration range of other spinel-bearing peridotites. Amphiboles contain 1.9 ± 0.5 wt.% of H_2O.

The effect of metasomatism on water abundances in NAMs is not straightforward. Hydrous metasomatism (i.e., leading to the crystallisation of OH-bearing amphibole) has no effect on the water content of the coexisting NAMs. This suggests thus that the occurrence of hydrous minerals, such as amphibole, does not systematically imply that the coexisting NAMs are water-rich (saturated). Further, the percolation of volatile-rich small volume melts, which is fingerprinted by the strong enrichment of the incompatible elements, has also no clear effect on the water content of the NAMs. These data are thus difficult to reconcile with the admitted highly incompatible behaviour of H in upper mantle minerals.

1. Introduction

The percolation and reaction of melts and/or fluids are ubiquitous processes within the mantle, which play a key role in the redistribution of elements throughout the Earth's upper mantle (e.g., Bedini et al., 1997; Bodinier et al., 1990; Menzies and Hawkesworth, 1987; Rudnick et al., 1993). Classically, two types of metasomatism are recognised: (1) modal metasomatism, for which new volatile-rich minerals precipitate, such as amphibole (am), phlogopite, apatite; and (2) cryptic metasomatism, for which no new phases crystallise, but primary phases, for instance clinopyroxene (cpx), which displays trace element enrichments not compatible with a simple melt depletion (e.g., Grégoire et al., 2000; O'Reilly et al., 1991). The term of metasomatism encompasses a diversity of processes involving a variety of not well-defined melt–fluid/rock interactions. These interactions occurred with different fluid/rock regimes in various geological environments, with percolating and metasomatising melts of variable compositions (O'Reilly and Griffin, 2013). Usually the percolating melt/fluid is often considered as a volatile-rich agent. Volatile such as H_2O and CO_2 lower the melt/fluid density, viscosity and the crystallisation temperature (e.g., Dasgupta and Hirschmann, 2006; Wyllie and Ryabchikov, 2000) and therefore ease the percolation of such melt/fluids within the cold mantle lithosphere. Deciphering the imprints of the various metasomatic processes on the mantle lithosphere is a key to better understand their effect on the physical properties of the mantle and thus on the geodynamic of the lithosphere, but also to constrain the volatile transfer at larger scale, from the deep Earth to the exospheres (i.e., the deep water cycle).

* Corresponding author. Tel.: +33 4 67 14 39 39; fax: +33 4 67 14 36 42.
E-mail address: carole.denis@gm.univ-montp2.fr (C.M.M. Denis).

http://dx.doi.org/10.1016/j.lithos.2015.08.013
0024-4937/

One of the key tools to decipher the type of metasomatism is the abundances and fractionation of incompatible trace elements such as Rare Earth Elements (REE). In addition, hydrogen (H) and carbon, two other trace elements, play a crucial role since they are both a potential indicator of metasomatic processes, but also a major constituent of metasomatic melts/fluids. Indeed, molecular water and water-derived species (H^+, OH^-, H_2) can be found as a major constituent (i.e., $H_2O \geq 1$ wt.%) in metasomatic hydrous minerals such as in amphibole and/or phlogopite. The precipitation of these hydrous minerals is canonically ascribed to the so-called hydrous metasomatism (e.g., Agrinier et al., 1993; Bodinier et al., 2004; McInnes et al., 2001). Nevertheless, H can also be incorporated in the lattice of nominally anhydrous minerals (NAMs) using atomic point defects (zero-dimension defect in the crystal lattice, e.g., Bell and Rossman, 1992; Ingrin and Skogby, 2000; Miller et al., 1987), such as olivine (ol), cpx and orthopyroxene (opx). Hydrogen is considered to behave like an incompatible trace element, with partition coefficient similar to La and Ce (Dixon et al., 2002) or even lower (e.g., Novella et al., 2014; O'Leary et al., 2010). Hydrogen could thus provide valuable and complementary information on metasomatic processes (e.g., nature of the melt/fluid, melt–fluid/rock ratio). Hydrogen incorporation into NAMs was mainly investigated through experimental petrology and mineralogy (e.g., Bai and Kohlstedt, 1993; Férot and Bolfan-Casanova, 2012; Kohlstedt et al., 1996; Mierdel et al., 2007) while data obtained on mantle xenolith suites are only recent (e.g., Baptiste et al., 2015; Bell and Rossman, 1992; Bell et al., 2004; Bizimis and Peslier, 2015; Bonadiman et al., 2009; Demouchy et al., 2006; Demouchy et al., 2015; Denis et al., 2013; Doucet et al., 2014; Grant et al., 2007a, 2007b; Hao et al., 2014a, 2014b; Li et al., 2008; Li et al., 2014; Peslier and Luhr, 2006; Peslier et al., 2002, 2015; Xia et al., 2010, 2013; Yang et al., 2008; Yu et al., 2011). However, H behaviour remains unclear during mantle processes and especially during metasomatic processes. Further, except for Yang et al. (2008) and Bonadiman et al. (2009), the distribution of H among NAMs in a so-called hydrous mantle assemblages such as amphibole-bearing peridotites, was not investigated.

We investigate here a suite of peridotite xenoliths from the Ray Pic Volcano located in the French Massif Central (FMC) showing various modal (amphibole) and cryptic metasomatic imprints. Ray Pic xenoliths are a well-known xenolith locality from the FMC, which were previously studied by Downes and Dupuy (1987), Lenoir et al. (2000) and Zangana et al. (1997, 1999). The main conclusions of these studies are that the xenoliths from Ray Pic represent a heterogeneous mantle in term of modal mineralogy, mineral chemistry, REE patterns and radiogenic isotopes. These heterogeneities resulted from the superimposition of metasomatic processes related to the impingement of the FMC plume/diapir on a variably depleted protolith (Zangana et al., 1997, 1999).

To establish the relationships between mantle processes (melting and metasomatism) and water content of the mantle minerals, we first identify mantle processes which have affected the Ray Pic peridotites, using major and trace element compositions, and confront them to water contents in NAMs measured by Fourier transform infrared (FTIR) spectroscopy.

2. Geological setting and samples

Alkali-basaltic volcanism of the FMC began in the early Cenozoic and ended ~0.01 Ma ago with a peak of volcanic activity at 4–6 Ma (Maury and Varet, 1980). This volcanic activity is related to an ascending asthenospheric plume/diapir beneath the FMC (e.g. Granet et al., 1995). Seismic tomography data pinpointed the mantle anomaly beneath the Eastern Massif Central between the 45°30′ and 44°30′ parallels to the east of the Sillon Houiller fault (Granet et al., 1995). Geochemical studies based on mantle xenoliths have also evidenced two contrasting mantle lithosphere domains on either side of the 45°30′ N parallel (Lenoir et al., 2000; Fig. 1). This contrast is based on lithology, trace element compositions, Pb, Lu–Hf, Sr and Nd isotope analyses (Downes et al., 2003; Wittig et al., 2007) and metasomatism styles (Lenoir et al., 2000; Touron et al., 2008). Peridotites from the southern domain are overall characterised by a common occurrence of secondary coarse granular microstructure (not protogranular), and less fractionated trace element patterns compared to northern domain peridotites. These characteristics were ascribed to the impingement of the FMC plume/diapir on a relatively fertile lithosphere (Lenoir et al., 2000). It is worth noting that hydrous metasomatic minerals such as phlogopite or amphibole are more commonly found in peridotite xenoliths from the southern FMC (i.e., in the Devès and the Velay, Fig. 1) than in the northern part. They were attributed to the reaction between the peridotite and alkali melts directly related to the asthenosphere plume/diapir (Lenoir et al., 2000).

The ten samples of this study are from the Ray Pic volcano, a Quaternary alkali basalt volcano, in the Velay volcanic district of the southern FMC (Fig. 1). Ray Pic volcano brought up numerous mantle xenoliths reflecting a large range of mineralogical and geochemical composition (Zangana et al., 1997, 1999). Variations in mineral microstructures, whole rock (WR) major, trace and REE compositions, as well as radiogenic isotope compositions of Ray Pic xenoliths were previously reported by Zangana et al. (1997, 1999). These variations were interpreted as the result of two major processes, which have affected the lithospheric mantle beneath Ray Pic: a depletion likely due to partial melting and subsequent dominant cryptic metasomatism (modal metasomatism was uncommon, Zangana et al., 1999).

3. Sample preparation and analytical method

Concentrations in major elements for the WR were obtained by wide-angle X-ray fluorescence (WDXRF). Mineral compositions were determined using an electron probe micro-analyser (EPMA) for major elements, using a laser ablation induced coupled plasma mass spectrometer (LA-ICP-MS) for trace elements, and using a FTIR spectrometer for hydrogen.

3.1. Sample preparation

All samples were cut far from weathered surfaces or from the enclosing basalt. Part of each sample was crushed with an anvil and a hammer, then reduced to powder using an agate ring mill for WR analyses. In situ major and trace element compositions of minerals were determined on 150 μm thick polished sections carbon-coated for EPMA analyses. FTIR analyses were performed on separated minerals, doubly polished by hand (~100–1000 μm of thickness) with a polishing jig and diamond-lapping films (grid sizes ranging from 0.2 to 30 μm).

3.2. Major and trace elements

Major element contents in WR were measured by WDXRF by a sequential spectrometer Bruker S4 Pioneer at the analytical services of the IACT (CSIC, Granada, Spain).

Major element contents in each mineral phase were determined at Microsonde Sud facility, at University of Montpellier (France) using a Cameca SX100 electron microprobe operating at 20 kV accelerating voltage. The thin sections were analysed with a counting time on peak and background of 20 s for the analysis of Fe, Mn and Ni, and 30 s for the other elements. The spot size was ~ 1 μm.

Equilibrium temperature of each sample is calculated using the two thermometers of Brey and Köhler (1990), one based on the Ca concentration in opx ($T°_{Ca\text{-}in\text{-}opx}$), and the other based on Fe–Mg exchange between opx and cpx (T_{BKN}).

Using WR and mineral compositions, the mineralogical mode of each sample is calculated using mass balance and a least squares method (Herrmann and Berry, 2002).

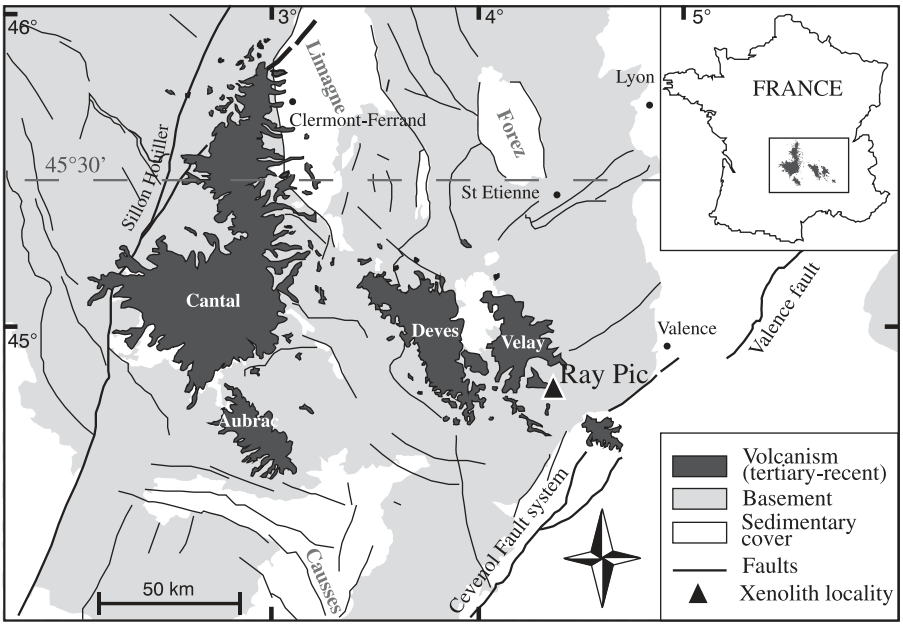

Fig. 1. Simplified geological map of the French Massif Central (FMC) modified after Lenoir et al. (2000), showing the location of the studied xenoliths from Ray Pic volcano (triangle), major towns (dot), and the main volcanic districts (dark grey areas). The dashed line (45°30′ parallel) represents the limit between the two lithospheric mantle domains, Northern and Southern Massif Central defined by Lenoir et al. (2000).

In situ trace element analyses were performed on cpx and amphibole by LA-ICP-MS at Géosciences Montpellier (Montpellier, France), using a ThermoFinnigan ELEMENT XR (eXtended Range) high resolution (HR) ICP-MS system. The ICP-MS is coupled with a Geolas (Microlas) automated platform housing a ArF 193 nm Compex 102 laser from LambdaPhysik. Measurements were conducted in a He atmosphere, which enhances the sensitivity and reduces inter-element fractionations. The helium gas stream and particles from the sample are mixed with Ar before entering the plasma. Signals are measured in time resolved acquisition mode, devoting 2 min for the blank, and 3 min for mineral analysis. The laser is fired using an energy density of 15 J/cm^2 at a frequency of 10 Hz and using a spot size of 77 μm. Oxide levels, measured using the UO/U ratio, are below 0.7%. The standard BIR-1G was included during the analytical runs and our measurements are in good agreement with working values for this international standard (Jochum et al., 2005). The concentrations are calibrated against the standard NIST 612 glass using the values given by Pearce et al. (1997). Data are subsequently reduced using the GLITTER software (Griffin et al., 2008) by carefully inspecting the time-resolved analysis to check for homogeneity in the analysed volume.

3.3. Fourier transform infrared spectroscopy

Hydroxyl bonds in the samples are detected in transmission mode by FTIR spectroscopy at the Laboratoire Charles Coulomb (LCC) at University of Montpellier (France). Unpolarised infrared spectra were acquired using a Bruker IFS66v, equipped with an MCT detector (Mercury Cadmium Telluride) cooled with liquid nitrogen, and coupled to a microscope Bruker HYPERION. This allows accurate optical visualisation of the sample prior and during acquisitions. A Globar light source and a Ge-KBr beam splitter are used to generate unpolarised mid-infrared radiation (between 4000–400 cm^{-1}). Measurements on olivine, opx, and cpx were performed with a square aperture yielding a beam spot with sizes ranging from 50 to 150 μm. For each measurement 200 scans are accumulated with a resolution of 4 cm^{-1}. The series of resulting interferograms is first ratioed against the reference spectrum (background), then treated manually with a baseline correction using the OPUS software, and finally normalised to 1 cm of thickness. From each spectrum, the quantification of the hydrogen concentration is deduced from the hydroxyl stretching absorption in the sample, based on the Beer–Lambert law. At first, we choose to use the calibration of Paterson (1982):

$$C_{OH} = \frac{\chi_i}{150\xi}\int \frac{k(\upsilon)}{3780-\upsilon}d\upsilon \quad (1)$$

This empirical and frequency-dependent equation gives the water concentration (C_{OH}) as a function of factor χ_i, which is a function of the density of the mineral i (χ_{ol} = 2695 ppm wt H_2O; χ_{opx} 2812 ppm wt H_2O; χ_{cpx} = 2752 ppm wt H_2O). ξ is the orientation factor and equals 1/3 for non-polarised IR analyses (on non-oriented samples, Paterson, 1982); $k(\upsilon)$, the absorption coefficient is a function of the wavenumber υ. The H concentration of the samples is calculated by integrating each spectrum between 3610 and 3150 cm^{-1} for olivine, 3670–2800 cm^{-1} for opx, and 3770–3000 cm^{-1} for cpx. This calibration allows a detection limit of about 0.5 ppm wt. H_2O for an olivine sample of 1 mm of thickness. Here H concentration is expressed as weight ppm of dihydrogen oxide = H_2O, also called water content by convention. The estimated error from the empirical calibration in the resulting H concentration is 30% (Paterson, 1982; Rauch, 2000). Average H concentrations are obtained from averaging at least 10 spectra from each grain and the maximal linear absorption of unnormalised spectra did not exceed 0.3 in agreement with the recommendations of Withers (2013) for unpolarised FTIR measurements.

Mineral-dependent FTIR calibration should always be favour to reduce uncertainties on the resulting water content. However, the mineral-dependent calibration for olivine from Bell et al. (2003) is not used here since it overestimates hydrogen concentrations (Withers et al., 2012). Ideally this calibration requires the use of crystallographically oriented olivine crystals and polarised IR radiation in order to sum the integrated absorbances from the three polarised spectra corresponding to the three crystallographic axis and for each analysed grain (i.e., $Absorbance_{total}$ = absorbance $_{[100]}$ + absorbance $_{[010]}$ + absorbance $_{[001]}$, e.g., Bell et al., 2003; Withers et al., 2012). We chose to use

the calibration of Paterson (1982) since it allowed us to determine hydrogen concentrations for a larger number of analyses, to compare the concentrations from the different mineral phases (i.e., one common methods for all phases) and to avoid to cut each grains in oriented cube, which will destroy the borders of the mineral grains (as in Schmädicke et al., 2013). Conversion to the most recent mineral-dependent calibration from Withers et al. (2012) for olivine can be calculated using a factor of 1.8 (Withers et al., 2012, see in their Fig. S1) and the concentration reported in results Table. (i.e., concentration from Paterson calibration — unpolarised × 1.8 ≈ average integrated unpolarised and normalised absorbance × 3 × 0.119).

Regarding the use of the calibration of Bell et al. (1995) for H in pyroxene, the H concentration can be calculated using the integrated area reported in this study. The resulting conversion factor between the calibration of Paterson and the one from Bell et al. (1995) is equal to 1.03 for opx and equals to 1.74 for cpx. The discrepancy is likely to be due to the use in their calibration of a single kimberlitic centimetric megacryst of clinopyroxene (augite: Ca- and Al-poor and Mg and Fe-rich) while the orthopyroxene is from a mantle peridotite. Thus only the orthopyroxene standard has the adequate composition compared to our samples and the application of this calibration for clinopyroxenes to mantle diopside is questionable. Recently, Mosenfelder and Rossman (2013b) have also document that a frequency-dependent calibration yields better results than the calibration of Bell et al. (1995) for clinopyroxene.

Another frequency-dependent IR calibration could be used as proposed by Libowitzky and Rossman (1997) as well as by Mosenfelder and Rossman (2013a, b). However, one must notice that for the wavenumbers under consideration in NAMs (3600–3000 cm^{-1}), the calibration of Paterson (1982) and the one from Libowitzky and Rossman (1997) are equivalent (see their Fig. 3 in Libowitzky and Rossman, 1997) and yield results within the error bars.

As indicated in Férot and Bolfan-Casanova (2012, see their supplementary material Figure S1), a factor of 3 can be used with confidence to convert the hydrogen concentrations in olivine and pyroxenes reported by unpolarised IR light to values equivalent to those obtained with the polarised IR method of Bell et al. (1995, 2003; see also Kovács et al., 2008).

Finally, conversion factors to concentration in atomic H per 10^6 atoms of Si (at. H/10^6 Si = at. ppm H/Si) historically used (e.g., Kohlstedt et al., 1996) are also given in the results' table.

The water contents of amphiboles from sample 13RP03 were measured by Karl–Fischer titration (KFT) using air as transporting gas and muscovite as standard, see Behrens et al, (1996) for details on the method.

4. Results

4.1. Petrography and mineralogy

Peridotite xenoliths from Ray Pic are all equilibrated in the spinel (spl) facies and range from lherzolite to harzburgite as previously reported by Downes and Dupuy (1987) and Zangana et al. (1997, 1999). The peridotite xenoliths investigated here are ten lherzolites with variable modal composition of olivine (ol: 51–67%), opx (19–33%), cpx (6–13%) and spl (1–3%) and one harzburgite (13RP14; ol: 77%; opx: 18%; cpx: 3%). Six samples contain significant amount of amphibole (am: 0.2–8%) as shown in Fig. 2. The selected peridotites have continuous textural variation evolving from porphyroclastic to equigranular and coarse granular microstructure as reported by Zangana et al. (1997, 1999). True protogranular textures according to the definition of Mercier and Nicolas (1975) are not found, and coarse-grained xenoliths are clearly secondary microstructure due to recrystallisation processes at subsolidus conditions. Indeed, most of our samples show transitional microstructure between porphyroclastic and equigranular or coarse-granular texture. Sub-grain boundaries as well as undulose extinctions are common in olivine. However, some of the crystals are free of intra-crystalline deformation features, progressing locally to triple junctions between minerals. The grain sizes range from 0.2 to 3 mm. Spinel defines the foliation in several samples, and occurs as holly-leaf shaped grains with curvilinear boundaries. Amphibole-bearing samples have relatively large pale brown amphiboles (Ø ≈ 1 mm) disseminated into the aggregate (i.e., in sample 13RP02, Fig. 2b). In some samples (i.e., sample 13RP03, Fig. 2) amphiboles are closely associated with spl and cpx forming brown patches. The texture and mineralogical compositions of the samples are summarised in Table 1.

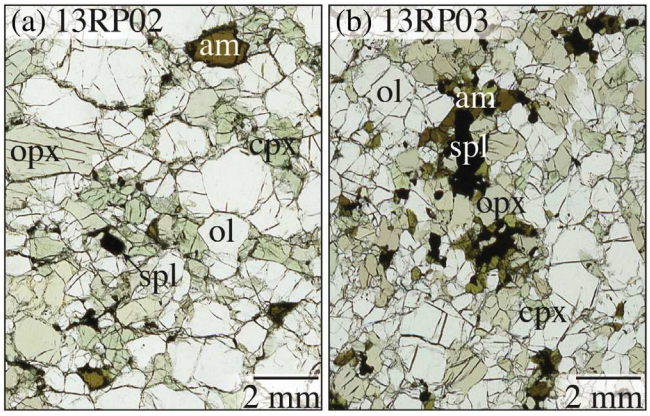

Fig. 2. Thin section micrographs in plane-polarized light for Ray Pic spinel-peridotite xenoliths: (a) sample 13RP02 showing olivine (ol), orthopyroxene (opx), clinopyroxene (cpx), spinel (spl) and disseminated amphibole (am), as well as the equigranular to coarse microstructure (b) sample 13RP03 showing a typical coarse granular microstructure. Note that amphibole is associated with spl and cpx. Colour version available online.

4.2. Major element compositions of minerals and geothermometry

Major element compositions of WR and minerals are given in Table 2. Whole-rock Al_2O_3 concentrations vary between 1.54–3.84 wt.%, which indicates a fertile composition in agreement with the petrographic observations. The composition of our samples is comparable to those previously reported in the southern domain of the FMC (Alard et al., 1996; Downes and Dupuy, 1987; Downes et al., 2003; Lenoir et al., 2000; Lorand and Alard, 2001; Touron et al., 2008; Xu et al., 1998). They are fully within the compositional range reported for Ray Pic xenoliths (Downes and Dupuy, 1987; Zangana et al., 1997, 1999; Fig. 3). The most fertile lherzolite is 13RP02, which also has the

Table 1
Sample list and summary of Ray Pic peridotite xenolith characteristics.

Ray Pic	Texture[a]	Modal mineralogy (%)[b]					Equilibration temp. (°C)[c]	
sample		olivine	opx	cpx	sp	am	T°Ca-opx	T°BKN
13RP05	Eq	67	21	9	2	–	841	710
13RP17	Crs	67	19	11	3	–	903	859
13RP01	Eq	65	23	9	2	<1	840	822
13RP02	Crs to Prc	51	33	13	3	<1	925	928
13RP12	Eq to Crs	63	23	12	1	1	952	964
13RP04	Crs to Prc	57	28	11	2	2	880	903
13RP14	Crs	77	18	3	1	2	912	851
13RP03	Eq to Crs	65	19	6	1	8	933	877
13RP11	Crs to Prc	67	22	10	2	–	1010	1044
14RP06	Crs	62	26	9	2	–	1070	1084

[a] Eq: equigranular; Crs: coarse; Prc: porphyroclastic.
[b] opx: orthopyroxene; cpx: clinopyroxene; sp: spinel; am: amphibole.
[c] T°(Ca-in-opx) and T° BKN from Brey and Köhler (1990), error ± 30 °C.

Table 2
Whole-rock and mineral major element average compositions (wt. %) determined by XRF and EPMA respectively.

Whole-rock										
Group			G1					G2		G3
			<1% am					>1% am		
Sample	13RP05	13RP17	13RP01	13RP02	13RP12	13RP04	13RP14	13RP03	13RP11	14RP06
T° Ca-opx	841	903	840	925	952	880	912	933	1010	1070
SiO_2	44.91	44.16	45.3	46.2	45.37	45.8	44.27	44.79	44.85	n.a.
TiO_2	0.11	0.18	0.15	0.21	0.19	0.18	0.11	0.18	0.13	n.a.
Al_2O_3	2.31	2.76	2.48	3.84	2.63	2.93	1.54	2.7	2.55	n.a.
Fe_2O_3	8.64	8.86	8.82	8.43	8.68	8.38	8.48	8.64	8.57	n.a.
MnO	0.13	0.14	0.14	0.14	0.13	0.13	0.13	0.14	0.13	n.a.
MgO	41.56	40.59	40.84	37.82	39.86	39.65	44.28	40.79	41.3	n.a.
CaO	2.28	2.64	2.13	3.09	2.9	2.73	1.14	2.51	2.31	n.a.
Na_2O	0.04	0.09	0.13	0.24	0.21	0.2	0.03	0.19	0.12	n.a.
K_2O	<0.02	<0.02	<0.02	<0.02	<0.02	<0.02	<0.02	<0.02	<0.02	n.a.
P_2O_5	<0.02	0.02	<0.02	<0.02	0.02	<0.02	<0.02	0.02	0.03	n.a.
LOI	0	0.53	0	0	0	0	0	0	0	n.a.
Total	99.98	99.97	99.99	99.97	99.99	100	99.98	99.96	99.99	–
mg# (WR)	*90.4*	*89.9*	*90.0*	*89.7*	*89.9*	*90.2*	*91.1*	*90.2*	*90.4*	–
Olivine										
Sample	13RP05	13RP17	13RP01	13RP02	13RP12	13RP04	13RP14	13RP03	13RP11	14RP06
n	4	5	17	2	6	8	17	6	9	4
SiO_2	41.49	41.30	41.45	40.98	41.18	41.07	41.34	41.36	41.34	40.81
TiO_2	0.01	0.00	0.01	0.00	0.01	0.01	0.01	0.01	0.01	0.01
Al_2O_3	0.00	0.01	0.01	0.02	0.02	0.01	0.01	0.02	0.02	0.04
Cr_2O_3	0.01	0.01	0.03	0.00	0.01	0.01	0.06	0.01	0.01	0.03
FeO	9.45	9.66	9.75	9.97	10.05	9.75	9.22	9.46	9.37	9.24
MnO	0.13	0.13	0.13	0.16	0.13	0.13	0.13	0.13	0.13	0.13
MgO	48.15	48.11	47.94	47.93	47.93	48.54	48.52	48.60	48.40	48.43
CaO	0.02	0.04	0.05	0.05	0.08	0.04	0.04	0.06	0.07	0.10
Na_2O	0.01	0.01	0.01	0.01	0.01	0.01	0.01	0.01	0.02	0.01
K_2O	0.00	0.00	0.00	0.00	0.01	0.00	0.00	0.00	0.00	0.00
NiO	0.42	0.39	0.40	0.38	0.40	0.42	0.41	0.37	0.39	0.38
Total	99.70	99.66	99.78	99.50	99.84	99.99	99.74	100.03	99.76	99.18
Fo%	*90.0*	*89.8*	*89.6*	*89.4*	*89.4*	*89.8*	*90.3*	*90.0*	*90.8*	*90.2*
Orthopyroxene = enstatite										
Sample	13RP05	13RP17	13RP01	13RP02	13RP12	13RP04	13RP14	13RP03	13RP11	14RP06
n	2	5	5	2	5	10	17	6	6	5
SiO_2	56.51	56.03	56.40	55.62	55.71	55.72	56.47	56.10	55.47	54.56
TiO_2	0.03	0.06	0.06	0.10	0.10	0.07	0.05	0.05	0.06	0.08
Al_2O_3	2.81	3.63	3.33	3.94	3.93	3.58	3.07	3.51	4.33	4.43
Cr_2O_3	0.24	0.26	0.30	0.31	0.27	0.29	0.36	0.34	0.39	0.56
FeO	6.28	6.47	6.48	6.51	6.41	6.35	5.89	6.31	6.16	6.03
MnO	0.14	0.14	0.13	0.12	0.15	0.15	0.13	0.15	0.14	0.12
MgO	33.19	32.69	32.75	32.47	32.58	33.18	33.27	33.02	32.32	32.00
CaO	0.37	0.51	0.37	0.56	0.63	0.48	0.49	0.60	0.82	1.05
Na_2O	0.03	0.04	0.05	0.07	0.09	0.07	0.04	0.06	0.10	0.12
K_2O	0.00	0.01	0.00	0.01	0.00	0.00	0.00	0.00	0.00	0.00
NiO	0.08	0.10	0.09	0.12	0.12	0.09	0.10	0.10	0.10	0.12
Total	99.68	99.95	99.96	99.82	99.98	99.98	99.88	100.25	99.89	99.08
mg# (opx)	*90.4*	*90*	*90*	*89.9*	*90.1*	*90.3*	*91*	*90.3*	*90.3*	*90.3*
[En]	86.6	85.5	85.5	85.2	85.5	86.6	86.9	86.2	85.2	85.5
[Fs]	11.3	11.5	12.1	11.1	10.7	9.5	10.7	10.4	10.5	9.7
[Wo]	2.1	3.0	2.4	3.6	3.8	3.9	2.5	3.4	4.2	4.7
Clinopyroxene = diopside										
Sample	13RP05	13RP17	13RP01	13RP02	13RP12	13RP04	13RP14	13RP03	13RP11	14RP06
n	6	4	13	2	6	5	15	4	7	4
SiO_2	53.31	52.64	52.81	52.03	52.06	52.20	53.07	53.26	52.16	51.35
TiO_2	0.12	0.28	0.49	0.45	0.54	0.42	0.18	0.20	0.28	0.34
Al_2O_3	3.49	4.74	6.08	6.09	6.20	5.63	4.18	3.90	6.13	6.22
Cr2O3	0.65	0.58	0.94	0.75	0.67	0.70	0.80	0.47	0.86	1.04
FeO	2.42	3.04	2.42	3.02	3.00	2.80	2.50	2.94	3.19	3.20
MnO	0.08	0.08	0.07	0.09	0.08	0.08	0.07	0.09	0.08	0.09
MgO	15.68	15.42	14.34	14.83	14.97	15.27	15.70	16.12	15.28	15.73
CaO	23.19	22.20	20.98	21.06	20.73	21.07	22.18	22.20	20.14	19.31
Na_2O	0.82	0.93	1.81	1.39	1.45	1.48	1.02	0.95	1.44	1.44
K_2O	0.00	0.00	0.00	0.00	0.00	0.00	0.00	0.00	0.00	0.01
NiO	0.05	0.03	0.03	0.03	0.06	0.04	0.04	0.03	0.04	0.06
Total	99.80	99.95	99.96	99.73	99.75	99.68	99.75	100.14	99.60	98.78
mg# (cpx)	*91.8*	*89.8*	*91.1*	*89.5*	*89.7*	*90.4*	*91.6*	*90.5*	*89.3*	*89.5*

Table 2 (*continued*)

Whole-rock										
Group			G1					G2		G3
			<1% am					>1% am		
Sample	13RP05	13RP17	13RP01	13RP02	13RP12	13RP04	13RP14	13RP03	13RP11	14RP06
T° Ca-opx	841	903	840	925	952	880	912	933	1010	1070
Spinel										
Sample	13RP05	13RP17	13RP01	13RP02	13RP12	13RP04	13RP14	13RP03	13RP11	14RP06
n	2	5	8	2	3	4	8	4	4	4
SiO_2	0.16	0.13	0.15	0.16	0.14	0.16	0.15	0.15	0.19	0.13
TiO_2	0.04	0.09	0.05	0.12	0.12	0.06	0.03	0.08	0.10	0.21
Al_2O_3	53.66	55.05	55.26	55.92	57.28	57.00	54.73	50.67	51.75	48.07
Cr2O3	13.78	11.53	13.09	11.64	10.41	10.87	13.26	16.42	16.05	19.12
FeO	12.77	13.74	12.23	12.14	11.62	11.94	12.54	14.30	12.56	12.47
MnO	0.15	0.13	0.13	0.12	0.11	0.11	0.13	0.14	0.13	0.14
MgO	18.49	19.06	18.85	19.44	20.04	19.84	18.92	18.66	19.38	18.72
CaO	0.02	0.01	0.02	0.00	0.10	0.00	0.02	0.01	0.02	0.03
Na_2O	0.01	0.00	0.00	0.00	0.00	0.00	0.00	0.00	0.00	0.00
K_2O	0.00	0.00	0.00	0.00	0.00	0.00	0.00	0.00	0.00	0.00
NiO	0.35	0.40	0.37	0.41	0.39	0.41	0.38	0.36	0.34	0.35
Total	99.44	100.13	100.16	99.97	100.21	100.40	100.16	100.81	100.54	99.24
mg# (spl)	*73.2*	*74.3*	*73.1*	*75.3*	*77.0*	*76.4*	*73.0*	*73.5*	*75.6*	*72.6*
cr# (spl)	*14.7*	*12.3*	*13.7*	*12.2*	*10.8*	*11.3*	*14.0*	*17.8*	*17.2*	*21.1*

Amphibole = Pargasite

Sample	13RP01	13RP02	13RP12	13RP04	13RP14	13RP03
% Am	0.2	0.5	1.1	1.6	1.8	8.1
n	6	2	4	8	5	6
SiO_2	42.68	43.41	43.26	43.18	43.48	43.24
TiO_2	2.42	1.89	2.21	1.71	1.21	1.25
Al_2O_3	14.54	15.21	15.25	15.31	14.78	15.04
Cr_2O_3	1.06	0.98	0.94	1.07	1.64	1.28
FeO	3.85	4.40	4.34	4.22	3.97	4.52
MnO	0.05	0.07	0.06	0.06	0.06	0.07
MgO	17.02	16.93	17.02	17.11	17.27	16.99
CaO	11.28	10.68	10.55	10.78	11.03	11.24
Na_2O	3.81	3.85	3.81	3.86	3.73	3.28
K_2O	0.10	0.03	0.03	0.01	0.03	0.61
NiO	0.10	0.13	0.13	0.13	0.13	0.10
Total	96.91	97.60	97.61	97.44	97.32	97.62
mg#	*88.6*	*87.1*	*87.3*	*87.7*	*88.4*	*86.8*
F	b.d.	n.a.	b.d.	b.d.	n.a.	n.a.
Cl	b.d.	n.a.	b.d.	b.d.	n.a.	n.a.
H_2O (KFT)	n.a.	n.a.	n.a.	n.a.	n.a.	1.9 ± 0.5

n: for n measurements; T° (Ca-in-opx) from Brey and Köhler (1990), with error ± 30 °C; mg# (Mg-number) and Fo% (forsterite content) = 100.Mg/(Mg + Fe); cr#: Cr-number = 100.Cr/(Cr + Al); Fo%, mg# and cr# are in italics, [En], [Fs], [Wo] are enstatite, Ferrosilite, Wollastonite end-members respectively; n.a.: not analysed; b.d.; below detection limit; ol: olivine; opx: orthopyroxene; cpx: clinopyroxene; spl: spinel; am: amphibole.

lowest MgO content and the highest Al_2O_3 and CaO content, whereas the most refractory harzburgite is 13RP14.

The relatively high fertility of the Ray Pic peridotites is reflected by their mineral compositions as well: forsterite contents (Fo%) vary between 89.4 and 90.8 with an average of 89.9 ± 0.4 and $cr\#_{spl}$ [100xCr/(Cr + Al)] varies coherently between 11.3 and 21.1 (Table 2). $mg\#_{spl}$ varies between 72.6 and 77.0 and is correlated to $cr\#_{spl}$. Orthopyroxene are Mg-rich enstatite (mg# = 89.7–90.8%; $En_{85.2–86.9}$; $Fs_{9.5–12.1}$; $Wo_{2.1–4.7}$) and cpx are Cr-diopsides (19.3 < CaO ≤ 23.2 wt.%; 6.8 < $cr\#_{cpx}$ < 11.1%) with $mg\#_{cpx}$ varying between 89.3 and 91.8%. No core–rim zoning was observed.

Amphiboles show a relatively homogeneous composition within and between each sample. There is no correlation between the microstructural occurrence of amphiboles and their composition. All amphiboles are Ti (calcic)-pargasite (CaO = 10.9 ± 0.3 wt.%; TiO_2 = 1.8 ± 0.5 wt.%) with $mg\#_{am}$ between 86.8 and 88.6%. These amphiboles show constant Na_2O content ca. 3.7 ± 0.2 wt.%. K_2O content varies between 0.01 and 0.61 wt.%. The sum of the common oxides (Table 2) is c.a. 97.4 ± 0.2 wt.%. Halogen contents are low, below the detection limit for F (i.e., <0.1 wt.%) and Cl contents are bracketed between 0.007 and 0.080 wt.%. Karl–Fischer titration analysis indicates H_2O content c.a. 1.9 ± 0.5 wt.% for amphibole in sample 13RP03. It is remarkably similar to water content in amphibole for similar mantle xenoliths worldwide (e.g. Bonadiman et al., 2014; Frezzotti et al., 2010; Litasov et al., 2000; Moine et al., 2000).

Equilibration temperatures (T) of the peridotites, calculated using the Ca-in-opx method from Brey and Köhler (1990), range from 840 to 1070 °C, while equilibration temperatures using the Fe–Mg distribution in two-pyroxene geothermometer (Brey and Köhler, 1990) yields values between 710 and 1084 °C. Both calculations have a typical standard deviation of ±30 °C. The occurrence and abundance of amphiboles have no obvious effect on equilibrium temperatures. Furthermore pyroxene geothermometers based on Fe–Mg, Na exchange between cpx and opx, or for Ca in opx, are relatively consistent and no

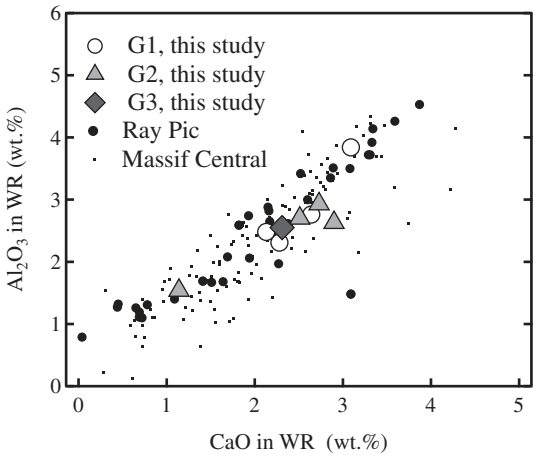

Fig. 3. Whole rock (WR) Al_2O_3 content as a function of WR CaO content in wt.% for Ray Pic spinel-peridotite xenoliths. Hollow circle: G1 Ray Pic peridotites; grey triangle: G2 Ray Pic peridotites; black diamonds: G3 Ray Pic peridotites (see text and Table 2 for details); black circles are previous data from Ray Pic (Zangana et al., 1997); small black dots are data from other Massif Central xenoliths from previous studies (Alard et al., 1996; Downes and Dupuy, 1987; Lorand and Alard., 2001).

systematic shift or clear inconsistency is observed for amphibole bearing samples.

Using amphibole modal abundances and equilibrium temperatures, the samples can be divided into three groups: Group 1 (G1): amphibole free/poor samples (am < 1%) with low equilibrium temperature (T < 1000 °C), Group 2 (G2): amphibole-rich peridotites (am > 1%) with low equilibrium temperature, Group 3 (G3): amphibole-free samples equilibrated at higher temperature (T > 1000 °C).

4.3. Trace element compositions of clinopyroxenes and coexisting amphiboles

The heavy REE (HREE) contents in cpx display significant variations (Table 3). For instance Yb varies from 0.94 up to 1.90 ppm and thus suggest variable degrees of melting. HREE abundances in cpx is broadly negatively correlated with fertility indexes such as Fo% and $cr\#_{spl}$ (Fig. 4a, d), or positively correlated with cpx modal abundance (Fig. 4b, c) or CaO content in cpx (not shown). These correlations suggest that HREE abundances in cpx are primarily governed by melting and melt extraction processes. No such correlation is observed for light-REE (LREE). Mid-REE show an intermediate behaviour, for instance Sm remains correlated to fertility indexes (e.g., cpx %, Fig. 4c) for the low temperature groups (G1 and G2); but Sm is enriched in G3 samples relative to the G1 and G2 groups. Chondrite normalised REE patterns in Fig. 5a, b, d are quite variable in shape for Ray Pic mantle xenoliths as previously observed by Zangana et al. (1997). Chondrite normalised REE patterns of G1 and G2 show a continuum from MREE-depleted to flat MREE–HREE segments ($0.85 < (Sm/Yb)_N \leq 1.18$; N indicates CI chondrite normalised; values after McDonough and Sun, 1995). In contrast, G3 patterns show overall a MREE enrichment relative to the HREE ($2.8 < (Sm/Yb)_N \leq 3.6$). LREE abundances are extremely variable, in particular for G1 and G2 peridotites, where $(La)_N$ varies from 2.7 to 103, leading to a significant variation of the La/Sm ratio ($0.3 < (La/Sm)_N \leq 15.7$). There is no straightforward relationship between the occurrence or abundance of amphibole and REE fractionation or concentration. Indeed, the most LREE-enriched pattern is seen for an

Table 3
LA-ICPMS trace and minor element concentrations in clinopyroxene and amphibole (ppm).

Clinopyroxene											Amphibole			BIR 1G
Group	G1				G2				G3		G2			Standard
	<1% am				>1% am						>1%			
Sample	13RP05	13RP17	13RP01	13RP02	13RP12	13RP04	13RP14	13RP03	13RP11	14RP06	13RP12	13RP04	13RP03	
T° Ca-opx	841	903	840	925	952	880	912	933	1010	1070	952	880	933	
n	3	3	3	3	3	3	3	3	3	3	3	3	3	11
Sc	77.8	77.9	67.1	67.3	63.3	87.3	77.5	60.3	59.5	63.5	42.1	41.3	57	45.4
V	220	n.a.	295	257	n.a.	270	n.a.	201	n.a.	n.a.	–	–	–	341
Co	17.2	n.a.	17.7	21.8	n.a.	17.2	n.a.	19	n.a.	n.a.	–	–	–	52.5
Rb	n.d.	<0.01	n.d.	n.d.	<0.0111	0.03	<0.0097	n.d.	<0.0118	<0.112	9.38	0.118	7.37	0.178
Sr	53.7	201	45	72.2	150	53.2	49	304	228	264	416	129	801	104
Y	15.9	16.7	10.6	16	16	21.5	9.96	7.88	17.4	20.2	17.8	27.6	15.4	13.8
Zr	28.1	23.9	20.2	28.6	32.4	40.4	11.9	8.84	30.4	22.7	38.5	34.4	13.5	12.3
Nb	0.035	0.061	0.221	0.104	0.476	0.041	0.107	0.078	0.843	1.1	14.7	1.9	8.28	0.512
Cs	n.d.	<0.0052	n.d.	n.d.	<0.0055	<0.009	<0.0047	n.d.	<0.0056	<0.0054	0.109	0.0161	0.0335	<0.01
Ba	<0.005	0.2	0.15	0.03	0.3	<0.03	0.1	0.06	0.156	0.136	258	2.09	867	5.77
Hf	0.887	0.78	0.658	0.902	0.963	1.02	0.382	0.302	0.649	0.7	0.888	0.795	0.483	0.509
Ta	0.0024	0.0039	0.0152	0.0071	0.0347	0.01	0.006	0.0054	0.082	0.0792	0.296	0.0645	0.461	0.0363
Pb	0.169	0.668	0.0738	0.259	0.461	0.111	0.667	0.516	0.17	0.0809	1.18	0.412	2.03	3.63
Th	0.023	4.87	0.026	0.256	3.03	0.02	0.523	3.7	0.385	0.379	2.73	0.0181	6.64	0.0277
U	0.007	1.62	0.02	0.103	0.704	0.005	0.37	0.769	0.101	0.0811	0.665	0.006	1.35	0.0141
La	0.845	21.4	0.643	2.76	14.4	1.01	3.97	24.4	13.3	13.3	17.1	1.2	39.9	0.569
Ce	2.74	19.6	1.74	5.21	20.1	3.25	3.25	51.1	43.2	36	22.8	3.99	76.3	1.79
Pr	0.548	0.881	0.365	0.735	1.7	0.591	0.338	3.92	6.15	5.04	1.8	0.726	5.37	0.335
Nd	3.55	3.46	2.67	4.08	6.32	3.67	1.91	9.51	26.6	22.4	6.44	4.52	12.7	2.20
Sm	1.4	1.46	1.23	1.55	1.75	1.57	0.84	1	5.18	4.6	1.78	1.85	1.47	1.01
Eu	0.552	0.589	0.522	0.632	0.695	0.571	0.335	0.346	1.67	1.41	0.728	0.738	0.546	0.453
Gd	1.8	2.13	1.37	1.91	2.19	2.3	1.15	1.64	4.19	4.3	2.55	2.76	1.96	1.60
Tb	n.a.	0.402	n.a.	n.a.	0.414	0.443	0.235	n.a.	0.572	0.612	0.438	0.524	0.335	0.311
Dy	2.88	2.99	2.09	2.89	2.9	3.22	1.75	1.37	3.42	3.9	3.16	3.93	2.52	2.34
Ho	n.a.	0.651	n.a.	n.a.	0.602	0.709	0.385	n.a.	0.649	0.74	0.667	0.865	0.573	0.517
Er	1.79	1.88	1.2	1.82	1.72	1.97	1.12	0.921	1.78	2.08	1.89	2.5	1.7	1.52
Tm	n.a.	0.273	n.a.	n.a.	0.249	0.282	0.168	n.a.	0.234	0.292	0.257	0.338	0.261	0.225
Yb	1.74	1.9	1.2	1.73	1.69	1.89	1.1	0.942	1.59	1.85	1.67	2.39	1.7	1.53
Lu	0.253	0.262	0.154	0.239	0.231	0.275	0.147	0.139	0.218	0.255	0.233	0.312	0.243	0.224

Average on n measurements; T° (Ca-in-opx) from Brey and Köhler (1990); with error ± 30 °C; n.a.: note analysed; n.d.: not detected; am: amphibole.

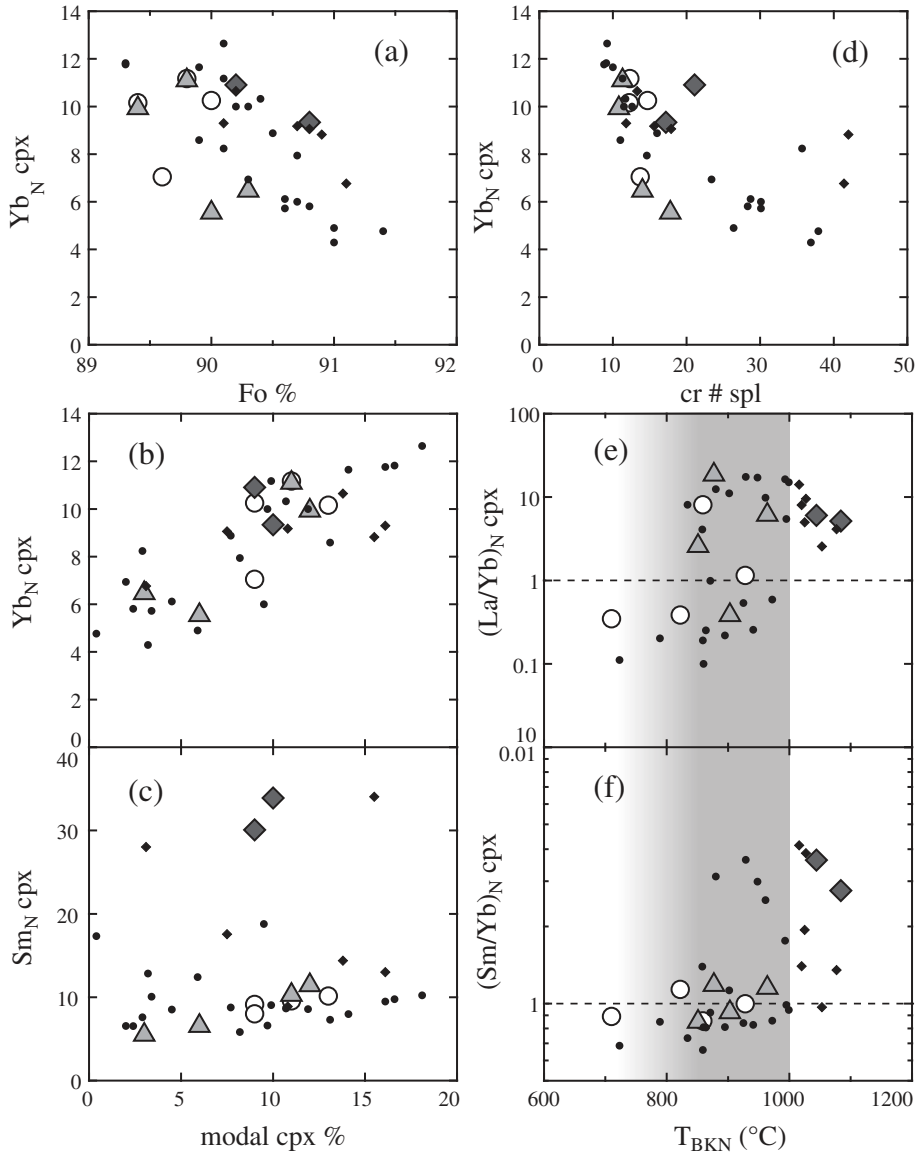

Fig. 4. (a) Yb_N in clinopyroxene (cpx) (N: normalised to CI chondrite values after McDonough and Sun (1995)) vs. forsterite content [Fo% = 100 × Mg/(Mg + Fe)]; (b) Yb_N in cpx vs. modal cpx %; (c) Sm_N in cpx vs. modal cpx %; (d) Yb_N in cpx vs. Cr-number [cr# = 100 × Cr/(Cr + Al)] in spinel; (e) $(La/Yb)_N$ vs. in T_{BKN} (°C) (equilibrium temperature from Brey & Köhler (1990), typical error is ± 30 °C); (f) $(Sm/Yb)_N$ in cpx vs. T_{BKN} (°C). Dash lines in (e) and (f) represent the CI-chondrite values; grey area: zone of amphibole crystallisation in Ray Pic samples; black circles are from Ray Pic, black diamonds are for high temperature samples from Zangana et al. (1997). Other symbols are as in Fig. 3.

amphibole-rich sample (13RP03), while several amphibole-poor samples (e.g. 13RP17) also have LREE enriched patterns with an extremely steep slope from Pr to La (Fig. 5a, b). Conversely, G2 cpx show LREE–MREE depleted pattern (e.g. 13RP14). Amphiboles from G2 have REE patterns parallel to the cpx with a $D^{am/cpx}(REE) = 1.05 \pm 0.07$ which is in agreement with experimental and natural literature data (Coltorti et al., 2000, 2004; Grégoire et al., 2000; Tiepolo et al., 2007; Vannucci et al., 1995). We conclude that amphibole and cpx are in equilibrium (Fig. 5b, c).

Extended trace element patterns of cpx from G1 and G2 shown in Fig. 5e, f are marked by pronounced negative anomalies of Nb and Ta relative to the LREE ($(Nb/Ce)_{PM} \leq 0.3$; PM denotes primitive mantle normalised values, after McDonough and Sun, 1995), and strong positive anomalies of U, Th ± Sr (i.e., $(U/Nb)_{PM}$ up to 916). While these anomalies also occur in G3 cpx, they are less prominent ($(U/Nb)_{PM} \leq 4.1$) than in the two other groups. Overall, G2 cpx show lower Rb–Ba content compared to amphibole-poor samples (G1), in agreement with their preferential partitioning into amphibole. Indeed, the coexisting amphiboles have Rb and Ba content at least 2 orders of magnitude higher that those of the coexisting cpx as shown in Fig. 5g. High Field Strength Elements (HFSE: Nb, Ta, Zr, Hf and Ti) are known to have more affinity for amphibole than for pyroxenes (e.g., Coltorti et al., 1999). Indeed, the HFSE content is significantly higher in the amphibole than in the coexisting cpx in samples 13RP12, 13RP04 and 13RP03 (see in Fig. 5f, g). However, only Ti shows a positive anomaly relative to the HREE and MREE, while Nb–Ta still display a negative anomaly relative to the neighbouring REE and LILE elements (U, Th). The fractionation of U and Th relative to LREE is extremely similar to the one of cpx ($kd^{am/cpx}(U,Th) = 1.1 \pm 0.4$). However, Sr displays a more marked anomaly relative to the neighbouring REE ($1 \leq (Sr/Ce)_{PM}$ in am ≤ 3) than observed in the cpx ($kd^{am/cpx}(Sr) = 2.7 \pm 0.03$ for 13RP12 and 13RP03).

4.4. Infrared spectra, OH absorption bands and calculated water contents

Water contents were obtained for 103 olivines, 90 opx and 83 cpx grains. The olivine spectra show three groups of absorption bands:

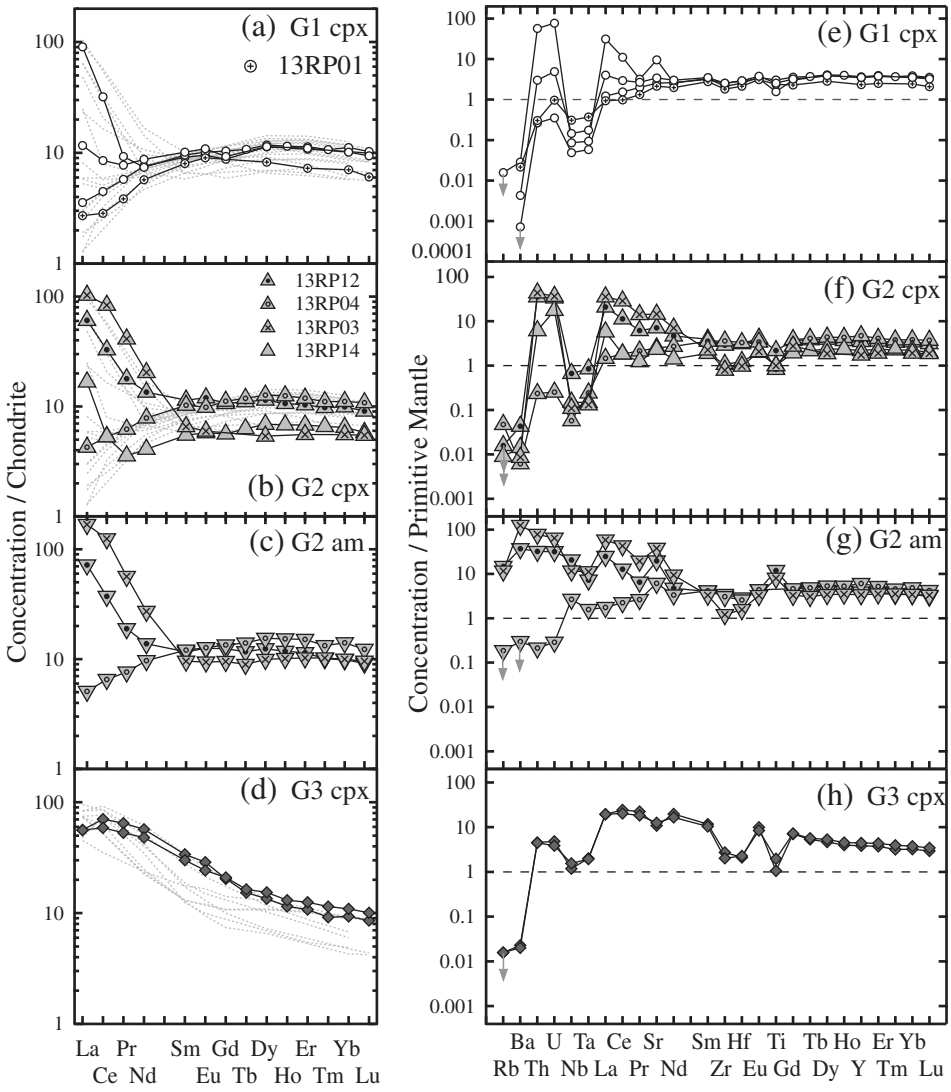

Fig. 5. (a), (b), (c) and (d) Chondrite-normalised REE compositions of clinopyroxene (cpx) and amphibole (am) for Ray Pic spinel-peridotite xenoliths. (a) cpx for G1; (b) cpx for G2; (c) am for G2; (d) cpx for G3. (e), (f), (g) and (h) primitive mantle normalised trace element compositions of cpx and am; (e) cpx for G1; (f) cpx for G2 ; (g) am for G2; (h) cpx for G3. CI-chondrite and primitive mantle from McDonough and Sun (1995). Thin grey dashed lines denote Ray Pic cpx from Zangana et al. (1997). Grey arrows in the right panel for Rb and Ba indicate a concentration below the detection limit (see Table 3).

group I from 3598 to 3420 cm^{-1}; group II from 3420 to 3280 cm^{-1} and group III from 3280 to 3195 cm^{-1} as shown in Fig. 6. The group II and/or III are not present in every spectrum, which could be due to the anisotropy of the crystal lattice, but are here mainly due to the low concentration of the stretching hydroxyl groups in the olivine lattice (e.g., Beran and Putnis, 1983; Denis et al., 2013; Miller et al., 1987). The absorption spectra of opx and cpx each show three major absorption bands at 3590, 3519, 3419 cm^{-1} and 3633, 3525 and 3452 cm^{-1}, respectively, as displayed in Fig. 6. These absorption bands are typical of olivine, opx and cpx from peridotite xenoliths in alkali basalt (Bell and Rossman, 1992; Demouchy et al., 2006, 2015; Denis et al., 2013; Grant et al., 2007a, 2007b; Ingrin and Skogby, 2000; Peslier and Luhr, 2006; Peslier et al., 2002; Skogby, 2006; Xia et al., 2010, 2013; Yang et al., 2008; Yu et al., 2011).

The range and average of water contents in minerals expressed in ppm wt. H_2O is reported in Table 4. In G1, the water content averages of olivine and cpx from 13RP17 (i.e., 6 and 329 ppm wt. H_2O for olivine and cpx respectively) are higher than for the other sample within group G1, which are around 3 and 220 ppm wt. H_2O for olivine and cpx, respectively, as presented in Fig. 7. The average water contents in NAMs for G2 are within the same range of concentration than G1 for cpx (220 ppm wt. H_2O), slightly lower for olivine (3 ppm wt. H_2O) and higher for opx (115 ppm wt. H_2O). The water contents averages for each minerals of the G3 are higher than both G1 and G2, i.e., 6, 140 and 280 for olivine, opx and cpx, respectively (Fig. 7). These water contents are typical of olivine, opx and cpx from spl-bearing peridotite xenoliths in alkali basalts whatever the calibration used (see Table 4; e.g., Baptiste et al., 2015; Bonadiman et al., 2009; Demouchy et al., 2015; Denis et al., 2013; Ingrin and Skogby, 2000; Peslier et al., 2002, 2015; Peslier and Luhr, 2006; Peslier, 2010; Yu et al., 2011; Xia et al., 2010, 2013).

FTIR measurements along transepts in three large olivine grains (length > 2 mm) and one pyroxene (length > 1.5 mm) did not reveal heterogeneous water content across mineral grains, which would be indicative of H loss (e.g., Demouchy et al., 2006; Denis et al., 2013; Peslier and Luhr, 2006; Thoraval and Demouchy, 2014).

At last, there is no positive correlation between H_2O content of the NAMs and the occurrence and/or abundance of amphibole as display in Fig. 8 and as reported by previous studies (e.g., Bonadiman et al., 2009; Demouchy et al., 2015).

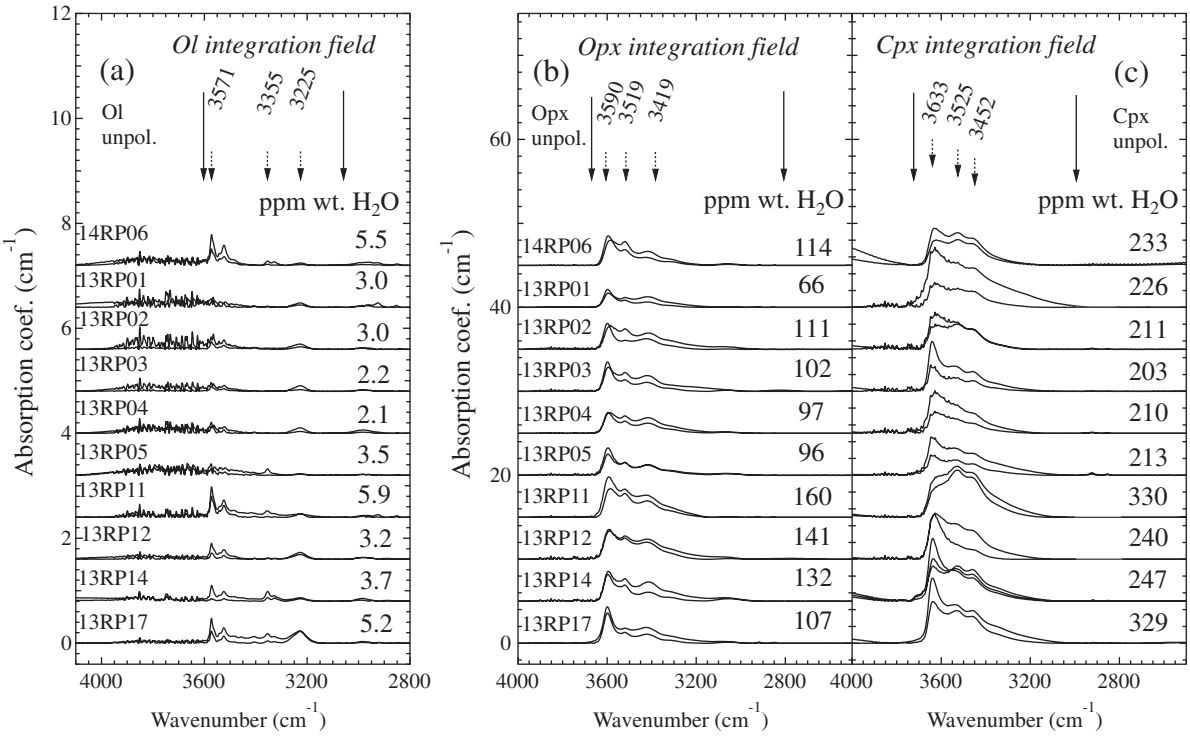

Fig. 6. Representative unpolarized FTIR spectra for Ray Pic spinel-peridotite xenoliths: (a) olivine (ol), (b) orthopyroxene (opx), and (c) clinopyroxene (cpx). Spectra with minimal and maximal absorbance are given for each sample. All spectra are normalised to 1 cm of thickness. Long black arrows indicate the integration range used for the IR calibration; the short dashed arrows indicate the major OH absorption bands of the mineral.

4.5. Recalculated whole-rock H_2O contents

Using mineral modal abundances and mineral water content obtained by FTIR (see above) and KFT (see Section 4.2), one can compute whole-rock H_2O content. We here define an 'amphibole-free whole-rock', which neglects the effect of amphibole on the whole-rock H_2O content (i.e., only NAMs are considered) and a 'whole-rock' which include NAMs and amphibole. H_2O content in amphibole-free whole-rock ranges between 34 and 71 ppm, while whole-rock may reach values as high as 1663 ± 201 ppm wt. H_2O for the amphibole-rich sample 13RP03 (Fig. 8d). These values are in good agreement with experimental data obtained on am-bearing peridotite at lithosphere conditions (1.5–2.5 GPa; 1000–1150 °C; Green et al., 2010). Thus, whole-rock H_2O contents are dominated by amphibole as shown in Fig. 8d. The H_2O content of amphibole-free whole-rocks are over-all correlated with fertility indexes reported in Fig. 9; only the G3 samples show a small shift toward higher H_2O content.

5. Discussion

5.1. Record of chemical depletion and metasomatism

The chemical composition of peridotite xenoliths results from two main processes: (1) melting, with variable degrees of melt extraction during partial melting, and (2) metasomatism, due to the percolation of a melt or a fluid through the peridotite matrix (e.g., Frey and Green, 1974; O'Reilly and Griffin, 2013).

We observe continuous depletion trend of the lithophile element content in minerals (e.g., Al and Na in cpx and opx; Al in spl); which is correlated with the decreasing modal abundances of cpx ± opx. At the whole rock scale, these covariations translate a decreasing trend of Al_2O_3 and CaO (Fig. 3). Such covariations are identical to the one reported for intracontinental spinel-peridotite from worldwide occurrence and are interpreted as resulting from melt depletion (e.g., McDonough and Sun, 1995). Correlation between fertility indexes related either to WR major element contents, mineral composition and mineral modal abundances, is here self-consistent (Figs. 8d; 9). This suggests that peridotites from Ray Pic represent a residue from variable degrees of partial melting and melt extraction from a fertile lherzolite source. The relationships between HREE content and melt depletion indexes such as cr#spl, Fo%, CaO content of cpx, suggest that HREE abundance was primarily controlled by melt depletion and extraction processes (Fig. 4) and even for the G3 or amphibole-rich samples (see below). The variation of HREE (i.e., Yb) content in cpx indicates two different ranges of melt-depletion (Fig. 5). Using the approach from Norman (1998) and a primitive mantle composition from McDonough and Sun (1995), we calculate that the most Yb-rich samples (e.g., 13RP17) have undergone 3 to 4% of partial melting using a batch melting model or 3 to 6% of partial melting using a fractional melting model as shown in Fig. 10. The significantly lower Yb values for samples 13RP01, 13RP14 and 13RP03 suggest a higher degree of melting estimated between 8 and 10% and between 12 and 16%, using both batch and fractional melting models, respectively (Fig. 10). We thus consider that modal abundances and major element characteristic of olivine and pyroxenes results from small to moderate percentage of partial melting and melt extraction. The results from Zangana et al. (1997; 1999), based on a larger number of xenoliths from Ray Pic, encompass our range of melt depletion (1–10% for batch and 1 to 18% for fractional melting). The high $^{143}Nd/^{144}Nd$ (0.51347–0.51305) and low $^{87}Sr/^{86}Sr$ (0.7019–0.7029), reported by Zangana et al. (1997) for LREE-depleted cpx, attest a long term melt-depletion of the mantle lithosphere beneath the Ray-Pic volcano, possibly since the late Proterozoic.

The occurrence of amphibole and/or the extremely variable abundances and fractionation of the LREE ± MREE, LILE and HFSE relative to the HREE show that the slightly to moderately depleted protolith (i.e., the parent rock) was overprinted by metasomatic events. Modal metasomatism is here shown by the occurrence of amphibole, with modal abundance up to 8%. Microstructural context, major element chemistry and trace element content of the amphibole show that

Table 4
Water content in olivine and pyroxenes (ppm wt H_2O, based on the calibration of Paterson, 1982 (P82) and also calculated for other calibrations, B2003 = Bell et al., 2003; W12 = Withers et al., 2012, B95 = Bell et al., 1995.

Group			G1			G2			G3	
			<1% am			>1% am				
Sample	13RP05	13RP17	13RP01	13RP02	13RP12	13RP04	13RP14	13RP03	13RP11	14RP06
Olivine: n	6	15	9	8	12	11	12	8	18	4
Calc. Area	18.6	34.0	16.2	15.5	18.8	12.3	21.1	12.8	31.0	26.2
±1SD	6.1	8.3	4.7	5.9	3.5	4.3	7.0	3.3	8.0	7.5
min P82	1.9	3.1	2	2.0	1.9	1.3	1.4	1.5	3.5	3.9
max P82	5.2	7.1	3.9	5.3	4.2	4.2	5.9	3.6	8.7	7.8
C_{OH} avg P82	3.5	5.2	3	3.0	3.2	2.1	3.7	2.2	5.9	5.5
±1SD	1.1	1.2	0.7	1.2	0.6	0.8	1.3	0.6	1.4	1.5
C_{OH} avg B2003	10.5	19.2	9.1	8.7	10.6	6.9	11.9	7.2	17.5	14.8
C_{OH} avg W12	6.6	12.1	5.8	5.5	6.7	4.4	7.5	4.6	11.1	9.4
Opx: n	6	6	10	11	9	10	8	12	12	6
Calc. area	496	531	335	566	733	494	694	505	847	555
±1SD	40	77	37	91	90	58	102	63	145	58
min P82	88	92	58	89	118	87	101	92	136	105
max P82	106	124	75	136	177	118	154	122	196	124
C_{OH} avg P82	96	107	66	111	141	97	132	102	160	114
±1SD	6	10.6	4.8	12.7	13.1	9	15.0	8.1	20.1	7.7
C_{OH} avg B95	100	107	68	114	148	100	140	102	171	112
Cpx: n	10	5	11	8	8	9	9	13	5	5
Calc. area	843	1320	901	857	923	792	1138	801	1472	977
±1SD	183	158	292	34	163	178	80	160	147	247
min P82	138	268	145	181	189	126	214	128	287	183
max P82	275	398	375	221	302	266	289	248	374	306
C_{OH} avg P82	213	329	226	211	240	210	247	203	330	233
±1SD	44	46.2	70.1	7.9	26.4	43	23.5	31.4	30.1	45.7
C_{OH} avg B95	357	559	381	363	391	335	482	339	623	413
C_{OH} WR (w/. am)	42	62	38	65	64	52	34	34	71	55
±1σ	7	10	11	11	11	9	6	6	12	9
C_{OH} WR (w. am)	42	62	78	165	285	378	389	1663	72	55
±1σ	7	10	11	23	37	48	48	201	12	9
$Kd^{cpx/opx}(H_2O)$	2.2	3.1	3.4	1.9	1.7	2.2	1.9	2.0	2.1	2.0
±1σ	0.5	0.5	1.1	0.2	0.3	0.5	0.3	0.4	0.3	0.4
$Kd^{cpx/ol}(H_2O)$	61	63	75	71	75	100	67	92	56	42
±1σ	24	18	31	30	17	44	29	32	15	15
$Kd^{opx/ol}(H_2O)$	27	20	22	37	44	46	36	47	27	21
±1σ	8.8	5.1	5.4	15.4	9.1	18.0	13.4	14.1	7.3	5.8
Factor[a] ol	16.32	16.33	16.35	16.36	16.36	16.33	16.30	16.32	16.26	16.31
Factor[a] opx	11.58	11.60	11.61	11.59	11.59	11.55	11.58	11.57	11.58	11.56
Factor[a] cpx	12.12	12.13	12.07	12.08	12.09	12.07	13.75	12.11	12.10	12.09

Average (avg) on n grains; 1σ: absolute uncertainties calculated by algebraic method; [a] denotes factor to convert water contents in ppm wt. H_2O to $H/10^6$ Si; opx: orthopyroxene; cpx: clinopyroxene; am: amphibole. In average, the intercalibration conversion factors (using unpolarized IR) are 3.14, 1.99, 1.03 and 1.73 for $(B2003/P82)_{ol}$, $(W12/P82)_{ol}$, $(B95/P82)_{opx}$ and $(B95/P82)_{cpx}$, respectively.

amphibole is in equilibrium with the other minerals (e.g., cpx). Despite variable modal abundance and distinct microstructural occurrence, all amphiboles show similar major element composition, suggesting that they are all related to the same metasomatic event involving the same mantle source.

However, amphibole-bearing samples show variable REE fractionation going from depleted [(La/Sm) < 1] to enriched [(La/Sm) > 1] pattern. The shape of REE pattern is clearly independent of the occurrence and/or abundance of amphibole (Fig. 5). Therefore, amphibole could have been a component of the protolith, perhaps formed during an earlier metasomatic event (n), postdating a partial melting event (n − 1). Then, within this scenario, the occurrence of amphibole is not related to the current trace element enrichments and fractionations due to, at least one more recent metasomatic event (n + 1), and which has overprinted the trace element signature related to the amphibole crystallisation events. However such scenario is hardly reconcilable with the fact that some amphibole shows LREE depleted pattern (13RP04). Alternatively, the necessary increase of H_2O fugacity in the percolating melt/fluid, which is required for crystallisation of amphibole, could have occurred at a higher distance from the source than the chromatographic front for LREE for instance (e.g., Le Roux et al., 2007), and produced an offset between the LREE enrichment zone and the amphibole crystallisation zone. This scenario is supported by the fact that LREE depleted amphibole occurred mostly in low-temperature samples (e.g., Alard et al., 2011; Touron et al., 2008), 13RP04 has also a low equilibrium temperature (T° Ca-in-opx = 880 ± 30 °C).

On the one hand, the strong LREE and LILE (U, Th, Sr) enrichment without concomitant enrichment of the HFSE and especially Nb–Ta (G1 and G2), is a trace element signature, which has been previously identified for peridotites from many localities and is generally ascribed to a carbonatitic or carbonated metasomatism (Alard et al., 2011; Coltorti et al., 1999; Dautria et al., 1992; Ionov et al., 1993; Rudnick et al., 1993; Yaxley et al., 1998). Sun and Kerrich (1995) has ascribed it to be H_2O–CO_2 fluids. While the true nature of the metasomatic melt/fluid remains unclear, all studies agree on (1) the volatile-rich nature of such metasomatic melt and (2) the need for this metasomatism to occur at low melt/rock ratio (≪1%; e.g., Bedini et al., 1997). The volatile-rich nature of the fluid is required to significantly lower the viscosity, dihedral angles and crystallisation temperature of the fluid/melts and thus allow a more efficient percolation through the upper and colder part of the subcontinental lithospheric mantle (SCLM; Minarik

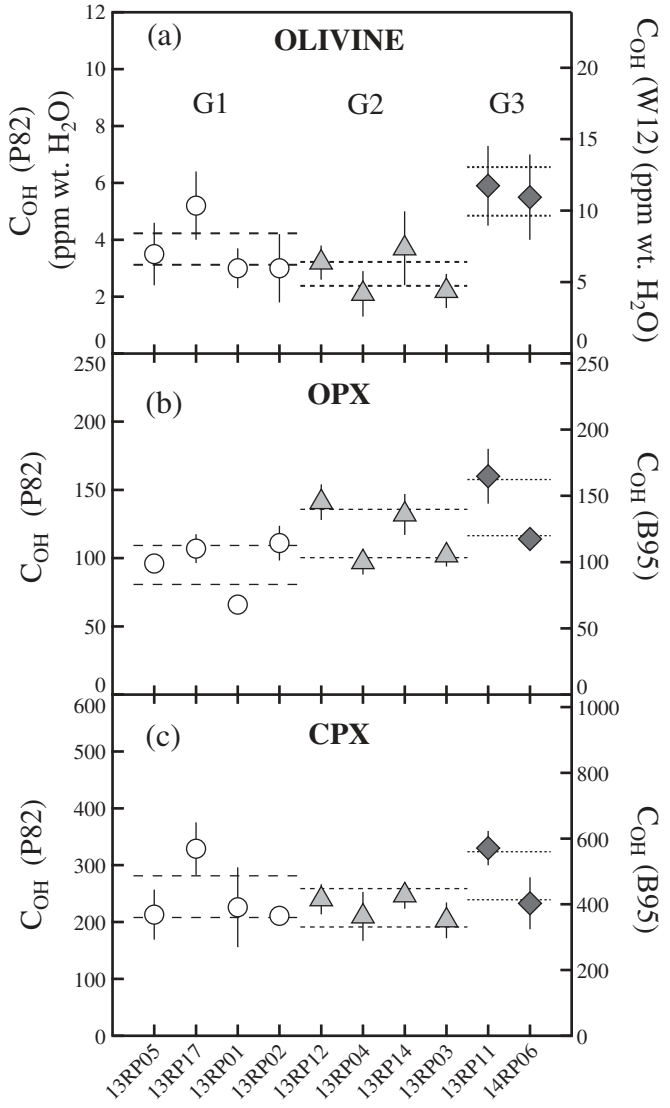

Fig. 7. Water contents in nominally anhydrous minerals for each Ray Pic spinel-peridotite xenoliths (in ppm wt. H_2O, based on calibration of Paterson, 1982 (P82); Withers et al., 2012 (W12); and Bell et al., 1995 (B95)). Symbols are average values from N analyses for each sample. Vertical lines across each symbol give the standard deviation of the average values of water content per sample (i.e., 1SD, see Table 4), and horizontal lines give the uncertainties on the average values per group (using 30% of uncertainty from calibration of Paterson, 1982). Opx: orthopyroxene; cpx: clinopyroxene; symbols are as in Fig. 3.

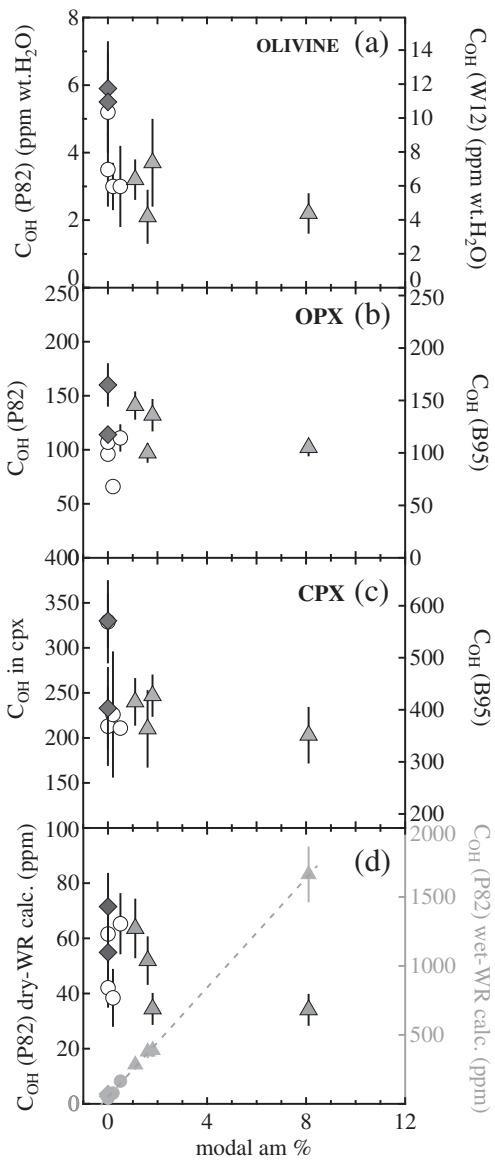

Fig. 8. Water contents for Ray Pic spinel-peridotite xenoliths (in ppm wt. H_2O, based on calibration of Paterson, 1982 (P82); Withers et al., 2012 (W12); and Bell et al., 1995 (B95); see Table 4) as a function of the mineral mode of amphibole in % for (a) olivine (ol), (b) orthopyroxene (opx), and (c) clinopyroxene (cpx), error bar on the average values of water content per sample is 1SD (Table 4); (d) water contents for amphibole-free whole rock (WR, C_{OH} WR (w/. am)), and whole rock (C_{OH} WR (w. am)). WR water contents (C_{OH} WR (w. am)) in grey refers to the grey axis on the right hand side; absolute uncertainty on the WR water content was calculated by algebraic method for error propagation. Symbols are as in Fig. 3.

and Watson, 1995; Watson and Brenan, 1987). Samples from the G1 and G2 groups have equilibrium temperature below 1000 °C. Strong fractionation between REE as observed in G1 and G2 samples, could be easily produced by melt percolation at low melt/rock ratio (Navon and Stolper, 1987). On the other hand, MREE enriched pattern is commonly observed for cpx metasomatised at high melt–rock ratio such as the one found near or within pyroxenite veinlets/dykes (Kourim et al., 2014; Witt-Eickschen and Kramm, 1998). Melt/fluid-percolation models (e.g., Bodinier et al., 1990; Navon and Stolper, 1987; Vasseur et al., 1991; Vernières et al., 1997) indicate that MREE enrichment over HREE can only be obtained for relatively large melt/rock ratios (i.e., ≥1%, Bodinier et al., 1990; Navon and Stolper, 1987). Melt percolation/reaction at higher melt/rock ratio will produce more steady and continuous enrichment from the HREE to the LREE (i.e., linear pattern) and reduce fractionation between incompatible elements as observed in G3. Although melt percolation and temperature propagation are two distinct processes, this type of interaction should occur closer to the melt source and thus peridotite samples should have a higher equilibrium temperature than measured in G1 and G2 samples (see also Alard et al., 1996; Xu et al., 1998). It is the case for the equilibrium temperature of G3 samples (>1000 °C). The relationship between REE fractionation and equilibrium temperature in the Ray Pic xenoliths is quite remarkable (Fig. 4e, f) and was first reported by Zangana et al. (1997). Accordingly, Fig. 4f shows that only samples equilibrated at high temperature (i.e., T > 1000 °C, G3 samples) are enriched in MREE relative to the HREE (i.e., $(Sm/Yb)_N > 1$). The large fractionation of the LREE relative to the HREE (and MREE not shown) requiring interactions at low melt/rock ratio that occur for xenoliths equilibrated at relatively low temperature (down to 850 °C). Samples equilibrated at low temperature (<850 °C) are not affected by the selective LREE enrichment (Fig. 4e), they are thus located ahead of the La-chromatographic front.

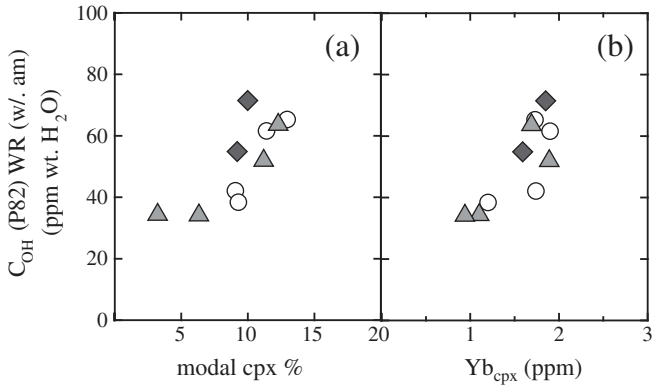

Fig. 9. Water contents for amphibole-free whole rock (C_{OH} WR (w/. am)) in ppm wt. H_2O as a function of (a) modal percentage of clinopyroxene (cpx in %); (b) Yb in cpx given in ppm. Hollow circle: G1 Ray Pic peridotites; grey triangle: G2 Ray Pic peridotites; black diamonds: G3 Ray Pic peridotites (see text and Table 2 for details). Concentrations are given for the calibration of Paterson (1982).

This relationship suggests that both types of metasomatic fingerprints are related to the same melt/fluid. The percolating melt evolved along the conductive geotherm by successive volume reduction, due to the reaction with the peridotite matrix and/or new crystallised phases. The resulting melt/fluids is thus enriched in the most incompatible elements, including the volatiles (e.g., Bedini et al., 1997). The scale at which these iterative metasomatic melt reactions operate is still under debate. Indeed, two hypotheses are possible: (1) a regional scale heterogeneity involving mantle diapir or plume (e.g., Bedini et al., 1997) or (2) a metre to centimetre scale heterogeneity involving melt channels (Bodinier et al., 1991; Grégoire et al., 2000; Kourim et al., 2014) and leaving behind pyroxenite dykes, veinlets and/or metasomatised wall-rocks. To favour one or the other scenarios depends on the interpretation of equilibrium temperatures: (i) either they record temperatures representing in situ conditions in the lithospheric mantle, then they are equivalent to the emplacement depth of the xenoliths; or (ii) they are related to the metasomatic process itself and its heating effect. On the basis of both geophysical data, which have imaged an asthenosphere diapir/plume beneath the FMC (Granet et al., 1995); and the isotopic composition of the LREE enriched xenoliths; Zangana et al. (1997) favoured the first hypothesis. Other authors working on the mantle lithosphere of the FMC (e.g., Alard et al., 1996; Lenoir et al., 2000; Xu et al., 1998) have also favoured this interpretation. However, the common occurrence of pyroxenites among the mantle xenoliths from Ray Pic (wherlites, websterites), the similarity of pyroxenite equilibrium temperatures (≈1030–1050 °C, Zangana et al., 1997) with temperatures obtained for the G3 peridotite xenoliths (≈1040 ± 30 °C) lead us to consider that the second scenario is here a relevant alternative.

5.2. The preservation of the initial water content of the mantle source

Given the high diffusivity of H in olivine (e.g., Demouchy and Mackwell, 2006; Mackwell and Kohlstedt, 1990), the relevance of the low H concentration in olivine as an indicator of the water content in mantle source was questioned (Demouchy and Mackwell, 2006; Hao et al., 2014a, 2014b; Ingrin and Skogby, 2000). It was argued that the low water content of olivine (<5 ppm wt. H_2O) in mantle xenoliths might be due to a rapid ionic diffusion (dehydration) during ascent toward the surface (Demouchy et al., 2006; Denis et al., 2013; Peslier and Luhr, 2006). However, such dehydration profiles are not ubiquitous in all mantle olivine and other parameters than temperature, controlling H ionic diffusion, remain to be identified and quantified. In this study, concentration profiles along transects across olivine and pyroxene grains evidence long concentration plateaus (e.g., to the contrary

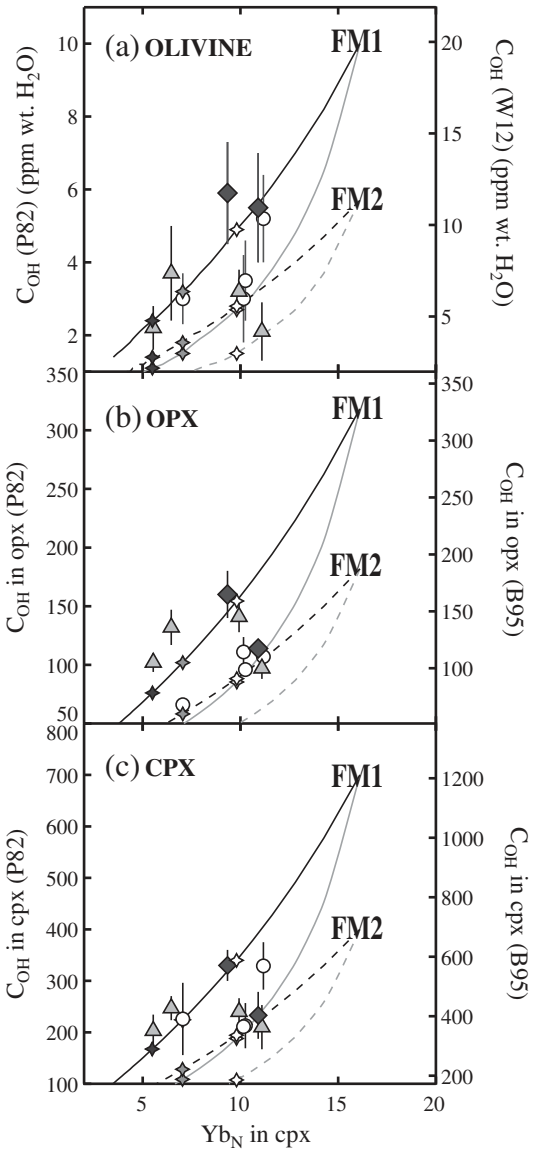

Fig. 10. Water contents for Ray Pic spinel-peridotite xenoliths (in ppm wt. H_2O, based on calibration of Paterson, 1982 (P82); Withers et al., 2012 (W12); and Bell et al., 1995 (B95)) as a function of Yb_N in cpx (N: normalised to CI chondrite values from McDonough and Sun (1995)) for (a) ol; (b) opx and (c) cpx. Symbols are as in Fig. 3. Solid lines are for batch melting using the method of Norman (1998). Fertile mantle (FM) contains 18% of cpx having either 700 ppm wt. H_2O (FM1), or 400 ppm wt. H_2O (FM2). This range (FM2–FM1) encompasses the variations of H_2O content in spinel reported in the literature (e.g., Bell and Rossman, 1992; Grant et al., 2007a, 2007b; Hao et al., 2014a, 2014b; Li et al., 2014; Peslier and Luhr, 2006; Peslier et al., 2002). Black lines are for a $D^{cpx/melt}$ (H_2O) = 0.25, grey lines are for a $D^{cpx/melt}$ (H_2O) = 0.1 (see main text for details). $D^{ol/melt}$ (H_2O) and $D^{opx/melt}$ (H_2O) were derived using $Kd^{cpx/ol}$ (H_2O) = 70 and $Kd^{cpx/opx}$ (H_2O) = 2.2 (see text and Fig. 11). White, grey and black stars indicate 5%, 10% and 15% of melting degrees, respectively.

to short plateau), which permit to rule out significant dehydration (see Thoraval and Demouchy, 2014).

Since olivine appears to be a weak indicator of the water source, the emphasis was put on pyroxenes (e.g., Denis et al., 2013; Hao et al., 2014a, 2014b; Xia et al., 2010). Indeed, the relatively constant water content ratio between cpx and opx in spl-bearing peridotites hosted in alkali basalts suggests that they preserve the initial H_2O contents of the mantle source (e.g., Denis et al., 2013; Hao et al., 2014a, 2014b; Peslier et al., 2012; Xia et al., 2010). For the Ray Pic xenoliths, the ratio of water concentration between opx and cpx range between 1.7 and 3.4, this variation is irrespective of amphibole occurrence, cpx or opx

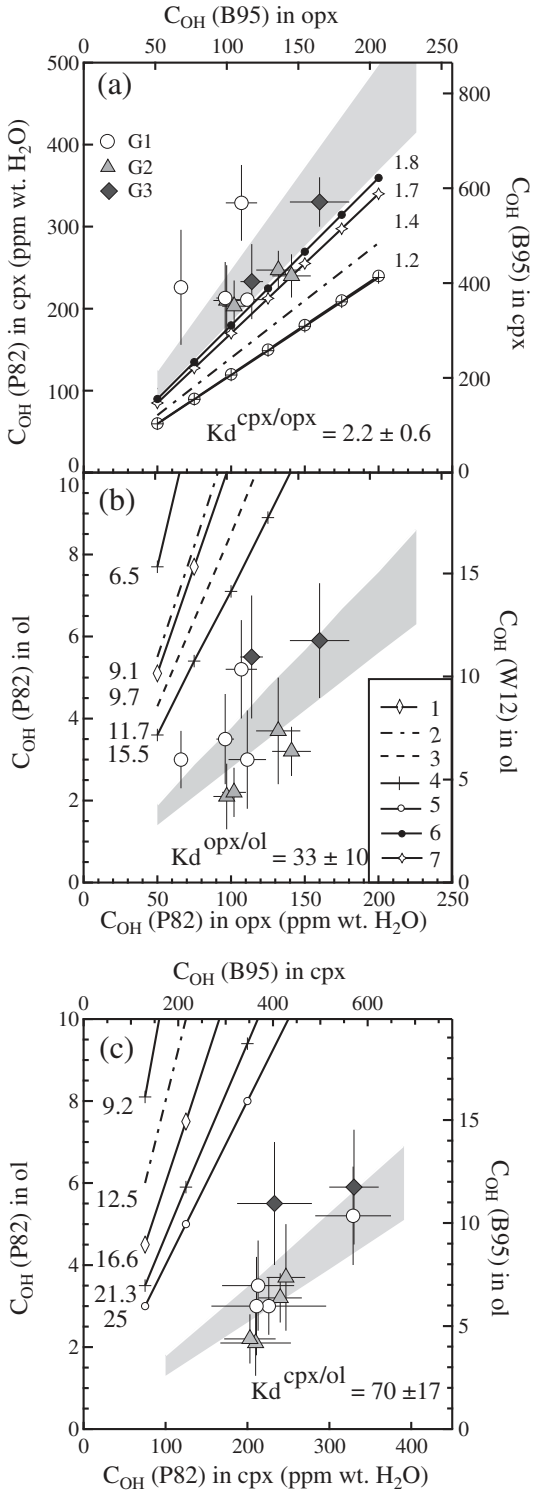

Fig. 11. Water contents for Ray Pic spinel-peridotite xenoliths (in ppm wt. H_2O, based on calibration of Paterson, 1982 (P82); Withers et al., 2012 (W12); and Bell et al., 1995 (B95)). (a) In ol as a function of water content in opx; (b) in cpx as a function of water content in opx; (c) in ol as a function of water content in cpx. Symbols are as in Fig. 3; grey areas are the average water content ratio using 30% of uncertainty for mantle-derived minerals of G1, G2 and G3. Black lines are experimentally determined partition coefficients from (1) Ardia et al., 2012 (5–8 GPa; 1400–1450 °C); (2) Aubaud et al., 2004 (1–2 GPa; 1230–1380 °C); (3) Grant et al., 2007a, 2007b (1.5 GPa; 1295–1320 °C); (4) Hauri et al., 2006 (cpx/opx: 1.2–1.6 GPa; 1185–1370 °C; cpx/ol and opx/ol: minimum and maximum values at 1.2–1.6 GPa; 1185–1370 °C); (5) Tenner et al., 2009 (3–5 GPa; 1350–1440 °C); (6) Novella et al., 2014 (6 GPa; 1400 °C); (7) Kovács et al., 2012 (2.5 GPa; 1000 °C). Values from IR-based studies (Grant et al., 2007a, 2007b; Kovács et al., 2012) were converted to Paterson's calibration for homogeneity.

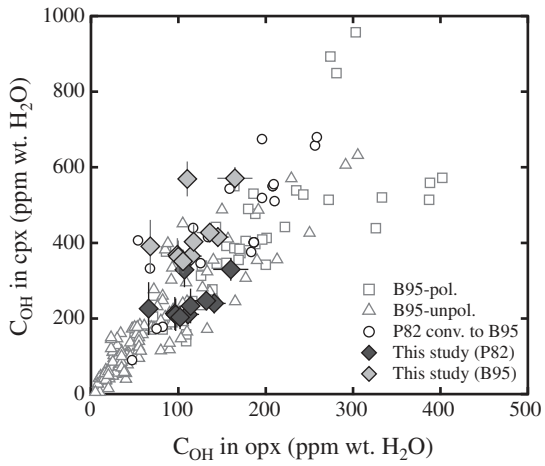

Fig. 12. Water contents in cpx as a function of water content in opx for spinel-peridotite xenoliths in alkali basalt (in ppm wt. H_2O, based on calibration of Paterson, 1982 (P82) and Bell et al., 1995 (B95)). Open squares are for polarized IR measurements using the calibration of Bell et al. (1995) (Grant et al., 2007a, 2007b; Li et al., 2008; Peslier et al., 2002, 2015; Peslier and Luhr, 2006; Peslier and Bizimis, 2015); open triangles are for unpolarized measurements using the calibration Bell et al. (1995) (Bonadiman et al., 2009; Falus et al., 2008; Xia et al., 2010; Yu et al., 2011); open circles are for values using the calibration Paterson (1982) with unpolarized measurements, then converted to the calibration of Bell et al. (1995) (Demouchy et al., 2015; Denis et al., 2013; Soustelle et al., 2013). Filled black and grey diamonds are for results from this study using the calibration of Paterson (1982) and using calibration of Bell et al. (1995) respectively. For clarity, error bars (1SD) are only shown for the results from this study.

modal abundances, melting or metasomatism indexes. These ratios of water concentration between opx and cpx can be interpreted as an apparent partition coefficient ($Kd^{cpx/opx}(H_2O)$). For the 10 Ray Pic-xenoliths $Kd^{cpx/opx}(H_2O)_{RP}$ is c.a., 2.2 ± 0.6 in average using the calibration of Paterson (grey area in Fig. 11), which is within error of the literature average $Kd^{cpx/opx}(H_2O) = 1.8 \pm 0.8$ obtained on a range of spl-bearing xenoliths in alkali basalts from worldwide occurrences (Demouchy et al., 2015; Denis et al., 2013; Soustelle et al., 2013). Using the calibration of Bell et al. (1995), $Kd^{cpx/opx}(H_2O)_{RP}$ range between 2.9 and 5.7 and average c.a. 3.8 ± 0.9. The range of $Kd^{cpx/opx}(H_2O)$ for spl-bearing xenoliths, excluding the one from cratons, varies from 0.5 up to 6.5 and yield an average value c.a. 2.6 ± 0.9 (N = 182, Bonadiman et al., 2009; Falus et al., 2008; Grant et al., 2007a, 2007b; Li et al., 2008; Peslier and Luhr, 2006; Peslier et al., 2002; 2015; Xia et al., 2010; Yu et al., 2011). Thus, although the average $Kd^{cpx/opx}(H_2O)$ for Ray-Pic xenoliths are slightly higher than the "global" average, it remains within error. The dataset used for calculated these $Kd^{cpx/opx}(H_2O)$ is shown in Fig. 12 where data are presented according to the calibration of Bell et al. (1995) as well as the calibration of Paterson (1982) for our data. Indeed, the water contents for Ray-Pic xenoliths are slightly higher than the "global" average after conversion but remains within the main trend (Fig. 12). These concentration ratios for natural pyroxenes are in relative good agreement with partition coefficients obtained by experimental petrology, notably with $Kd^{cpx/opx}(H_2O) = 1.4$ from Aubaud et al. (2004) at equilibrium conditions (1 GPa, 1200 °C); $Kd^{cpx/opx}(H_2O) = 1.8$ from Novella et al. (2014) at equilibrium conditions (6 GPa, 1400 °C) and $Kd^{cpx/opx}(H_2O) = 1.7$ from Kovács et al. (2012) at equilibrium conditions (2.5 GPa, 1000 °C; Fig. 11a). We also note that the $Kd^{opx/ol}$ and $Kd^{cpx/ol}$ for the Ray Pic xenoliths are, like the $Kd^{cpx/opx}$, relatively constant (same relative standard deviation) and equal to 33 ± 10 and 70 ± 17, respectively (Fig. 11b, c). These relatively constant water content ratios further support that water content in olivine has not been affected by significant dehydration process. Finally, dehydration processes are unlikely to preserve correlations of olivine water contents with fertility indexes (see next section). Therefore, these observations suggest that the water content of NAMs in the Ray

Pic xenoliths have not been significantly modified during ascent toward the surface.

5.3. Hydrogen behaviour during mantle processes

5.3.1. Partial melting

Water contents in ol, opx and cpx are roughly correlated with $[Yb]_{cpx}$ (Fig. 10), which is used here as a proxy of melt depletion (Fig. 4). Similarly, calculated H_2O content in the amphibole-free WR is correlated to fertility indexes (Fig. 9). In particular for G1 and G2 samples. Therefore these correlations suggest that water abundances in Ray-Pic NAMs could be mainly related to melting processes. Despite some scatter, melting curves reproduce broadly the observed distribution of the Ray Pic samples within the $[Yb]_{cpx}$–$C_{OH}^{cpx,opx,ol}$ spaces (Fig. 10). The best data fits are obtained for $D^{cpx/melt}$ (H_2O) ranging between 0.1 and 0.25 and for an initial cpx water content between 400 and 700 ppm (see also Fig. 10 for further detail). The range of $D^{cpx/melt}$ (H_2O) used here is at least one order of magnitude higher than results from experimental petrology in modelled systems ($D^{cpx/melt}$ = 0.013–0.048; Aubaud et al., 2004; Aubaud et al., 2008; Hauri et al., 2006; Novella et al., 2014; O'Leary et al., 2010; Tenner et al., 2009). Nevertheless, such low experimental $D^{cpx/melt}$ (H_2O) (i.e., 0.01–0.05) implies that the mantle will be completely deprived of its water (i.e., $C_{OH}^{cpx} < 50$ ppm, using a batch-melting model) from the first melting increments (i.e., 1–5%). On the other hand, $D^{cpx/melt}(H_2O)$ ranging between 0.1 and 0.25 are in good agreement with the water content in pyroxenes from Hao et al. (2014a, 2014b), who suggest $D^{peridotite/melt}(H_2O) \approx 0.1$. Relative to lithophile elements, $D^{cpx/melt}(H_2O) \approx 0.1$–0.25 would suggest that H behaves as a moderately incompatible element as Sm ($D^{cpx/melt}(Sm) \approx 0.25$; e.g., Hart and Dunn, 1993; Witt-Eickschen and Kramm, 1998) and not as a very incompatible elements ($D^{cpx/melt}(Ce) \approx 0.075$; $D^{cpx/melt}(La) \approx 0.055$; Hart and Dunn, 1993; Norman et al., 1996) as it was previously proposed (Dixon et al., 2002).

Although, we do not intend to ascribe all variations of water contents in NAMs to a single melting processes, it appears that for the Ray-Pic xenoliths under consideration, melting processes can possibly account for a large part of water contents variability within NAMs. Nevertheless, the residual scatter of the data around the melting curves (Fig. 10) also suggests that other mantle processes besides partial melting have been involved.

5.3.2. Modal hydrous metasomatism

While it was shown that amphibole could be hydroxyl-poor and halogen-rich (e.g., Hawthorne et al., 1998; King et al., 1999; Oberti et al., 2007), a large number of mantle pargasites were proven to be water-rich ($H_2O \approx$ 1–2 wt.%; e.g., Bonadiman et al., 2014; Moine et al., 2000). Therefore, the occurrence of amphibole in mantle rocks is recurrently taken as a water indicator. Numerous authors refer, sometimes abusively, to amphibole-bearing mantle rock as "wet" mantle, while amphibole-free samples are usually coined as "dry" mantle. In the xenoliths from Ray Pic, no correlation between the water content of the NAMs and the occurrence or abundance of amphibole is found (Fig. 8). Indeed the NAMs in amphibole-poor/free xenoliths from G1 and amphibole-rich xenoliths from G2 show the same range of water contents. Major element and trace element contents of the amphibole show that they are in equilibrium with the coexisting silicates. Therefore, this could lead to the conclusion that the pargasite from Ray Pic samples could be water-poor. However, here the pargasites from Ray Pic are water-rich amphiboles. Karl–Fischer titration analyses of pargasite from 13RP03 sample has yield content ca. 1.9 ± 0.5 wt.% H_2O. Given the compositional homogeneity of the amphiboles from Ray Pic, all amphiboles from Ray Pic are considered water-rich.

This lack of effect and/or correlation between amphibole abundance and the water content of NAMs was also recently observed by Schmädicke et al. (2013) for olivine in Eifel xenoliths, by Demouchy et al. (2015) for NAMs in Ontong Java Plateau xenoliths and by Bonadiman et al. (2009) for cpx and opx in the Baker rock xenoliths (Antartica). The study of Bonadiman et al. (2009; 2014) shows that the amphiboles contain 0.84–1.42 wt.% of H_2O, with water contents of opx and cpx ranging from low water contents (39 and 83 ppm wt. H_2O for opx and cpx, respectively), to fairly typical contents (166 and 399 ppm wt. H_2O for opx and cpx) according to spinel-bearing peridotites worldwide (e.g., Bolfan-Casanova, 2005; Ingrin and Skogby, 2000; Peslier, 2010). Although, it may be seen as counterintuitive, wet amphibole containing up to 2 wt.% of H_2O, has no effect on the water content of coexisting NAMs, nor on water distribution between NAMs. In other words, the so-called hydrous metasomatism has no effect on the water content of NAMs and its only effect is to crystallise a water-rich mineral: amphibole. Further NAMs in equilibrium with water rich pargasite are not water richer (or poorer) than NAMs in amphibole free peridotite, suggesting thus that H diffusion from amphibole to NAMs was extremely reduced. It may be due to the difference in speciation of H in these two solid phases. Indeed, in amphibole, H occurs as an independent hydroxyl group (OH) in the O3 structural site of the lattice, while in NAMs, only H (proton, no external oxygen companion) is located in the lattice mineral as impurities in cationic vacant sites (point defect).

Using our data, from 13RP03, we derive a concentration ratio which, assuming that thermodynamic equilibrium was achieved in the natural rock, could be equivalent to partition coefficient at high temperature between pargasite and NAMs: $Kd^{ol/am}(H_2O) = 0.11 \pm 0.04 \times 10^{-3}$; $Kd^{opx/am}(H_2O) = 5.9 \pm 0.6 \times 10^{-3}$ and $Kd^{cpx/am}(H_2O) = 11.4 \pm 2.5 \times 10^{-3}$. These results (once converted to the same calibration) agree with the data of Bonadiman et al. (2009, 2014) for which we can derived an estimate $Kd^{opx/am}(H_2O)_{BR\ avg} \approx 9.8 \times 10^{-3}$ and $Kd^{cpx/am}(H_2O)_{BR\ avg} \approx 17 \times 10^{-3}$ (BR avg: average for Baker Rock peridotite xenoliths).

5.3.3. Cryptic metasomatism

The relationship between cryptic metasomatism and water content of the NAMs is not straightforward. Indeed there is no obvious correlation between the classic metasomatic indexes such as LREE content (e.g., $(La)_N$; Fig. 13a, b, c) or REE fractionation (e.g., $(La/Sm)_N$; $(La/Yb)_N$ not shown; or $(Sm/Yb)_{PM}$ Fig. 13d, e, f) and the water content of NAMs. This suggests that H does not behave as a highly incompatible element (e.g., like La) as discussed above for melt-depletion processes. Indeed, despite strong chromatographic enrichment of the LREE relative to the HREE and MREE, there is no correlated water enrichment. The G3 samples show overall a relatively high water content, in particular for olivine (Fig. 13 d), which would suggest that water enrichment is only possible for NAMs previously modified by reactions at high melt/rock ratio.

The lack of correlation between water content of the NAMs and the Th/Nb_{PM} ratio (Fig. 12g, h, i) is of particular interest. Indeed, the fractionation of the LILE and LREE relative to the HFSE is seen as symptomatic of the so-called carbonatitic metasomatism (Dautria et al., 1992; Ionov et al., 1993; Rudnick et al., 1993; Yaxley et al., 1998). This type of metasomatic melt/fluid is meant to be rich in volatile (H_2O–CO_2) as proposed by Sun and Kerrich (1995). However, for the Ray-Pic xenoliths, there is no significant enhancement effect on hydrogen incorporation into NAMs, related to the percolation of such melt/fluid. Thus, either the volatile inventory of this melt/fluid does not include water, or the coexistence of CO_2 and H_2O has drastically lowered the fugacity of water in this system (Baptiste et al., 2015; Shirey et al., 2013). However in both cases, the low fH_2O should preclude the crystallisation of H_2O–bearing pargasite and thus lead to consider that amphiboles were part of a previous metasomatic event, which is not our preferred interpretation.

It could be argued that the water contents in opx shows some degree of correlation with metasomatic indexes (Fig. 13b, e). However, water incorporation into opx seems linked to the Ca (Fig. 14) and Al contents (not shown). This was also observed by previous works (e.g., Bell et al.,

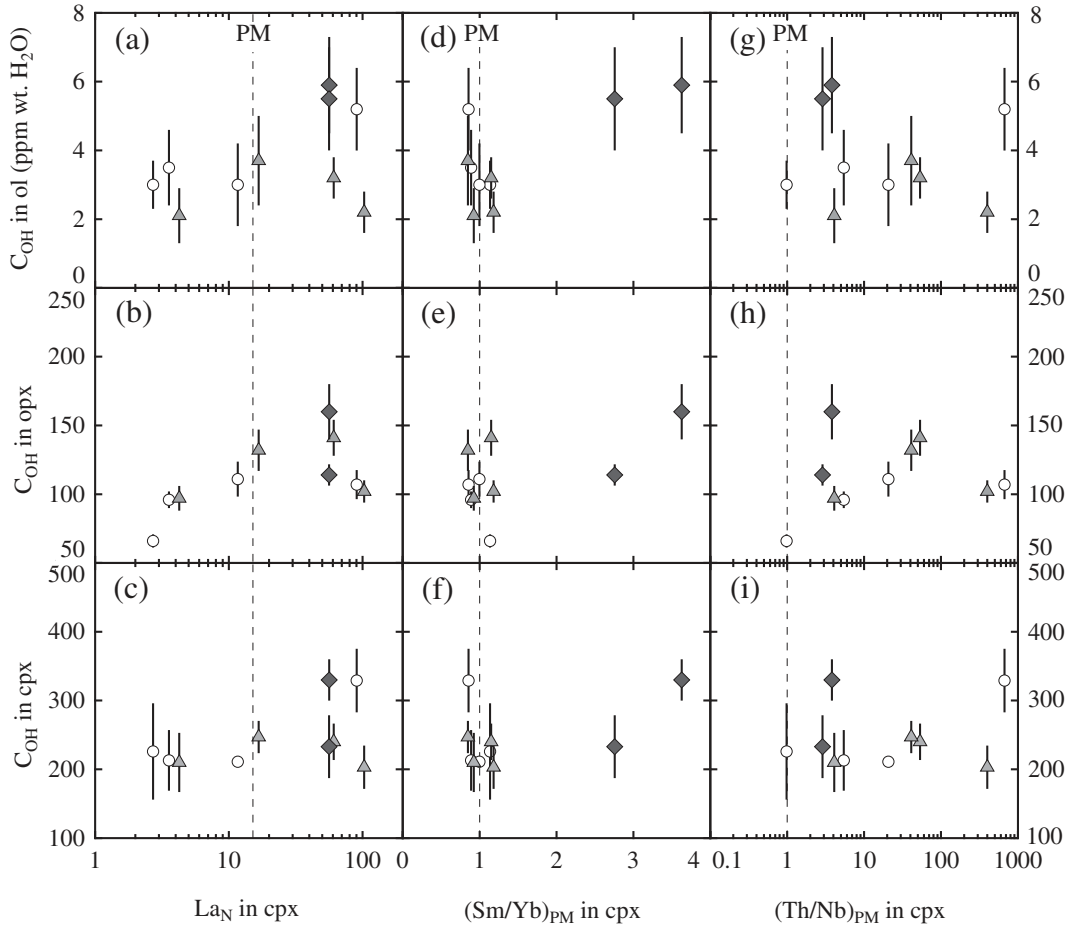

Fig. 13. Water contents in minerals (ol, opx and cpx) as a function of trace element indexes of metasomatism. Water contents are given in ppm wt. H_2O using the calibration of Paterson (1982). (a), (b) and (c) water content in minerals as a function of La_N in cpx. (d), (e) and (f) water contents in minerals as a function of $(Sm/Yb)_{PM}$ in cpx. (g), (h) and (i) are water contents in minerals as a function of $(Th/Nb)_{PM}$ in cpx. PM and N: normalised to Primitive mantle and CI chondrite values, respectively, from McDonough and Sun (1995); symbols are as in Fig. 3; dashed lines denote primitive mantle values; error bar on the average values of water content per sample is 1SD.

2004; Ingrin and Skogby, 2000; Jurewicz and Watson, 1988; Peslier et al., 2002). Ca partitioning between cpx and opx is highly temperature dependent (e.g., Brey and Khöler, 1990). As discussed above (see Section 5.1; Fig. 4b) REE fractionations and enrichments are here linked to the equilibrium temperature (see also Zangana et al., 1997) (Fig. 14) and thus are related to the sample position relative to the metasomatic melt source. Therefore the apparent correlation between water content in opx and REE fractionation, reflect rather a temperature effect (i.e., which could be related to metasomatism, see Section 5.1). It yields to the incorporation of a higher amount of Ca, producing then a higher abundance of impurities at atomic scale and associated hydrogen-bearing point defects in opx.

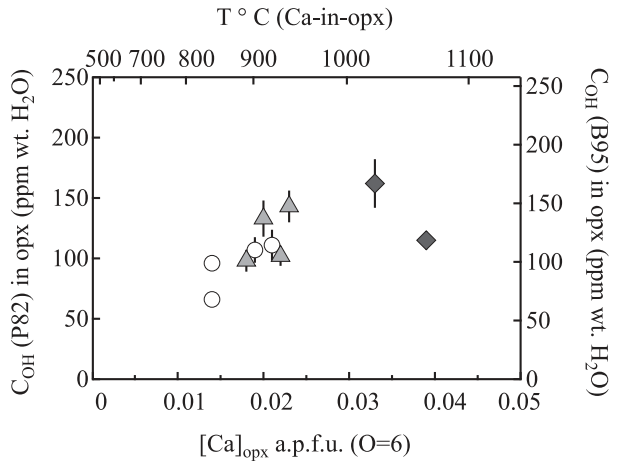

Fig. 14. Water contents in opx (in ppm wt. H_2O, based on calibration of Paterson, 1982 (P82); and Bell et al., 1995 (B95)) as a function of [Ca] a.p.f.u (atom per formula unit calculated for 6 bonding oxygens) for Ray Pic spinel-peridotite xenoliths. Corresponding temperature (in °C) was calculated using Brey and Köhler (1990) '$T°_{Ca\text{-}in\text{-}opx}$' geothermometer. Error bar on the average values of water content per sample is 1SD.

As shown here, the relationships between the H_2O content of NAMs and metasomatism is not straightforward. Indeed, our observations suggest that H partitioning between melt/fluid and NAMs is dependent of the nature of the melt/fluid and in particular of its H_2O and/or volatile fugacity. In one hand we observe H_2O enrichment in NAMs when these latters interact with relatively large melt fraction (melt/rock ratio ≥ 1%) and thus when the fH_2O is relatively low, suggesting that H behaves as a mid-REE. On the other hand, the crystallisation of LREE-depleted amphiboles would suggest that H_2O behave in the melts as an highly incompatible elements; its chromatographic front is further away from the source than the LREE chromatographic front thus $D(H_2O) < D(LREE)$, as suggested by Demouchy et al., 2015. Then, when peridotites interact with such small volume melt or fluid, which are volatiles-rich and have a high fH_2O leading to the crystallisation of amphibole, then NAMs are not enriched in H_2O. Is it due to the crystallisation of amphibole, which then sequesters all the water available? Or is it due to a drastic change of partitioning between NAMs and volatile-rich fluids?

These complexities are probably due, at least in part, to the dual behaviour of H as major vs. trace elements and to its related different types of incorporation into the mineral structure.

6. Conclusion

In this study, water content in NAMs can be broadly explained by depletion during partial melting event(s) using relatively straightforward melting models. The metasomatism, expressed by LREE and LILE enrichment without concomitant HFSE enrichment, thus involving small volume melt enriched in volatiles (also coined as carbonatitic metasomatism), has no obvious effect on the water content of NAMs. Hydrogen in NAMs is not correlated with canonical metasomatism indicator such as La and Ce abundances of La/Sm La/Yb ratio, and hydrogen seems to rather behave similarly to a MREE during melting and metasomatism. However some of our data suggest that water contents in NAMs were then possibly modified afterward by melt–rock reactions at relatively high melt/rock ratio (i.e., ≥1%). Our results for the Ray Pic xenoliths call for further studies, specially integrating data on trace elements and water content of NAMs necessary to truly assess the behaviour of water during melting and metasomatism.

Hydrous metasomatism (i.e., leading to the crystallisation of OH-bearing amphibole) has no effect on water content of NAMs. Thus the occurrence of amphibole does not warrant the water-saturation of coexisting NAMs. Therefore, its presence should not be used as a justification for the application of weak and wet flow law for olivine.

Acknowledgements

CNRS supported this study through INSU 2011, 2012 & 2013 programmes to S. Demouchy and O. Alard. The University of Montpellier supported this study through a Ph.D fellowship “Bourse Président” to C. Denis. We thank F. Parat for informal review and H. Behrens for KFT measurements. We also thank C. Nevado and D. Delmas for providing impeccable thin sections. One anonymous reviewer and Prof. Xia are thanked for detailed reviews, which have improved the quality of the manuscript. Electron microprobe analyses were performed at ‘Microsconde SUD’ and carried out with the help of B. Boyer and C. Merlet. FTIR analyses were carried out with the assistance of D. Maurin at the Laboratoire Charles Coulomb, University of Montpellier, France.

References

Agrinier, P., Mével, C., Bosch, D., Javoy, M., 1993. Metasomatic hydrous fluids in amphibole peridotites from Zabargad Island (Red Sea). Earth and Planetary Science Letters 120, 187–205. http://dx.doi.org/10.1016/0012-821X(93)90239-6.

Alard, O., Dautria, J.-M., Bodinier, J.-L., 1996. Nature du manteau supérieur et processus métasomatiques de part et d'autre du Sillon Houiller (Massif Central). Comptes rendus de l'Académie des sciences. Série 2. Sciences de la terre et des planètes 323, 763–770.

Alard, O., Lorand, J.-P., Reisberg, L., Bodinier, J.-L., Dautria, J.-M., O'Reilly, S.Y., 2011. Volatile-rich metasomatism in Montferrier xenoliths (Southern France): implications for the abundances of chalcophile and highly siderophile elements in the subcontinental mantle. Journal of Petrology 52, 2009–2045. http://dx.doi.org/10.1093/petrology/egr038.

Ardia, P., Hirschmann, M.M., Withers, A.C., Tenner, T.J., 2012. H_2O storage capacity of olivine at 5–8GPa and consequences for dehydration partial melting of the upper mantle. Earth and Planetary Science Letters 345–348, 104–116. http://dx.doi.org/10.1016/j.epsl.2012.05.038.

Aubaud, C., Hauri, E.H., Hirschmann, M.M., 2004. Hydrogen partition coefficients between nominally anhydrous minerals and basaltic melts. Geophysical Research Letters 31. http://dx.doi.org/10.1029/2004GL021341.

Aubaud, C., Hirschmann, M.M., Withers, A.C., Hervig, R.L., 2008. Hydrogen partitioning between melt, clinopyroxene, and garnet at 3 GPa in a hydrous MORB with 6 wt.% H2O. Contributions to Mineralogy and Petrology 156, 607–625. http://dx.doi.org/10.1007/s00410-008-0304-2.

Bai, Q., Kohlstedt, D.L., 1993. Effects of chemical environment on the solubility and incorporation mechanism for hydrogen in olivine. Physics and Chemistry of Minerals 19, 460–471. http://dx.doi.org/10.1007/BF00203186.

Baptiste, V., Tommasi, A., Vauchez, A., Demouchy, S., Rudnick, R.L., 2015. Deformation, hydration, and anisotropy of the lithospheric mantle in an active rift: constraints from mantle xenoliths from the North Tanzanian Divergence of the East African Rift. Tectonophysics 639, 34–55. http://dx.doi.org/10.1016/j.tecto.2014.11.011.

Bedini, R.M., Bodinier, J.-L., Dautria, J.-M., Morten, L., 1997. Evolution of LILE-enriched small melt fractions in the lithospheric mantle: a case study from the East African Rift. Earth and Planetary Science Letters 153, 67–83. http://dx.doi.org/10.1016/S0012-821X(97)00167-2.

Behrens, H., Romano, C., Nowak, M., Holtz, F., Dingwell, D.B., 1996. Near-infrared spectroscopic determination of water species in glasses of the system MAlSi 3O 8 (M = Li, Na, K): an interlaboratory study. Chemical Geology 128, 41–63.

Bell, D.R., Rossman, G.R., 1992. Water in Earth's mantle: the role of nominally anhydrous minerals. Science 255, 1391–1397. http://dx.doi.org/10.1126/science.255.5050.1391.

Bell, D.R., Ihinger, P.D., Rossman, G.R., 1995. Quantitative and analysis of trace OH in garnet and pyroxenes. American Mineralogist 80, 465–474.

Bell, D.R., Rossman, G.R., Maldener, J., Endisch, D., Rauch, F., 2003. Hydroxide in olivine: a quantitative determination of the absolute amount and calibration of the IR spectrum. Journal of Geophysical Research 108. http://dx.doi.org/10.1029/2001JB000679.

Bell, D.R., Rossman, G.R., Moore, R.O., 2004. Abundance and partitioning of OH in a high-pressure magmatic system: megacrysts from the Monastery Kimberlite, South Africa. Journal of Petrology 45, 1539–1564. http://dx.doi.org/10.1093/petrology/egh015.

Beran, A., Putnis, A., 1983. A model of the OH positions in olivine, derived from infrared-spectroscopic investigations. Physics and Chemistry of Minerals 9, 57–60. http://dx.doi.org/10.1007/BF00308148.

Bizimis, M., Peslier, A.H., 2015. Water in Hawaiian garnet pyroxenites: implications for water heterogeneity in the mantle. Chemical Geology 397, 61–75.

Bodinier, J.L., Vasseur, G., Vernières, J., Dupuy, C., Fabries, J., 1990. Mechanisms of mantle metasomatism: geochemical evidence from the Lherz orogenic peridotite. Journal of Petrology 31, 597–628. http://dx.doi.org/10.1093/petrology/31.3.597.

Bodinier, J.-L., Menzies, M.A., Thirlwall, M.F., 1991. Continental to oceanic mantle transition—REE and Sr–Nd isotopic geochemistry of the Lanzo Lherzolite Massif. Journal of Petrology 191–210 http://dx.doi.org/10.1093/petrology/Special_Volume.2.191 (Special Volume).

Bodinier, J.-L., Menzies, M.A., Shimizu, N., Frey, F.A., McPherson, E., 2004. Silicate, hydrous and carbonate metasomatism at Lherz, France: contemporaneous derivatives of silicate melt–harzburgite reaction. Journal of Petrology 45, 299–320. http://dx.doi.org/10.1093/petrology/egg107.

Bolfan-Casanova, N., 2005. Water in the Earth's mantle. Mineralogical Magazine 69, 229–258. http://dx.doi.org/10.1180/0026461056930248.

Bonadiman, C., Hao, Y., Coltorti, M., Dallai, L., Faccini, B., Huang, Y., Xia, Q., 2009. Water contents of pyroxenes in intraplate lithospheric mantle. European Journal of Mineralogy 21, 637–647. http://dx.doi.org/10.1127/0935-1221/2009/0021-1935.

Bonadiman, C., Nazzareni, S., Coltorti, M., Comodi, P., Giuli, G., Faccini, B., 2014. Crystal chemistry of amphiboles: implications for oxygen fugacity and water activity in lithospheric mantle beneath Victoria Land, Antarctica. Contributions to Mineralogy and Petrology 167, 1–17. http://dx.doi.org/10.1007/s00410-014-0984-8.

Brey, G.P., Köhler, T., 1990. Geothermobarometry in Four-phase Lherzolites II. New thermobarometers, and practical assessment of existing thermobarometers. Journal of Petrology 31, 1353–1378. http://dx.doi.org/10.1093/petrology/31.6.1353.

Coltorti, M., Bonadiman, C., Hinton, R.W., Siena, F., Upton, B.G.J., 1999. Carbonatite metasomatism of the oceanic upper mantle: evidence from clinopyroxenes and glasses in ultramafic xenoliths of Grande Comore, Indian Ocean. Journal of Petrology 40, 133–165. http://dx.doi.org/10.1093/petroj/40.1.133.

Coltorti, M., Beccaluva, L., Bonadiman, C., Salvini, L., Siena, F., 2000. Glasses in mantle xenoliths as geochemical indicators of metasomatic agents. Earth and Planetary Science Letters 183, 303–320. http://dx.doi.org/10.1016/S0012-821X(00)00274-0.

Coltorti, M., Beccaluva, L., Bonadiman, C., Faccini, B., Ntaflos, T., Siena, F., 2004. Amphibole genesis via metasomatic reaction with clinopyroxene in mantle xenoliths from Victoria Land, Antarctica. Lithos 75, 115–139. http://dx.doi.org/10.1016/j.lithos.2003.12.021.

Dasgupta, R., Hirschmann, M.M., 2006. Melting in the Earth's deep upper mantle caused by carbon dioxide. Nature 440, 659–662. http://dx.doi.org/10.1038/nature04612.

Dautria, J.M., Dupuy, C., Takherist, D., Dostal, J., 1992. Carbonate metasomatism in the lithospheric mantle: peridotitic xenoliths from a melilititic district of the Sahara basin. Contributions to Mineralogy and Petrology 111, 37–52. http://dx.doi.org/10.1007/BF00296576.

Demouchy, S., Mackwell, S., 2006. Mechanisms of hydrogen incorporation and diffusion in iron-bearing olivine. Physics and Chemistry of Minerals 33, 347–355. http://dx.doi.org/10.1007/s00269-006-0081-2.

Demouchy, S., Jacobsen, S.D., Gaillard, F., Stern, C.R., 2006. Rapid magma ascent recorded by water diffusion profiles in mantle olivine. Geology 34, 429. http://dx.doi.org/10.1130/G22386.1.

Demouchy, S., Ishikawa, A., Tommasi, A., Alard, O., Keshav, S., 2015. Characterization of hydration in the mantle lithosphere: peridotite xenoliths from the Ontong Java Plateau as an example. Lithos 212–215, 189–201. http://dx.doi.org/10.1016/j.lithos.2014.11.005.

Denis, C.M.M., Demouchy, S., Shaw, C.S.J., 2013. Evidence of dehydration in peridotites from Eifel Volcanic Field and estimates of the rate of magma ascent. Journal of Volcanology and Geothermal Research 258, 85–99. http://dx.doi.org/10.1016/j.jvolgeores.2013.04.010.

Dixon, J.E., Leist, L., Langmuir, C., Schilling, J.-G., 2002. Recycled dehydrated lithosphere observed in plume-influenced mid-ocean-ridge basalt. Nature 420, 385–389. http://dx.doi.org/10.1038/nature01215.

Doucet, L.S., Peslier, A.H., Ionov, D.A., Brandon, A.D., Golovin, A.V., Goncharov, A.G., Ashchepkov, I.V., 2014. High water contents in the Siberian cratonic mantle linked to metasomatism: an FTIR study of Udachnaya peridotite xenoliths. Geochimica et Cosmochimica Acta 137, 159–187. http://dx.doi.org/10.1016/j.gca.2014.04.011.

Downes, H., Dupuy, C., 1987. Textural, isotopic and REE variations in spinel peridotite xenoliths, Massif Central, France. Earth and Planetary Science Letters 82, 121–135. http://dx.doi.org/10.1016/0012-821X(87)90112-9.

Downes, H., Reichow, M.K., Mason, P.R.D., Beard, A.D., Thirlwall, M.F., 2003. Mantle domains in the lithosphere beneath the French Massif Central: trace element and isotopic evidence from mantle clinopyroxenes. Chemical Geology 200, 71–87. http://dx.doi.org/10.1016/S0009-2541(03)00126-8.

Falus, G., Tommasi, A., Ingrin, J., Szabó, C., 2008. Deformation and seismic anisotropy of the lithospheric mantle in the southeastern Carpathians inferred from the study of mantle xenoliths. Earth and Planetary Science Letters 272, 50–64. http://dx.doi.org/10.1016/j.epsl.2008.04.035.

Férot, A., Bolfan-Casanova, N., 2012. Water storage capacity in olivine and pyroxene to 14GPa: implications for the water content of the Earth's upper mantle and nature of seismic discontinuities. Earth and Planetary Science Letters 349–350, 218–230. http://dx.doi.org/10.1016/j.epsl.2012.06.022.

Frey, F.A., Green, D.H., 1974. The mineralogy, geochemistry and origin of lherzolite inclusions in Victorian basanites. Geochimica et Cosmochimica Acta 38, 1023–1059. http://dx.doi.org/10.1016/0016-7037(74)90003-9.

Frezzotti, M.L., Ferrando, S., Peccerillo, A., Petrelli, M., Tecce, F., Perucchi, A., 2010. Chlorine-rich metasomatic H2O–CO2 fluids in amphibole-bearing peridotites from Injibara (Lake Tana region, Ethiopian plateau): nature and evolution of volatiles in the mantle of a region of continental flood basalts. Geochimica et Cosmochimica Acta 74, 3023–3039. http://dx.doi.org/10.1016/j.gca.2010.02.007.

Granet, M., Wilson, M., Achauer, U., 1995. Imaging a mantle plume beneath the French Massif Central. Earth and Planetary Science Letters 136, 281–296. http://dx.doi.org/10.1016/0012-821X(95)00174-B.

Grant, K., Ingrin, J., Lorand, J.P., Dumas, P., 2007a. Water partitioning between mantle minerals from peridotite xenoliths. Contributions to Mineralogy and Petrology 154, 15–34. http://dx.doi.org/10.1007/s00410-006-0177-1.

Grant, K.J., Kohn, S.C., Brooker, R.A., 2007b. The partitioning of water between olivine, orthopyroxene and melt synthesised in the system albite–forsterite–H2O. Earth and Planetary Science Letters 260, 227–241. http://dx.doi.org/10.1016/j.epsl.2007.05.032.

Green, D.H., Hibberson, W.O., Kovács, I., Rosenthal, A., 2010. Water and its influence on the lithosphere–asthenosphere boundary. Nature 467, 448–451. http://dx.doi.org/10.1038/nature09369.

Grégoire, M., Moine, B.N., O'reilly, S.Y., Cottin, J.Y., Giret, A., 2000. Trace element residence and partitioning in mantle xenoliths metasomatized by highly alkaline, silicate- and carbonate-rich melts (Kerguelen Islands, Indian Ocean). Journal of Petrology 41, 477–509. http://dx.doi.org/10.1093/petrology/41.4.477.

Griffin, W.L., Powell, W., Pearson, N.J., O'Reilly, S.Y., 2008. GLITTER: data reduction software for laser ablation ICP-MS. Laser Ablation-ICP-MS in the Earth Sciences vol. 40. Mineralogical Association of Canada Short Course Series, pp. 204–207 (Appendix 2).

Hao, Y., Xia, Q., Li, Q., Chen, H., Feng, M., 2014a. Partial melting control of water contents in the Cenozoic lithospheric mantle of the Cathaysia block of South China. Chemical Geology 380, 7–19.

Hao, Y., Xia, Q., Li, Q., Chen, H., Feng, M., 2014b. Partial melting control of water contents in the Cenozoic lithospheric mantle of the Cathaysia block of South China. Chemical Geology 380, 7–19. http://dx.doi.org/10.1016/j.chemgeo.2014.04.017.

Hart, S.R., Dunn, T., 1993. Experimental cpx/melt partitioning of 24 trace elements. Contributions to Mineralogy and Petrology 113, 1–8. http://dx.doi.org/10.1007/BF00320827.

Hauri, E.H., Gaetani, G.A., Green, T.H., 2006. Partitioning of water during melting of the Earth's upper mantle at H2O-undersaturated conditions. Earth and Planetary Science Letters 248, 715–734. http://dx.doi.org/10.1016/j.epsl.2006.06.014.

Hawthorne, F.C., Oberti, R., Zanetti, A., Czamanske, G.K., 1998. The role of Ti in hydrogen-deficient amphiboles; sodic-calcic and sodic amphiboles from Coyote Peak, California. The Canadian Mineralogist 36, 1253–1265.

Herrmann, W., Berry, R.F., 2002. MINSQ — a least squares spreadsheet method for calculating mineral proportions from whole rock major element analyses. Geochemistry: Exploration, Environment, Analysis 2, 361–368. http://dx.doi.org/10.1144/1467-787302-010.

Ingrin, J., Skogby, H., 2000. Hydrogen in nominally anhydrous upper-mantle minerals concentration levels and implications. European Journal of Mineralogy 12, 543–570. http://dx.doi.org/10.1127/0935-1221/2000/0012-0543.

Ionov, D.A., Dupuy, C., O'Reilly, S.Y., Kopylova, M.G., Genshaft, Y.S., 1993. Carbonated peridotite xenoliths from Spitsbergen: implications for trace element signature of mantle carbonate metasomatism. Earth and Planetary Science Letters 119, 283–297. http://dx.doi.org/10.1016/0012-821X(93)90139-Z.

Jochum, K.P., Nohl, U., Herwig, K., Lammel, E., Stoll, B., Hofmann, A.W., 2005. GeoReM: a new geochemical database for reference materials and isotopic standards. Geostandards and Geoanalytical Research 29, 333–338. http://dx.doi.org/10.1111/j.1751-908X.2005.tb00904.x.

Jurewicz, A.J.G., Watson, E.B., 1988. Cations in olivine, Part 1: calcium partitioning and calcium–magnesium distribution between olivines and coexisting melts, with petrologic applications. Contributions to Mineralogy and Petrology 99, 176–185. http://dx.doi.org/10.1007/BF00371459.

King, P.L., Hervig, R.L., Holloway, J.R., Vennemann, T.W., Righter, K., 1999. Oxy-substitution and dehydrogenation in mantle-derived amphibole megacrysts. Geochimica et Cosmochimica Acta 63, 3635–3651. http://dx.doi.org/10.1016/S0016-7037(99)00162-3.

Kohlstedt, D.L., Keppler, H., Rubie, D.C., 1996. Solubility of water in the α, β and γ phases of (Mg, Fe)2SiO4. Contributions to Mineralogy and Petrology 123, 345–357. http://dx.doi.org/10.1007/s004100050161.

Kourim, F., Bodinier, J.-L., Alard, O., Bendaoud, A., Vauchez, A., Dautria, J.-M., 2014. Nature and evolution of the lithospheric mantle beneath the Hoggar Swell (Algeria): a record from mantle xenoliths. Journal of Petrology 55, 2249–2280. http://dx.doi.org/10.1093/petrology/egu056.

Kovács, I., Green, D.H., Rosenthal, A., Hermann, J., O'neill, H.S.C., Hibberson, W.O., Udvardi, B., 2012. An experimental study of water in nominally anhydrous minerals in the upper mantle near the water-saturated solidus. Journal of Petrology 53, 2067–2093. http://dx.doi.org/10.1093/petrology/egs044.

Kovács, I., Hermann, J., O'Neill, H.S.C., Gerald, J.F., Sambridge, M., Horváth, G., 2008. Quantitative absorbance spectroscopy with unpolarized light: Part II. Experimental evaluation and development of a protocol for quantitative analysis of mineral IR spectra. American Mineralogist 93, 765–778. http://dx.doi.org/10.2138/am.2008.2656.

Le Roux, V., Bodinier, J.-L., Tommasi, A., Alard, O., Dautria, J.-M., Vauchez, A., Riches, A.J.V., 2007. The Lherz spinel lherzolite: refertilized rather than pristine mantle. Earth and Planetary Science Letters 259, 599–612. http://dx.doi.org/10.1016/j.epsl.2007.05.026.

Lenoir, X., Garrido, C.J., Bodinier, J.-L., Dautria, J.-M., 2000. Contrasting lithospheric mantle domains beneath the Massif Central (France) revealed by geochemistry of peridotite xenoliths. Earth and Planetary Science Letters 181, 359–375. http://dx.doi.org/10.1016/S0012-821X(00)00216-8.

Li, Z.X.A., Lee, C.T.A., Peslier, A., Lenardic, A., Mackwell, S.J., 2008. Water contents in mantle xenoliths from the Colorado Plateau and vicinity: implications for the mantle rheology and hydration-induced thining of continental lithosphere. Journal of Geophysical Research 113. http://dx.doi.org/10.1029/2007JB005540.

Li, P., Xia, Q.-K., Deloule, E., Chen, H., Gu, X.-Y., Feng, M., 2014. Temporal variation of H2O content in the lithospheric mantle beneath the eastern North China Craton: implications for the destruction of cratons. Gondwana Research http://dx.doi.org/10.1016/j.gr.2014.03.012.

Libowitzky, E., Rossman, G.R., 1997. An IR absorption calibration for water in minerals. American Mineralogist 82, 1111–1115.

Litasov, K.D., Foley, S.F., Litasov, Y.D., 2000. Magmatic modification and metasomatism of the subcontinental mantle beneath the Vitim volcanic field (East Siberia): evidence from trace element data on pyroxenite and peridotite xenoliths from Miocene picrobasalt. Lithos 54, 83–114. http://dx.doi.org/10.1016/S0024-4937(00)00016-5.

Lorand, J.-P., Alard, O., 2001. Platinum-group element abundances in the upper mantle: new constraints from in situ and whole-rock analyses of Massif Central xenoliths (France). Geochimica et Cosmochimica Acta 65, 2789–2806. http://dx.doi.org/10.1016/S0016-7037(01)00627-5.

Mackwell, S.J., Kohlstedt, D.L., 1990. Diffusion of hydrogen in olivine: implications for water in the mantle. Journal of Geophysical Research 95, 5079. http://dx.doi.org/10.1029/JB095iB04p05079.

Maury, R.C., Varet, J., 1980. Le volcanisme tertiaire et quaternaire en France. 107 Éditions du BRGMpp. 137–159.

McDonough, W.F., Sun, S.-s., 1995. The composition of the Earth. Chemical Geology 120, 223–253. http://dx.doi.org/10.1016/0009-2541(94)00140-4.

McInnes, B.I.A., Gregoire, M., Binns, R.A., Herzig, P.M., Hannington, M.D., 2001. Hydrous metasomatism of oceanic sub-arc mantle, Lihir, Papua New Guinea: petrology and geochemistry of fluid-metasomatised mantle wedge xenoliths. Earth and Planetary Science Letters 188, 169–183. http://dx.doi.org/10.1016/S0012-821X(01)00306-5.

Menzies, M.A., Hawkesworth, C., 1987. Upper mantle processes and composition. Mantle Xenoliths. John Wiley & Sons, pp. 725–738.

Mercier, J.-C.C., Nicolas, A., 1975. Textures and fabrics of upper-mantle peridotites as illustrated by xenoliths from basalts. Journal of Petrology 16, 454–487. http://dx.doi.org/10.1093/petrology/16.2.454.

Mierdel, K., Keppler, H., Smyth, J.R., Langenhorst, F., 2007. Water solubility in aluminous orthopyroxene and the origin of Earth's asthenosphere. Science 315, 364–368. http://dx.doi.org/10.1126/science.1135422.

Miller, G.H., Rossman, G.R., Harlow, G.E., 1987. The natural occurrence of hydroxide in olivine. Physics and Chemistry of Minerals 14, 461–472. http://dx.doi.org/10.1007/BF00628824.

Minarik, W.G., Watson, E.B., 1995. Interconnectivity of carbonate melt at low melt fraction. Earth and Planetary Science Letters 133, 423–437. http://dx.doi.org/10.1016/0012-821X(95)00085-Q.

Moine, B.N., Cottin, J.-Y., Sheppard, S.M.F., Grégoire, M., O'reilly, S.Y., Giret, A., 2000. Incompatible trace element and isotopic (D/H) characteristics of amphibole- and phlogopite-bearing ultramafic to mafic xenoliths from Kerguelen Islands (TAAF, South Indian Ocean). European Journal of Mineralogy 12, 761–777. http://dx.doi.org/10.1127/0935-1221/2000/0012-0761.

Mosenfelder, J.L., Rossman, G.R., 2013a. Analysis of hydrogen and fluorine in pyroxenes: I. Orthopyroxene. American Mineralogist 98, 1026–1041.

Mosenfelder, J.L., Rossman, G.R., 2013b. Analysis of hydrogen and fluorine in pyroxenes: II. Clinopyroxene. American Mineralogist 98, 1042–1054.

Navon, O., Stolper, E., 1987. Geochemical consequences of melt percolation: the upper mantle as a chromatographic column. The Journal of Geology 95, 285–307.

Norman, M.D., 1998. Melting and metasomatism in the continental lithosphere: laser ablation ICPMS analysis of minerals in spinel lherzolites from eastern Australia. Contributions to Mineralogy and Petrology 130, 240–255. http://dx.doi.org/10.1007/s004100050363.

Norman, M.D., Pearson, N.J., Sharma, A., Griffin, W.L., 1996. Quantitative analysis of trace elements in geological materials by laser ablation icpms: instrumental operating conditions and calibration values of nist glasses. Geostandards Newsletter 20, 247–261. http://dx.doi.org/10.1111/j.1751-908X.1996.tb00186.x.

Novella, D., Frost, D.J., Hauri, E.H., Bureau, H., Raepsaet, C., Roberge, M., 2014. The distribution of H2O between silicate melt and nominally anhydrous peridotite and the onset of hydrous melting in the deep upper mantle. Earth and Planetary Science Letters 400, 1–13. http://dx.doi.org/10.1016/j.epsl.2014.05.006.

O'Leary, J.A., Gaetani, G.A., Hauri, E.H., 2010. The effect of tetrahedral Al3 + on the partitioning of water between clinopyroxene and silicate melt. Earth and Planetary Science Letters 297, 111–120. http://dx.doi.org/10.1016/j.epsl.2010.06.011.
O'Reilly, S.Y., Griffin, W.L., 2013. Mantle metasomatism. Metasomatism and the Chemical Transformation of Rock, Lecture Notes in Earth System Sciences. Springer Berlin Heidelberg, pp. 471–533.
O'Reilly, S.Y., Griffin, W.L., Ryan, C.G., 1991. Residence of trace elements in metasomatized spinel lherzolite xenoliths: a proton-microprobe study. Contributions to Mineralogy and Petrology 109, 98–113. http://dx.doi.org/10.1007/BF00687203.
Oberti, R., Ventura, G.D., Cámara, F., 2007. New amphibole compositions: natural and synthetic. Reviews in Mineralogy and Geochemistry 67, 89–124. http://dx.doi.org/10.2138/rmg.2007.67.3.
Paterson, M.S., 1982. The determination of hydroxyl by infrared absorption in quartz, silicate glasses and similar materials. Bulletin de Mineralogie 105, 20–29.
Pearce, N.J.G., Perkins, W.T., Westgate, J.A., Gorton, M.P., Jackson, S.E., Neal, C.R., Chenery, S.P., 1997. A compilation of new and published major and trace element data for NIST SRM 610 and NIST SRM 612 glass reference materials. Geostandards and Geoanalytical Research 21, 115–144. http://dx.doi.org/10.1111/j.1751-908X.1997.tb00538.x.
Peslier, A.H., 2010. A review of water contents of nominally anhydrous natural minerals in the mantles of Earth, Mars and the Moon. Journal of Volcanology and Geothermal Research 197, 239–258. http://dx.doi.org/10.1016/j.jvolgeores.2009.10.006.
Peslier, A.H., Bizimis, M., 2015. Water in Hawaiian peridotite minerals: A case for a dry metasomatized oceanic mantle lithosphere. Geochemistry, Geophysysics, Geosystems 16, 1211–1232. http://dx.doi.org/10.1002/2015GC005780.
Peslier, A.H., Luhr, J.F., 2006. Hydrogen loss from olivines in mantle xenoliths from Simcoe (USA) and Mexico: mafic alkalic magma ascent rates and water budget of the sub-continental lithosphere. Earth and Planetary Science Letters 242, 302–319. http://dx.doi.org/10.1016/j.epsl.2005.12.019.
Peslier, A.H., Luhr, J.F., Post, J., 2002. Low water contents in pyroxenes from spinel-peridotites of the oxidized, sub-arc mantle wedge. Earth and Planetary Science Letters 201, 69–86. http://dx.doi.org/10.1016/S0012-821X(02)00663-5.
Peslier, A.H., Woodland, A.B., Bell, D.R., Lazarov, M., Lapen, T.J., 2012. Metasomatic control of water contents in the Kaapvaal cratonic mantle. Geochimica et Cosmochimica Acta 97, 213–246. http://dx.doi.org/10.1016/j.gca.2012.08.028.
Peslier, A.H., Bizimis, M., Matney, M., 2015. Water disequilibrium in olivines from Hawaiian peridotites: recent metasomatism, H diffusion and magma ascent rates. Geochimica et Cosmochimica Acta 154, 98–117. http://dx.doi.org/10.1016/j.gca.2015.01.030.
Rauch, M., 2000. Der Einbau von Wasser in Pyroxene. Bayreuth Universität, Bayreuth, p. 141.
Rudnick, R.L., McDonough, W.F., Chappell, B.W., 1993. Carbonatite metasomatism in the northern Tanzanian mantle: petrographic and geochemical characteristics. Earth and Planetary Science Letters 114, 463–475. http://dx.doi.org/10.1016/0012-821X(93)90076-L.
Schmädicke, E., Gose, J., Witt-Eickschen, G., Bratz, H., 2013. Olivine from spinel peridotite xenoliths: hydroxyl incorporation and mineral composition. American Mineralogist 98, 1870–1880. http://dx.doi.org/10.2138/am.2013.4440.
Shirey, S.B., Cartigny, P., Frost, D.J., Keshav, S., Nestola, F., Nimis, P., Pearson, D.G., Sobolev, N.V., Walter, M.J., 2013. Diamonds and the geology of mantle carbon. Reviews in Mineralogy and Geochemistry 75, 355–421. http://dx.doi.org/10.2138/rmg.2013.75.12.
Skogby, H., 2006. Water in natural mantle minerals I: pyroxenes. Reviews in Mineralogy and Geochemistry 62, 155–167. http://dx.doi.org/10.2138/rmg.2006.62.7.
Soustelle, V., Tommasi, A., Demouchy, S., Franz, L., 2013. Melt–rock interactions, deformation, hydration and seismic properties in the sub-arc lithospheric mantle inferred from xenoliths from seamounts near Lihir, Papua New Guinea. Tectonophysics 608, 330–345. http://dx.doi.org/10.1016/j.tecto.2013.09.024.
Sun, M., Kerrich, R., 1995. Rare earth element and high field strength element characteristics of whole rocks and mineral separates of ultramafic nodules in Cenozoic volcanic vents of southeastern British Columbia, Canada. Geochimica et Cosmochimica Acta 59, 4863–4879. http://dx.doi.org/10.1016/0016-7037(95)00341-X.
Tenner, T.J., Hirschmann, M.M., Withers, A.C., Hervig, R.L., 2009. Hydrogen partitioning between nominally anhydrous upper mantle minerals and melt between 3 and 5 GPa and applications to hydrous peridotite partial melting. Chemical Geology 262, 42–56. http://dx.doi.org/10.1016/j.chemgeo.2008.12.006.
Thoraval, C., Demouchy, S., 2014. Numerical models of ionic diffusion in one and three dimensions: application to dehydration of mantle olivine. Physics and Chemistry of Minerals 41, 709–723. http://dx.doi.org/10.1007/s00269-014-0685-x.
Tiepolo, M., Oberti, R., Zanetti, A., Vannucci, R., Foley, S.F., 2007. Trace-element partitioning between amphibole and silicate melt. Reviews in Mineralogy and Geochemistry 67, 417–452. http://dx.doi.org/10.2138/rmg.2007.67.11.
Touron, S., Renac, C., O'Reilly, S.Y., Cottin, J.-Y., Griffin, W.L., 2008. Characterization of the metasomatic agent in mantle xenoliths from Deves, Massif Central (France) using coupled in situ trace-element and O, Sr and Nd isotopic compositions. Geological Society, London, Special Publications 293, 177–196. http://dx.doi.org/10.1144/SP293.9.
Vannucci, R., Piccardo, G.B., Rivalenti, G., Zanetti, A., Rampone, E., Ottolini, L., Oberti, R., Mazzucchelli, M., Bottazzi, P., 1995. Origin of LREE-depleted amphiboles in the subcontinental mantle. Geochimica et Cosmochimica Acta 59, 1763–1771. http://dx.doi.org/10.1016/0016-7037(95)00080-J.
Vasseur, G., Vernières, J., Bodiner, J.-L., 1991. Modelling of trace element transfer between mantle melt and heterogranular peridotite matrix. Journal of Petrology 41–54 http://dx.doi.org/10.1093/petrology/Special_Volume.2.41 (Special Volume).
Vernières, J., Godard, M., Bodinier, J.-L., 1997. A plate model for the simulation of trace element fractionation during partial melting and magma transport in the Earth's upper mantle. Journal of Geophysical Research 102, 24771–24784. http://dx.doi.org/10.1029/97JB01946.
Watson, B.E., Brenan, J.M., 1987. Fluids in the lithosphere, 1. Experimentally-determined wetting characteristics of CO2H2O fluids and their implications for fluid transport, host-rock physical properties, and fluid inclusion formation. Earth and Planetary Science Letters 85, 497–515. http://dx.doi.org/10.1016/0012-821X(87)90144-0.
Withers, A.C., 2013. On the use of unpolarized infrared spectroscopy for quantitative analysis of absorbing species in birefringent crystals. American Mineralogist 98, 689–697. http://dx.doi.org/10.2138/am.2013.4316.
Withers, A.C., Bureau, H., Raepsaet, C., Hirschmann, M.M., 2012. Calibration of infrared spectroscopy by elastic recoil detection analysis of H in synthetic olivine. Chemical Geology 334, 92–98. http://dx.doi.org/10.1016/j.chemgeo.2012.10.002.
Witt-Eickschen, G., Kramm, U., 1998. Evidence for the multiple stage evolution of the subcontinental lithospheric mantle beneath the Eifel (Germany) from pyroxenite and composite pyroxenite/peridotite xenoliths. Contributions to Mineralogy and Petrology 131, 258–272. http://dx.doi.org/10.1007/s004100050392.
Wittig, N., Baker, J.A., Downes, H., 2007. U–Th–Pb and Lu–Hf isotopic constraints on the evolution of sub-continental lithospheric mantle, French Massif Central. Geochimica et Cosmochimica Acta 71, 1290–1311. http://dx.doi.org/10.1016/j.gca.2006.11.025.
Wyllie, P.J., Ryabchikov, I.D., 2000. Volatile components, magmas, and critical fluids in upwelling mantle. Journal of Petrology 41, 1195–1206. http://dx.doi.org/10.1093/petrology/41.7.1195.
Xia, Q.-K., Hao, Y., Li, P., Deloule, E., Coltorti, M., Dallai, L., Yang, X., Feng, M., 2010. Low water content of the Cenozoic lithospheric mantle beneath the eastern part of the North China Craton. Journal of Geophysical Research 115, B07207. http://dx.doi.org/10.1029/2009JB006694.
Xia, Q.-K., Hao, Y.-T., Liu, S.-C., Gu, X.-Y., Feng, M., 2013. Water contents of the Cenozoic lithospheric mantle beneath the western part of the North China Craton: peridotite xenolith constraints. Gondwana Research 23, 108–118. http://dx.doi.org/10.1016/j.gr.2012.01.010.
Xu, Y.-G., Menzies, M.A., Bodinier, J.-L., Bedini, R.M., Vroon, P., Mercier, J.-C.C., 1998. Melt percolation and reaction atop a plume: evidence from the poikiloblastic peridotite xenoliths from Borée (Massif Central, France). Contributions to Mineralogy and Petrology 132, 65–84. http://dx.doi.org/10.1007/s004100050405.
Yang, X.-Z., Xia, Q.-K., Deloule, E., Dallai, L., Fan, Q.-C., Feng, M., 2008. Water in minerals of the continental lithospheric mantle and overlying lower crust: a comparative study of peridotite and granulite xenoliths from the North China Craton. Chemical Geology 256, 33–45.
Yaxley, G.M., Green, D.H., Kamenetsky, V., 1998. Carbonatite metasomatism in the Southeastern Australian Lithosphere. Journal of Petrology 39, 1917–1930. http://dx.doi.org/10.1093/petroj/39.11-12.1917.
Yu, Y., Xu, X.-S., Griffin, W.L., O'Reilly, S.Y., Xia, Q.-K., 2011. H_2O contents and their modification in the Cenozoic subcontinental lithospheric mantle beneath the Cathaysia block, SE China. Lithos 126, 182–197. http://dx.doi.org/10.1016/j.lithos.2011.07.009.
Zangana, N.A., Downes, H., Thirlwall, M.F., Hegner, E., 1997. Relationship between deformation, equilibration temperatures, REE and radiogenic isotopes in mantle xenoliths (Ray Pic, Massif Central, France): an example of plume–lithosphere interaction? Contributions to Mineralogy and Petrology 127, 187–203. http://dx.doi.org/10.1007/s004100050275.
Zangana, N., Downes, H., Thirlwall, M., Marriner, G., Bea, F., 1999. Geochemical variation in peridotite xenoliths and their constituent clinopyroxenes from Ray Pic (French Massif Central): implications for the composition of the shallow lithospheric mantle. Chemical Geology 153, 11–35. http://dx.doi.org/10.1016/S0009-2541(98)00150-8.

Chapitre V : Mécanisme de percolation en bord de filon et comportement de l'hydrogène

Ce chapitre détaille l'étude de l'effet de la percolation d'un fluide dans la péridotite en bordure de veine sur l'hydrogène des minéraux de la peridotite hôte.

V.1 Introduction

Dans le chapitre précédent le comportement de l'hydrogène lors des processus de fusion et de métasomatisme a été étudié. Les relations entre la concentration de l'H dans les minéraux dit anhydres (NAMs) et les processus de métasomatisme, détectés par le fractionnement des REE notamment, n'est pas évidente. Pourtant, la concentration en eau des liquides issus de la fusion des péridotites tels que les basaltes est largement supérieure à celle des péridotites. Elle est estimée entre 0.12 et 0.8 wt% H_2O, pour les MORB et basaltes d'Hawai (Sobolev et Chaussidon 1996 ; Anderson et Brown 1993 ; Wallace et Anderson, 1998) et jusqu'à 6-8 wt.% H_2O pour les basaltes de zone de subduction (Sisson et Grove, 1993; Roggensack *et al.*, 1997; Newman *et al.,* 2000; Pichavant *et al.*, 2002; Grove *et al.*, 2005 ; Métrich et Wallace, 2008). Tandis que la concentration en H pour le manteau nominalement anhydre à spinelle (*i.e.*, ne contenant pas d'amphibole et/ou de phlogopite) est estimée à 0.007 wt.% H_2O (soit 70 ±30 ppm wt. H_2O, pour une péridotite contenant de l'olivine, de l'opx et du cpx avec un mode de 64, 25, 10 respectivement (+ 1% de sp), et des concentrations en H de 4, 150 315 ppm wt. H_2O respectivement) suggérant que l'H se comporte comme un incompatible lors de la fusion.

Le rapport entre H_2O sur un élément chimique un peu plus compatible tel que le Ce (H_2O/Ce) est corrélé positivement avec des marqueurs des caractéristiques mantelliques (enrichissement/appauvrissement du manteau source) tels que $(La/Sm)_N$, K_2O/TiO_2) (*e.g.*, Dixon *et al.,* 2002 ; Danyushevsky *et al*., 2000 ; Simons *et al*., 2002). Néanmoins l'étude des xénolites de Ray Pic ne montre pas de relation évidente entre, d'une part, l'enrichissement des LREE par rapport aux HREE et/ou MREE, et d'autre part la concentration en H_2O des NAMs (voir chapitre précédent).

Afin de mieux cerner le comportement de l'H durant les processus métasomatiques, 5 xénolites composites ont été étudiés, dans lesquels la péridotite jouxte l'agent métasomatique principal. Les minéraux présents dans la veine reflètent la composition du fluide qui a circulé. Le choix des échantillons visait à englober une large gamme de veines et donc d'agent métasomatique a priori facilement identifiables afin de suivre les processus de percolation/réaction en fonction de la distance par rapport au liquide métasomatique (i.e. veine de pyroxénite). À l'échelle centimétrique, (imposée par la taille des xénolites), nous reprenons ainsi la philosophie d'un des articles clefs dans l'étude des processus métasomatiques mantelliques publié par Bodinier *et al.* (1990) intitulé « *Mechanism of Metasomatism : Geochemical evidence from the Lherz orogenic peridotite* ». Dans cette étude les auteurs décrivent à l'échelle déca-centimétrique à métrique l'évolution des processus métasomatiques via notamment le fractionnement des REE en fonction de la distance à l'agent métasomatique principal, ici une veine de pyroxenite à amphibole (Figure V.1).

Ce chapitre est présenté dans un format pré-soumission, il est donc en anglais.

V.2 H distribution during fluid percolation in peridotite from vein wall rocks: a pyroxenites and amphibolite study.

V.2.1 Introduction

Metasomatism is an ubiquitous process in the Earth mantle and is related to the movement of fluid/melt through the mantle, as such it is a key processes leading to redistribution of elements, including element of economic and/or strategic interest, throughout the mantle and especial in the sub continental lithospheric mantle (SCLM).

Two main processes have been described.

- *Large scale porous flow* related to pluri-kilometric scale processes such a the chemical and thermal erosion of the lithosphere by asthenosphere as described for Ronda massif, Spain (Van der Waal and Bodinier, 1996) and Lherz massif, France (Le Roux *et al.*, 2007), but also in several xenolith suites such as the one from Borée in the massif Central (Xu *et al.*, 1998) or in Ethiopia (Bedini *et al.*, 1997).
- *Vein-dyke*, which affect a lesser volume of mantle. However the advective transport through conduit allow to go further and overwhelmed the temperature gradient imposed by the conductive geotherm which has the tendency to freeze melt and thus limit their migration toward the shallower level in the cooler mantle lithosphere. In that case the authors refer to wall-rock metasomatism (in Massif: Bodinier *et al.*, 1991; McPherson *et al.*, 1996; in xenoliths: Wilshire *et al.,* 1980; Grégoire *et al.,* 2000).

As pointed out by numerous authors, the difference between these two processes is difficult, especially in the case of xenoliths for which no structural/geometric relationships are available (see also previous chapter).

However, irrespective of the scale of interaction it is possible to distinguish between two domains:

A proximal domain is a zone where high melt rock ratio leads to the crystallization of solid phases either new phases such as amphibole (modal metasomatism) or phases already existing (e.g. cpx at the expense of ol, crypto-modal metasomatism). In this proximal domain, trace elements redistribution is controlled by (solid-liquid) diffusion ($m^2.s^{-1}$). In the case of a pyroxenite vein, this domain is referred as the wall-rock of the vein, extending form the vein-peridotite contact up to the **reaction front.**

Whereas further away, downstream relative to the reaction front, the host peridotites is affected by a cryptic metasomatism (no change in modal abundances), in which trace element fractionation are percolation ($m.s^{-1}$) controlled. This domain is thus delimited down-stream by the **percolation front** and up-stream by the reaction front.

Pioneer work by Bodinier *et al.,* 1990, 1991 provides a theoretical framework on wall-rock metasomatism (e.g., chromatographic element front). They note that the movement of trace elements associated with magma infiltration through mantle rocks results from three

main mechanisms: (1) Advection in the liquid phase, whereby the elements are carried along by the movement of the magma, (2) Diffusion and kinematic dispersion within the liquid phase, and (3) diffusion within the solid matrix considered to be immobile.

Our sampling scale (few cm) may not allow investigating both domains (diffusion-reaction *vs* percolation-chromatography), (this will be checked through trace element enrichment and fractionation trend). The extend of the various domains depend on the temperature, pressure conditions, the fluid composition and volume, the modal composition of host rock, and time. Bodinier *et al.* described it on meter scale, with a reaction front at ≈20 cm; while the percolation front was estimated about 60 cm away from the amphibole-bearing pyroxenite.

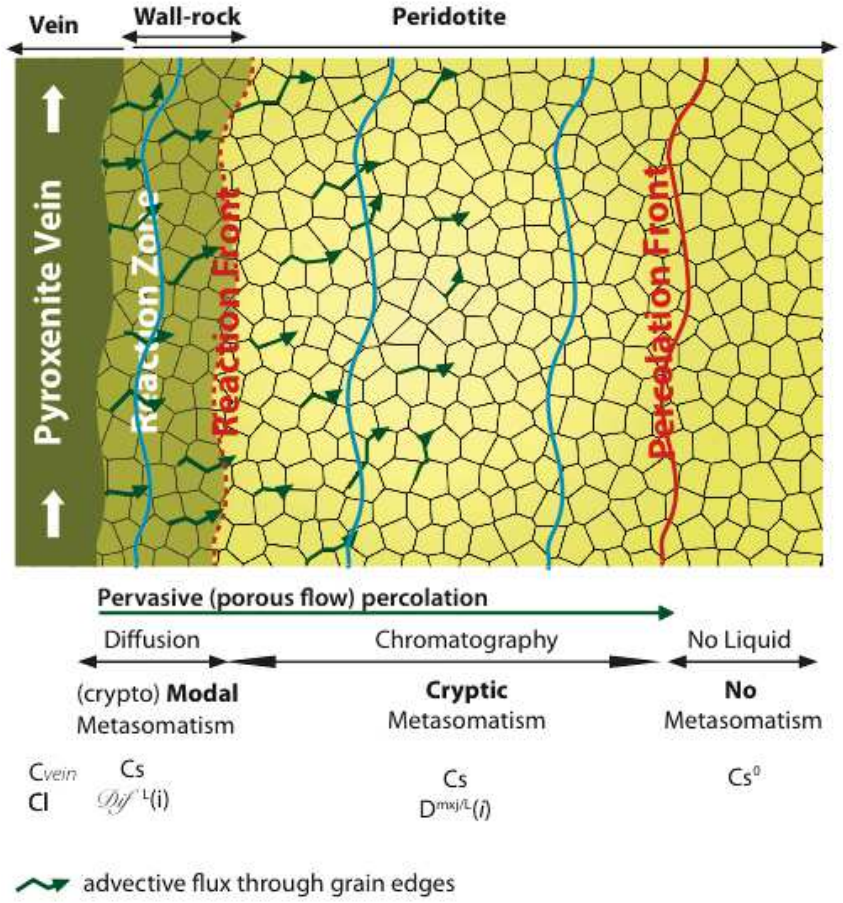

Figure V.1. – Schematic representation of the wall-rock metasomatism evolution of the transport of element away from the vein.

H concentrations in natural sample for all mineral phases is commonly studied in peridotite for the last decade but only one study gives data on REE and H from pyroxenites (Bizimis and Peslier, 2015). For the first time, our study focus on H concentrations in nominally anhydrous minerals (NAMs) and amphibole, along major and trace element concentrations in minerals were analysed in reactive porous infiltration context close to a vein. Sample from peridotitic massifs are not a good object to study H behaviour in the

mantle because of the exhumation processes and the alteration of the rock. That is why, four composite xenoliths with different types of veins were chosen as function as the mineral composition of the vein and the host peridotite. One vein contains glass, whereas the others contain different proportions of pyroxenes and amphibole.

V.2.2 Newer volcanic field (Australia): 14V81

The sample **14V81** come from the Newer Volcanic Field (NVF), located mostly in the Victoria State (SE-Australia). This late Neogene large volcanic field is related to the East Australian hotspot (Yaxley *et al.*, 1991; 1997; O'Reilly and Griffin, 1988). This sample consists in a spinel lherzolite showing a diffused contact with a basaltic patch (Figure V.1). Optically the transition is marked by the opx that evolves from a clear brown to a dark brown colour in the lava-impregnated part (Figure V.1a).

The peridotite part shows a porphyroclastic texture, showing large olivine and opx porphyroclastes (Ø up to 10 mm). Modal abundance obtained from the peridotite section indicate cpx abundances ca. of 5 % and for olivine abundances ca. 64 %, indicating thus that this sample is a cpx-rich harzburgite (Table V.1). Olivine compositions obtained as far away as possible from the contact (*i.e.* ≈ 8-9 mm) have a Fo% ranging between 88.5 and 89.1. Such a low Fo% is not in agreement either with the relatively high mg# of the pyroxene ($mg\#_{Opx}$≈ 91.4; $mg\#_{cpx}$ ≈ 91.7 %) nor with the high $cr\#_{spl}$ ca. 38 %, which are in agreement with the harzburgite-like mineralogy. The clear brown opx are enstatite (En_{89}; Fs_{9} and Wo_{3}; Table V.2). The cpx are diopsides (mg# 91.8; cr# 19.1; 21.3 wt. % CaO; Table V.2).

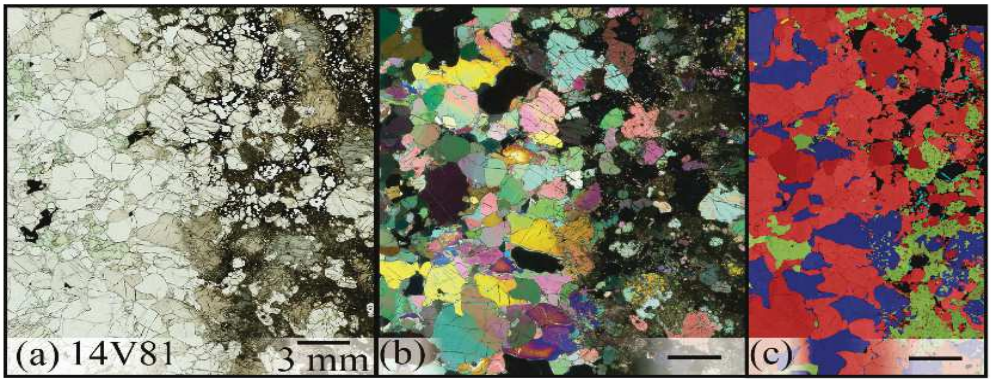

Figure V.1. – Thin section micrographs (**a**) in plane-polarized light and (**b**) in cross-polarized light for Sample 14V81; (**c**) associate SEM-EBSD maps are in the right column. In these maps, red is for olivine, dark-blue is for orthopyroxene, green is for clinopyroxene, yellow is for spinel, and pale-blue is for plagioclase. Scale bar is identical for the three micrographs (3 mm).

In the basalt impregnated part of the thin section - the "dark" unit (Figure V.1a) contains hazy relic grains of olivine (Fo% 80.1), dark brown opx (En_{77}; Fs_{16} and Wo_{7} mg# 80.9; cr# 1.3) and clinopyroxenes occurring in heterogeneous patches (mg# 79.9; cr# 1.4; 20.3 wt. % CaO) along with interstitial glassy patches with quench crystals of small (0.1 mm) plagioclase microlites (An% 59.8). Our EMP analyses indicate a glass composition enriched

in SiO_2 (46.7 and 52.6 wt. %) and $Na_2O + K_2O$ ranging between 6.0 and 7.2 wt. % (Table V.2). However, we suspect that these analyses have been partly contaminated by plagioclase microlites. Indeed trachy basalts are uncommon in the NVF (*e.g.*, Jordan *et al.*, 2015, Price *et al.*, 1997; Crawford *et al.*, 1985; Gray and McDougall, 2009).

2.1 Geochemical variations within 14V81

Note that the following chemical variations of the minerals from the host rock are described from the peridotite toward the patch. The distance to the contact is given in mm. Zero denotes the contact. Positive distances denote measurements in the host rock side, while negative values refer to analyses obtained in the basaltic patch side.

Major elements composition of constituting minerals. In the host harzburgite, olivine and pyroxenes grain cores show enrichments in FeO, MnO and TiO_2 and decreasing MgO, NiO and SiO_2 contents toward the contact with the basaltic patch (from around 5) (Figure V.2). In olivine, Fo% decreases gradually toward the contact from 89.8 to around 80 whereas the SiO_2 content of olivine varies continuously from 40 wt. % in the host peridotite to 38.5 wt. % in the basaltic vein. Although highly scattered (probably due to analytical variability, close to detection limit), TiO_2 in olivine seems to increase "regularly" toward the basaltic patch. NiO content of olivine shows an inverse behaviour as expected (Figure V.2d). We note that in Figure V.2a we do not reach a compositional plateau for the olivine into the peridotite. Therefore, in term of olivine composition, we have no insurance that we have observed the initial olivine composition i.e., not affected by the basaltic impregnation. The coexisting opx show a decrease in mg#, and cr# from 91.3 and 11.8 in the peridotite toward 80.8 and 1.2 in the basaltic contaminated section, respectively, while TiO_2 content varies from < 0.05 to 0.4. However, the concentration gradient across the contact is remarkably different of those described in the olivines. Indeed the shift toward lower mg# and cr# and higher TiO_2 is rather sharp, almost step wise (≈ 1 mm around the contact) and not continuous as observed in olivines (≈ 5 mm around the contact). Although the spatial resolution for cpx is not as good as the one obtained for olivine and opx it seems that, the composition of cpx varies rather smoothly than sharply with an intermediate gradient between those observed for olivine and opx. We also note that cpx are more strongly zoned (*i.e.*, difference core-rim) than observed for olivine and opx especially near the peridotite-lava contact. Indeed, for the clinopyroxene in the host lherzolite, a core-rim variation is clearly identified from 5 mm to the contact. Clinopyroxene rims are enriched compared to the core in Al_2O_3, TiO_2, FeO, MnO and depleted in CaO, MgO, Cr_2O_3 (up to cr# of 15.4 and 8 for core and rim at 1 mm, Figure V.2h). No core-rim variations are identified in olivine and opx. Due to the low abundance of spl, the picture is less clear, however clearly, $cr\#_{spl}$ drop sharply in the immediate vicinity of the contact (from ≈ 37 down to 29 % at 0.5 mm from the contact). While TiO_2 increase from 0.1 to 0.9 wt.%.

Table V.1– Modal mineralogy and equilibrium temperature of sample 14V81.

	Sample	**14V81**	
	Locality	Victoria field	
		host	vein
modal mineralogy (%)	ol	64	44
	opx	31	15
	cpx	5	24
	sp	<0.2	-
	am	-	-
	phl	-	-
	pl	-	1.3
	glass	-	15
Eq. T (°C)	B&K	932	958
	SD (B&K)	77	14
	BKN	942	979
	SD (BKN)	71	23
	Ca-opx	892	1230*
	SD (Ca-opx)	30	43*

Eq. T.: equilibrium temperature using Brey and Köhler, 1990 (error ± 30 °C): B&K based on Fe-Mg exchange between pyroxenes; BKN based on Ca distribution between pyroxenes; Ca-opx based on Ca concentration in orthopyroxene. v.: temperature determined on vein minerals; p.: temperature determined on host peridotite minerals; ol: olivine; opx: orthopyroxene; cpx: clinopyroxene; sp: spinel; am: amphibole; phl: phlogopite; pl: plagioclase. * data determined on a single crystal of opx.

Given the short scale variation of the composition of the mineral equilibrium temperature are uneasy to calculate, and their significance in term of equilibrium temperature is questionable. Calculation using the opx-cpx couple, at position further away from the contact ($x \approx 8.5$ mm) yields temperature ca. 902 ± 36; and 892 ±34ºC, for the BKN and Ca-opx geothermometers (Brey & Kholer, 1990), respectively. Temperature obtained for cpx-opx couple in the basalt-impregnated zone ($-2 < x < -5$ mm) yield TºBKN ca. 958 °C ± 17; and TºCa-opx between 1014 and 1254 ºC. This extremely large range of variation is due to the extreme variability of CaO content (0.8-3.0 wt. %) between opx grains and within grain (strong core-rim zonation).

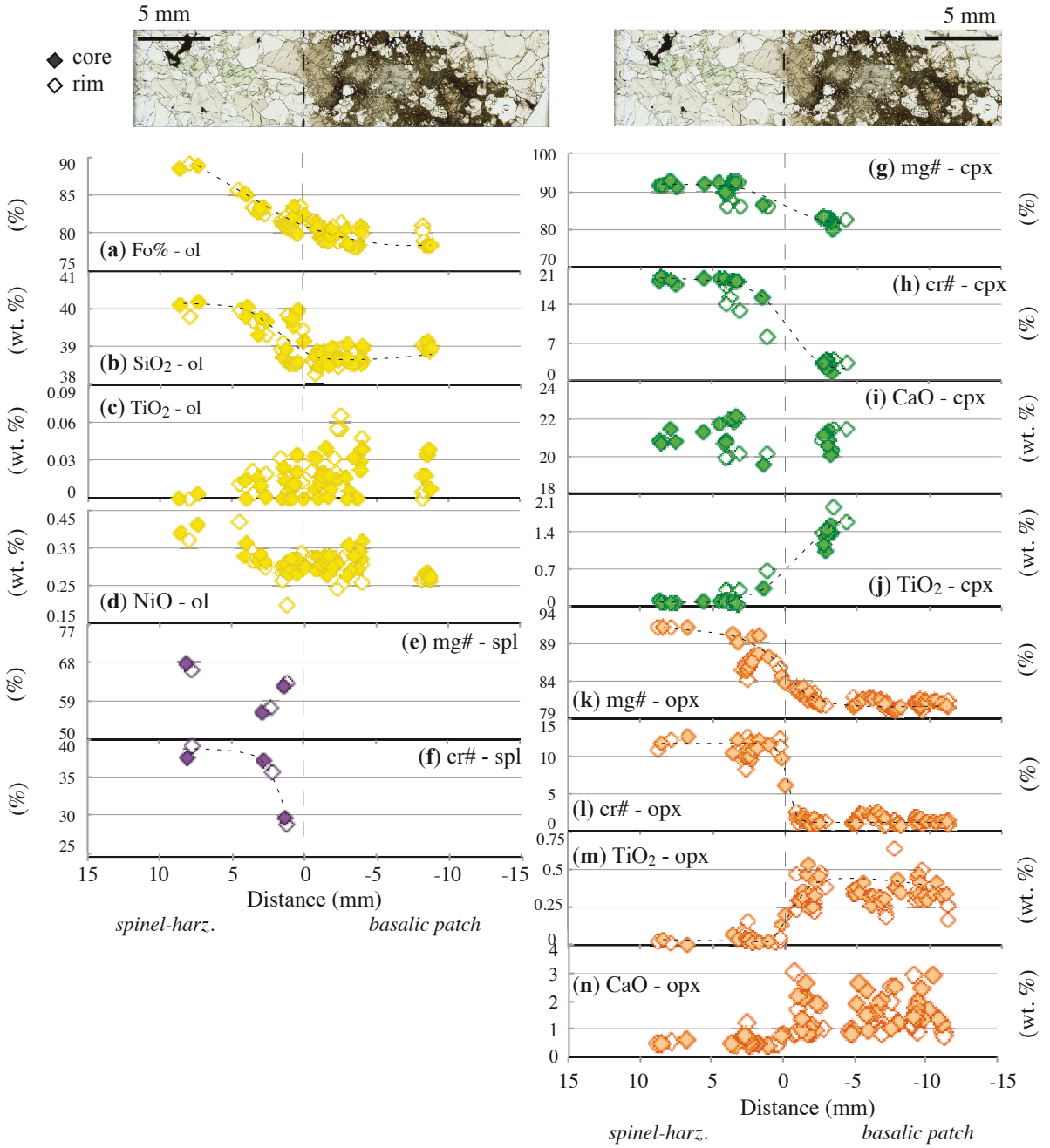

Figure V.2. – Main chemical variations on major elements concentration (wt.%) are given as a function of distance from the contact between the lherzolite and the glassy patch for ol from (**a**) to (**d**); for spinel (spl) from (**e**) to (**f**); for cpx from (**g**) to (**j**) and for opx from (**k**) to (**m**).

Table V.2 – Representative major compositions (wt. %) of each phase core from each part of the sample 14V81.

14V81									
Phase	Olivine		Orthopyroxene = enstatite		Clinopyroxene = diopside		Spinel	Pl	Glass
	host	vein	host	vein	host	vein	host	vein	vein
n	18	26	15	38	11	7	3	3	7
SiO_2	40.18	38.67	56.58	52.49	52.26	48.94	0.14	52.22	49.55
TiO_2	0.00	0.03	0.03	0.33	0.11	1.39	0.06	0.19	4.25
Al_2O_3	0.00	0.03	2.29	5.07	3.39	7.48	35.96	29.50	14.17
Cr_2O_3	0.02	0.00	0.46	0.10	1.19	0.16	32.38	0.00	0.02
FeO	10.78	18.53	5.75	11.78	2.60	5.86	15.44	0.64	12.80
MnO	0.11	0.18	0.15	0.16	0.08	0.14	0.17	0.00	0.15
MgO	47.94	42.14	34.00	28.07	16.41	13.07	15.92	0.15	3.88
CaO	0.05	0.08	0.46	1.36	21.29	20.32	0.00	12.08	6.26
Na_2O	0.02	0.01	0.05	0.15	1.18	1.05	0.03	4.32	3.42
K_2O	0.01	0.01	0.00	0.00	0.00	0.20	0.00	0.26	3.23
NiO	0.41	0.36	0.11	0.09	0.03	0.05	0.21	0.00	0.00
Total	99.52	100.04	99.89	99.60	98.55	98.66	100.31	99.37	97.73
Mg#	*88.7*	*80.1*	*91.3*	80.9	*91.8*	*79.9*	*67.7*	/	/
cr#			*11.8*	1.3	*19.1*	*1.4*	*37.6*	/	/
[En]			88.6	77.1					
[Fs]			8.9	16.1					
[Wo]			2.5	6.9					

Representative analysis of n measurements; ol: olivine; opx: orthopyroxene; cpx: clinopyroxene; sp: spinel; am: amphibole; pl: plagioclase; [En], [Fs], [Wo] are enstatite, Ferrosilite, Wollastonite end-members respectively; Fo%: forsterite content = $100\times Mg/(Mg+Mn+Fe_{tot})$; mg#: Mg-number = $100\times Mg/(Mg+Fe_{tot})$; cr#: Cr-number = $100\times Cr/(Cr+Al_{tot})$.

Trace elements. Chondrite normalised REE patterns of Cpx are characterised by a strong and smooth enrichment from Lu to La (Figure V.3a, Table V.3). The normalised abundance of Lu is low and ranges between 3.3 and 4.1 ppm, which implies a relatively high degree of batch melting between 20 and 26 %, in agreement with the cpx poor mineralogy, the high mg# of the pyroxenes and the high $cr\#_{spl}$. The abundance of La ranges between 51 and 75 times the chondrite value. We note that the rims of the cpx are statistically poorer in LREE ($(La)_N = 59 \pm 7$) than the core ($(La)_N = 69 \pm 5$). The extended trace element patterns show negative anomalies in HFSE (except for Nb) and high U, Th and Sr. U and Th show also a systematic depletion in the rim compared to the core ($(Th)_{PM} = 8 \pm 2$ *vs.* $(Th)_{PM} = 11 \pm 2$).

A plot showing trace element concentration in cpx versus distance from the contact (Figure V.3e-i) shows that core composition varies. La content decrease (from 16 to 12.5 ppm) as Lu content increase (from 0.088 to 0.104 ppm) when moving toward the contact. Sm shows a constant concentration across the thin section. In details, the rim of clinopyroxene grains have always La contents of 2 or 3 ppm below those from the core (Figure V.3e).

The glass patches within the basaltic shows straight and continuous enrichment from Lu to La. As shown in Figure V.3c, the chondrite normalised REE patterns is broadly parallel to the basaltic lava (*sensus lato*) from the Newer Volcanic Province (*e.g.*, McDonough *et al.*, 1985). However, here again, the observed variability is ascribed to the difficulty to analyse only glass. This is shown for instance by the small positive Eu anomaly displayed by some of the REE patterns which suggest that plagioclase have been included in these analyses The

extended trace element pattern is marked by moderate positive anomalies in Ti and Nb-Ta. Such positive anomalies are characteristics of alkali basalts in intra continental setting (e.g., Aldanmaz, 2002; Pearce and Cann, 1973).

Table V.3 – Representative trace elements compositions (ppm) of cpx in the lherzolite of the sample 14V81

14V81	cpx	glass	Th	1.16	19.9
	host	vein	U	0.227	6.40
n	14	7	La	17.2	252
Sc	103	136	Ce	42.2	529
V	n.a.	2266	Pr	5.35	64.0
Co	n.a.	267	Nd	21.8	294
Rb	< 0.0072	273	Sm	3.91	65.8
Sr	311	2764	Eu	1.18	24.6
Y	7.51	188	Gd	2.82	56.6
Zr	30.3	1647	Tb	0.347	8.05
Nb	0.362	366	Dy	1.83	42.0
Cs	< 0.0038	1.25	Ho	0.297	7.66
Ba	< 0.0109	2694	Er	0.706	17.2
Hf	0.227	40.2	Tm	0.103	2.27
Ta	0.0518	19.1	Yb	0.651	13.9
Pb	1.1700	12.4	Lu	0.0949	1.90

Representative analysis of n measurements; ol: olivine; opx: orthopyroxene; cpx: clinopyroxene; sp: spinel; am: amphibole.

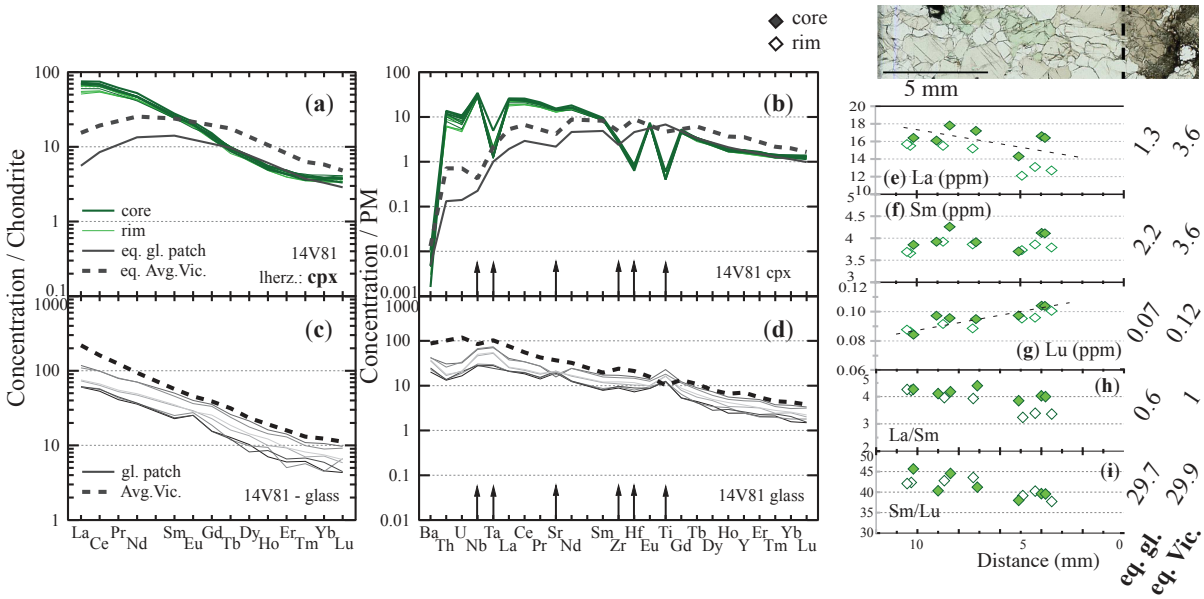

Figure V.3. – Trace element concentrations normalised to chondrite values and normalised to the primitive mantle (PM) in cpx ((**a**), (**c**)); and in glass ((**b**), (**d**)) (normalisation values are from McDonough and Sun, 1995). Dashed-line in (**c**) is the average lava composition for the NVF from Georoc. In (**a**) grey line is the calculated cpx in equilibrium with the patch glass and the dashed-line is with the average NVF lavas. Black arrows underline the position of Nb, Ta, Sr, Zr, Hf and Ti. Graphs (**e**) to (**i**) are the trace element concentrations (ppm) of sample 14V81 clinopyroxene as a function of distance from the contact between the peridotite and the basaltic. At the right of these graphs, the indicated value is for the cpx in equilibrium with the patch glass and the average NVF lavas.

2.2 Sample 14V81: H concentrations in NAMs

H concentrations were determined in olivine and pyroxenes in the lherzolite but only in olivine in the basaltic patch. FTIR absorption spectra are typical of spinel lherzolite minerals (Figure V.4). Unfortunately, due to opacity and important alteration of pyroxenes in the basaltic vein, the FTIR absorption spectra were too contaminated by a broad band and OH peaks could not be identified or deconvoluted.

H concentrations in olivine in the lherzolite range between 4 and 1 ppm wt. H_2O, while in the basalt impregnated domain H_2O in olivine range between 3 and > 1 ppm wt. H_2O. Low H concentrations in olivine are obtained in both side of the contact. A statistical analysis of the dataset of C_{OH} (olivine) identify two groups of data. The first one is localised in the lherzolite (5 < x mm) of the contact with a C_{OH} (olivine) *ca.* 3.6 ± 0.44 ppm wt. H_2O. The second one encompass part of the peridotite near the contact and the basalt impregnated zone (x < 5 mm) where C_{OH} (olivine) is lower *ca.* 1.3 ± 0.28 ppm wt. H_2O (Figure V.5-a). Average C_{OH}(opx) is 59 ± 8 ppm wt. H_2O and C_{OH}(cpx) of is 125 ± 26 ppm wt. H_2O (Table V.4) Contrary to olivine, H concentrations in pyroxenes do not seem to vary toward the contact. Further, there is no clear core-rim variation. The apparent H partition coefficient between cpx and opx ($Kd_H^{cpx/opx}$) is about 2.1 ± 0.6. This value is within error of the literature average ($Kd_H^{cpx/opx}$ = 1.8 ± 0.8; using the same calibration), obtained on a range of spl-bearing xenoliths in alkali basalts from worldwide occurrences (Demouchy *et al.,* 2015; Denis *et al.,* 2013 and 2015; Soustelle *et al.,* 2013)

Table V.4 – H concentration (C_{OH}) in olivine and pyroxenes of 14V81 (ppm wt H_2O, based on the calibration of Paterson, 1982 (P82) and also calculated for other calibrations, W12=Withers *et al.,* 2012, B95=Bell *et al.,* 1995.

14V81	**Ol**		**Opx**		**Cpx**		**14V81**	**WR**
	host	vein	host	vein	host	vein		host
n	13	10	15	0	7	0	C_{OH} WR	26.2
Factor	**17.1**	16.4	**11.8**	11.5	**12.3**	12.1	±1σ	*4.5*
min P82	0.9	0.7	47	-	96	-		
max P82	3.9	2.9	69	-	157	-		
C_{OH} avg P82	**2.5**	**1.9**	**59**	**/**	**125**	**/**	Kd cpx/opx (H_2O)	2.1
±1SD	*1.1*	*0.7*	*7.7*	/	*26.2*	/	±1σ	*0.6*
C_{OH} avg W12	**2.2**	**1.2**	-	-	-	-	Kd cpx/ol (H_2O)	50
±1SD	*1.4*	*0.4*	-	-	-	-	±1σ	*15*
C_{OH} avg B95	-	-	**62**	**/**	**196**	**/**	Kd opx/ol (H_2O)	24
±1SD	-	-	*11.2*	/	*50.6*	/	±1σ	*7*

Average (avg) on n grains; *1σ*: absolute uncertainties calculated by algebraic method; factor is to convert water contents in ppm wt. H_2O to $H/10^6$ Si; ol: olivine; opx: orthopyroxene; cpx: clinopyroxene, WR: whole rock.

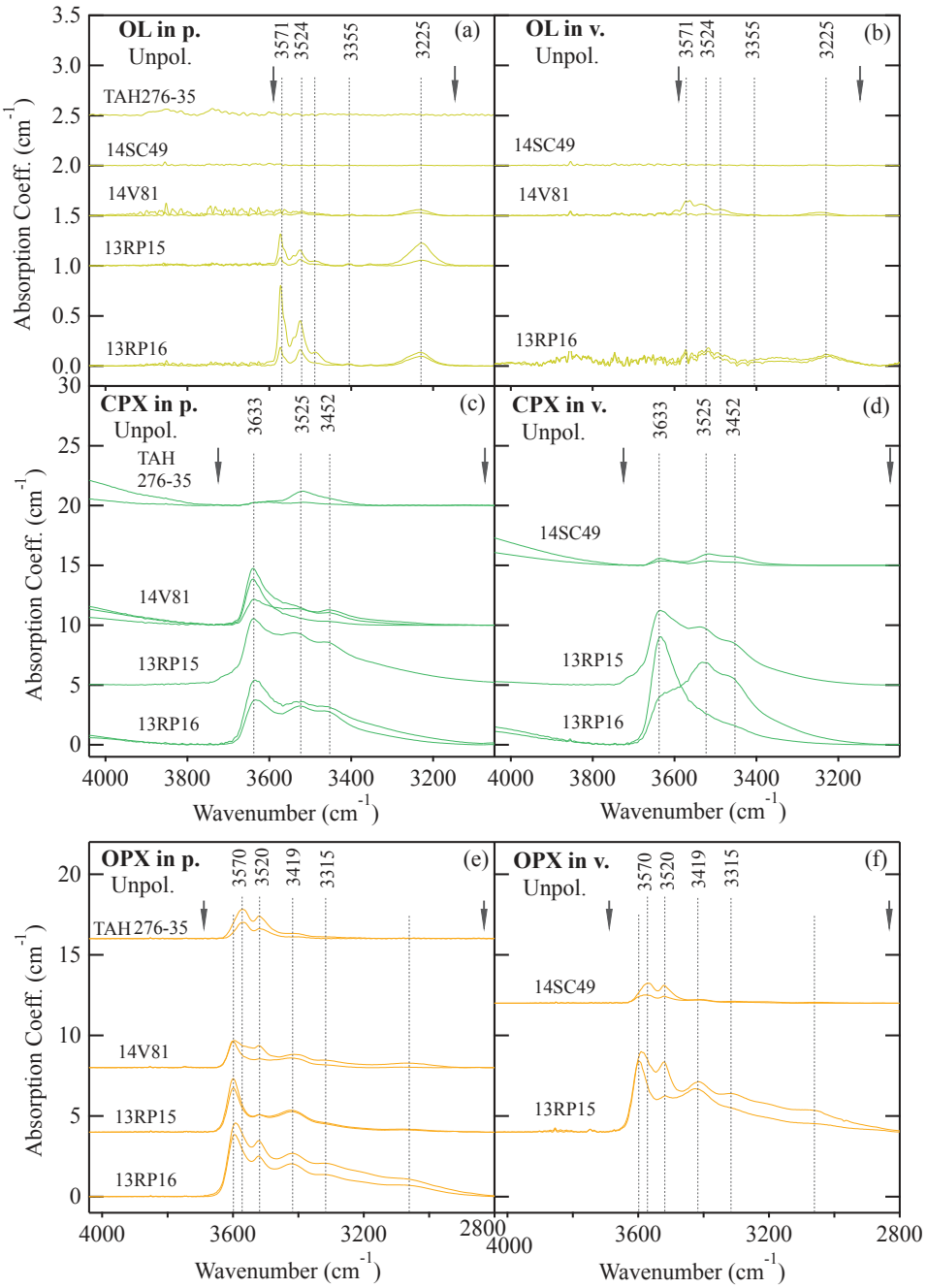

Figure V.4. – Representative unpolarized FTIR spectra of olivine (ol), clinopyroxene (cpx) and orthopyroxene (opx) for the host peridotite (p.) in (**a**) (**c**) and (**e**), for the associate minerals in the vein in (**b**), (**d**), and (**f**). Spectra with minimal and maximal absorbance are given for each sample. All spectra are normalised to 1 cm of thickness. Black arrows indicate the integration range used for the IR calibration; vertical dashed lines indicate the major OH absorption bands of the mineral.

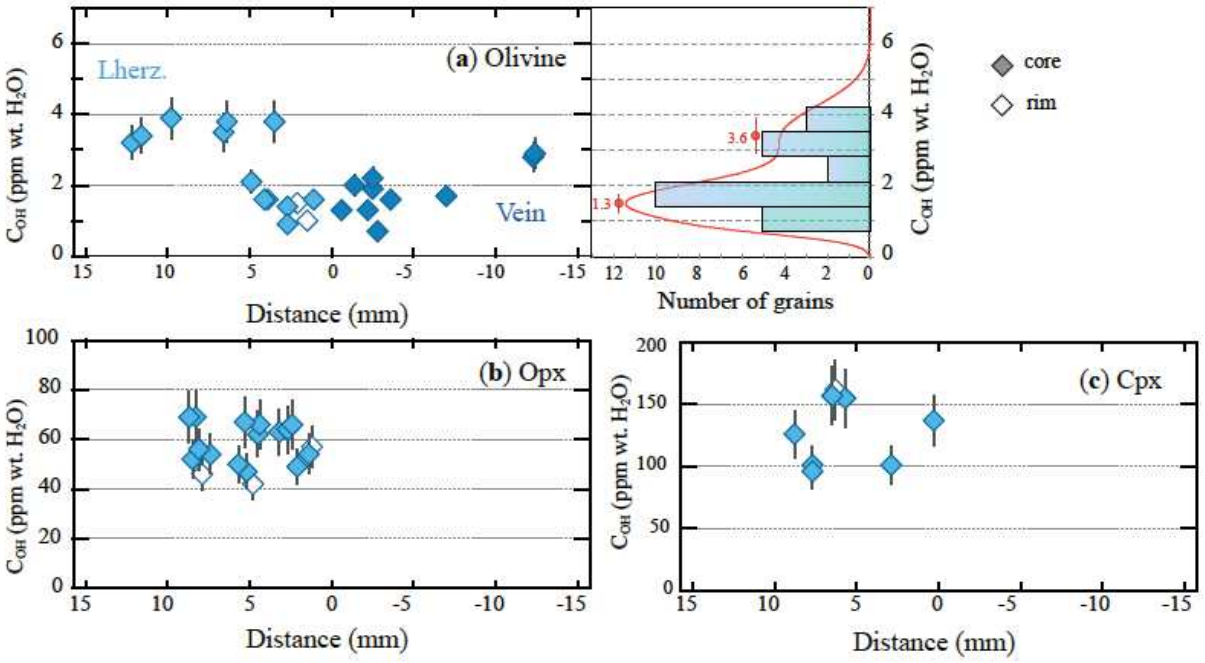

Figure V.5. – H concentration (ppm wt. H_2O) for olivine (ol) (a), orthopyroxene (opx) (b), clinopyroxene (cpx) (c) as a function as the distance from the contact between the peridotite and the glassy patch.

2.3 Sample 14V81: a case study for xenolith-host lava contamination

Major elements variations in the main silicate phases are clearly spatially organised around the harzburgite - basaltic patch contact. Increase in TiO_2 (and FeO, not shown here) content and decrease in mg# and cr#, are usually associated to basalt-rock interaction (*e.g.,* Arai and Abe, 1995; Wilshire and Shervais, 1975; Pearson *et al.,* 2003). The different chemical gradients (continuous vs. step-wise) observed for the various elements (*e.g.*, Cr, Ca *vs.* Fe and Mg) within the different silicate phases (*e.g.*, ol vs. opx) are related to specific diffusion kinetics for each elements in each silicate phase.

Trace element patterns of the peridotite cpx indicate that these cpx were extensively metasomatised. Given first the proximity of the basaltic melt; second the similar REE abundances between cpx and glasses and thirdly the apparent broad parallelism between the REE patterns of the glass patches and those of the peridotites cpx, we may propose that cpx represent frozen trapped basaltic melt. However, this hypothesis does not agree with several observations: (i) the cpx abundances and major element chemistry are in agreement with the abundances and major element chemistry of the other coexisting minerals such as opx, ol and spl; (ii) in detail the LREE and HREE ends of the cpx's patterns are concave downward and upward, respectively; (iii) During such process one would expect the opposite core-rim zonation than the one observed *i.e.*, incompatible elements impoverishment of the rim.

The liquid in equilibrium with the peridotite cpx is in fact extremely enriched in LREE (e.g. $(La)_N \geq 1000$) and do not resemble the glass patches ($(La)_N < 150$). Inversely cpx in equilibrium with the glasses are much less LREE enriched ($(La)_N<7$) and have a very

different REE pattern (Figure V.3). This implies that the metasomatic melt was not the basalt sampled through the glass patches. From there, two scenarios are possible.

First, the peridotites were metasomatised prior to the basalts-peridotite interaction. This is most likely (in any scenario), however what we suggest here is that most of the trace element characteristics of the peridotites were acquired by a previous metasomatic event. In that case, the trace element variations as a function of the distance to the contact are only due to reequilibration through diffusion either through the interstitial liquid/melt or between solids.

However, the discrepancy in term of REE abundances and patterns between the alleged metasomatic melt and the basalt does not necessarily preclude the involvement of the basaltic melt sampled through the nearby glass patches. In fact, the occurrence of positive HFSE anomalies in the cpx are reminiscent of those found in the glass patches and are usually uncommon in extremely LREE enriched metasomatic melt such as carbonatitic/volatile-rich small volume melts which results usually in cpx affected by pronounced negative HFSE anomalies (*e.g.*, Dautria *et al.,* 1992; Ionov *et al*., 1993; Yaxley *et al*., 1991; Grégoire et al., 2000; Rudnick *et al.,* 1993). Indeed, an alternative scenario will involve a residual melt issue of the massive crystallisation/trapping of this basaltic melt. Thus, in this case reaction front and contact are merged. Such residual melt would be enriched in the most incompatible elements and would percolate easily downward relative to the reaction front/contact due to its volatile richness. Chromatographic processes (*e.g.*, Navon and Stolper, 1987; Bodinier *et al*., 1990) would then lead for the distance considered here to a uniform LREE and MREE enrichment (*i.e.*, constant La/Sm) due to the fact that the LREE and MREE chromatographic fronts are further away downstream. In contrast the variations of the HREE abundances as a function of the distance suggest (*e.g*., Lu, Figure V.3g) that the chromatographic front of Lu for instance is few mm away from the contact. Then rapid diffusion within the interstitial liquid (± slow diffusion in the solid) will smooth (and displace) the front to give the progressive variation observed here (Figure V.3g). This imply that the peridotite's cpx has low Lu abundance (*i.e*., $(Lu)_N \leq 3.6$) in agreement with its harzburgitic composition. Similarly, the decreasing La abundance observed near the contact (Figure V.3e) has to be related to a diffusive reequilibration with a buffered melt or with the nearby basalts. This effect is not visible for the Sm because the concentration difference between the basalt and the peridotite's cpx is much less than for La and a higher spatial resolution near the contact (6-0 mm) is probably required.

As mentioned earlier, H concentrations vary only in the olivine, the pyroxenes do not show any remarkable (*i.e*., related to x) variations, no H concentrations in the pyroxenes in the veins were obtained. In 14V81, H concentrations for olivine range between 0.7 and 3.9 ppm while in opx and cpx is ca 59 ± 7 and 129 ± 57 compare to 0.5 to 9.5 ppm (average 4.7 ± 2.1 ppm) 256 ± 117 ppm (range from 54 - 402) and 478 ±167 ppm (199-893) for ol, opx and cpx respectively in spl-harzburgite xenoliths from worldwide localities (*e.g*., Li *et al.*,

2008; Peslier et Luhr, 2006; Denis *et al*., 2015). Thus although H concentrations in the NAMs of the 14V81 harzburgite sections are within the range found in other spl-bearing harzburgite worldwide, they rather describe the low end of the range.

Thus, the relatively low H_2O abundances in the NAMs of the peridotite here contrast strongly with the strong LREE enrichment and LREE/HREE fractionation observed in Cpx clearly related to metasomatism. This suggests once again that the relationships between H-enrichment and metasomatism is complex and that LREE (*e.g*., La, Ce) cannot be used as a proxy for H. Alternatively, the relatively low H_2O abundances in the NAMs of the 14V81 peridotite could be related to a dehydration process due to the proximity of (and interaction with) the basalt. However, (i) first of all we note that Lherzolites from the same data base show less extreme and less scattered values; for instance, H concentrations in opx average ca. 127 ± 60 (39-276) in lherzolite compare to 256 ± 117 ppm (range from 54 - 402), suggesting that H_2O abundances in harzburgites included in this database have been severely modified by various processes (*e.g*., metasomatism). (ii) H concentrations in pyroxene do not show any variations across the peridotites sections and especially toward the contact; (iii) no dehydration profiles have been identified even within the large grains in the peridotite.

If we consider that H concentrations in the NAMs 5 mm away from the contact are representative of initial concentration in the harzburgite protolith (*i.e*., due to melting), we still need to explain the low H concentrations in the vicinity ($x \leq 5$ mm) of the basalt. If this hypothesis is true, it would mean that (i) H loss related to the host lava interaction with the peridotite xenolith is limited to a 5 mm thick rim around the xenolith nodule and (ii) affect only the olivine and not the pyroxenes as advocated by several authors (Hao *et al*., 2014; Xia *et al*., 2010; Denis *et al*., 2013, 2015) on the basis of constant $Kd_{H2O}^{cpx/opx}$ as found here.

The fact that only olivine shows a variation would suggest this decrease in H concentrations in the olivine is related to the higher diffusivity of H in olivine compare to pyroxenes. Yet, the shape of the H concentration gradient is unexpected. Indeed, with the spatial resolution achieved here, it seems that we do not observe a smooth gradient as observed for the diffusion of Fe-Mg (Figure V.2a). However, diffusion coefficient for H ($D_{Ol}(H)= 10^{-12}$ $m^2.s^{-1}$; at 1100 °C, Demouchy and Mackwell, 2006) is several order of magnitude faster than Fe-Mg ($D_{Ol}(Fe\text{-}Mg)\approx 10^{-18}$ $m^2.s^{-1}$; at 1000°C, Fo=88.5, $fO_2=10^{-15}$ bar; Dohmen *et al*., 2007). As pointed out earlier the diffusion profile for Fe-Mg in olivine clearly extend beyond the area investigated (*i.e.* $x > 15$ mm). Water content seems to shift from low to high value in less than 5 mm. This discrepancy will suggest that H diffusion is slowed by other processes, and likely linked to H trapped in associated point defects. Si vacancies, Mg vacancies, titanium substitution, and trivalent cations are point defects where the H can bond with an O in the olivine lattice (Berry *et al*., 2005, 2007; Beran and Putnis, 1983; Demouchy and Mackwell, 2006; Kovács *et al.*, 2010; Padron-Navarta *et al.*, 2014). One hypothesis is that this variation close to the error of the FTIR spectroscopy is a readjustment of the H concentration due to the variation of TiO_2, MgO and SiO_2 contents in olivine. This variations are themselves controlled by slower ionic diffusion, notably Si which is the slowest diffusion

species in olivine (Chakraborty, 2008). In Figure V.6, H_2O and the major element variation patterns in olivine are overlaid. From this Figure V.6, we could rule out a possible Ti effect. This is due to the fact that Ti abundances in mantle olivine is generally too low. However, we have a relatively good agreement between the spatial variation of H_2O and SiO_2. At this stage, it is not possible to exclude the effect of Mg related defect on the diffusion process of H. However, both processes could contribute to H diffusion processes.

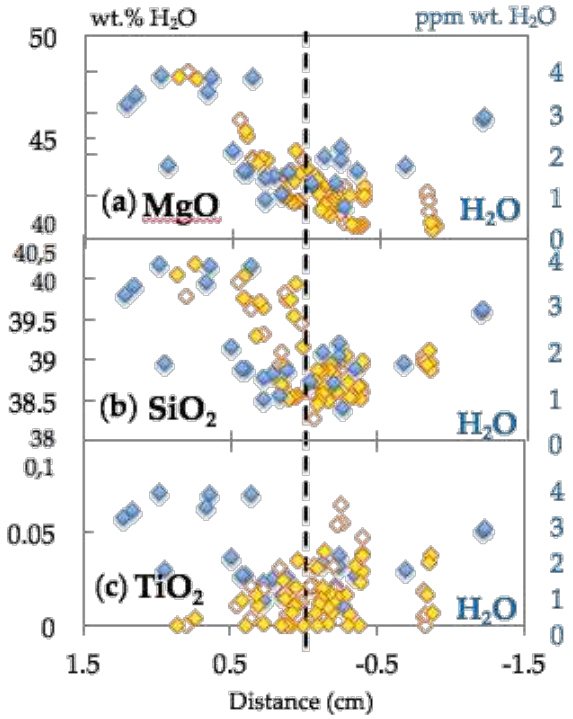

Figure V.6. – H concentrations variations in olivine compare to the (**a**) MgO, (**b**) SiO_2, and (**c**) TiO_2 contents of olivine as a function of the distance to the contact between the harzburgite and the basaltic patch.

Finally, we note than as in olivine, cpx and opx show diffusion profile for major elements (*e.g.* Fe-Mg; D_{cpx}(Fe-Mg)≈ 10^{-21} $m^2.s^{-1}$; at T=1000°C; Dimanov and Sautter, 2000). La in cpx seems to show a diffusive profile despite large D_{cpx}(La) (≈ 10^{-23} $m^2.s^{-1}$; T=1000ºC; Van Orman *et al.,* 2001). However, no variation in H has been observed.

V.2.3 Amphibole-bearing veins: 13RP15, 13RP16 and TAH 276-35

Three xenoliths crosscut by a pyroxenite veins have been selected. These pyroxénites show an increasing amount of amphibole 14 %, 27 % and 98 % for 13RP16, 13RP15 and TAH276-35, respectively (Table V.5; Figure V.7). Samples 13RP16 and 13RP15 come from the Ray Pic volcano, which belong to the southern part of the French Massif Central (Vivarais volcanic unit; see chapter IV). Xenoliths from this locality have been extensively studied (Zangana *et al.,* 1997, 1999; Denis *et al*., 2015). Sample TAH276-35 come from the Tahalra volcanic field (Southern Algeria) and was previously investigated by Dautria (1988; thesis; Dautria *et al*., 1987) and by Kourim *et al*., 2015. TAH276-25 is part of a type II xenoliths suite characteristic of occidental Tahalra domain (Dautria *et al*, 1987; Kourim *et al.*, 2015). This suite include webserite, (ol-) clinopyroxenite and numerous amphibolite xenoliths. In these localities, amphibole can reach size as large as 5 mm. Both volcanic fields (Vivarais and Tahalra) are located on top of a mantle diapir in a continental setting (Granet *et al.,* 1995; Rougier *et al.,* 2013).

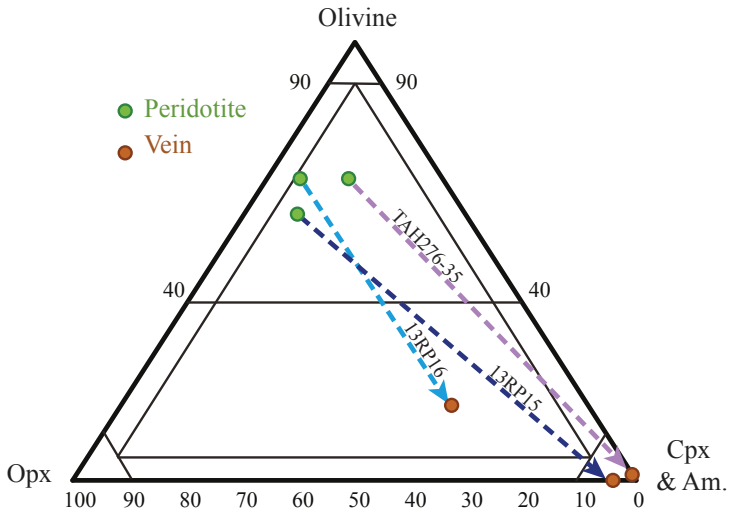

Figure V.7. – Sample 13RP16, 13RP15 and TAH 276-35 in the classification of the ultramafic rocks modified after Streckeisen (1973).

.

Table V.5 – Modal mineralogy and equilibrium temperature of samples 13RP16, 13RP15 and TAH276-35.

	Sample	**13RP15**		**13RP16**		**TAH276-35**	
	Locality	Ray Pic		Ray Pic		Tahalra	
		host	vein	host	vein	host	vein
modal mineralogy (%)	ol	58	<0.3	68	16	68	2
	opx	29	4	25	22	16	-
	cpx	8	62	5	40	14	<0.2
	sp	4	7	<0.7	9	2	<0.1
	am	<0.6	27	1.2	14	<0.9	98
Eq. T (°C)	B&K	810	748	1048	1043	977	-
	SD (B&K)	21	-	4	11	15	-
	BKN	821	842	1047	1044	985	-
	SD (BKN)	19	-	4	11	12	-
	Ca-opx	882	876	992	1002	1010	-
	SD (Ca-opx)	1	-	10	33	26	-

Eq. T.: equilibrium temperature using Brey and Köhler, 1990 (error ± 30 °C): B&K based on Fe-Mg exchange between pyroxenes; BKN based on Ca distribution between pyroxenes; Ca-opx based on Ca concentration in orthopyroxene. v.: temperature determined on vein minerals; p.: temperature determined on host peridotite minerals; ol: olivine; opx: orthopyroxene; cpx: clinopyroxene; sp: spinel; am: amphibole

3.1 Pyroxenite petrography and mineral composition.

Petrography. Pyroxenite of sample **13RP16** contains 40 % of cpx and 22 % of opx (Table V.5) and a significant amount of ol (16 %). The contact between the pyroxenitic vein and the lherzolite is relatively diffuse and jagged (Figure V.8a-c). The clinopyroxenes of the vein are green Cr-diopsides with exsolutions of spinel. Iddingsite gives an orange tint to the olivines in the pyroxenite.

Pyroxenite of sample **13RP15** is a 20 mm wide clinopyroxenite vein (Figure V.8d-g). The vein itself is divided in two different parts which can be distinguished by the relative proportion of brown interstitial amphiboles and cpx. Within the vein core, amphibole modal content reaches ≈ 27 %, while cpx abundance is *ca.* 62 % while in the vein rim amphibole abundance drop to 5 % but cpx abundance increase up to 86 % (Table V.5). Noting that the sum of the amphibole and cpx modal abundances is constant in both parts of the vein *ca.* 90 %. Olivine (not analyzed) is rare about 0.3 % in the vein core and *ca.* 2.1 % in the rim. Orthopyroxene modal content vary between 4 and 4.7 %. All the clinopyroxenes in the vein are brownish and commonly present numerous exsolutions lamellae of amphibole. Samples 13RP15 and 13RP16 have relatively similar major element phase compositions (Table V.6). However, in detail orthopyroxenes have a lower CaO (0.45 *vs.* 0.96 wt.%) and Al_2O_3 (4.3 *vs.* 5.4 wt.%) and higher mg# (86.3 *vs.* 85.4 %) ; while cpx have a higher CaO (22.1 *vs.* 20.0 wt.%), Al_2O_3 (8.1 *vs.* 7.4 wt.%) contents and mg# (90.1 *vs.* 89.3 %) in 13RP15 compare to 13RP16. respectively. Accordingly, amphiboles have a higher CaO (11.5 *vs.* 10.3 wt.%),

Al_2O_3 (14.9 *vs*. 15.6 wt.%) and mg# (87.1 *vs.* 86.4 %)in 13RP15 than in 13RP16. Olivines in 13RP16 have a Fo% *ca.* 89.7, which is indistinguishable than from the peridotite olivine (Fo% ≈ 89.4).

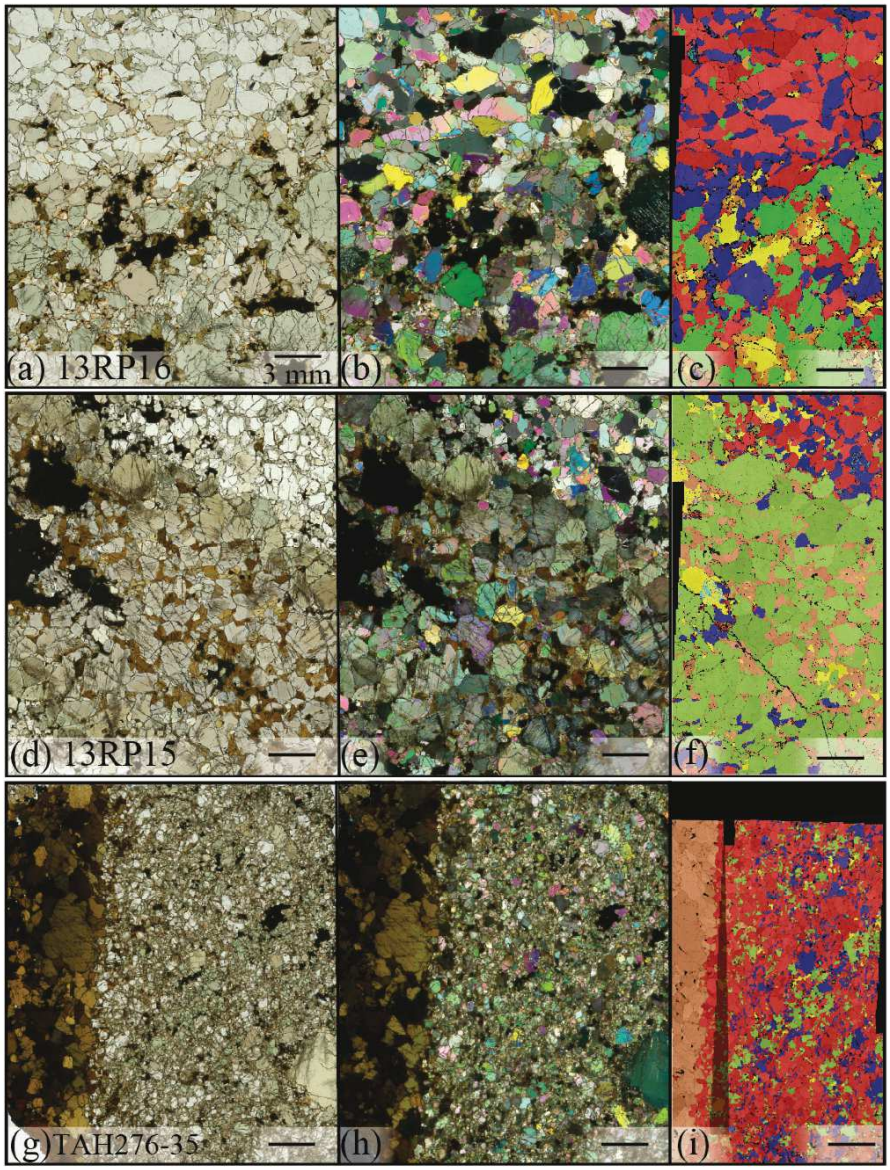

Figure V.8. – Thin section micrographs in plane-polarized light and in cross-polarized light for Ray Pic spinel xenoliths are given in the left and the middle column respectively. Associate SEM-EBSD maps are in the right column. In these maps, red is for olivine (ol), dark-blue is for orthopyroxene (opx), green is for clinopyroxene (cpx), yellow is for spinel (spl), orange is for amphibole (am) and pale-blue is for plagioclase (pl). Sample 13RP16 (a), (b), (c); sample 13RP15 (d), (e), (f) sample TAH 276-35 (g), (h), (i). Note that the scale of 3 mm is given by the line in the lower right corner of each image.

Equilibrium temperatures calculated using Fe-Mg and Ca exchange between opx-cpx (T°B&K and T°BKN, respectively) indicate a temperature *ca*. 748°C and 842°C respectively for 13RP15 (determine on one pair of opx-cpx) and 1043°C ± 11 and 1044°C ± 11 for 13RP16 for the pyroxenitic assemblage. These temperatures have been computed without integrating the spinel exsolution in cpx from 13RP16, nor the amphibole exsolution in the opx from 13RP15.

Sample **TAH 276-35** vein is an amphibolite and contain up to 98 % of amphibole. The interface between the amphibolite and the peridotite is extremely sharp and linear. The amphibolite vein shows a cumulate microstructure and has undergone a static recrystallization

or annealing phase indicated by well-developed triple junctions of amphibole grains. Magnesian-ilmenite rich in titano-magnetite exsolution and rare small phlogopite enclosed within large amphibole crystal occur. The amphibole located further away from the amphibolite-peridotite interface are pargasite with mg# *ca.* 78%, TiO_2 ≈ 4.7 and K_2O = 1.9 wt.% (Table V.6). This composition evolves toward the interface to higher mg# lower TiO_2 and K_2O which are about 82 %, 3.9 wt.% and 1.7 wt%, respectively at the contact. However, the original sample displayed a thicker amphibolite (up to 3 cm in thickness) in the original samples studied by Dautria *et al.* (1987). This study described a change in the mineralogy and phase composition within this vein. At the core of the vein the amphiboles are kaersutite with low mg# (≈70 ± 1%) high TiO_2 (> 4 wt.%) and K_2O (≈ 2 wt.%) which evolves within the last 5 mm toward the pargasite like composition (Dautria *et al*., 1987) as observed in our sample. Compare to the two amphibole bearing pyroxenite from Ray Pic, amphiboles from TAH 276-35 are significantly richer in K_2O, in FeO_{am} (7.4 *vs*. 4.4-4.8 wt.%) yielding a lower mg# (78 *vs.* 86.4-87.1 %), and are poorer in Na_2O (2.3 *vs.* 3.5-3.6 wt.%) and in Cr_2O_3 (cr# = 0.5 *vs* 2.3-2.9 %), respectively.

Trace elements. Trace element patterns of amphibole and cpx from the vein are very similar within each pyroxenite although quite different from pyroxenites (Figure V.9, Table V.7). In the two RP samples cpx and amphibole are clearly in equilibrium ($Kd^{am/cpx}$(REE)≈1). The REE patterns of both cpx and amphibole in 13RP16 are characterised by a flat (slightly negative slope) segment from Lu to Pr *ca.* 10 times the chondrite values, as well as a very steep Pr to La segment with $(La)_N$ reaching values as high as 50. This fractionation confer to the REE pattern a "convex" downward shape, which contrast strongly with the convex upward patterns of the two other samples (13RP16 and TAH 276-35). It is expected for cpx and/or amphibole equilibrated with alkaline mantle melts (*e.g.*, Irving, 1980; Irving & Frey, 1984; Bodinier *et al*., 1987). Regarding TAH 276-35, we note that the trace element patterns of this sample is virtually indistinguishable from those observed in the high and intermediate temperature groups defined by Kourim *et al.,* 2015 for the Tahalra xenoliths.

Amphiboles of sample 13RP15 have a convex upward pattern (Figure V.9b). Amphiboles of sample TAH 276-35 are more depleted in HREE and more enriched in LREE and MREE than those from 13RP15. All three samples show positive anomalies in Nb and Ta and negative anomalies in Zr, Hf in the cpx. U and Th are enriched relative to the LREE especially for 13RP16 for which U/Ce reachs value as high as 0.15. Amphiboles in all samples show a Ti and Nb–Ta positive anomalies (except for 13RP16), in agreement with the known preferential partitioning of these elements for amphibole (*e.g.,* Adam and Green, 2006). Amphiboles from 13RP16 differ from the others by having first, a negative Nb–Ta anomalie and second, a pronounced U–Th enrichment relative to LREE, which is not observed for the others amphiboles.

Table V.6 – Representative major compositions (wt. %) of each phase core from each part of the samples 13RP16, 13RP15 and TAH276-35.

Olivine

Sample	13RP15		13RP16		14TAH1
	host	vein	host	vein	host
n	19	-	11	4	14
SiO_2	40.44	-	40.72	40.40	40.59
TiO_2	0.00	-	0.00	0.02	0.00
Al_2O_3	0.00	-	0.02	0.02	0.02
Cr_2O_3	0.00	-	0.00	0.01	0.01
FeO	10.01	-	9.95	9.78	12.47
MnO	0.13	-	0.15	0.14	0.19
MgO	48.13	-	47.47	48.63	46.62
CaO	0.02	-	0.08	0.09	0.05
Na_2O	0.01	-	0.05	0.00	0.00
K_2O	0.00	-	0.00	0.01	0.00
NiO	0.39	-	0.38	0.41	0.36
Total	99.13	-	98.81	99.50	100.32
Fo%	*89.4*	*/*	*89.4*	*89.7*	*86.8*

Orthopyroxene = enstatite

Sample	13RP15		13RP16		14TAH1
	host	vein	host	vein	host
n	14	3	21	15	17
SiO_2	55.85	55.25	54.60	53.88	54.45
TiO_2	0.15	0.13	0.11	0.09	0.11
Al_2O_3	3.49	4.32	4.63	5.44	4.87
Cr_2O_3	0.20	0.01	0.22	0.13	0.37
FeO	6.66	6.29	6.45	6.32	7.92
MnO	0.15	0.16	0.13	0.13	0.15
MgO	33.09	33.08	32.18	32.20	31.52
CaO	0.47	0.45	0.80	0.96	0.88
Na_2O	0.05	0.04	0.12	0.11	0.08
K_2O	0.01	0.00	0.00	0.00	0.00
NiO	0.11	0.09	0.10	0.10	0.10
Total	100.23	99.80	99.34	99.37	100.47
mg# (opx)	*89.9*	*90.4*	*89.9*	*90.1*	*87.6*
cr# (opx)	*3.7*	*0.1*	*3.1*	*1.6*	*4.8*
[En]	86.2	86.3	85.3	85.4	83.2
[Fs]	10.2	9.2	9.4	7.8	10.9
[Wo]	3.6	4.5	5.3	6.8	5.9

Clinopyroxene = diopside

Sample	13RP15		13RP16		14TAH1
	host	vein	host	vein	host
n	9	39	2	14	16
SiO_2	51.80	50.16	50.95	50.54	50.67
TiO_2	0.79	1.21	0.44	0.42	0.50
Al_2O_3	5.41	8.06	6.53	7.37	6.53
Cr_2O_3	0.46	0.04	0.55	0.25	0.68
FeO	2.79	2.75	3.45	3.34	4.02
MnO	0.09	0.08	0.07	0.11	0.10
MgO	15.19	14.10	15.25	15.64	14.96
CaO	22.39	22.10	19.82	19.99	20.53
Na2O	1.09	1.35	1.26	1.24	1.20
K2O	0.00	0.00	0.01	0.01	0.00
NiO	0.06	0.05	0.06	0.06	0.05
Total	100.07	99.91	98.38	98.98	99.23
mg# (cpx)	*90.6*	*90.1*	*88.7*	*89.3*	*86.9*
cr# (cpx)	*5.4*	*0.4*	*5.3*	*2.2*	*6.5*

Spinel

Sample	13RP15		13RP16		14TAH1
	host	vein	host	vein	host
n	4	6	2	3	7
SiO_2	0.13	0.14	0.12	0.11	0.17
TiO_2	0.12	0.08	0.13	0.08	0.19
Al_2O_3	60.22	67.25	58.35	63.18	53.04
Cr_2O_3	6.81	0.47	7.79	3.35	11.27
FeO	11.77	9.93	11.84	10.70	16.52
MnO	0.12	0.08	0.10	0.09	0.14
MgO	19.81	21.51	20.53	21.98	18.23
CaO	0.00	0.00	0.03	0.00	0.02
Na_2O	0.00	0.00	0.01	0.00	0.00
K_2O	0.00	0.01	0.00	0.00	0.00
NiO	0.44	0.51	0.40	0.45	0.38
Total	99.43	99.97	99.30	99.94	99.96
mg# (spl)	*76.1*	*79.7*	*79.0*	*82.4*	*71.9*
cr# (spl)	*7.0*	*0.5*	*8.2*	*3.4*	*12.5*

Representative analysis of n measurements; ol: olivine; opx: orthopyroxene; cpx: clinopyroxene; sp: spinel; am: amphibole; pl: plagioclase; [En], [Fs], [Wo] are enstatite, Ferrosilite, Wollastonite end-members respectively; Fo%: forsterite content = $100\times Mg/(Mg+Mn+Fe_{tot})$; mg#: Mg-number = $100\times Mg/(Mg+Fe_{tot})$; cr#: Cr-number = $100\times Cr/(Cr+Al_{tot})$.

Table V. 6 – *(suite)*

Amphibole						
Sample	13RP15		13RP16		14TAH1	
	host	vein	host	vein	host	vein
n	1	11	4	3	14	10
SiO_2	42.56	42.72	41.97	42.37	42.02	40.88
TiO_2	3.15	3.25	1.56	1.84	2.63	4.68
Al_2O_3	16.02	14.93	16.26	15.63	14.36	14.16
Cr_2O_3	0.06	0.52	0.49	0.70	1.17	0.10
FeO	4.21	4.41	4.63	4.82	5.86	7.43
MnO	0.07	0.05	0.07	0.06	0.05	0.07
MgO	16.31	16.75	17.37	17.20	16.09	14.60
CaO	11.57	11.52	10.52	10.32	11.24	11.35
Na_2O	3.57	3.57	3.58	3.51	2.86	2.32
K_2O	0.14	0.02	0.23	0.24	1.10	1.92
NiO	0.12	0.13	0.14	0.13	0.10	0.05
Total	97.77	97.87	96.82	96.81	97.46	97.56
mg# (am)	*87.3*	*87.1*	*87.0*	*86.4*	*83.0*	*77.8*
cr# (am)	*0.3*	*2.3*	*2.0*	*2.9*	*5.2*	*0.5*

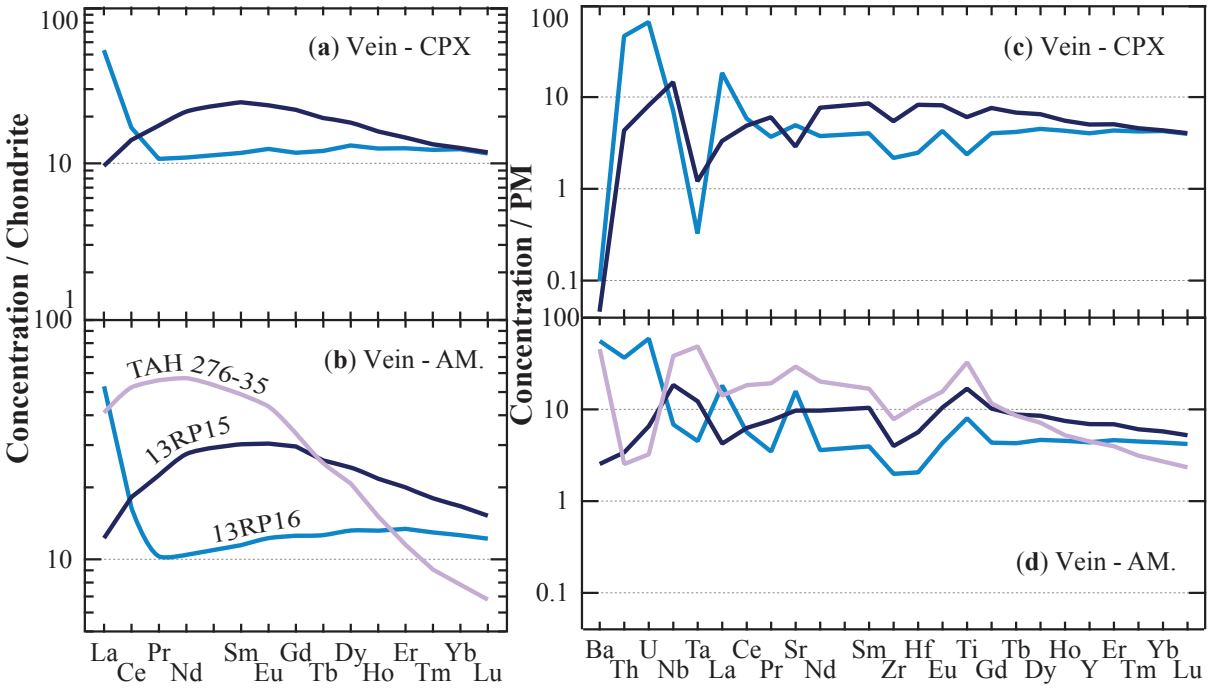

Figure V.9. – Trace element concentrations in cpx and amphibole normalised to chondrite values in (**a**), (**b**) respectively; normalised to the primitive mantle (PM) in (**c**), (**d**), respectively (normalisation values are from McDonough and Sun, 1995).

Table V.7 – Representative trace elements compositions (ppm wt.) of each phase from each part of the samples 13RP16, 13RP15 and TAH276-35.

	13RP15					**13RP16**						**14TAH1**			
	opx host	cpx host	opx vein	cpx vein	am vein	opx host	cpx host	am host	opx vein	cpx vein	am vein	opx host	cpx host	am host	am vein
n	3	7	3	5	3	4	11	2	7	9	4	9	12	4	4
Sc	15.5	76.0	14.2	59.9	48.3	18.4	57.8	39.6	14.4	66.3	46.0	21.0	59.4	57.5	44.1
V	n.a.	n.a.	n.a.	n.a.	n.a.	95.1	257	370	89.0	287	n.a.	n.a.	n.a.	n.a.	n.a.
Co	n.a.	n.a.	n.a.	n.a.	n.a.	64.8	23.1	44.8	62.2	28.0	n.a.	n.a.	n.a.	n.a.	n.a.
Rb	< 0.0033	0.0328	< 0.0042	0.0411	0.589	< 0.0126	< 0.021	2.45	< 0.033	< 0.0123	8.95	< 0.0036	< 0.0079	15.1	17.1
Sr	0.0280	57.1	0.0467	68.1	193	0.373	132	393	0.437	95.6	313	0.243	90.5	469	638
Y	0.832	20.3	0.851	23.3	29.4	1.35	16.4	19.9	0.785	16.8	18.9	1.38	17.3	22.9	19.8
Zr	1.42	44.0	1.93	63.5	42.4	1.63	24.2	24.1	1.17	22.2	19.7	2.01	41.3	67.2	89.3
Nb	0.0037	0.175	0.0011	0.257	4.79	0.0061	0.120	2.93	0.0121	0.0845	3.44	0.0157	0.349	30.1	28.0
Cs	< 0.0306	0.0136	< 0.0024	< 0.0058	0.0306	< 0.0064	< 0.0109	0.0690	< 0.0175	< 0.0067	0.0555	0.0026	< 0.0044	< 0.0209	< 0.0191
Ba	< 0.0052	1.03	< 0.0052	0.805	14.4	< 0.0140	0.153	121	0.0650	0.109	541	< 0.0046	< 0.0138	210	345
Hf	0.0472	1.23	0.0793	2.95	1.67	0.0301	0.615	0.670	0.0076	0.569	0.513	0.0482	1.03	1.85	3.68
Ta	0.0007	0.0285	< 0.0007	0.0842	0.483	0.0012	0.0141	0.157	0.0703	0.0153	0.189	0.0020	0.0749	1.88	1.81
Pb	0.0352	0.462	0.0819	0.128	0.288	0.0364	0.671	2.99	0.0293	0.722	3.25	0.0313	0.137	0.519	0.408
Th	0.0050	1.05	0.0019	0.199	0.112	0.0221	4.08	3.40	0.0140	3.69	2.87	0.0158	0.432	0.204	0.156
U	0.0031	0.329	0.0016	0.120	0.0673	0.0318	1.22	1.18	0.0289	1.43	1.23	0.0079	0.135	0.122	0.0438
La	0.0038	3.23	0.0033	2.26	2.73	0.0400	18.2	16.6	0.0468	11.4	11.0	0.0253	6.10	9.46	9.31
Ce	0.0095	7.59	0.0148	9.01	10.9	0.0655	16.9	14.5	0.0633	9.37	8.59	0.0882	19.0	30.7	31.5
Pr	0.0023	1.32	0.0036	1.73	2.01	0.0086	1.31	1.11	0.0094	0.965	0.877	0.0160	2.91	4.79	5.07
Nd	0.0222	7.50	0.0240	11.3	12.7	0.0584	5.39	5.28	0.0244	4.99	4.51	0.0940	13.9	23.5	27.0
Sm	0.0169	2.69	0.0199	4.11	4.23	0.0128	1.65	2.05	< 0.0045	1.66	1.62	0.0448	3.51	6.19	7.62
Eu	0.0067	1.01	0.0083	1.48	1.68	0.0171	0.657	0.719	0.0145	0.747	0.695	0.0192	1.17	2.11	2.70
Gd	0.0341	3.50	0.0439	4.81	5.70	0.0900	2.39	2.83	0.0410	2.24	2.37	0.0763	3.43	5.78	7.03
Tb	0.0101	0.573	0.0129	0.794	0.884	0.0202	0.407	0.484	0.0109	0.423	0.433	0.0207	0.535	0.819	0.959
Dy	0.1051	3.83	0.101	4.99	5.89	0.159	3.21	3.50	0.0720	3.19	3.20	0.180	3.55	5.07	5.14
Ho	0.0326	0.778	0.0294	0.954	1.15	0.0496	0.661	0.810	0.0305	0.670	0.703	0.0518	0.695	0.935	0.857
Er	0.1087	2.07	0.113	2.51	3.01	0.209	1.85	2.23	0.119	1.91	2.12	0.190	1.87	2.31	1.87
Tm	0.0228	0.316	0.0223	0.366	0.417	0.0374	0.284	0.314	0.0210	0.278	0.325	0.0383	0.261	0.308	0.230
Yb	0.233	1.99	0.219	2.17	2.7	0.335	1.93	2.08	0.150	1.99	2.07	0.300	1.58	1.87	1.25
Lu	0.0470	0.274	0.0389	0.292	0.358	0.0585	0.256	0.283	0.0183	0.266	0.309	0.0571	0.225	0.260	0.144

Representative analysis of n measurements; ol: olivine; opx: orthopyroxene; cpx: clinopyroxene; sp: spinel; am: amphibole

The high olivine modal content in 13RP16 and the convex downward REE pattern due to the strong fractionation of the LREE (along with U and Th) relative to the MREE-HREE indicate that this lithology was obtained through the interaction of an evolved melt (see below) with a peridotite. The term "evolved melt" refer here to a melt which results from a melt-rock reaction leading to a significant decrease of the melt/rock ratio and thus to a significant enrichment in the most incompatible elements in the newly produced melt. Thus, the "pyroxenite part" is a vein wall rock. Therefore, in the case of 13RP16 we do not have a direct access to the "true" pyroxenite.

In most samples, obtaining water content in the pyroxenitis NAMS was challenging. This was due to the common occurrence of exsolution which strongly disrupt the absorption spectra in FTIR. However, the few cpx and opx analysed indicate that water content using the calibration of Paterson (1982) for the 11 cpx measures in 13RP15 and 13RP16 varies between 250 and 488 ppm and from 149 to 253 in the opx (n=15) (Table V.8). Using the calibration of Bell *et al.* (1995) cpx range between 300 and 530 ppm (average= 480 ± 65 ppm), which is comparable to the range, reported in garnet-spl pyroxenite from Hawaii (260-576 ppm; average = 435 ± 87 ppm) by Bizimis *et al.,* (2015) using this same calibration. The same observation is true for the opx (C_{OH}(opx) = 241 ± 42 ppm wt. H_2O *vs* for Bizimis *et al.* (2015) C_{OH}(opx) = 216 ± 42 ppm wt. H_2O). These values are similar to the average water content for cpx and opx in spl-peridotites that is *ca*. 478 ± 167 and 256 ± 117, respectively.

3.2 Geochemical variation in the peridotite wall rock – major and trace elements including H

The representative major element concentrations of minerals in both sides of the contact of the selected xenoliths are in Table V.6. The representative trace element concentrations associated are in given Table V.7. Finally, the statistics of H concentration of the analysable minerals are given in Table V.8. More exhaustive datasets are available in Annexe 2 for each samples of this study. The same convention as in section V.2.2 is used here to describe the chemical variations of the minerals within the host rock. They are described from the peridotite toward the patch. The distance to the contact is given in mm. Zero denotes the contact. Positive distances denote analyses made in the host rock side, while negative values refer to analyses obtained in the pyroxenite side.

Modal abundances away from the pyroxenitic part indicate that 13RP16 is a cpx poor lherzolite (cpx = 5 %) containing 1 % of disseminated amphibole. Olivines in the lherzolite part are transparent grains (up to 3 mm) and have a Fo% *ca*. 89.4 away from the contact (at x ≈ +10 mm). Fo content increases through the contact up to 89.9 at x ≈ -15 mm (Figure V.10a). Thus, olivines in the pyroxenitic part are more refractory than in the Lherzolite.

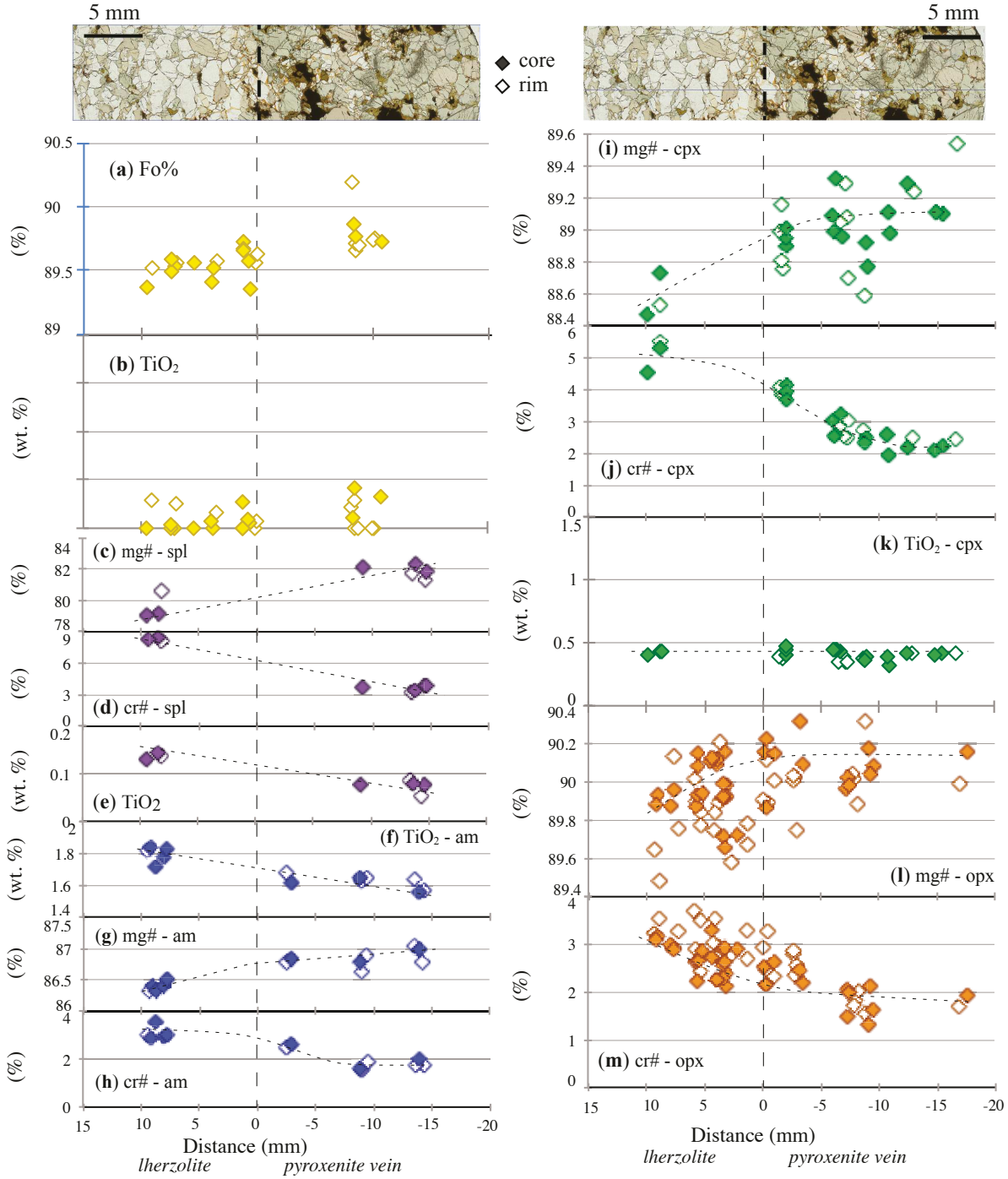

Figure V.10. – Main chemical variations on major elements concentration (wt.%) for sample 13RP16 are given as a function of distance from the contact between the lherzolite and the glassy patch for ol from (**a**) to (**b**); for spinel (spl) from (**c**) to (**e**); for amphibole (am) (**f**) to (**h**); for cpx from (**i**) to (**k**) and for opx from (**l**) to (**m**).

Spinel has a low cr# (≈ 9 %) which decreases further toward and within the ol-websterite (down to ≈ 3 %). The low Fo% and $cr\#_{spl}$ are more akin to fertile lherzolite and are thus not in agreement with the low cpx modal abundances. The opx have mg# about 88.9 % in the peridotite and their composition seems to evolve toward a more refractory composition in the ol-websterite ($mg\#_{opx}$ up to 90.2, Figure V.10.l). $Cr\#_{opx}$ decreases continuously from *ca*.

3.9 in the peridotite down to 1.2 % in the ol-websterite. However, the more striking features here is the extreme variability of the composition between and within (strong core-rim zonation) opx grains. They also display core-rim variations in cr# with higher values in the rim (due mainly to higher Al_2O_3 =5.2 *vs*. 4.5 wt. %) than in the core (Al_2O_3 = 4.5 wt. %). This core-rim variations of cr# vanish in opx at x = -5 mm (in the vein).

The equilibrium temperature calculated with the geothermometer of Brey and Köhler (1990) based on the Ca distribution between pyroxenes is ca. 1047 °C within error of the one obtained for the ol-websterite part (1044 °C).

Clinopyroxenes and amphiboles in the peridotite part, show a flat HREE to MREE segment and a strong enrichment of the most incompatible LREE (*i.e.,* La, Ce and Pr; La_N up to 80; (Figure V.11). These patterns are identical to the one described earlier for the ol-websterite for cpx and amphibole. However, the abundance of La is higher in the peridotite than in the websterite. Furthermore, a continuous trend of La enrichment across the whole length of the thin section is observed; *i.e*., from the websterite right end ($(La)_N$ = 48 at x = -20 mm) toward the left end of the peridotite ($(La)_N$ = 76.6 at x = +12 mm). Sm remains relatively constant across the whole section, as well as Lu abundance (Figure V.12). Even if the spatial resolution for measurement in amphibole is poorer (less analyses), it shows the same variations than cpx (Figure V.12). Amphibole and cpx display Zr, Hf, Nb and Ta negative anomalies as in the websterite part (Figure V.9). However, clinopyroxenes show a Nb fractionation relative to Ta, which in not present in amphibole nor in opx. This fractionation is almost constant across the whole-section.

H concentrations were determined in olivine and pyroxenes in both lherzolite and pyroxenite. H concentrations (within 30 % of error) for each phase show no variations across the contact (Figure V.13). However, we note that water content in olivine is highly variable from 2 to 9 ppm. In the lherzolite, the average C_{OH} equals 5.3 ± 2.2, 220 ± 33, 263 ± 51 ppm wt. H_2O for olivine, opx and cpx respectively (Table V.8). In the pyroxenite, the average H contents are 5.4 ± 1.5, 211 ± 14, 343 ± 65 ppm wt. H_2O for olivine, opx and cpx respectively. However, a slight variation in the partition coefficients $Kd_{H2O}^{cpx/opx}$ is observed (1.2 ± 0.3 and 1.6 ± 0.5 for the lherzolite and the vein respectively).

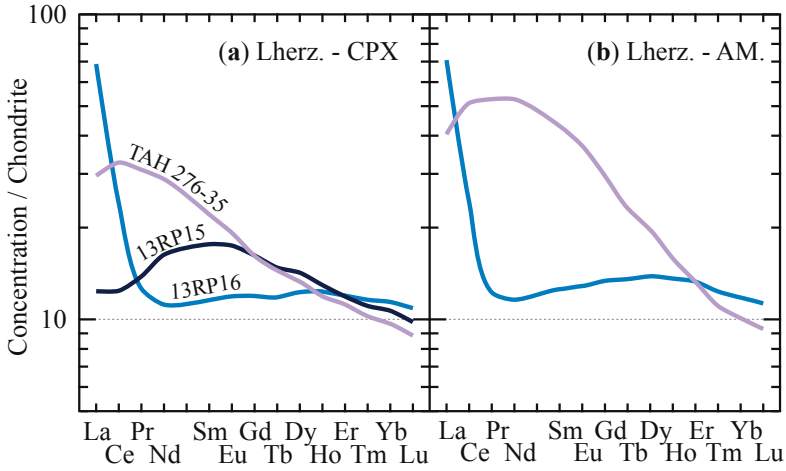

Figure V.11. – Trace element concentrations in (**a**) cpx and in (**b**) amphibole of the peridotite part of each sample (normalisation to chondrite values using from McDonough and Sun, 1995).

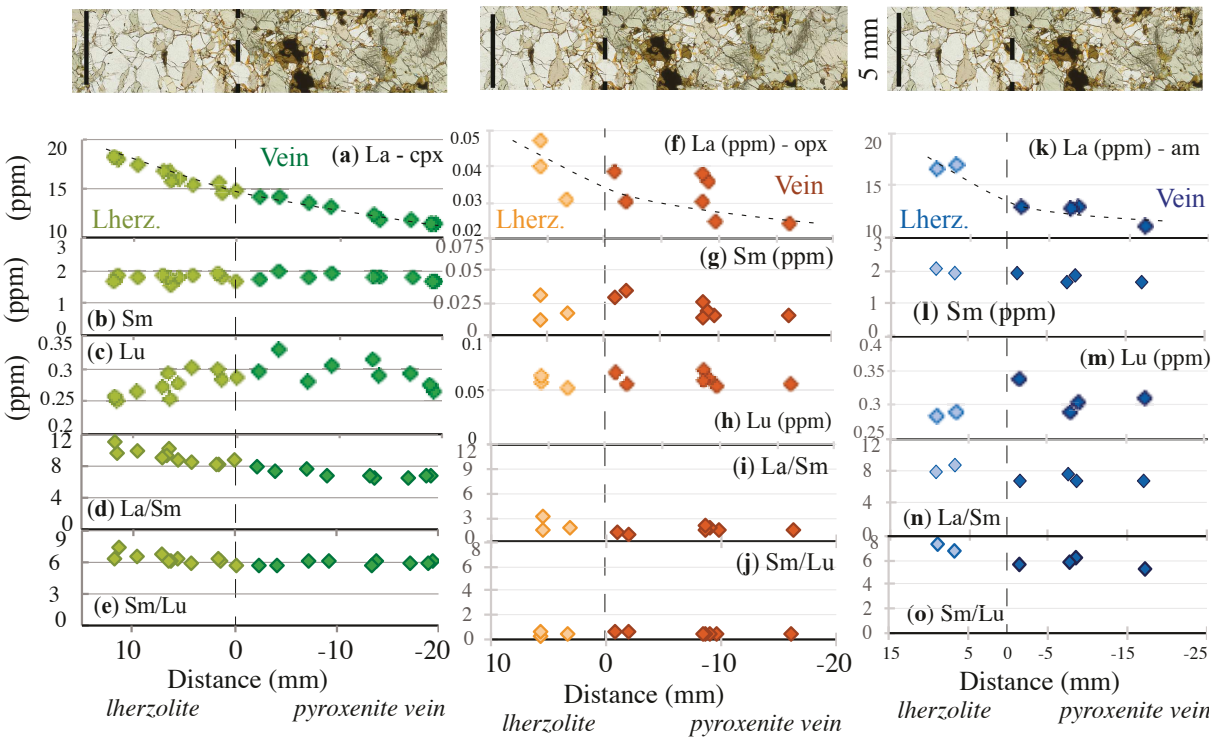

Figure V.12. – Trace element concentrations (ppm) of sample 13RP16 minerals as a function of the contact between the lherzolite and the pyroxenite vein for clinopyroxene (cpx) from (**a**) to (**e**), for orthopyroxene (opx) from (**f**) to (**j**) and for amphibole (am) from (**k**) to (**o**).

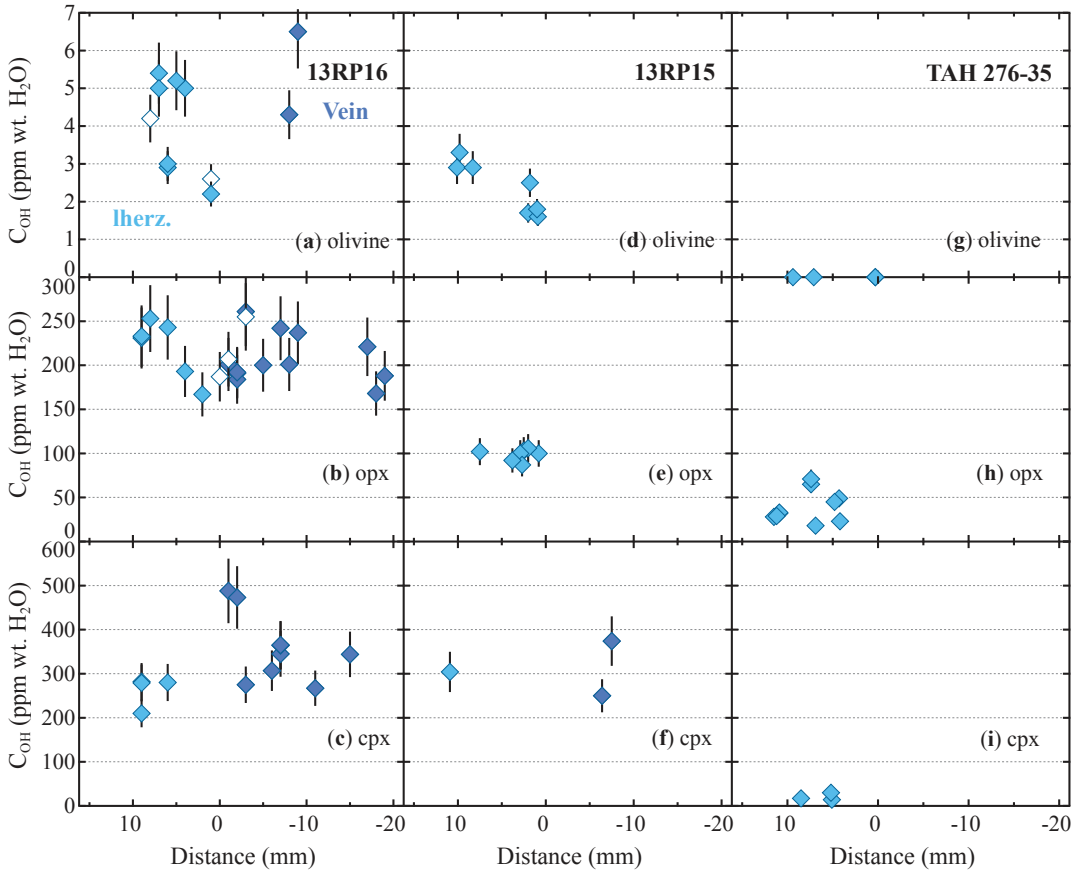

Figure V.13. – Hydrogene concentration (C_{OH}) in olivine, orthopyroxene (opx) and clinopyroxene (cpx) as a function of distance from the contact between the lherzolite and the amphibole bearing vein for sample 13RP16 ((**a**) to (**c**)); sample 13RP15 ((**d**) to (**f**)) and sample TAH 276-35 ((**g**) to (**i**)).

Sample **13RP15** has a coarse grain microstructure and is a lherzolite (cpx =8 %) containing few rare grains of amphibole (0.6 %). Olivines in the lherzolite part have a Fo% *ca*. 89.4 away from the contact (x ≈ +10 mm) as in 13RP16. Fo content slightly increases toward the contact up to 89.7 (Figure V.14a). As in 13RP16 spinels have a low cr# (≈ 7 %) and decrease further toward and within the pyroxenite, *ca.* 5.5 % at the contact, about 4. % in the pyroxenite border and down to ≈ 0.5 % in the pyroxenite centre. Opx in the peridotite part way from the contact have $mg\#_{opx}$ about 89.9 ± 0.1% in equilibrium with the olivine. SiO_2, FeO and Cr_2O_3 contents in opx decrease toward the contact and within the vein while the Al_2O_3 content increases (Figure V.14). However, CaO content in opx remains constant throughout the entire samples (CaO_{opx}=0.46 ± 0.02wt.%). The most remarkable feature is a strong chemical variation between and within (core-rim) variation observed for almost all elements in the contact zone (0<x<5 mm). Cpx away from the contact have mg# *ca*. 90.0 ± 0.2% and $cr\#_{cpx}$= 5 ± 0.1 %; CaO, Al_2O_3 and NaO content about 22.4 ± 0.2, 5.5 ± 0.2 and 1.1 ± 0.05 wt.%, respectively. Toward the contact, CaO content is quite variable and remains in average roughly constant despite large variability (21.6−22.6 wt.%) as SiO_2, MgO, FeO and Na_2O; while Al_2O_3 and TiO_2 increase slightly up to 6.3 and 1.05 ± 0.05, respectively. $Cr\#_{cpx}$ decreases down to 3.5%. The slope of this variation is greatly enhanced in the border of the pyroxenite (-3<x<0 mm). It is worth noting that the cpx rims show less variation, in

particular in the pyroxenite part. For instance TiO_2 and Al_2O_3 content in the rims of the cpx from the pyroxenite is *ca.* 0.88 ± 0.06 and 5.9 ± 0.4 wt.% much lower than the core composition about 1.28 ± 0.07 and 8.0 ± 0.2 wt.%, respectively, but comparable to the cpx composition from the peridotite (*ca.* 0.89 ± 0.11 and 5.8 ± 0.4 wt.%, for TiO_2 and Al_2O_3 respectively). Amphiboles display a notable enrichment in K_2O toward the core of the vein.

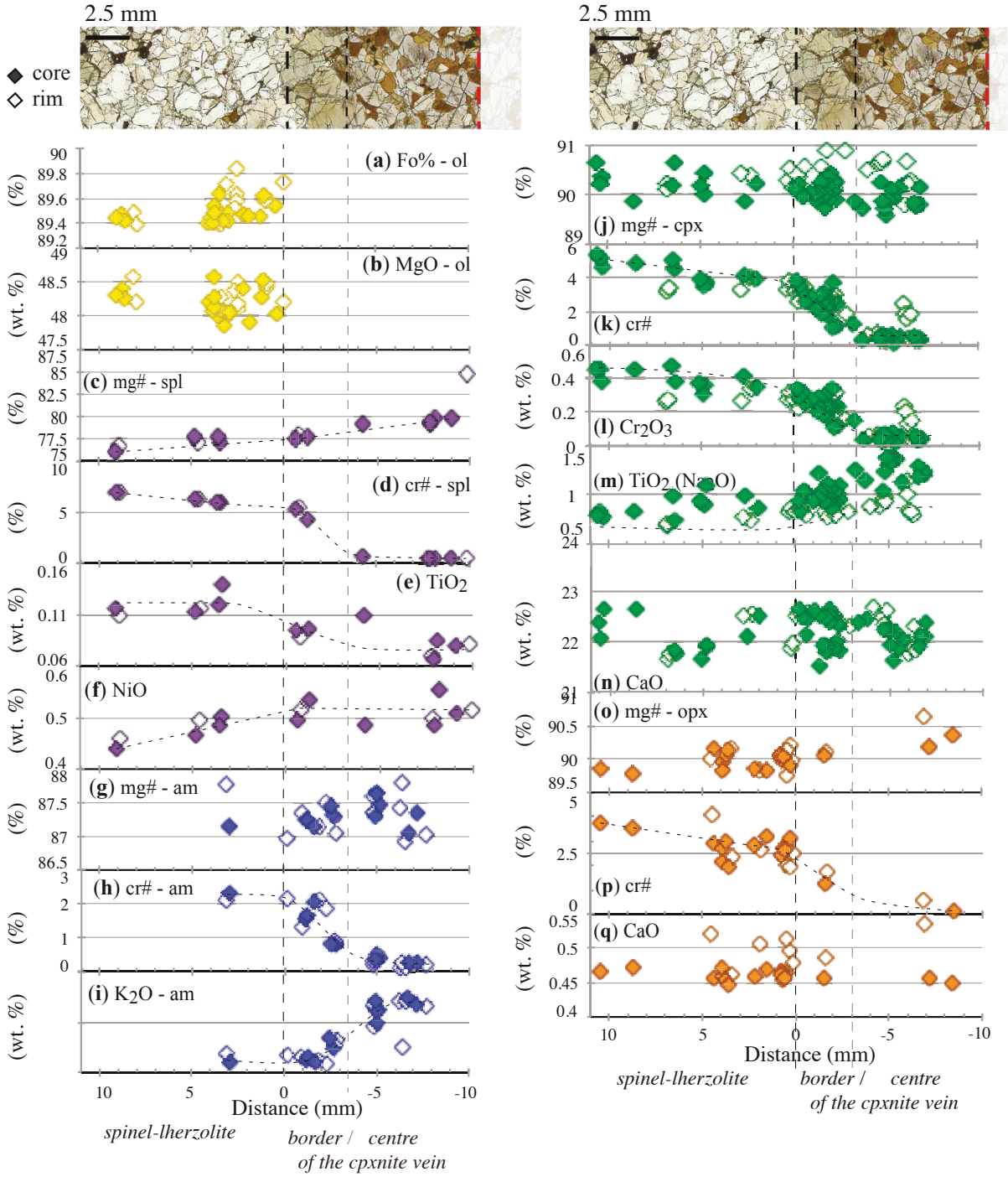

Figure V.14. – Main chemical variations on major elements concentration (wt.%) for sample 13RP15 are given as a function of distance from the contact between the lherzolite and the glassy patch for ol from (**a**) to (**b**); for spinel (spl) from (**c**) to (**f**); for amphibole (am) (**g**) to (**h**); for cpx from (**i**) to (**k**) and for opx from (**l**) to (**m**).

The equilibrium temperature calculated with the geothermometer of Brey and Köhler (1990) yield a temperature ca. 821 °C ± 19 within error of the one obtained for the co-existing clinopyroxenite (842°C).

Diopsides in the peridotite part have a convex upward pattern, due to the specific enrichment of the MREE relative to the HREE and LREE (Figure V.11). These patterns are broadly similar to those found in the cpx from the pyroxenite (Figure V.9). However, compare to the cpxs from the clinopyroxenite, cpxs from the peridotite are characterised by (i) lower REE abundances, for instance $8.7<(Lu)_N<10.8$ relative to $10.8<(Lu)_N<12.3$; (ii) a less convex upward patterns as shown by their lower $(Sm/Lu)_N$ *ca.* 10.9 ± 0.9 compare to $(Sm/Lu)_N$ ca. 12.6 ± 1.1; and (iii) they are characterised by a selective enrichment of La relative to Ce not observed for the pyroxenite's cpx and higher La abundances ($(La)_N$) ranging between 11.2 up to 13.6 compare to 9.6 ± 0.4. A similar effect is also observed for U and Th. The extended trace element patterns similar in both parts of the sample (Annexe 2) are also marked by pronounced Nb and moderate Zr-Ti and Sr negative anomalies. However, Hf and Ta are not depleted relative to their neighbouring REE, La and Eu respectively. This lead to extremely high $((Nb/Ta)_{PM}$ up to ~30 at 12 mm from the contact. The Zr/Hf and Th/Ta ratio decreased in the lherzolite toward the centre of the vein in both pyroxenes (Annexe 2).

Most trace elements show significant variation at the scale of the thin section. All show an almost linear (straight) variation with the distance (x in mm) (Figure V.15). However these correlations are either negative (*i.e.*, increase toward and within the pyroxenite) for all the REE except La, and all the HFSE, or positive for La, Th, U, Pb, (Cs) and Rb. For Nb the extreme variability (may be due to the incorporation in variable amount of exsolution) between and within grains does not allow to reach a firm conclusion on its behaviour. Clearly, the difference of behaviour between these two groups of elements is related to their difference in term of incompatibility. This is clear if we consider the distinct behaviour of La relative to the others REE. Th, U, Pb, Cs and Rb are all more incompatible than La (*i.e.* $D^{cpx/melt}$ (U,Th, Pb, Cs,Rb) < $D^{cpx/melt}$ (La)). Thus, the increasing abundances of these incompatible elements downstream demonstrate that the peridotite part is downstream stream relative to the percolation front and upstream relative to the percolation front and chromatographic front of La.

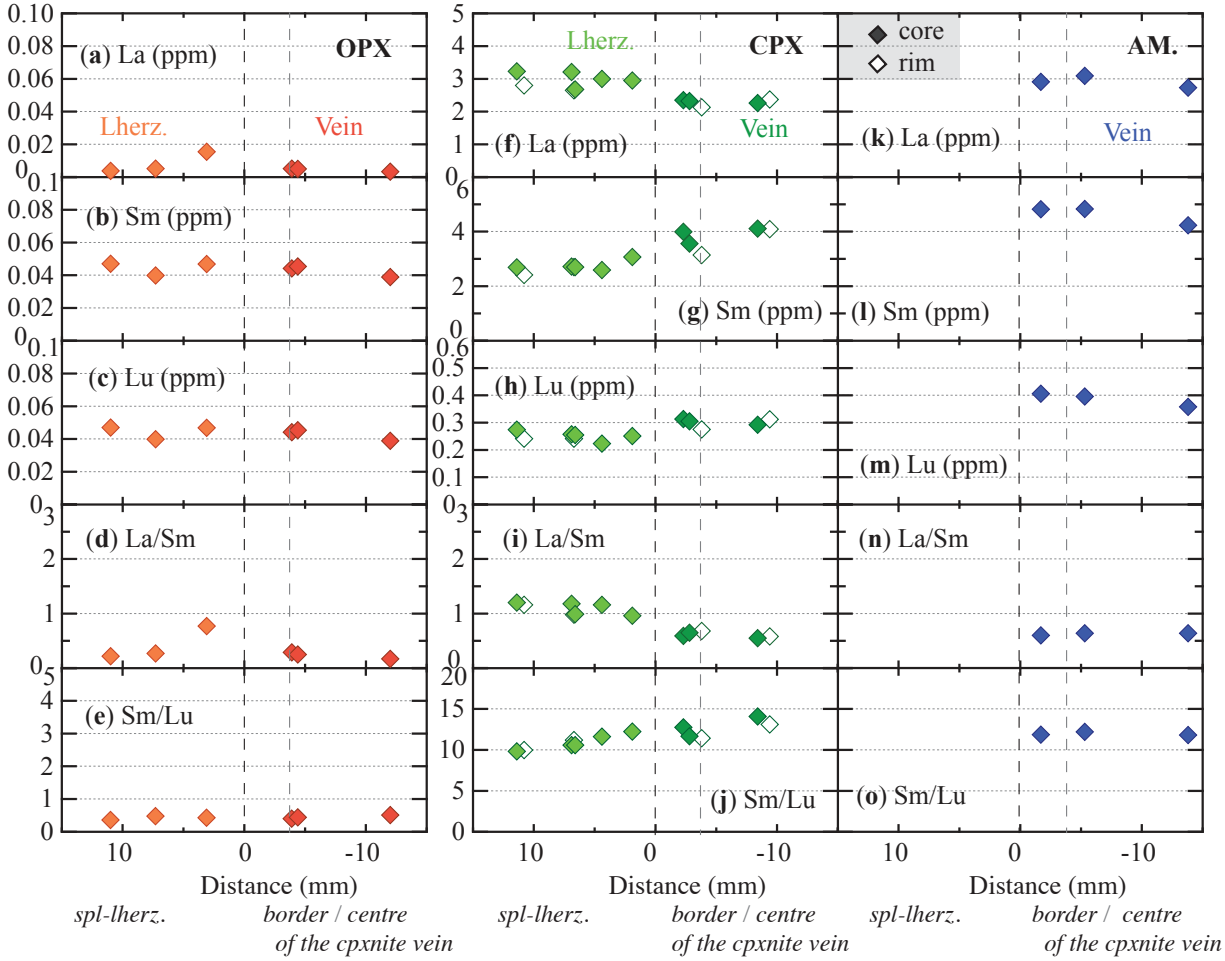

Figure V.15. – Trace element concentrations (ppm) of sample 13RP15 minerals as a function of the contact between the lherzolite and the pyroxenite vein for cpx from (**a**) to (**e**), for orthopyroxene (opx) from (**f**) to (**j**) and for amphibole (am.) (from (**k**) to (**o**).

H concentrations were determined in olivine and pyroxenes in both lherzolite and pyroxenite. Unfortunately the IR spectra obtained were, for a large number of pyroxenes, not of sufficient quality to yield a reliable water concentration for many grains. Hydrogen concentrations for seven olivine grains (which only occur in the peridotites part) range between 1.5 and 3.3 ppm wt. H_2O. Although, olivine near the contact have in average lower H concentration *ca*. 1.9 ± 0.4 ppm wt. H_2O than downstream olivine which have H concentration *ca*. 3.0 ± 0.2 ppm wt. H_2O. The high uncertainty (*i.e.* 30 %) inherent to these measurements and the weak statistic preclude to conclude that olivine shows a variation. Furthermore this is supported by the homogenous H concentrations of the opx within the peridotite part (C_{OH}(opx) = 99 ± 7 ppm) (Figure V.13, Table V.8). No data are available for the pyroxenite's opx. The three successful analyses of the cpx suggest that there is not variation across the samples. Indeed H concentrations in cpx are about 304 (n=1) and 312 ± 88 for the peridotite and the core pyroxenites, respectively. $Kd_{H2O}^{cpx/opx}$ in the lherzolite is 3.1 ± 0.9.

Table V.8 – H concentration in ppm wt. H_2O for available/analysable minerals of each sample 13RP15, 13RP16 and TAH276-35.

13RP15	**Ol**		**Opx**		**Cpx**	
	host	vein	host	vein	host	vein
n	7	0	7	0	1	2
Factor	16.35	-	11.57	11.57	12.09	12.07
min P82	1.6	-	87	-	-	250
max P82	3.3	-	106	-	-	374
C_{OH} avg P82	**2.4**	*2.5*	**99**	*149*	**304**	**312**
±1SD	*0.7*	/	*6.7*	/	/	*87.7*
C_{OH} avg W12	**3.0**	/	-	-	-	-
±1SD	*0.7*	/	-	-	-	-
C_{OH} avg B95	-	-	**105**	/	**529**	**530**
±1SD	-	-	*9.1*	/	/	*94.3*

13RP15	**WR**	
	host	vein
C_{OH} WR (w/. am)[a]	54.5	199
±1σ	*9.3*	*35.3*
C_{OH} WR (w. am)[b]	175	5639
±1σ	*24*	*688*
Kd cpx/opx (H_2O)	3.1	/
±1σ	0.9	/
Kd cpx/ol (H_2O)	127	/
±1σ	38	/
Kd opx/ol (H_2O)	41	/
±1σ	12	/

13RP16	**Ol**		**Opx**		**Cpx**	
	host	vein	host	vein	host	vein
n	13	2	7	14	3	9
Factor	16.35	16.34	11.55	11.55	12.09	12.08
min P82	2.2	4.3	167	168	267	267
max P82	8.9	6.5	253	261	282	488
C_{OH} avg P82	**5.3**	**5.4**	**220**	**211**	**263**	**343**
±1SD	*2.2*	*1.5*	*32.5*	*13.9*	*51.0*	*65.0*
C_{OH} avg W12	**3.2**	**3.6**	-	-	-	-
±1SD	*1.2*	*1.0*	-	-	-	-
C_{OH} avg B95	-	-	**269**	**241**	**480**	**612**
±1SD	-	-	*46.3*	*41.9*	*65.3*	*130.6*

13RP16	**WR**	
	host	vein
C_{OH} WR (w/. am)[a]	69.2	192
±1σ	*11.8*	*32.7*
C_{OH} WR (w. am)[b]	309	2952
±1σ	*55*	*376*
Kd cpx/opx (H_2O)	1.2	1.6
±1σ	0.3	0.5
Kd cpx/ol (H_2O)	42	39
±1σ	13	20
Kd opx/ol (H_2O)	50	63
±1σ	13	12

TAH276-35	**Ol**	**Opx**	**Cpx**
	host	host	host
n	4	10	3
Factor	16.55	11.66	12.14
min P82	0.0	18	14
max P82	0.0	71	30
C_{OH} avg P82	**0.0**	**39**	**20**
±1SD	*0.0*	*17.7*	*8.8*
C_{OH} avg W12	**0.0**	-	-
±1SD	*0.0*	-	-
C_{OH} avg B95	-	**36**	**35**
±1SD	-	*17.9*	*14.8*

TAH276-35	**WR**
	host
C_{OH} WR (w/. am)[a]	9.2
±1σ	*1.6*
C_{OH} WR (w. am)[b]	189
±1σ	*25*
Kd cpx/opx (H_2O)	0.5
±1σ	*0.2*
Kd cpx/ol (H_2O)	/
±1σ	/
Kd opx/ol (H_2O)	/
±1σ	/

C_{OH} avg P82 are average H concentration on n grains using calibration of Paterson (1982); C_{OH} avg W12 are Average H concentration on n grains using calibration of Withers *et al.* (2012); C_{OH} avg B95 are Average H concentration on n grains using calibration of Bell *et al.* (1995); ol: olivine; opx: orthopyroxene; cpx: clinopyroxene; sp: spinel; am: amphibole; Grey values are estimated H concentrations to calculated the whole rock H content C_{OH} WR taking in count amphibole ([a]) or not ([b]).

The peridotite part of the composite xenolith **TAH276-35** shows a porphyroclastic microstructure dominated by fine-grained neoblasts in which rare but large porphyroclasts of opx occur. The modal abundances of the peridotite part indicate a spl-lherzolite mineralogy. However, the high cpx/opx ratio *ca.* 0.82 indicate that this mineralogy is not primary, *i.e*. residual after melting. This is confirmed by the Fe-rich composition of the olivine (Fo% 86.8) which is not compatible with the high $cr\#_{spl}$ (*ca.* 71.9 %) (Table V.6). Disseminated dark-brown amphiboles occur (0.9 %) but only in the first 5 mm in contact with the amphibolite. Opx away from the contact have a low mg# (87.5%) in equilibrium with the olivine and high CaO content about 0.9 wt.%. Cpx are diopsides with low mg# (87%) and CaO content ca. 20.4 wt.%. The disseminated amphiboles are pargasites with a mg# varying between 82 and 83% which are quite rich in Cr_2O_3 (up to 1.2 wt.%).

The equilibrium temperature of the lherzolite is 985 °C ± 12 using the two pyroxenes Brey and Köhler (1990) geothermometer. Strong variations of the mineral composition occur like all phases are enriched in FeO (lower mg#) moving toward the contact and are enriched in TiO_2 (Figure V.16). Such variations were classically described in amphibolite wall rock (*e.g.* Bodinier *et al*., 1991).

Clinopyroxenes have a REE patterns characterised by a continuous enrichment from Lu to Nd (Figure V.11). Then, although the LREE are enriched relative to the HREE and MREE, their normalised abundance vary significantly. For instance, $(La)_N$ range from 21 near the contact to 51 away from the contact. As shown in Figure V.17 the convex upward pattern inherited from the pyroxenite is progressively smoothed up. The ratio (La/Ce) evolve from 0.85 to 1.15. Concomitantly, the abundances of HREE increase away from the contact *i.e*., $(Lu)_N$ range from 5.6 to 10.6. Accordingly to the $Kd^{cpx/amp}$(REE) near unity (Coltorti *et al.,* 2000, 2004; Grégoire *et al*., 2000; Tiepolo *et al*., 2007; Vannucci *et al*., 1995), the REE pattern of amphibole mirrors those of the neighbouring cpx, U−Th and Nb behave like La. The extended trace element patterns of the cpx are otherwise characterised by Ta, Zr−Hf, Ti moderate negative anomalies and low Sr and Rb−Ba. The amphiboles show the inverse anomalies: positive Nb−Ta and Ti anomalies, high Sr, Rb−Ba abundances and pronounced negative U−Th anomalies.

The Amphibolite TAH 276-35 is characterised by a cpx-rich mineralogy and an overall enrichment in FeO and TiO_2 (*i.e.,* mg# ~77 %) in the lherzolite indicate that this wall rock have been extensively reequilibrated with the parent melt of the amphibolite (a volatile rich alkali melt). This would imply that the entire peridotite wall rock was upstream relative to the reaction front. However, the over enrichment of the LREE observed in the cpx away from the contact and the variation of the HREE suggests that this front reseeded in a second time down to the limit of the disseminated amphibole (ie. $x < 5mm$) and that the remaining melt percolated downstream. Leading to the chromatographic enrichment of LREE, Th and U.

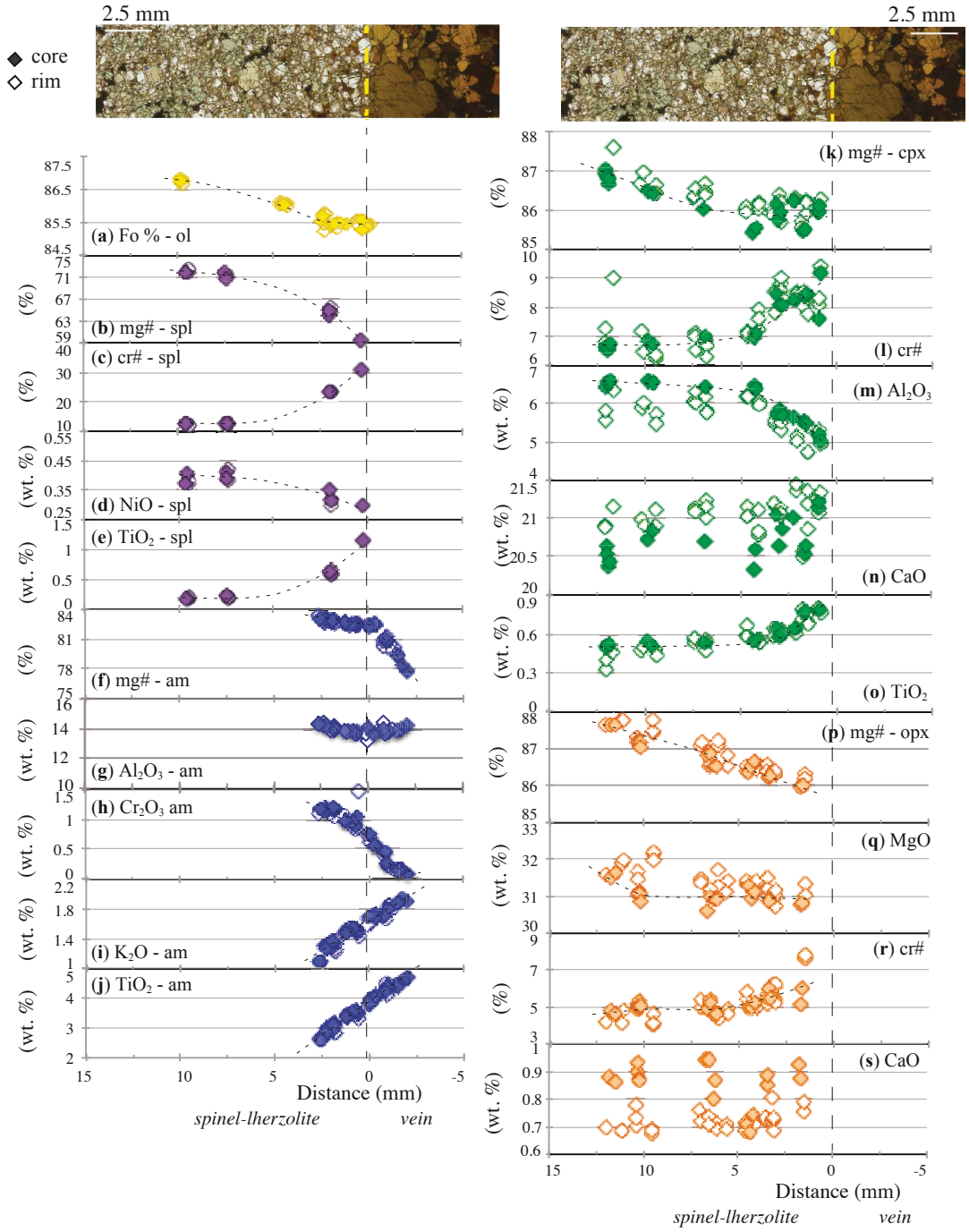

Figure V.16. – Main chemical variations on major elements concentration (wt.%) for sample TAH 276-35 are given as a function of distance from the contact between the lherzolite and the glassy patch for ol from (**a**); for spinel (spl) from (**b**) to (**e**); for amphibole (am) (**f**) to (**j**); for cpx from (**k**) to (**o**) and for opx from (**p**) to (**s**).

H concentrations were determined in olivine and pyroxenes in the lherzolite. The absence of OH stretching peaks in olivine spectra indicates the absence of H in olivine (Figure V.4). Average H contents are very low 0, 39 ± 18, 20 ± 9 ppm wt. H_2O for olivine, opx and cpx respectively (Table V.8). Then, it gives an unusual $Kd_{H2O}^{cpx/opx}$<1. It is probably due to the very low H concentrations in the NAMs from TAH-276-35. Nevertheless, H concentrations in all phases do not show variations toward or near the contact with the amphibolite.

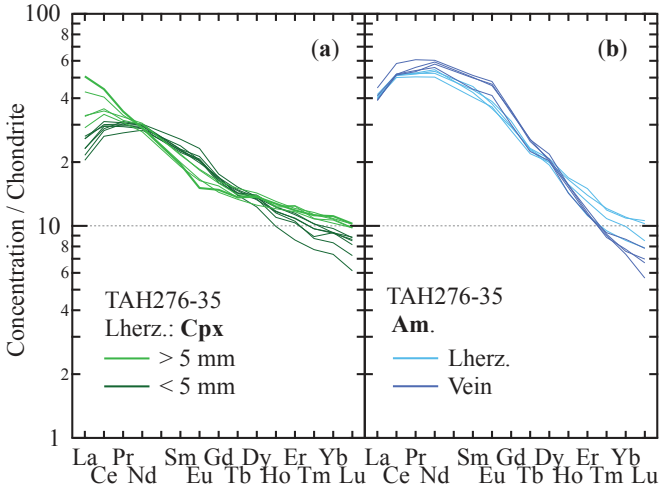

Figure V.17. – (on the left) Trace element concentrations in cpx and amphibole normalised to chondrite values in (**a**), (**b**) respectively (normalisation values are from McDonough and Sun, 1995).

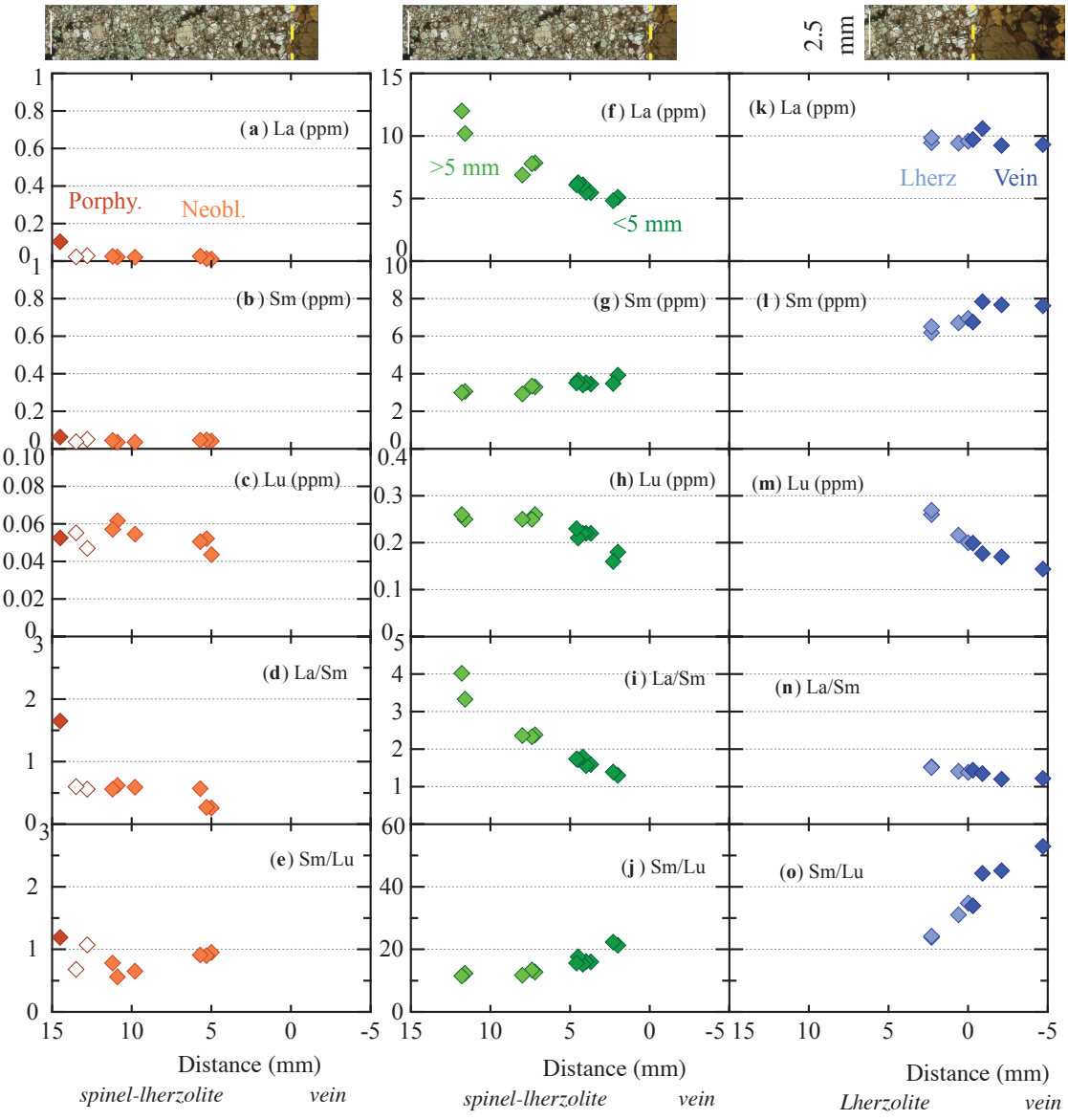

Figure V.18. – Trace element concentrations (ppm) of sample TAH 276-35 minerals as a function of the contact between the lherzolite and the amphibolite vein for opx from (**a**) to (**e**), for opx from (**f**) to (**j**) and for olivine (from (**k**) to (**o**).

3.3 Hydrogen behaviour in wall rock during percolation mechanism

The concentration is homogeneous within each phase of each sample (Figure V.13), taking into account the 30 % of error in the C_{OH} value. In other words, no clear variations of C_{OH} are observed in NAMs toward the contact with the vein. However, the concentration in the NAMs of the lherzolite seems correlated inversely with the modal content of amphibole in the vein. This suggests that, contrary to what one could expect, water within the peridotite NAMS are "sucked out" by the amphibole. Indeed, if we consider that water solubility in silicate melt decreases with decreasing pressure, one could suggest that the interaction and/or crystallisation with and/or within the mantle lithosphere will release water flux which could hydrate the surrounding dry lithospheric mantle (wall rock metasomatism). Such scenario is hardly in disagreement with our observations and measurements.

Hydrogen concentration of the cpx and opx in the pyroxenite are not particularly enriched in water compared to the same phases in peridotites. For instance, sample 13RP15 and 13RP16 show the same range of H concentration than the non-composite samples from this locality (Denis *et al.*, 2015) where C_{OH}(ol) = 2.1-5.9 ppm wt. H_2O; C_{OH}(opx) = 66-160 ppm wt. H_2O and C_{OH}(cpx) = 203-330 ppm wt. H_2O. H is inferred to be an incompatible element however, the three veins studied here contain significant amount of amphibole (14-98%). Thus, it could be argued that most of the water is stored in (and partition into) the amphibole (see figure V.19). Yet, the concentration range and average water content in the pyroxenes of the studied amphibole-bearing pyroxenites are comparable to those reported by Bizimis *et al.*, (2015) for "dry"(amphibole-free) pyroxenites. Such agreement between these two contrasted mineralogies is unexpected and will require further investigations. The petrology and geochemistry of these pyroxenites suggest that they were produced by the interaction of alkali-melts with the percolated peridotite and/or by the crystallisation at depth of alkali-melts. Alkali basalts commonly contain between 0.2 and 0.6 wt.% of water (Metrich and Wallace, 2008 and

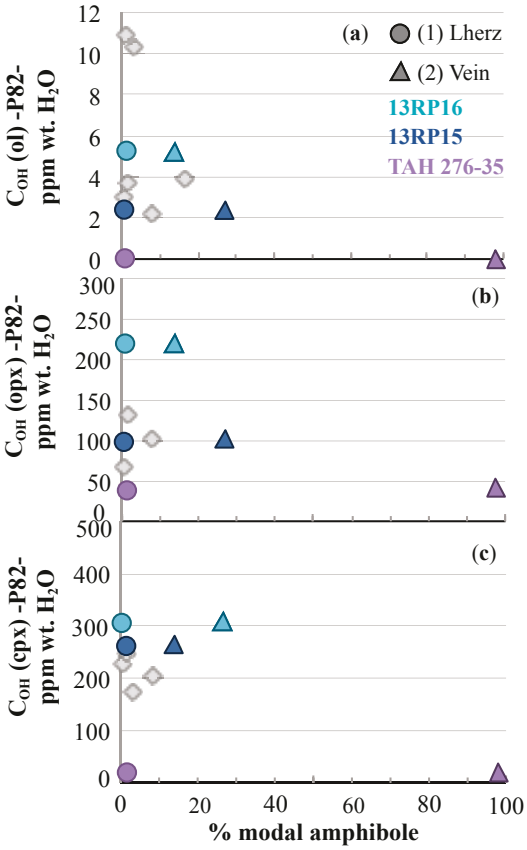

Figure V.19 – Hydrogen concentration (C_{OH}) in NAMS using calibration of Paterson (1982) (P82) in the lherzolite as a function of modal amphibole in (1) in the lherzolite, (2) in the vein. (grey diamonds are H concentration of the NAMs as a function of modal amphibole of the peridotite from Denis *et al.*, 2015 and Demouchy *et al.*, 2015).

references therein). Thus, this may suggest that a large part of water is not incorporated in the silicate during the pyroxenite crystallisation. In this case the crystallisation of pyroxenite could then be an interesting mechanism to produce small volume melt enriched in the most incompatible elements (such as LREE, U and Th) and in H_2O.

However, despite significant variations in incompatible trace elements in the wall rock of these veins due either to chromatographic effect or to reequilibration through diffusion liquid-solid in the reaction zone, no clear variation of the water abundance of the NAMs has been identified. This is unexpected, given that H is considered as incompatible as Ce. Although this unexpected behaviour require further investigation and numerical modelisation, a explanation for this lack of variation is maybe due to the high diffusivity of H which may at the mm scale smooth out quite rapidly any variations due to the percolation of volatile rich melts.

Chapitre VI : Conclusions générales

Ce chapitre détaille les impacts majeurs de l'étude, ainsi que les limites qui ont été atteintes et des propositions pour les dépasser.

Cette étude, focalisée sur la détermination des concentrations en H d'échantillons mantelliques naturels des xénolites du faciès à spinelle, apporte de nouvelles contraintes sur le comportement de l'H lors des processus magmatiques et mantelliques encore fortement débattu.

VI.1 Contraintes sur les concentrations H dans les péridotites à spinelle

VI.1.1 Préservation des concentrations lors de la remontée

Les effets de la remontée dans la plomberie magmatique sur les concentrations en H des minéraux des xénolites ont pu être étudiés sur une série de xénolites du champ volcanique d'Eifel. Une variation intracristalline de concentration en H a été identifiée uniquement dans l'olivine (pas dans les pyroxènes coexistants). Ces profils de concentration en H permettent l'estimation des vitesses de remontée des magmas, avec dans le cas des péridotites de Eifel des vitesses estimées entre 3.5 et 12 $m.s^{-1}$ (Denis *et al.,* 2013). Les variations de ces estimations, toutes obtenues pour des magmas hôtes de type basaltique, montrent aussi l'importance (i) de l'estimation de la profondeur de la source, (ii) de la prise en compte du caractère anisotropique de la diffusion de l'H dans un cristal en 3-dimensions, ainsi que (iii) du choix des coefficients de diffusion expérimentaux de l'H. Une amélioration envisageable de cet outil serait l'utilisation de péridotites à grenat qui ont l'avantage de permettre d'estimer avec plus de précision que pour les péridotites à spinelle la profondeur d'équilibre. Pour les échantillons à grenat, un géobaromètre tel que Nickel et Green (1985) donne ainsi des pressions d'une précision de ± 0,2 GPa.

La particularité de l'étude de Denis *et al.* (2013) repose sur la détermination des concentrations en H de l'ensemble des NAMs des xénolites. Les variations de concentration en H de l'olivine indiquent le potentiel de l'olivine à être un outil d'étude des systèmes magmatiques, et attestent d'une dévolatilisation n'affectant que l'olivine. Les concentrations en H dans les olivines des xénolites de péridotite peuvent sous-estimer les concentrations mantelliques de ces olivines.

Les pyroxènes coexistants avec ces olivines présentent des concentrations en H homogènes. Cette observation est en contradiction avec les données expérimentales qui donnent des coefficients de diffusions similaires à ceux de l'olivine pour une température donnée (10^{-11}–10^{-9} $m^2 \cdot s^{-1}$) (*e.g.,* Demouchy et Mackwell, 2006 ; Ingrin et Blanchard, 2006 ; Farver, 2010 ; Hercule et Ingrin, 1999). Lors d'un changement de conditions d'équilibre, l'H dans l'olivine est échangé avec le milieu extérieur par diffusion ionique tandis que dans les pyroxènes, l'H semble être bloqué dans la structure cristalline. Ce travail a mis l'accent sur la préservation des concentrations en H dans les pyroxènes. L'homogénéité des concentrations en H des pyroxènes indique qu'ils peuvent être utilisés comme un proxy de la concentration de l'H dans la source mantellique (Denis *et al*. 2013).

Une première hypothèse pouvant expliquer cette dichotomie entre les concentrations en H des olivines et des pyroxènes se rapporte aux coefficients de diffusion de l'H déterminés lors d'expériences d'hydratation des NAMs, potentiellement non-applicables au cas de la déshydratation par diffusion ionique (différentes énergies d'activation ? différents mécanismes de diffusion ?). Une seconde hypothèse réside, elle, dans l'effet d'un paramètre autre que la température (ou d'une conjonction de paramètres) qui accélère la diffusion de l'H dans l'olivine et/ou la ralentit voire l'inhibe dans les pyroxènes. Afin de contraindre le processus de déshydratation des NAMs et d'ajuster les modélisations de diffusion ionique de nouveaux travaux expérimentaux sont nécessaires. Une première approche serait de contraindre quels défauts (ponctuels ou à une dimension) sont thermodynamiquement privilégiés lors de la déshydratation. Une autre approche serait la mise en place d'une expérience de déshydratation d'un agrégat (olivine + opx + cpx). Une telle expérience, présentant ou pas les mêmes variations en H des NAMs des xénolites, permettrait de cibler le paramètre ou l'ensemble de paramètres qui affecte la diffusion de l'H dans les différents minéraux.

VI.1.2 Combien y a-t-il d'eau dans l'olivine ?

La préservation des concentrations en H dans les pyroxènes permet hypothétiquement d'évaluer la concentration initiale (mantellique) d'H dans l'olivine coexistante via les coefficients de partage expérimentaux de l'H ($Kd^{ol/opx}(H_2O)$ et $Kd^{ol/cpx}(H_2O)$).

Alors que le coefficient de partage de l'H cpx/opx semble être constant (2.1 pour la calibration de Bell *et al.,* 1995) dans les échantillons de péridotite à spinelle remontés par des basaltes en contexte intracontinental, les rares coefficients expérimentaux applicables à cette gamme de pression sont moins élevés (Aubaud *et al*., 2004 : $Kd^{cpx/opx}(H_2O) = 1.4$, à 1–2 GPa;1230 – 1380 °C ; Hauri *et al*.,2006 : $Kd^{cpx/opx}(H_2O) = 1.2$, à 1.2 – 1.6 GPa; 1185 – 1370°C). Ces coefficients expérimentaux sont le plus souvent obtenus dans des systèmes chimiques simplifiés pouvant entrainer cette différence. Une autre possibilité est liée au fait que ces expériences soient réalisées à saturation en H, ce qui n'est pas le cas dans le manteau sommital. Il est possible qu'un seuil proche de la saturation du système enclenche un mécanisme de diffusion différent dans certains solides cristallins affectant la solubilité de l'H dans ce solide. Cette perturbation des valeurs de coefficients de partage serait en cohérence avec les problèmes de modélisation des profils de déshydratation.

En se basant sur les coefficients de partage et les concentrations mesurées, on peut estimer la déshydratation subie par l'olivine. Le $Kd^{ol/opx}(H_2O)$ de 0.11, déterminé à 1 - 2 GPa et 1230 °C est le plus adapté au faciès à spinelle (Aubaud *et al.,* 2004). Les rapports de concentration en H entre olivine et opx coexistants ont une grande dispersion (Figure VI.1). Cette variation caractérise une perte en H de l'olivine jusqu'à 90 % de la concentration initiale. Les concentrations en H des minéraux des harzburgites suggèrent que l'olivine perd

plus d'eau que ceux des lherzolites. Dans cette thèse, les olivines analysées auraient majoritairement perdu 75 % de leur concentration initiale (soit un $Kd^{ol/opx}(H_2O)$ de 0.03) et aucune distinction n'est visible entre harzburgites et lherzolites (Figure VI.1).

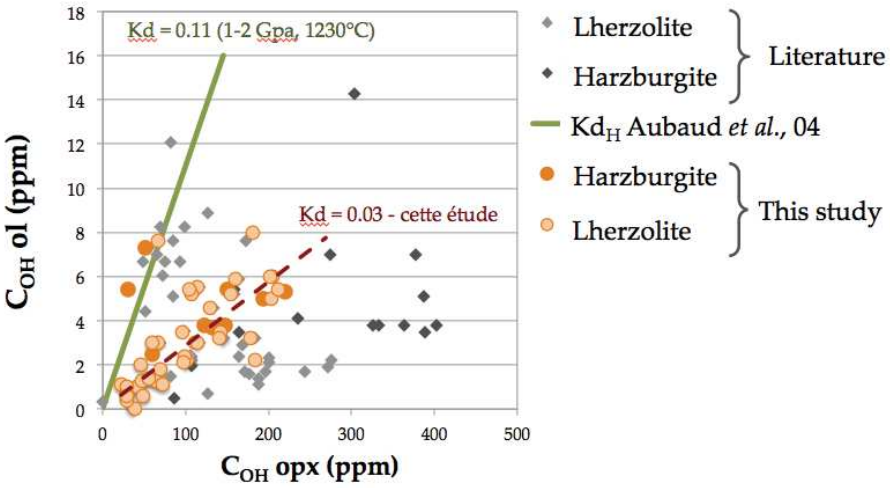

Figure VI.1– Concentration en H des olivines (ol) en fonction de la concentration en H des orthopyroxènes coexistants (opx). Dans le cas de lherzolites et d'harzburgites à spinelle.

VI.1.3 Quel minéral contrôle l'eau dans le manteau ?

L'olivine composant majoritaire du manteau, contrôle les propriétés physico-chimiques du manteau. Or les concentration en H de l'olivine sont faibles, sa participation dans le budget de l'eau du manteau est limitée. Les pyroxènes, bien que participants dans une moindre mesure aux propriétés physico-chimiques globales du manteau, permettent par le couplage de leurs concentrations avec des coefficients de partage expérimentaux adaptés (pression, température, système chimique) d'évaluer le budget de l'eau dans le manteau. Il est alors possible de contraindre l'influence réelle de la présence de l'H sur les propriétés de la roche (*e.g.*, anomalie de conductivité électrique).

Le budget de l'eau dans le manteau lithosphérique du faciès à spinelle, en absence de minéraux hydratés, est contrôlé par les pyroxènes. Généralement, le cpx a des concentrations en H deux fois plus élevées que l'opx (Denis *et al.,* 2015), c'est pourquoi il contrôle le budget en eau dans le cas des lherzolites. Cependant, le cpx étant plus fusible que l'opx, des épisodes de fusion partielle modifient la composition modale de la roche (cpx < 5 % vol., *i.e.* harzburgites). À l'aide de modèle de fusion, la participation de chaque minéral dans le budget de la roche peut être estimée. En faisant varier dans ces modèles, la concentration en H initiales dans le manteau, ainsi qu'en utilisant la gamme de coefficients de partage de l'H, on note que le rôle de l'opx devient alors prépondérant après quelques pourcents de fusion. (Fig VI.2).

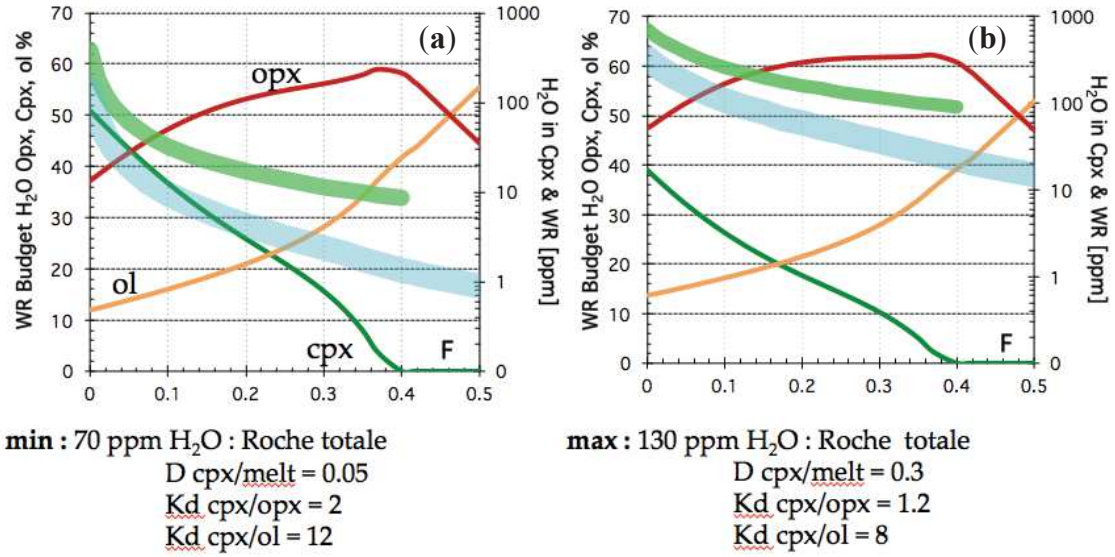

min : 70 ppm H_2O : Roche totale
D cpx/melt = 0.05
Kd cpx/opx = 2
Kd cpx/ol = 12

max : 130 ppm H_2O : Roche totale
D cpx/melt = 0.3
Kd cpx/opx = 1.2
Kd cpx/ol = 8

Figure VI.2 – Pourcentage de participation des NAMs au budget de la péridotite (lignes fines se rapportant à l'axe de gauche) en fonction du taux de fusion d'après le modèle de Kostopoulos (1992) ; ainsi que les concentrations associées dans le clinopyroxène (cpx, en vert clair) et la roche totale (WR, en bleu claire) (lignes épaisses se rapportant à l'axe de droite). Pour un manteau initial contenant 52, 27, 18.5, 2.5 % d'ol (Fo% 89.1), d'opx, de cpx et de spinelle respectivement.

Dans le cas du manteau lithosphérique du faciès à spinelle en présence de minéraux hydratés (*e.g.*, amphibole) le budget de l'eau est contrôlé par l'amphibole dès une proportion modale de 0,5 % d'amphibole dans une lherzolite (Figure VI.3a).

A priori la présence d'un minéral hydraté et donc d'un réservoir à H dans la roche pourrait impliquer des concentrations en H dans les NAMs élevées. A l'inverse, l'amphibole pourrait pomper l'H du système lors de sa cristallisation ce qui se traduirait par des concentrations en H dans les NAMs plus faibles. Or les concentrations en H des minéraux de la péridotite n'ont pas de corrélation avec la proportion d'amphibole coexistante (Fig.VI.3b). Aucune observation ne suggère que l'amphibole n'hydrate ou ne déshydrate la péridotite adjacente. Cependant dans le cas particulier d'une lherzolite recoupée par une amphibolite (Fig.VI.3b ; TAH276-35) la concentration en H des NAMs est particulièrement basse (< 50 ppm wt. H_2O pour les pyroxènes), l'effet de l'amphibole sur les concentrations en H des NAMs semble minime mais un biais d'échantillonnage ne peut être exclue.

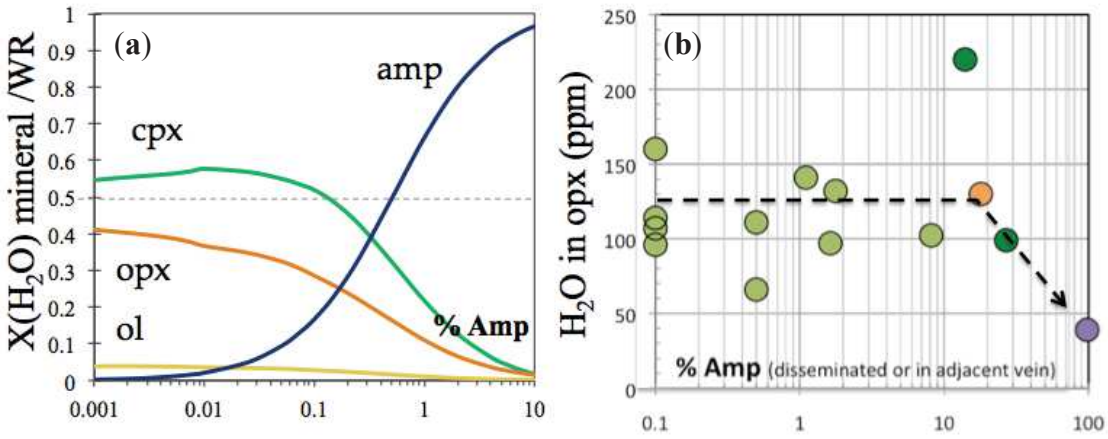

Figure VI.3– (a) Fraction des minéraux d'une péridotite à spinelle du budget en eau de la roche (WR), ol : olivine ; opx : orthopyroxène ; cpx : clinopyroxène ; amp : amphibole. Calcul pour C_{OH} de 6, 200 et 400 ppm wt. H_2O pour l'olivine, l'opx et le cpx, respectivement ; et 2 wt.% (20 000 ppm) H_2O pour l'amphibole, et pour un mode variant de 70 – 64.8 pour l'olivine, de 12 – 9.2 pour l'opx, de 18 – 16 pour le cpx et de 0 – 10 pour l'amphibole. (b) concentration en H dans l'opx en ppm wt. H_2O en fonction de la quantité d'amphibole dans la roche ou, pour les échantillons composite, la quantité d'amphibole dans le filon. Verts : Ray Pic, France, orange : Maroc, violet : TAH276-35, Algérie.

VI.2 Comportement de l'H lors des processus mantelliques

Les concentrations en H du manteau ont subi des épisodes successifs de fusion et de métasomatisme. On considère n'observer que le dernier épisode n de fusion et un épisode suivant n+1 de métasomatisme. Les concentrations en H des pyroxènes n'étant affectées par le processus secondaire d'extraction par le magma présentent l'avantage d'être un des objets sur lequel baser l'étude du comportement de l'H dans les processus mantelliques. Les éléments en trace tels que les REE dans les cpx sont des marqueurs des deux processus mantelliques principaux, la fusion partielle et le métasomatisme (*e.g.*, Griffin *et al*., 1996 ; Maury *et al.,* 1992 ; Ionov *et al*., 1993).

Précédemment, le comportement de l'H a été suggéré similaire à celui de La, Ce (*e.g.,* Dixon et al., 2002). Une telle incompatibilité induit que le dernier épisode de métasomatisme « efface » l'effet de l'épisode précédent de fusion.

VI.2.1 Le métasomatisme

D'une part, Denis *et al*., 2015 présente pour la première fois les résultats d'une étude multiéléments (majeurs et en trace, dont l'H) d'une suite de xénolites de péridotite en contexte de point chaud en présence de minéraux hydratés (amphibole). Les concentrations en H des minéraux ne suggèrent pas de lien avec le métasomatisme subit par la roche, qu'il soit modal (amphibole) ou cryptique (métasomatisme par de faibles fractions de liquides enrichis en volatils et d'éléments incompatibles).

D'autre part, l'étude basée sur des xénolites composites associant une péridotite accolée à un agent métasomatique (patch basaltique, filon de pyroxénite à amphibole) a pour originalité d'avoir ciblé l'influence du métasomatisme de petite échelle sur les concentrations en H des NAMs. L'interaction péridotite—basalte-hôte est caractérisée par un rééquilibrage des concentrations en éléments majeurs avec le liquide dans les olivines et les pyroxènes. La diminution des concentrations en H observées dans les olivines en se rapprochant du contact avec le patch basaltique est corrélée avec leurs variations de concentrations en SiO_2 et MgO. Plus les olivines sont rééquilibrées avec le liquide moins elles contiennent d'H. Une nouvelle fois, les pyroxènes ne présentent pas les variations de concentration en H aux abords du contact, observées dans l'olivine, alors qu'eux aussi présentent des variations de concentration en éléments majeurs.

Les échantillons présentant des filons (pyroxénite et amphibolite) ont permis l'étude du comportement de l'H lors du métasomatisme d'éponte, où les concentrations en H pour chacune des phases minérales sont homogènes. Cependant, plus les filons contiennent d'amphibole moins il y a d'H dans les NAMs.

Par ailleurs, l'ensemble des résultats acquis pendant cette thèse associé à ceux de la littérature ne montrent aucune corrélation entre la concentration en H et les enrichissements en LREE, ni avec le fractionnement entre les REE légères et moyennes (La/Sm) (Figure VI.4).

Ces observations sont en désaccord avec les études précédentes accordant à l'H un comportement plus proche d'une LREE (entre La et Ce) permettant ainsi à différents auteurs d'utiliser le rapport H_2O/Ce comme marqueur des processus mantelliques (*e.g.*, Danyushevsky *et al.,* 2000 ; Dixon *et al.,* 2002 ; Bizimis et Peslier, 2015 ; Peslier *et al*. 2015).

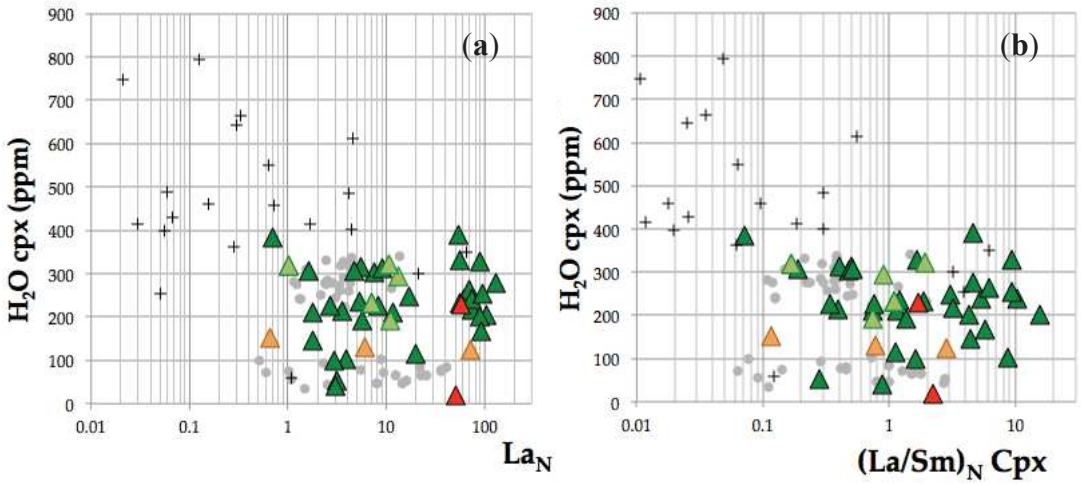

Figure VI.4 – Concentration en H du cpx en fonction de la concentration en La et le rapport La/Sm du cpx normalisés au manteau primitif (valeurs de normalisation Sun et McDonough, 1989). Croix : (péridotites abyssales) Warren et Haurri, 2014; points gris : (données mondiales péridotites mantelliques) Li *et al.,* 2008 ; Peslier *et al.,* 2006 ; Hao *et al.,* 2014 ; Peslier et Bizimis, 2015 ; triangles vert foncé : massif central français, triangle vert clair : Eifel, Allemagne, triangles orange : Newer volcanic field, Australie ; triangles rouges : Afrique du Nord.

VI.2.2 La fusion

Le métasomatisme n+1 n'a pas d'effet visible sur les concentrations en H des NAMs, ce qui suggère que les concentrations en H observées sont acquises lors de l'épisode n de fusion. En comparant les concentrations en H avec un marqueur de la fusion partielle (Yb du cpx) l'H semble avoir un comportement similaire à une MREE ($D^{cpx/liquide}(H_2O) \approx 0{,}25 \pm 0{,}05$; *e.g.*, Sm; $D^{cpx/liquide} = 0.29$; Johnson *et al*., 1998) (Figure VI.5).

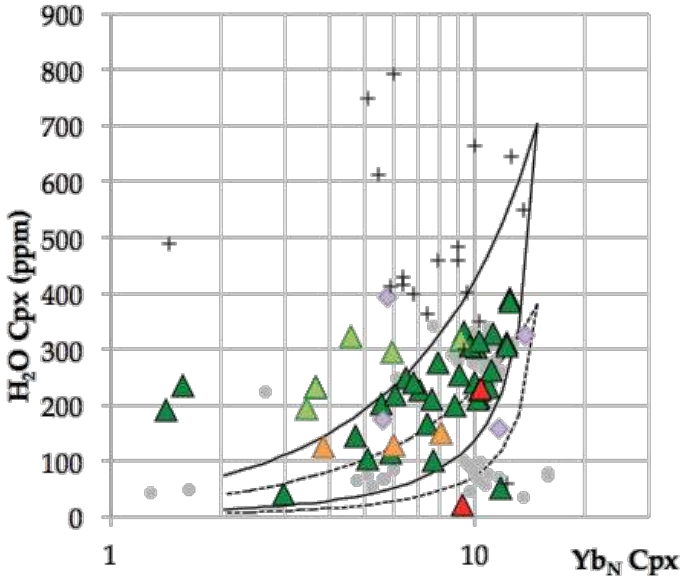

Figure VI.5 – Concentration en H du cpx en fonction de la concentration en Yb du cpx normalisés au manteau primitif (valeurs de normalisation Sun et McDonough, 1989). Voir légende Figure VI.4. losange : Demouchy *et al.*, 2015. Concentration en H du clinopyroxène lors de la fusion à l'équilibre d'après le modèle de Noman, 1998 d'un manteau contenant 18% de clinopyroxène ayant une concentration initiale en H de 700 ppm wt. H_2O (ligne) ou 400 ppm wt. H_2O (pointillés). La courbe supérieure, pour chaque lithologie, est calculée pour $D^{cpx/liquide}(H_2O) = 0.30$; courbe inférieure pour $D^{cpx/liquide}(H_2O) = 0.05$.

VI.2.3 H et processus mantelliques : une relation complexe.

Une analyse statistique des concentrations en H des NAMs (où l'H est incompatible) de xénolites hors-craton indique que les minéraux des harzburgites contiennent en moyenne plus d'H que ceux des lherzolites (Figure VI.6). Si les concentrations en H des NAMs étaient uniquement liées au taux de fusion subit par la roche, les harzburgites (roches réfractaires) devraient contenir moins d'eau que les lherzolites. Or les harzburgites sont statistiquement plus enrichies en H que les lherzolites (Figure VI.6). Cette constatation est similaire aux enrichissements en LREE observés dans les deux lithologies. Les harzburgites étant plus riches en olivine, leur minéralogie favorise la percolation des liquides (voir paragraphe I.5.3).

Les harzburgites sont donc potentiellement plus métasomatisées que les lherzolites. L'effet sur les concentrations en H du métasomatisme ne peut donc être exclu. Des études complémentaires sur les différents types de métasomatisme sont nécessaires pour conclure sur la contribution de ce processus dans le cycle profond de l'eau.

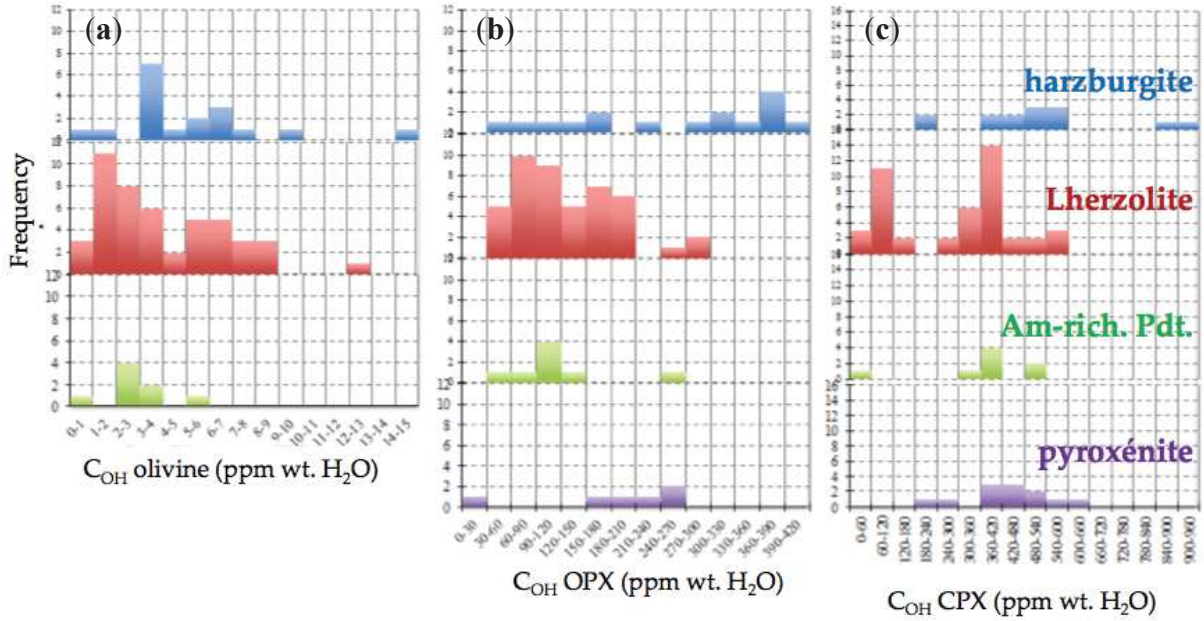

Figure VI.6 – Histogramme de fréquence représentant le nombre d'échantillons des concentrations en fonction de la concentration en H des NAMs des lherzolites, harzburgites, (am-rich. Pdt.) péridotites à amphibole et pyroxénites. (**a**) pour l'olivine d'après les calibrations de Bell *et al.,* 2003; (**b**) pour l'orthopyroxène (opx) et (**c**) pour le clinopyroxène (cpx) d'après la calibration de Bell *et al.*, 1995 ; (Li *et al.,* 2008 ; Peslier et Luhr, 2006 ; Denis *et al.*, 2013 ; Denis *et al.*, 2015, Denis *et al.*, *en préparation* ; Grant *et al.,* 2007 ; Soustelle *et al*., 2013 ; Yu *et al*., 2011).

En résumé, ces travaux de thèse ont montré que :

- Les concentrations en H des olivines sont sensibles à la dévolatilisation lors de la remontée dans le système magmatique et le rééquilibrage avec le magma. Elles ne sont donc pas représentatives des concentrations mantelliques.
- Au contraire, les concentrations en H des pyroxènes, spécialement l'opx, sont très homogènes suggérant que les concentrations mantelliques sont préservées.
- La présence d'amphibole (métasomatisme modal) n'implique pas un enrichissement en H des NAMs coexistant. Dans ce manteau dit hydraté, l'olivine coexistant avec l'amphibole contient en moyenne moins d'H que dans une péridotite sans amphibole. L'influence de l'H sur les propriétés rhéologiques de la roche est donc moindre dans le cas d'un manteau contenant une faible quantité de minéraux hydratés.
- Le comportement de l'H lors de la fusion partielle et du métasomatisme reste complexe ; cependant nos données suggèrent que l'H suit les MREE tel que le Sm.

Références bibliographiques

A

Adam, J. & Green, T. Trace element partitioning between mica- and amphibole-bearing garnet lherzolite and hydrous basanitic melt: 1. Experimental results and the investigation of controls on partitioning behaviour. *Contributions to Mineralogy and Petrology* **152,** 1–17 (2006).

Agrinier, P., Mével, C., Bosch, D., Javoy, M. Metasomatic hydrous fluids in amphibole peridotites from Zabargad Island (Red Sea). *Earth and Planetary Science Letters* 120, 187–205. (1993).

Aines R.D., Rossman, G. R., Water in minerals? A peak in the infrared. *Journal of Geophysical Research*, **89**, 4059-4071. (1984a).

Alard, O., Dautria, J.-M., Bodinier, J.-L. Nature du manteau supérieur et processus métasomatiques de part et d'autre du Sillon Houiller (Massif Central). Comptes rendus de l'Académie des sciences. Série 2. *Sciences de la terre et des planètes* **323**, 763–770. (1996).

Alard, O., Lorand, J.-P., Reisberg, L., Bodinier, J.-L., Dautria, J.-M., O'Reilly, S.Y. Volatile-rich Metasomatism in Montferrier Xenoliths (Southern France): Implications for the Abundances of Chalcophile and Highly Siderophile Elements in the Subcontinental Mantle. *Journal of Petrology* **52**, 2009–2045. (2011).

Aldanmaz, E. Mantle Source Characteristics of Alkali Basalts and Basanites in an Extensional Intracontinental Plate Setting, Western Anatolia, Turkey: Implications for Multi-stage Melting. *International Geology Review* **44,** 440–457 (2002).

Alt, J. C. *et al.* Recycling of water, carbon, and sulfur during subduction of serpentinites: A stable isotope study of Cerro del Almirez, Spain. *Earth and Planetary Science Letters* **327-328,** 50–60 (2012).

Anderson, A. T. & Brown, G. G. CO_2 contents and formation pressures of some Kilauean melt inclusions. *American Mineralogist* **78**, 794–803 (1993).

Aoki, K. Origin of phlogopite and potassic richterite bearing peridotite xenoliths from South Africa. *Contributions to Mineralogy and Petrology*, **53,** 145–156 (1975).

Arai, S., & Abe, N. Reaction of orthopyroxene in peridotite xenoliths with alkali-basalt melt and its implication for genesis of alpine-type chromitite. *American Mineralogist*, **80**(9), 1041-1047. (1995).

Arai, S. Characterization of spinel peridotites by olivine-spinel compositional relationships: Review and interpretation. *Chemical Geology* **113,** 191–204 (1994).

Ardia, P., Hirschmann, M.M., Withers, A.C., Tenner, T.J. H_2O storage capacity of olivine at 5–8GPa and consequences for dehydration partial melting of the upper mantle. *Earth and Planetary Science Letters* **345-348**, 104–116. (2012).

Aubaud, C. Hydrogen partition coefficients between nominally anhydrous minerals and basaltic melts. *Geophysical Research Letters* **31,** (2004).

Aubaud, C., Hauri, E.H., Hirschmann, M.M. Hydrogen partition coefficients between nominally anhydrous minerals and basaltic melts. *Geophysical Research Letters* **31**. (2004).

Aubaud, C., Hirschmann, M.M., Withers, A.C., Hervig, R.L. Hydrogen partitioning between melt, clinopyroxene, and garnet at 3 GPa in a hydrous MORB with 6 wt.% H_2O. *Contributions to Mineralogy and Petrology* **156**, 607–625. (2008).

B

Bai, Q., Kohlstedt, D.L. Effects of chemical environment on the solubility and incorporation mechanism for hydrogen in olivine. *Physics and Chemistry of Minerals* **19**, 460–471. (1993).

Bali, E., Bolfan-Casanova N, and Koga, K., Pressure and temperature dependence of H solubility in forsterite: an implication to water activity in the Earth interior. *Earth and Planetary Science Letters*, **268**, 354-363. (2008).

Baptiste, V., Tommasi, A., Demouchy, S., Deformation and hydration of the lithospheric mantle beneath the Kaapvaal craton, South Africa, *Lithos*. Sp. Issue « Formation, reactivation and destruction of cratons », 149,31-50, (2012).

Baptiste, V., Tommasi, A., Vauchez, A., Demouchy, S. & Rudnick, R. L. Deformation, hydration, and anisotropy of the lithospheric mantle in an active rift: Constraints from mantle xenoliths from the North Tanzanian Divergence of the East African Rift. *Tectonophysics* **639,** 34–55 (2015).

Bédard, J. H. Disequilibrium mantle melting. *Earth and Planetary Science Letters* **91,** 359–366 (1989).

Bedini, R.M., Bodinier, J.-L., Dautria, J.-M., Morten, L., Evolution of LILE-enriched small melt fractions in the lithospheric mantle: a case study from the East African Rift. *Earth and Planetary Science Letters* **153**, 67–83. (1997).

Beer, A. Bestimmung der Absorption des rothen Lichts in farbigen Flüssigkeiten. Annalen der Physik und Chemie, 86, 78-88. (1852).

Behrens, H., Romano, C., Nowak, M., Holtz, F. & Dingwell, D. B. Near-infrared spectroscopic determination of water species in glasses of the system MAlSi 3O 8 (M = Li, Na, K) : an interlaboratory study. *Chemical Geology* **128,** 41–63 (1996).

Bell, D. and Rossman, G., Water in Earth's mantle: The role of nominally anhydrous minerals. *Science,* **255**, 1391-1397. (1992).

Bell, D. R., Ihinger, P. D. & Rossman, G. R. Quantitative analysis of trace OH in garnet and pyroxenes. *American Mineralogist* **80,** 465–474 (1995).

Bell, D. R., Rossman, G. R., Maldener, J., Endisch, D. & Rauch, F. Hydroxide in olivine: A quantitative determination of the absolute amount and calibration of the IR spectrum. *Journal of Geophysical Research* **108,** (2003).

Bell, D.R., Rossman, G.R., Moore, R.O. Abundance and Partitioning of OH in a High-pressure Magmatic System: Megacrysts from the Monastery Kimberlite, South Africa. *Journal of Petrology* **45**, 1539–1564. (2004).

Bell, K., Kjarsgaard, B. A. & Simonetti, A. Carbonatites--Into the Twenty-First Century. *Journal of Petrology* **39,** 1839–1845 (1998).

Beran, A., Putnis, A., A model of the OH positions in olivine, derived from infrared-spectroscopic investigations. *Physics and Chemistry of Minerals* **9**, 57–60. (1983).

Berry, A. J., O'Neill, H. S. C., Hermann, J. & Scott, D. R. The infrared signature of water associated with trivalent cations in olivine. *Earth and Planetary Science Letters* **261**, 134–142 (2007).

Berry, A. J., Hermann, J., O'Neill, H. S. C. & Foran, G. J. Fingerprinting the water site in mantle olivine. *Geology* **33**, 869 (2005).

Beyer, E. E., Griffin, W. L. & O'reilly, S. Y. Transformation of Archaean Lithospheric Mantle by Refertilization: Evidence from Exposed Peridotites in the Western Gneiss Region, Norway. *J. Petrology* **47,** 1611–1636 (2006).

Bizimis, M., Peslier, A.H., Water in Hawaiian garnet pyroxenites: Implications for water heterogeneity in the mantle. *Chemical Geology* **397**, 61–75. (2015).

Bodinier, J. L., Guiraud, M., Fabriés, J., Dostal, J. & Dupuy, C. Petrogenesis of layered pyroxenites from the Lherz, Freychinéde and Prades ultramafic bodies (Ariége, French Pyrénées). *Geochimica et Cosmochimica Acta* **51**, 279–290 (1987).

Bodinier, J. L., Vasseur, G., Vernieres, J., Dupuy, C. & Fabries, J. Mechanisms of Mantle Metasomatism: Geochemical Evidence from the Lherz Orogenic Peridotite. *Journal of Petrology* **31,** 597–628 (1990).

Bodinier, J.-L., & Godard, M. Orogenic, ophiolitic, and abyssal peridotites. *Treatise on geochemistry*, **2**, 103-170 (2003).

Bodinier, J.-L., Menzies, M.A., Shimizu, N., Frey, F.A., McPherson, E. Silicate, Hydrous and Carbonate Metasomatism at Lherz, France: Contemporaneous Derivatives of Silicate Melt–Harzburgite Reaction. Journal of Petrology 45, 299–320. (2004).

Bodinier, J.-L., Menzies, M.A., Thirlwall, M.F. Continental to Oceanic Mantle Transition--REE and Sr-Nd Isotopic Geochemistry of the Lanzo Lherzolite Massif. *Journal of Petrology* **Special Volume**, 191–210 (1991).

Bolfan-Casanova, N. Water in the Earth's mantle. *Mineralogical Magazine* **69,** 229–258 (2005).

Bonadiman, C., Hao, Y., Coltorti, M., Dallai, L., Faccini, B., Huang, Y., Xia, Q., Water contents of pyroxenes in intraplate lithospheric mantle. *European Journal of Mineralogy* **21**, 637–647. (2009).

Bonadiman, C., Nazzareni, S., Coltorti, M., Comodi, P., Giuli, G., Faccini, B., 2014. Crystal chemistry of amphiboles: implications for oxygen fugacity and water activity in lithospheric mantle beneath Victoria Land, Antarctica. *Contributions to Mineralogy and Petrology* **167**, 1–17. ().

Brey, G.P., Köhler, T. Geothermobarometry in Four-phase Lherzolites II. New Thermobarometers, and Practical Assessment of Existing Thermobarometers. *Journal of Petrology* **31**, 1353–1378. (1990).

Bromiley, G. D., Nestola, F., Redfern, S. A. T. & Zhang, M. Water incorporation in synthetic and natural MgAl2O4 spinel. *Geochimica et Cosmochimica Acta* **74,** 705–718 (2010).

Budweg, M., Bock, G. and Weber, M. The Eifel Plume imaged with converted seismic waves. *Geophysical Journal International*, **166**, 579–589. (2006).

Bureau, H. & Keppler, H. Complete miscibility between silicate melts and hydrous fluids in the upper mantle: experimental evidence and geochemical implications. *Earth and Planetary Science Letters* **165,** 187–196 (1999).

C

Carey, S., Gardner, J. and Sigurdsson, H. The Intensity and Magnitude of Holocene Plinian Eruptions from Mount St-Helens Volcano. *Journal of Volcanology and Geothermal Research*, **66**, 1-4, 185-202. (1995).

Caron J.M., Gauthier A., Schaaf A., Ulysse J., Wozniak J. Comprendre et enseigner la planète Terre*, ed.* Ophrys, Paris (1989).

Carpenter Woods, S., Mackwell, S. J., and Dyar, D. Hydrogen in diopside: Diffusion profiles. *American Mineralogist*, **85**, 480-487. (2000).

Carpenter, S.J. The Kinetics of Hydrogen Diffusion in Single-Crystal Orthopyroxene, Ph.D. Thesis, Pennsylvania State University, p 410. (2000).

Carslaw, H. S. and Jaeger J. C. Conduction of heat in solids, second edition, Oxford. P. 184. (1959).

Chakraborty, S. Diffusion in Solid Silicates: A Tool to Track Timescales of Processes Comes of Age. Annual *Review of Earth and Planetary Sciences* **36**, 153–190 (2008).

Chakraborty, S. Rates and mechanisms of Fe-Mg interdiffusion in olivine at 980 °-1300 °C. *Journal of Geophysical Research* **102**, 12317-12331 (1997).

Chaufaud, J., Alard, O., Demouchy, S., Dautria, J-M. and O'Reilly, S.Y. Water behaviour during mantle melt percolation-reaction: a case study from the Borée peridotite xenoliths (Massif Central, France). AGU Fall Meet. 2011 Suppl., Abstract DI21A-2061. (5-9/12/2011).

Chen, S., Hiraga, T. & Kohlstedt, D. L. Water weakening of clinopyroxene in the dislocation creep regime. *Journal of Geophysical Research* **111,** B08203 (2006).

Coltorti, M., Beccaluva, L., Bonadiman, C., Faccini, B., Ntaflos, T., Siena, F. Amphibole genesis via metasomatic reaction with clinopyroxene in mantle xenoliths from Victoria Land, Antarctica. *Lithos* **75**, 115–139. (2004).

Coltorti, M., Beccaluva, L., Bonadiman, C., Salvini, L. & Siena, F. Glasses in mantle xenoliths as geochemical indicators of metasomatic agents. *Earth and Planetary Science Letters* **183,** 303–320 (2000).

Coltorti, M., Bonadiman, C., Hinton, R. W., Siena, F. & Upton, B. G. J. Carbonatite Metasomatism of the Oceanic Upper Mantle: Evidence from Clinopyroxenes and Glasses in Ultramafic Xenoliths of Grande Comore, Indian Ocean. *Journal of Petrology* **40,** 133–165 (1999).

Costa, F. and Dungan, M. Short time scales of magmatic assimilation from diffusion modeling of multiple elements in olivine. *Geology*, **33**, 837-840. (2005).

Costa, F. and S. Chakraborty. Decadal time gaps between mafic intrusion and silicic eruption obtained from chemical zoning patterns in olivine. *Earth and Planetary Science Letters*. **227**, 3-4, 517-530. (2004).

Crank, J. The mathematics of diffusion, Oxford. p. 32 & p. 151. (1975).

Crawford, A. J. & Cameron, W. E. Petrology and geochemistry of Cambrian boninites and low-Ti andesites from Heathcote, Victoria. *Contributions to Mineralogy and Petrology* **91**, 93–104 (1985).

D

Dalton, John A., and Dean C. Presnall. The continuum of primary carbonatitic–kimberlitic melt compositions in equilibrium with lherzolite: data from the system CaO–MgO–Al2O3–SiO2–CO2 at 6 GPa. *Journal of Petrology* **39** 1953-1964 (1998)

Danyushevsky, L. V. H2O Abundance in Depleted to Moderately Enriched Mid-ocean Ridge Magmas; Part I: Incompatible Behaviour, Implications for Mantle Storage, and Origin of Regional Variations. *Journal of Petrology* **41**, 1329–1364 (2000).

Dasgupta, R. Ingassing, Storage, and Outgassing of Terrestrial Carbon through Geologic Time. *Reviews in Mineralogy and Geochemistry* **75,** 183–229 (2013).

Dasgupta, R., Hirschmann, M.M., 2006. Melting in the Earth's deep upper mantle caused by carbon dioxide. Nature 440, 659–662. ().

Dautria, J. M., Liotard, J. M., Cabanes, N., Girod, M. & Briqueu, L. Amphibole-rich xenoliths and host alkali basalts: petrogenetic constraints and implications on the recent evolution of the upper mantle beneath Ahaggar (Central Sahara, Southern Algeria). *Contributions to Mineralogy and Petrology*. **95**, 133–144 (1987).

Dautria, J. (1988). Relation entre les heterogeneites du manteau superieur et le magnetisme en domaine distensif. Exemple des basaltes alcalins du Hoggar,(Sahara central, Algerie) et leurs enclaves (Doctoral dissertation, These Doc. Etat, CGG, Montpellier Fr).

Dautria, J. M., Dupuy, C., Takherist, D. & Dostal, J. Carbonate metasomatism in the lithospheric mantle: peridotitic xenoliths from a melilititic district of the Sahara basin. *Contributions to Mineralogy and Petrology* **111,** 37–52 (1992).

Davies, G, Numerical evaluation of mantle plume spacing, size, flow rates and unsteadiness, *Journal of Geophysical Research* **104**, 7377-87 (1999).

Dawson, J. B. & Smith, J. V. Upper-mantle amphiboles: a review. *Mineralogical Magazine* **45,** 35–46 (1982).

Dawson, J. B. Contrasting types of upper-mantle metasomatism. *Kimberlites II. Elsevier, Amsterdam*, 289-294 (1984).

Dawson, J., Hill, P., & Kinny, P. Mineral chemistry of a zircon-bearing, composite, veined and metasomatised upper-mantle peridotite xenolith from kimberlite. *Contributions to Mineralogy and Petrology*, **140**(6), 720-733 (2001).

Deer, W. A., R. A. Howie, and J. Zussman. "Rock-forming minerals, Volume 2B, Double-chain silicates." *The Geological Society, London*. 1997.

Demouchy, S., Deloule, E., Frost, D.J. and Keppler, H. Effect of temperature and pressure on water solubility in wadsleyite. Geochimica Et Cosmochimica Acta, 68(11): A32-A32. (2004).

Demouchy, S., Jacobsen, S. D., Gaillard, F. & Stern, C. R. Rapid magma ascent recorded by water diffusion profiles in mantle olivine. *Geology* **34,** 429 (2006).

Demouchy, S. and Mackwell, S., Mechanisms of hydrogen incorporation and diffusion in iron-bearing olivine. *Physics and Chemistry of Minerals*, **33**, 347-355. (2006).

Demouchy, S., Mackwell, S. J. & Kohlstedt, D. L. Influence of hydrogen on Fe–Mg interdiffusion in (Mg,Fe)O and implications for Earth's lower mantle. *Contributions to Mineralogy and Petrology* **154,** 279–289 (2007).

Demouchy, S. Hydrogen diffusion in spinel grain boundaries and consequences for chemical homogenization in hydrous peridotites. *Contributions to Mineralogy and Petrology*160, 887-898, (2010).

Demouchy, S., Tommasi, A., Barou, F., Mainprice, D. and Cordier, P. Deformation of Olivine in Torsion under Hydrous Conditions. *Physics of the Earth and Planetary Interiors*, **203-203**, 56-70. (2012).

Demouchy, S., Tommasi, A., Boffa Ballaran, T. & Cordier, P. Low strength of Earth's uppermost mantle inferred from tri-axial deformation experiments on dry olivine crystals. *Physics of the Earth and Planetary Interiors* **220,** 37–49 (2013).

Demouchy, S., Ishikawa, A., Tommasi, A., Alard, O. & Keshav, S. Characterization of hydration in the mantle lithosphere: Peridotite xenoliths from the Ontong Java Plateau as an example. *Lithos* **212-215,** 189–201 (2015).

Demouchy S. and Bolfan-Casanova N. Distribution and Transport of Hydrogen in the Lithospheric Mantle: A Review *Lithos* submitted (2015)

Denis, C.M.M., Demouchy, S., Shaw, C.S.J. Evidence of dehydration in peridotites from Eifel Volcanic Field and estimates of the rate of magma ascent. *Journal of Volcanology and Geothermal Research* **258**, 85–99. (2013).

Denis, C.M.M., Alard, O. & Demouchy, S. Water content and hydrogen behaviour during metasomatism in the uppermost mantle beneath Ray Pic volcano (Massif Central, France). *Lithos* **236-237**, 256–274 (2015).

Denis, C.M.M., Alard, O. & Demouchy, S. Hydrogen in wall-rock metasomatism, melt contamination and fluid percolation. (in preparation)

Dick, H. J. B. & Bullen, T. Chromian spinel as a petrogenetic indicator in abyssal and alpine-type peridotites and spatially associated lavas. *Contributions to Mineralogy and Petrology.* **86,** 54–76 (1984).

Dimanov, A. & Sautter, V. 'Average' interdiffusion of (Fe,Mn)-Mg in natural diopside. European *Journal of Mineralogy* **12**, 749–760 (2000).

Dixon, J. E., Leist, L., Langmuir, C. & Schilling, J.-G. Recycled dehydrated lithosphere observed in plume-influenced mid-ocean-ridge basalt. *Nature* **420**, 385–389 (2002).

Dohmen, R., & Chakraborty, S. (2007). Fe–Mg diffusion in olivine II: point defect chemistry, change of diffusion mechanisms and a model for calculation of diffusion coefficients in natural olivine. *Physics and Chemistry of Minerals*, *34*(6), 409-430.

Doucet, L.S., Peslier, A.H., Ionov, D.A., Brandon, A.D., Golovin, A.V., Goncharov, A.G., Ashchepkov, I.V. High water contents in the Siberian cratonic mantle linked to metasomatism: An FTIR study of Udachnaya peridotite xenoliths. *Geochimica et Cosmochimica Acta* **137**, 159–187. (2014).

Downes, H., Dupuy, C. Textural, isotopic and REE variations in spinel peridotite xenoliths, Massif Central, France. Earth and Planetary Science Letters 82, 121–135. ().

Downes, H., Reichow, M.K., Mason, P.R.D., Beard, A.D., Thirlwall, M.F., 2003. Mantle domains in the lithosphere beneath the French Massif Central: trace element and isotopic evidence from mantle clinopyroxenes. *Chemical Geology* **200**, 71–87. (1987).

E-F

Eiler, J.M. and Kitchen, N. Hydrogen-isotope analysis of nanomole (picoliter) quantities of H2O. *Geochimica et Cosmochimica Acta*, **65**(24): 4467-4479. (2001).

Erlank, A.J., Waters, F.G., Hawkesworth, C.J., Haggerty, S.E., Allsopp, H.L., Rickard, R.S. and Menzies, M.A. Evidence for mantle metasomatism in peridotite nodules from the Bultfontein Floors, Kimberley, South Africa. In: M.A. Menzies and C.J. Hawkesworth (Editors), Mantle Metasomatism. Academic Press, London, pp. 221-311. (1987)

Falus, G., Tommasi, A., Ingrin, J., Szabó, C. Deformation and seismic anisotropy of the lithospheric mantle in the southeastern Carpathians inferred from the study of mantle xenoliths. *Earth and Planetary Science Letters* **272**, 50–64. (2008).

Farver, J. R. Oxygen and Hydrogen Diffusion in Minerals. *Diffusion in Minerals and Melts* **72**, 447-507. (2010).

Fei, H., Wiedenbeck, M., Yamazaki, D. & Katsura, T. Small effect of water on upper-mantle rheology based on silicon self-diffusion coefficients. *Nature* **498**, 213–215 (2013).

Férot, A. & Bolfan-Casanova, N. Water storage capacity in olivine and pyroxene to 14GPa: Implications for the water content of the Earth's upper mantle and nature of seismic discontinuities. *Earth and Planetary Science Letters* **349-350,** 218–230 (2012).

Fischer, T. P., Burnard, P., Marty, B., Hilton, D. R., Füri, E., Palhol, F. & Mangasini, F. Upper-mantle volatile chemistry at Oldoinyo Lengai volcano and the origin of carbonatites. *Nature*, **459** (7243), 77-80 (2009).

Frey, F. A. & Green, D. H. The mineralogy, geochemistry and origin of Iherzolite inclusions in Victorian basanites. *Geochimica et Cosmochimica Acta* **38,** 1023–1059 (1974).

Frey, F. A. & Prinz, M. Ultramafic inclusions from San Carlos, Arizona: Petrologic and geochemical data bearing on their petrogenesis. *Earth and Planetary Science Letters* **38,** 129–176 (1978).

Frezzotti, M.L., Ferrando, S., Peccerillo, A., Petrelli, M., Tecce, F., Perucchi, A. Chlorine-rich metasomatic H2O–CO2 fluids in amphibole-bearing peridotites from Injibara (Lake Tana

region, Ethiopian plateau): Nature and evolution of volatiles in the mantle of a region of continental flood basalts. *Geochimica et Cosmochimica Acta* **74**, 3023–3039. (2010).

G

Gaetani, G.A., Grove, T.L., Bryan W.B. The influence of water on the petrogenesis of subduction-related igneous rocks. *Nature*, **365**, 6444, 332-334 (1993).

Gaetani, G.A., O'Leary, J.A., Shimizu, N., Bucholz, C.E., and Newville, M. Rapid reequilibration of H_2O and oxygen fugacity in olivine-hosted melt inclusions. *Geology*.**40**, 915-918 (2012).

Garcia-Castellanos, D., Cloetingh, S., van Balen, R.T. Modelling the Middle Pleistocene uplift in the Ardennes–Rhenish Massif: thermo-mechanical weakening under the Eifel? *Global and Planetary Change* **27**, 39–52. (2000).

Gast, P. W. Trace element fractionation and the origin of tholeiitic and alkaline magma types. *Geochimica et Cosmochimica Acta* **32,** 1057–1086 (1968).

Gavrilenko, P. Water solubility in diopside. Doctoral thesis, University of Bayreuth (2008).

Ghiorso, M.S. and Sack R. O. Chemical mass-transfer in magmatic processes .4. A revised and internally consistent thermodynamic model for the interpolation and extrapolation of liquid-solid equilibria in magmatic systems at elevated-temperatures and pressures *Contributions to Mineralogy and Petrology* **119**, 197-212 (1995).

Goldschmidt, V. M. The principles of distribution of chemical elements in minerals and rocks. *Journal of chemical Society*, 655-673 (1937).

Goldsmith, J.R. Al/Si interdiffusion in albite: effect of pressure and the role of hydrogen, *Contributions to Mineralogy and Petrology* **95**, 311-321. (1987).

Granet, M., Wilson, M., Achauer, U. Imaging a mantle plume beneath the French Massif Central. *Earth and Planetary Science Letters* **136**, 281–296. (1995).

Grant, K., Ingrin, J., Lorand, J.P., Dumas, P. Water partitioning between mantle minerals from peridotite xenoliths. *Contributions to Mineralogy and Petrology* 154, 15–34. (2007).

Grant, K.J., Kohn, S.C., Brooker, R.A. The partitioning of water between olivine, orthopyroxene and melt synthesised in the system albite–forsterite–H2O. *Earth and Planetary Science Letters* **260**, 227–241. (2007).

Gray, C. M. & McDougall, I. K-Ar geochronology of basalt petrogenesis, Newer Volcanic Province, Victoria. *Australian Journal of Earth Sciences* **56**, 245–258 (2009).

Green, D.H., Hibberson, W.O., Kovács, I., Rosenthal, A. Water and its influence on the lithosphere–asthenosphere boundary. *Nature* **467**, 448–451. (2010).

Green, D.H. & Ringwood, A. E. The stability fields of aluminous pyroxene peridotite and garnet peridotite and their relevance in upper mantle structure. *Earth and Planetary Science Letters* **3,** 151–160 (1967).

Grégoire, M., Moine, B.N., O'reilly, S.Y., Cottin, J.Y., Giret, A. Trace Element Residence and Partitioning in Mantle Xenoliths Metasomatized by Highly Alkaline, Silicate- and Carbonate-rich Melts (Kerguelen Islands, Indian Ocean). *Journal of Petrology* **41**, 477–509. (2000).

Griffin, W. L., Smith, D., Ryan, C. G., O'Reilly, S. Y. & Win, T. T. Trace-element zoning in mantle minerals; metasomatism and thermal events in the upper mantle. *The Canadian Mineralogist* **34**, 1179–1193 (1996).

Griffin, W.L., Powell, W., Pearson, N.J., O'Reilly, S.Y. GLITTER: data reduction software for laser ablation ICP-MS., in: *Laser Ablation-ICP-MS in the Earth Sciences*. Mineralogical Association of Canada Short Course Series. **40**, Appendix 2, 204–207. (2008).

Griggs, D. T. and Blacic, J. D. Quartz: Anomalous Weakness of Synthetic Crystals. Science. 147, 292-295. (1965).

Grove, T. L. et al. Magnesian andesite and dacite lavas from Mt. Shasta, northern California: products of fractional crystallization of H2O-rich mantle melts. *Contributions to Mineralogy and Petrology* **148**, 542–565 (2004).

Gudfinnsson, G. H. & Presnall, D. C. Continuous Gradations among Primary Carbonatitic, Kimberlitic, Melilititic, Basaltic, Picritic, and Komatiitic Melts in Equilibrium with Garnet Lherzolite at 3–8 GPa. *Journal of Petrology* **46,** 1645–1659 (2005).

H

Haggerty, S. E. The mineral chemistry of new titanates from the jagersfontein kimberlite, South Africa: Implications for metasomatism in the upper mantle. *Geochimica et Cosmochimica Acta* **47,** 1833–1854 (1983).

Haggerty, S. E., & Sautter, V. Ultradeep (greater than 300 kilometers), ultramafic upper mantle xenoliths. *Science*, **248** (4958), 993-996 (1990).

Hamada, M., Kawamoto T., Takahashi, E. and Fujii, T. Polybaric degassing of island arc low-K tholeiitic basalt magma recorded by OH concentrations in Ca-rich plagioclase *Earth and Planetary Science Letters*, **308**, 259–266. (2011).

Hamilton, W.B. Crustal geologic processes in the United States. *Geological Society of America Memoirs*. **172**, p. 743-781 (1989).

Hao, Y., Xia, Q., Li, Q., Chen, H., Feng, M. Partial melting control of water contents in the Cenozoic lithospheric mantle of the Cathaysia block of South China. *Chemical Geology* **380**, 7–19. (2014).

Hart, S.R., Dunn, T. Experimental cpx/melt partitioning of 24 trace elements. *Contributions to Mineralogy and Petrology*. **113**, 1–8. (1993).

Harte, B. Mantle peridotites and processes—the kimberlite sample. In *Continental basalts and mantle xenoliths* (pp. 46-91). Shiva Nantwich. (1983).

Hauri, E.H., Gaetani, G.A., Green, T.H. Partitioning of water during melting of the Earth's upper mantle at H2O-undersaturated conditions. *Earth and Planetary Science Letters* **248**, 715–734. (2006).

Hawkesworth, C. J., Blake, S., Evans, P., Hughes, R., Macdonald, R., Thomas, L. E., Turner, S. P., and Zellmer, G. Time scales of crystal fractionation in magma chambers - integrating physical, isotopic and geochemical perspectives. *Journal of Petrology* **41**, 991-1006. (2000).

Hawthorne, F.C., Oberti, R., Zanetti, A., Czamanske, G.K. The role of Ti in hydrogen-deficient amphiboles; sodic-calcic and sodic amphiboles from Coyote Peak, California. *The Canadian Mineralogist* **36**, 1253–1265. (1998).

Hercule, S., & Ingrin, J. Hydrogen in diopside: Diffusion, kinetics of extraction-incorporation, and solubility. *American Mineralogist*, **84**, 1577-1587. (1999).

Herrmann, W., Berry, R.F. MINSQ – a least squares spreadsheet method for calculating mineral proportions from whole rock major element analyses. *Geochemistry: Exploration, Environment, Analysis* **2**, 361–368. (2002).

Hier-Majumder, S., Anderson, I. M., and Kohlstedt, D. L. Influence of Protons on Fe-Mg interdiffusion in olivine. *Journal of Geophysical Research*. **110**, (2004).

Hiraga, T., Anderson, I.M. and Kohlstedt, D. L. Chemistry of grain boundaries in mantle rocks. *American Mineralogist*, **88**, 1015–1019. (2003).

Hiraga, T., Hirschmann, M.M. and Kohlstedt , D.L. Equilibrium interface segregation in the diopside-forsterite system 2: Applications of interface enrichment to mantle geochemistry. *Geochimica et Cosmochimica Acta*, **71**: 1281-1289. (2007).

Hirschmann, M. M., Aubaud, C., Withers, A. C. Storage capacity of H_2O in nominally anhydrous minerals in the upper mantle. *Earth and Planetary Science Letters* **236**(1-2): 167-181. (2005).

Hirth, G. & Kohlstedt, D.L. Water in the oceanic upper mantle: implications for rheology, melt extraction and the evolution of the lithosphere. *Earth and Planetary Science Letters* **144,** 93–108 (1996).

Hofmann, A. W. & White, W. M. Mantle plumes from ancient oceanic crust. *Earth and Planetary Science Letters* **57,** 421–436 (1982).

Holloway, J.R. The system pargasite-H2O-CO2: a model for melting of a hydrous mineral with a mixed-volatile fluid—I. Experimental results to 8 kbar. *Geochimica et Cosmochimica Acta* **37,** 651–666 (1973).

Humphreys, M., Menand, T., Blundy, J.D., Klimm K. Magma ascent rates in explosive eruptions: Constraints from H_2O diffusion in melt inclusions. *Earth and Planetary Science Letters*, **270**, 25–40. (2008).

I

Ingrin, J. & Skogby, H. Hydrogen in nominally anhydrous upper-mantle minerals concentration levels and implications. *European Journal of Mineralogy* **12,** 543–570 (2000).

Ingrin, J. and Blanchard, M. Diffusion of hydrogen in minerals. In: H. Keppler and J.R. Smyth (Editors), Water in Nominally Anhydrous Minerals. Review in Mineralogy and geochemistry. American Mineralogical Society Geochemical Society, Chantilly (Vir.), **62**: 291-320. (2006).

Ingrin, J., Hercule, S., and Charton, T. Diffusion of hydrogen in diopside: Results of dehydration experiments. *Journal of Geophysical Research*. **100**, 15,489-15,499. (1995).

Ingrin, J., Latrous, K., Doukhan, J.-C. & Doukhan, N. Water in diopside: an electron microscopy and infrared spectroscopy study. *European Journal of Mineralogy* **1**, 327–342 (1989).

Ionov, D.A., Bodinier, J.L., Mukasa, S.B. & Zanetti, A. Mechanisms and sources of mantle metasomatism: Major and trace element compositions of peridotite xenoliths from Spitsbergen in the context of numerical modelling. *Journal of. Petrology* **43,** 2219–2259 (2002).

Ionov, D.A., Dupuy, C., O'Reilly, S.Y., Kopylova, M.G. & Genshaft, Y.S. Carbonated peridotite xenoliths from Spitsbergen: implications for trace element signature of mantle carbonate metasomatism. *Earth and Planetary Science Letters* **119,** 283–297 (1993).

Irving, A. J. & Frey, F. A. Trace element abundances in megacrysts and their host basalts: Constraints on partition coefficients and megacryst genesis. *Geochimica et Cosmochimica Acta* **48**, 1201–1221 (1984).

Irving, A. J. Petrology and geochemistry of composite ultramafic xenoliths in alkalic basalts and implications for magmatic processes within the mantle. *American Journal of Science*, **280**(2), 389-426. (1980).

J

Jackson, C. R. M., Parman, S. W., Kelley, S. P. & Cooper, R. F. Noble gas transport into the mantle facilitated by high solubility in amphibole. *Nature Geosciences* **6,** 562–565 (2013).

Jacobsen, S. D., & Smyth, J. R. Effect of water on the sound velocities of ringwoodite in the transition zone. *Geophysical monograph-american geophysical union*, **168**, 131 (2006).

Jacobsen, S. D., Smyth, J. R., Spetzler, H. A., and Frost, D. J. Sound velocities and elastic constant of iron-bearing hydrous ringwoodite. *Physics of the Earth and Planetary Interiors* **143-144**, 47-56. (2004).

Jambon, A. and Zimmermann, J. L. Water in oceanic basalts" evidence for dehydration of recycled crust. *Earth and Planetary Science Letters*, **101**, 323-331. (1990).

Jochum, K.P., Nohl, U., Herwig, K., Lammel, E., Stoll, B., Hofmann, A.W. GeoReM: A New Geochemical Database for Reference Materials and Isotopic Standards. *Geostandards and Geoanalytical Research* **29**, 333–338. (2005).

Johnson, E.A. and Rossman, G.R. The concentration and speciation of hydrogen in feldspars using FTIR and H-1 MAS NMR spectroscopy. *American Mineralogist*, **88**(5-6): 901-911. (2003).

Johnson, K. T. M. Experimental determination of partition coefficients for rare earth and high-field-strength elements between clinopyroxene, garnet, and basaltic melt at high pressures. *Contributions to Mineralogy and Petrology* **133,** 60–68 (1998).

Jones, A. P., Smith, J. V., & Dawson, J. B. Mantle metasomatism in 14 veined peridotites from Bultfontein Mine, South Africa. *The Journal of Geology*, 435-453 (1982).

Jordan, S. C., Jowitt, S. M. & Cas, R. a. F. Origin of temporal - compositional variations during the eruption of Lake Purrumbete Maar, Newer Volcanics Province, southeastern Australia. *Bulletin of Volcanology* **77**, 1–15 (2014).

Jurewicz, A.J.G., Watson, E.B. Cations in olivine, Part 1: Calcium partitioning and calcium-magnesium distribution between olivines and coexisting melts, with petrologic applications. *Contributions to Mineralogy and Petrology* **99**, 176–185. (1988).

K

Kamenetsky, V.S., Maas, R., Kamenetsky, M.B., Paton, C., Phillips, D., Golovin, A.V. and Gornova, M.A. Chlorine from the mantle: Magmatic halides in the Udachnaya-East kimberlite, Siberia. *Earth and Planetary Science Letters*, **285**, 96-104. (2009).

Karato, S. The role of hydrogen in the electrical conductivity of the upper mantle. *Nature* **347,** 272–273 (1990).

Karato, S.-I. Remote sensing of hydrogen in the earth's mantle. *Reviews in Mineralogy and Geochemistry*, **62**, 343-375. (2006).

Katz, R. F., Spiegelman, M., & Langmuir, C. H. A new parameterization of hydrous mantle melting. *Geochemistry, Geophysics, Geosystems*, **4**(9) (2003).

Kelemen, P. B. Reaction Between Ultramafic Rock and Fractionating Basaltic Magma I. Phase Relations, the Origin of Calc-alkaline Magma Series, and the Formation of Discordant Dunite. *Journal of. Petrology* **31,** 51–98 (1990).

Keyser, M., Ritter, J. R.R., Jordaneyser, M. 3D shear-wave velocity structure of the Eifel plume, Germany. *Earth and Planetary Science Letters*, **203**, 59-82. (2002).

King, P.L., Hervig, R.L., Holloway, J.R., Vennemann, T.W., Righter, K. Oxy-substitution and dehydrogenation in mantle-derived amphibole megacrysts. *Geochimica et Cosmochimica Acta* **63**, 3635–3651. (1999).

Kinzler, R. J., & Grove, T. L. Primary magmas of mid-ocean ridge basalts 1. Experiments and methods. *Journal of Geophysical Research*, **97**(B5), 6885-6906 (1992).

Klein, C., & Hurlbut Jr, C. S. Manual of Mineralogy (after James D. Dana), 21st edn, revised. (1999).

Klein, F.W., Koyanagi, R.Y., Nakata, J.S., Tanigawa, W.R. The seismicity of Kilauea's magma system. In: Volcanism in Hawaii Decker RW, Wright TL Staufer PH (eds) U.S. Geol Survey Prof Paper 1350:1019-1185 (1987).

Koga, K., Hauri, E., Hirschmann, M.M., and Bell, D. Hydrogen concentration analyses using SIMS and FTIR: comparison and calibration for nominally anhydrous minerals. *Geochemistry, Geophysics, Geosystems* **4**(2), (2003).

Kohlstedt, D. L. and Mackwell, S. J. Solubility and diffusion of "water" in silicate minerals. In: K. Wright and R. Catlow. (Eds.), Microscopic Properties and Processes in Minerals. Kluwer Academic Publishers, Dordrecht, 593-559. (1999).

Kohlstedt, D.L., Keppler, H., Rubie, D.C. Solubility of water in the α, β and γ phases of (Mg,Fe)2SiO4. *Contributions to Mineralogy and Petrology* **123**, 345–357. (1996).

Kourim, F., Vauchez, A., Bodinier, J.-L., Alard, O. & Bendaoud, A. Subcontinental lithosphere reactivation beneath the Hoggar swell (Algeria): Localized deformation, melt channeling and heat advection. *Tectonophysics* **650**, 18–33 (2015).

Kourim, F., Bodinier, J.-L., Alard, O., Bendaoud, A., Vauchez, A., Dautria, J.-M. Nature and Evolution of the Lithospheric Mantle beneath the Hoggar Swell (Algeria): a Record from Mantle Xenoliths. *Journal of Petrology* **55**, 2249–2280. (2014).

Kovács, I., O'Neill, H. S. C., Hermann, J. & Hauri, E. H. Site-specific infrared O-H absorption coefficients for water substitution into olivine. *American Mineralogist* **95**, 292–299 (2010).

Kovács, I., Green, D.H., Rosenthal, A., Hermann, J., O'neill, H.S.C., Hibberson, W.O., Udvardi, B. An Experimental Study of Water in Nominally Anhydrous Minerals in the Upper Mantle near the Water-saturated Solidus. *Journal of Petrology* **53**, 2067–2093. (2012).

Kröger, F. A. & Vink, H. J. Relations between the concentrations of imperfections in solids. *Journal of Physics and Chemistry of Solids* **5,** 208–223 (1958).

Kushiro, I. The system forsterite-diopside-silica with and without water at high pressures. *American Journal Sciences*, **267**, 269-294. (1969).

Kushiro, I. Effect of water on the composition of magmas formed at high pressures. *Journal of Petrology*, **13**, 311–334. (1972).

L

La Tourette T. Hervig R. L. , Holoway J. R., Trace element partitioning between amphibole, phlogopite and basanite melt. *Eart and planetary Science Letters*, **135**, 13-30 (1995)

Lambert, J.H. Photometria, sive de mensura et gradibus luminis, colorum et umbrae, Sumptibus Vidae Eberhardi Klett. (1760).

Le Roux, V., Bodinier, J.-L., Tommasi, A., Alard, O., Dautria, J.-M., Vauchez, A., Riches, A.J.V. The Lherz spinel lherzolite: Refertilized rather than pristine mantle. *Earth and Planetary Science Letters* **259**, 599–612. (2007).

Lee, W.-J. & Wyllie, P. J. Processes of Crustal Carbonatite Formation by Liquid Immiscibility and Differentiation, Elucidated by Model Systems. *Journal of Petrology* **39,** 2005–2013 (1998).

Leibecker ,J., Gatzemeier, A. and Honig, M. Evidence of electrical anisotropic structures in the lower crust and the upper mantle beneath the Rhenish Shield. *Earth and Planetary Science Letters*, **202**, 2, 289-302, (2002).

Lenoir, X., Garrido, C.J., Bodinier, J.-L., Dautria, J.-M. Contrasting lithospheric mantle domains beneath the Massif Central (France) revealed by geochemistry of peridotite xenoliths. *Earth and Planetary Science Letters* **181**, 359–375. (2000).

Li, P., Xia, Q.-K., Deloule, E., Chen, H., Gu, X.-Y., Feng, M. Temporal variation of H2O content in the lithospheric mantle beneath the eastern North China Craton: Implications for the destruction of cratons. *Gondwana Research*. (2014).

Li, Z.X.A., Lee, C.T.A., Peslier, A., Lenardic, A., Mackwell, S.J. Water contents in mantle xenoliths from the Colorado Plateau and vicinity: implications for the mantle rheology and hydration-induced thining of continental lithosphere. *Journal of Geophysical Research* **113**, (2008).

Libowitzky, E., Rossman, G.R. An IR absorption calibration for water in minerals. *American Mineralogist* **82**, 1111–1115. (1997).

Litasov, K. D. & Ohtani, E. Effect of water on the phase relations in Earth's mantle and deep water cycle. *Geological Society of America Special Papers* **421,** 115–156 (2007).

Litasov, K.D., Foley, S.F., Litasov, Y.D. Magmatic modification and metasomatism of the subcontinental mantle beneath the Vitim volcanic field (East Siberia): evidence from trace element data on pyroxenite and peridotite xenoliths from Miocene picrobasalt. *Lithos* **54**, 83–114. (2000).

Liu Y, Anderson AT, Wilson CJN. Melt pockets in phenocrysts and decompression rates of silicic magmas before fragmentation. *Journal of Geophysical Research*, **112**. B06204 (2007).

Lloyd, A.S., Plank, T, Ruprecht, P., Hauri, E.H. and Rose, W. Volatile loss from melt inclusions in pyroclasts of differing sizes. *Contributions to Mineralogy and Petrology*. (2012).

Lorand, J.-P., Alard, O. Platinum-group element abundances in the upper mantle: new constraints from in situ and whole-rock analyses of Massif Central xenoliths (France). *Geochimica et Cosmochimica Acta* **65**, 2789–2806. (2001).

M

MacKenzie, J. M., and Canil, D. Volatile heavy metal mobility in silicate liquids: Implications for volcanic degassing and eruption prediction. *Earth and Planetary Science Letters*, **269**, 3-4, 488. (2008).

Mackwell S.J., Kohlstedt, D.L. Diffusion of hydrogen in olivine - implication for water in the mantle *Journal of Geophysical Research*, **95**, B4, 5079-5088 (1990).

Mackwell, S. J., Kohlstedt, D. L. & Paterson, M. S. The role of water in the deformation of olivine single crystals. *Journal of Geophysical Research* **90,** 11319 (1985).

Marty, B. The origins and concentrations of water, carbon, nitrogen and noble gases on Earth. *Earth and Planetary Science Letters* **313-314,** 56–66 (2012).

Maury, R. C., Defant, M. J. & Joron, J.-L. Metasomatism of the sub-arc mantle inferred from trace elements in Philippine xenoliths. *Nature* **360**, 661–663 (1992).

Maury, R.C., Varet, J. Le volcanisme tertiaire et quaternaire en France. 107 Éditions du BRGM, pp. 137–159. (1980).

McDonough, W. F., McCulloch, M. T. & Sun, S. S. Isotopic and geochemical systematics in Tertiary-Recent basalts from southeastern Australia and implications for the evolution of the sub-continental lithosphere. *Geochimica et Cosmochimica Acta* **49**, 2051–2067 (1985).

McDonough, W. F. & Sun, S.-S. The composition of the Earth. *Chemical Geology* **120,** 223–253 (1995).

McInnes, B.I.A., Gregoire, M., Binns, R.A., Herzig, P.M., Hannington, M.D. Hydrous metasomatism of oceanic sub-arc mantle, Lihir, Papua New Guinea: petrology and geochemistry of fluid-metasomatised mantle wedge xenoliths. *Earth and Planetary Science Letters* **188**, 169–183. (2001).

McKenzie D. The Generation and Compaction of Partially Molten Rock. *Journl of Petrology* **25,** 713–765 (1984).

McKenzie, D. Constraints on melt generation and transport from U-series activity ratios. *Chemical Geology* **162,** 81–94 (2000).

McKenzie, D. Some remarks on the movement of small melt fractions in the mantle. *Earth and Planetary Science Letters* **95,** 53–72 (1989).

McMillan, P. F. Water solubility and speciation models. *Reviews in Mineralogy and Geochemistry*, **30**(1), 132-156. (1994).

McPherson, E. et al. Geochemistry of metasomatism adjacent to amphibole-bearing veins in the Lherz peridotite massif. *Chemical Geology* **134**, 135–157 (1996).

Mei, S., & Kohlstedt, D. L. Influence of water on plastic deformation of olivine aggregates: 1. Diffusion creep regime. *Journal of Geophysical Research: Solid Earth (1978–2012)*, **105**(B9), 21457-21469 (2000a).

Mei, S., & Kohlstedt, D. L. Influence of water on plastic deformation of olivine aggregates: 2. Dislocation creep regime. *Journal of Geophysical Research: Solid Earth (1978–2012)*, **105** (B9), 21471-21481 (2000b).

Menzies, M. & Chazot, G. Fluid processes in diamond to spinel facies shallow mantle. *Journal of Geodynamics* **20,** 387–415 (1995).

Menzies, M. A. & Dupuy, C. Orogenic Massifs: Protolith, Process and Provenance. *Journal of Petrology* **Special_Volume,** 1–16 (1991).

Menzies, M. A. *et al.* Evidence from mantle xenoliths for an enriched lithospheric keel under the Outer Hebrides. *Nature* **325,** 44–47 (1987).

Menzies, M. A., Leeman, W. P. & Hawkesworth, C. J. Isotope geochemistry of Cenozoic volcanic rocks reveals mantle heterogeneity below western USA. *Nature [London]* **303,** 205–209 (1983).

Menzies, M.A., Hawkesworth, C. Upper mantle processes and composition, in: *Mantle Xenoliths*. John Wiley & Sons, pp. 725–738. (1987).

Mercier, J.-C.C., Nicolas, A. Textures and Fabrics of Upper-Mantle Peridotites as Illustrated by Xenoliths from Basalts. *Journal of Petrology* **16**, 454–487. (1975).

Mertes, H. and Schmincke, H.U. Mafic potassic laves ofthe quaternary west Eifel volcanic field .1. Major and trace-elements. *Contributions to Mineralogy and Petrology*, **89**, 4, 330-345. (1985).

Métrich, N. & Wallace, P. J. Volatile Abundances in Basaltic Magmas and Their Degassing Paths Tracked by Melt Inclusions. *Reviews in Mineralogy and Geochemistry* **69**, 363–402 (2008).

Michael, P. J. The concentration, behavior and storage of H2O in the suboceanic upper mantle: Implications for mantle metasomatism. *Geochimica et Cosmochimica Acta*, **52**, 2, 555-566. (1988).

Mierdel, K., Keppler, H., Smyth, J. R. & Langenhorst, F. Water Solubility in Aluminous Orthopyroxene and the Origin of Earth's Asthenosphere. *Science* **315,** 364–368 (2007).

Miller, G.H., Rossman, G.R., Harlow, G.E. The natural occurrence of hydroxide in olivine. *Physics and Chemistry of Minerals* 14, 461–472. (1987).

Minarik, W.G., Watson, E.B. Interconnectivity of carbonate melt at low melt fraction. *Earth and Planetary Science Letters* **133**, 423–437. (1995).

Moine, B.N., Cottin, J.-Y., Sheppard, S.M.F., Grégoire, M., O'reilly, S.Y., Giret, A. Incompatible trace element and isotopic (D/H) characteristics of amphibole- and phlogopite-bearing ultramafic to mafic xenoliths from Kerguelen Islands (TAAF, South Indian Ocean). *European Journal of Mineralogy* **12**, 761–777. (2000).

Mosenfelder, J.L., Rossman, G.R. Analysis of hydrogen and fluorine in pyroxenes: II. Clinopyroxene. *American Mineralogist* **98**, 1042–1054. (2013).

N

Navon, O. & Stolper, E. Geochemical Consequences of Melt Percolation: The Upper Mantle as a Chromatographic Column. *The Journal of Geology* **95,** 285–307 (1987).

Newman, S., Stolper, E. & Stern, R. H_2O and CO_2 in magmas from the Mariana arc and back arc systems. *Geochemistry, Geophysics, Geosystems*. **1**, 1013 (2000).

Nickel, K. G. & Green, D. H. Empirical geothermobarometry for garnet peridotites and implications for the nature of the lithosphere, kimberlites and diamonds. *Earth and Planetary Science Letters* **73**, 158–170 (1985).

Nicolas, A.A Melt extraction model based on structural studies in mantle peridotites. *Journal of Petrology*, **27**(4), 999-1022. (1986).

Niu, Y. & Batiza, R. Trace element evidence from seamounts for recycled oceanic crust in the Eastern Pacific mantle. *Earth and Planetary Science Letters* **148,** 471–483 (1997).

Nixon, P. H., Rogers, N. W., Gibson, I. L. & Grey, A. Depleted and Fertile Mantle Xenoliths from Southern African Kimberlites. *Annual Review of Earth and Planetary Sciences* **9,** 285–309 (1981).

Norman, M. D. Melting and metasomatism in the continental lithosphere: laser ablation ICPMS analysis of minerals in spinel lherzolites from eastern Australia. *Contributions to Mineralogy and Petrology* **130,** 240–255 (1998).

Norman, M. D., Pearson, N. J., Sharma, A., Griffin, W. L. Quantitative Analysis of Trace Elements in Geological Materials by Laser Ablation Icpms: Instrumental Operating Conditions and Calibration Values of Nist Glasses. *Geostandards Newsletter* **20**, 247–261. (1996).

Novella, D. *et al.* The distribution of H_2O between silicate melt and nominally anhydrous peridotite and the onset of hydrous melting in the deep upper mantle. *Earth and Planetary Science Letters* **400,** 1–13 (2014).

Novella, D., Bolfan-Casanova, N., Nestola, F. & Harris, J. W. H_2O in olivine and garnet inclusions still trapped in diamonds from the Siberian craton: Implications for the water content of cratonic lithosphere peridotites. *Lithos* **230,** 180–183 (2015).

Nowell, D.A.G., Jones, M.C. and Pyle, D.M. Episodic Quaternary volcanism in France and Germany. *Journal of Quaternary Science*. **21**, 645-675 (2006).

O

O'Leary, J.A., Gaetani, G.A., Hauri, E.H. The effect of tetrahedral Al3+ on the partitioning of water between clinopyroxene and silicate melt. *Earth and Planetary Science Letters* **297**, 111–120. (2010).

O'Reilly, S. Y. & Griffin, W. L. Mantle metasomatism beneath western Victoria, Australia: I. Metasomatic processes in Cr-diopside lherzolites. *Geochimica et Cosmochimica Acta* **52**, 433–447 (1988).

O'Reilly, S.Y., Griffin, W.L. Mantle Metasomatism, in: *Metasomatism and the Chemical Transformation of Rock*, Lecture Notes in Earth System Sciences. Springer Berlin Heidelberg, pp. 471–533. (2013).

O'Reilly, S.Y., Griffin, W.L., Ryan, C.G. Residence of trace elements in metasomatized spinel lherzolite xenoliths: a proton-microprobe study. *Contributions to Mineralogy and Petrology* **109**, 98–113. (1991).

Oberti, R., Ventura, G.D., Cámara, F. New Amphibole Compositions: Natural and Synthetic. *Reviews in Mineralogy and Geochemistry* **67**, 89–124. (2007).

Ohlhorst, S., Behrens, H. and Holtz, F. Compositional dependence of molar absorptivities of near-infrared OH- and H2O bands in rhyolitic to basaltic glasses. *Chemical Geology*, **174**(1-3): 5-20. (2001).

P-Q

Padrón-Navarta, J. A., Hermann, J. & O'Neill, H. S. C. Site-specific hydrogen diffusion rates in forsterite. *Earth and Planetary Science Letters* **392,** 100–112 (2014).

Papale, P., Neri, A. and Macedonio, G. The role of magma composition and water content in explosive eruptions - 1. Conduit ascent dynamics. *Journal of Volcanology and Geothermal Research*, **87**, 1-4, 75-93. (1998).

Paterson, M. S. The determination of hydroxyl by infrared absorption in quartz, silicate glasses and similar materials. *Bulletin de Mineralogie* **105,** 20–29 (1982).

Pearce, J., and Cann, J. R, Tectonic setting of basic volcanic rocks determined using trace element analysis, *Earth and Planetary Science Letters*., **19**: 290-300. (1973)

Pearce, N.J.G., Perkins, W.T., Westgate, J.A., Gorton, M.P., Jackson, S.E., Neal, C.R., Chenery, S.P. A Compilation of New and Published Major and Trace Element Data for NIST SRM 610 and NIST SRM 612 Glass Reference Materials. *Geostandards and Geoanalytical Research* **21**, 115–144. (1997).

Pearson, D. G. *et al.* Hydrous mantle transition zone indicated by ringwoodite included within diamond. *Nature* **507,** 221–224 (2014).

Pearson, D. G., Canil, D., & Shirey, S. B. Mantle samples included in volcanic rocks: xenoliths and diamonds. *Treatise on geochemistry*, ***2***, 171-275. (2003).

Peslier, A.H., Luhr, J.F., Post, J. Low water contents in pyroxenes from spinel-peridotites of the oxidized, sub-arc mantle wedge. *Earth and Planetary Science Letters* **201**, 69–86. (2002).

Peslier, A. & Luhr, J. Hydrogen loss from olivines in mantle xenoliths from Simcoe (USA) and Mexico: Mafic alkalic magma ascent rates and water budget of the sub-continental lithosphere. *Earth and Planetary Science Letters* **242,** 302–319 (2006).

Peslier, A. H., Woodland, A. B. and Wolff, J. A. Fast kimberlite ascent rates estimated from hydrogen diffusion profiles in xenolithic mantle olivines from southern Africa. *Geochimica et Cosmochimica Acta*, **72**, 2711-2722. (2008).

Peslier, A.H., Woodland, A.B., Bell, D.R., Lazarov, M. Olivine water contents in the continental lithosphere and the longevity of cratons. *Nature* **467**, 78–81. (2010).

Peslier, A.H. A review of water contents of nominally anhydrous natural minerals in the mantles of Earth, Mars and the Moon. *Journal of Volcanology and Geothermal Research* **197**, 239–258. (2010).

Peslier, A.H., Woodland, A.B., Bell, D.R., Lazarov, M., Lapen, T.J. Metasomatic control of water contents in the Kaapvaal cratonic mantle. *Geochimica et Cosmochimica Acta* **97**, 213–246. (2012).

Peslier, A. H., Bizimis, M. & Matney, M. Water disequilibrium in olivines from Hawaiian peridotites: Recent metasomatism, H diffusion and magma ascent rates. *Geochimica et Cosmochimica Acta* **154,** 98–117 (2015).

Pichavant, M., Mysen, B. O. & Macdonald, R. Source and H2O content of high-MgO magmas in island arc settings: an experimental study of a primitive calc-alkaline basalt from St. Vincent, lesser antilles arc. *Geochimica et Cosmochimica Acta* **66**, 2193–2209 (2002).

Pili, É., Ricard, Y., Lardeaux, J.-M. & Sheppard, S. M. F. Lithospheric shear zones and mantle-crust connections. *Tectonophysics* **280,** 15–29 (1997).

Pitzer, K.S. and Sterner, S.M. Equations of state valid continuously from zero to extreme pressures for H_2O and CO_2. *Journal of Chemical Physics*, **101**: 3111-3116. (1994).

Poe, B. T., Romano, C., Nestola, F. & Smyth, J. R. Electrical conductivity anisotropy of dry and hydrous olivine at 8GPa. *Physics of the Earth and Planetary Interiors* **181,** 103–111 (2010).

Poe, B.T., Romano, C., Nestola, F. and Smyth, J.R. Electrical conductivity anisotropy of dry and hydrous olivine at 8 GPa. *Physics of the Earth and Planetary Interiors*, **181**, 3-4, 103-111. (2010).

Pommier A. and Le Trong E. SIGMELTS: A web portal for electrical conductivity calculations in geosciences". *Computers and Geosciences*, **37**, 1450-1459. (2011).

Preusser, F., Rufer, D. and Schreurs, G. Direct dating of Quaternary phreatic maar eruptions by luminescence methods. *Geology*, **39**, 12, 1135-1138. (2011).

Price, R. C., Gray, C. M. & Frey, F. A. Strontium isotopic and trace element heterogeneity in the plains basalts of the Newer Volcanic Province, Victoria, Australia. *Geochimica et Cosmochimica Acta* **61**, 171–192 (1997).

R

Rauch, M. & Keppler, H. Water solubility in orthopyroxene. *Contributions to Mineralogy and Petrology* **143,** 525–536 (2002).

Rauch, M. Der Einbau von Wasser in Pyroxene. Bayreuth Universität, Bayreuth 141. (2000).

Ringwood, A. E. The principles governing trace element distribution during magmatic crystallization Part I: The influence of electronegativity. *Geochimica et Cosmochimica Acta*, **7**(3), 189-202. (1955).

Ritter, J., R.R, Jordan, M., Christensen, U., R. A mantle plume below the Eifel volcanic fields, Germany. *Earth and Planetary Science Letters*. **186**, 7-14. (2001).

Roggensack, K., Hervig, R. L., McKnight, S. B. & Williams, S. N. Explosive Basaltic Volcanism from Cerro Negro Volcano: Influence of Volatiles on Eruptive Style. *Science* **277**, 1639–1642 (1997).

Rosenthal, A., Hauri, E. H. & Hirschmann, M. M. Experimental determination of C, F, and H partitioning between mantle minerals and carbonated basalt, CO_2/Ba and CO_2/Nb systematics of partial melting, and the CO_2 contents of basaltic source regions. *Earth and Planetary Science Letters* **412,** 77–87 (2015).

Rossman, G. and Smyth, J. Hydroxyl contents of accessory minerals in mantle eclogites and related rocks. *American Mineralogist*, **75**, 775-780. (1990).

Rossman, G.R. Vibrational spectroscopy of hydrous species. *Review in Mineralogy*, **18**, 193-206. (1988).

Rougier, S. et al. Eocene exhumation of the Tuareg Shield (Sahara Desert, Africa). *Geology* **41**, 615–618 (2013).

Rudnick, R.L., McDonough, W.F., Chappell, B.W. Carbonatite metasomatism in the northern Tanzanian mantle: Petrographic and geochemical characteristics. *Earth and Planetary Science Letters* **114**, 463–475. (1993).

Rutherford, M.J. and Devine, J.D. Magmatic conditions and magma ascent as indicated by hornblende phase equilibria and reactions in the 1995-2002 Soufriere Hills magma. *Journal of Petrology*, 44, 8, 1433-1454. (2003).

S

Sakurai, M., Tsujino, N., Sakuma, H., Kawamura, K. & Takahashi, E. Effects of Al content on water partitioning between orthopyroxene and olivine: Implications for lithosphere–asthenosphere boundary. *Earth and Planetary Science Letters* **400,** 284–291 (2014).

Sautter, V., Haggerty, S. E., & Field, S. Ultradeep (> 300 kilometers) ultramafic xenoliths: petrological evidence from the transition zone. *Science*, 252(5007), 827-830. (1991).

Schmädicke, E., Gose, J., Witt-Eickschen, G., Bratz, H. Olivine from spinel peridotite xenoliths: Hydroxyl incorporation and mineral composition. *American Mineralogist* 98, 1870–1880. (2013).

Schmincke, H.U. Volcanism. Springer, Berlin-Heildelberg. p. 324. (2007).

Schmincke, H.U., Lorenz, V., Seck, H.A., 1983. The Quaternary Eifel volcanic fields. In: Fuchs, K. Ed.), Plateau Uplift. Springer, Berlin, pp. 139-151. ( ).

Serway, R.A., Moses, C. J. and Moyer, C.A. Moderns Physics, 2nd ed. Saunders Colle : pp 580. (1997).

Shaw C.S.J. Caught in the act — The first few hours of xenolith assimilation preserved in lavas of the Rockeskyllerkopf volcano, West Eifel, Germany. *Lithos* ,112, 511–523. (2009).

Shaw, C.S.J. The temporal evolution of three magmatic systems in the West Eifel volcanic field, Germany. *Journal of Volcanology and Geothermal Research*, 131, 213-240. (2003).

Shaw, C.S.J. and Klugel, A. The pressure and temperature conditions and timing of glass formation in mantle-derived xenoliths from Baarley, West Eifel, Germany: the case for amphibole breakdown, lava infiltration and mineral-melt reaction. *Mineralogy and Petrology* **74** (2-4), 163-187 (2002).

Shaw, C.S.J. and Eyzaguirre, J. Origin of megacrysts in the mafic alkaline lavas of the West Eifel volcanic field, Germany. *Lithos*, **50**, 75–95. (2000).

Shaw, C.S.J. and Woodland, A.B. The role of magma mixing in the petrogenesis of mafic alkaline lavas, Rockeskyllerkopf Volcanic Complex, West Eifel, Germany. *Bulletin of Volcanology*. 74,359-376. (2012).

Shaw, C.S.J. Regional variations in the mineralogy of metasomatic assemblages in mantle xenoliths from the West Eifel volcanic field, Germany. *Journal of Petrology*, **46**, 945-972. (2005).

Shaw, C.S.J., Woodland, A.B., Hopp, J., Trenholm, N.D. Structure and evolution of the Rockeskyllerkopf Volcanic Complex, West Eifel Volcanic Field, Germany. *Bulletin of Volcanology*. **72**, 971-990 (2010).

Shaw, D. M. Trace element fractionation during anatexis. *Geochimica et Cosmochimica Acta* **34,** 237–243 (1970).

Shirey, S.B., Cartigny, P., Frost, D.J., Keshav, S., Nestola, F., Nimis, P., Pearson, D.G., Sobolev, N.V., Walter, M.J. Diamonds and the Geology of Mantle Carbon. *Reviews in Mineralogy and Geochemistry* **75**, 355–421 (2013).

Simons, K., Dixon, J., Schilling, J.-G., Kingsley, R. & Poreda, R. Volatiles in basaltic glasses from the Easter-Salas y Gomez Seamount Chain and Easter Microplate: Implications for geochemical cycling of volatile elements. *Geochemistry, Geophysics, Geosystems*. **3**, 1–29 (2002).

Sisson, T. W. & Grove, T. L. Temperatures and H2O contents of low-MgO high-alumina basalts. *Contributions to Mineralogy and Petrology*. **113**, 167–184 (1993).

Skogby, H. & Rossman, G. R. OH- in pyroxene: An experimental study of incorporation mechanisms and stability. *American Mineralogist* **74,** 1059–1069 (1989).

Skogby, H. OH incorporation in synthetic clinopyroxene. *American Mineralogist* **79,** 240–249 (1994).

Skogby, H. Water in Natural Mantle Minerals I: Pyroxenes. *Reviews in Mineralogy and Geochemistry* **62**, 155–167. (2006).

Skogby, H., Bell, D. R. & Rossman, G. R. Hydroxide in pyroxene; variations in the natural environment. *American Mineralogist* **75,** 764–774 (1990).

Smyth, J. R. & Jacobsen, S. D. in *Geophysical Monograph Series* (eds. Jacobsen, S. D. & van der Lee, S.) **168,** 1–11 (American Geophysical Union, 2006).

Smyth, J. R. et al. Crystal chemistry of wadsleyite II and water in the Earth's interior. *Physics and chemistry of minerals* **31**, 691–705 (2005).

Smyth, J. R. Hydrogen in High Pressure Silicate and Oxide Mineral Structures. *Reviews in Mineralogy and Geochemistry* **62,** 85–115 (2006).

Smyth, J.R. b-Mg_2SiO_4 a potential host for water in the mantle? *American Mineralogist*, **72**, 1051-1055. (1987).

Sobolev, A. V. & Chaussidon, M. H2O concentrations in primary melts from supra-subduction zones and mid-ocean ridges: Implications for H2O storage and recycling in the mantle. *Earth and Planetary Science Letters* **137,** 45–55 (1996).

Soustelle, V., Tommasi, A., Demouchy, S., Franz, L. Melt-rock interactions, deformation, hydration and seismic properties in the sub-arc lithospheric mantle inferred from xenoliths from seamounts near Lihir, Papua New Guinea. *Tectonophysics* **608**, 330–345. (2013).

Sparks, R.S.J, Baker, L., Brown, R.J., Field, M., Schumacher, J., Stripp, G., Walters, A. Dynamical constraints on kimberlitic volcanism. *Journal of Volcanology and Geothermal Research* **155**, 18-48 (2006).

Spera, F. J. "Aspects of magma transport." *Physics of magmatic processes* 7 (1980).

Spera, F. J. Carbon dioxide in petrogenesis: III. Role of volatiles in the ascent of alkaline magma with special refer- ence to xenolith-bearing mafic lavas, *Contributions to Mineralogy and Petrology*, **88**, 217–232 (1984).

Stalder, R. and Skogby, H. Hydrogen diffusion in natural and synthetic orthopyroxene. *Physics and Chemistry of Minerals*, **30**, 12-19. (2003).

Stalder, R. Influence of Fe, Cr and Al on hydrogen incorporation in orthopyroxene. *European Journal of Mineralogy*, **16**(5), 703-711. (2004).

Stalder, R., Klemme, S., Ludwig, T. & Skogby, H. Hydrogen incorporation in orthopyroxene: interaction of different trivalent cations. *Contributions to Mineralogy and Petrology* **150,** 473–485 (2005).

Stevenson, D. J. On the role of surface tension in the migration of melts and fluids. *Geophysical Research Letters*, **13**(11), 1149-1152. (1986).

Streckeisen. Plutonic rocks. Clasification and nomenclature recommanded by the IUGS subcommission on the systematics of igneous rocks. *Geotimes*.**18**(10). P. 26-30(1973)

Sun, M., Kerrich, R. Rare earth element and high field strength element characteristics of whole rocks and mineral separates of ultramafic nodules in Cenozoic volcanic vents of southeastern British Columbia, Canada. *Geochimica et Cosmochimica Acta* **59**, 4863–4879. (1995).

Suzuki, A. and Mishin, Y. Atomic mechanism of grain boundary diffusion: low versus high temperatures. *Journal of Materials Science* **40**: 3155 – 3161. (2005).

T-U

Tenner, T. J., Hirschmann, M. M., Withers, A. C. & Hervig, R. L. Hydrogen partitioning between nominally anhydrous upper mantle minerals and melt between 3 and 5 GPa and applications to hydrous peridotite partial melting. *Chemical Geology* **262,** 42–56 (2009).

Tepley, F. J., III , Davidson, J. P., Tilling, R. I. & Arth, J. G. Magma mixing, recharge, and eruption histories recorded in plagioclase phenocrysts from El Chichón Volcano, Mexico. *Journal of Petrology* , **41**, 1397-1411. (2000).

Thompson, A. B. & Connolly, J. A. D. The nature of the lower continental crust Metamorphic fluids and anomalous porosities in the lower crust. *Tectonophysics* **182**, 47–55 (1990).

Thoraval, C., Demouchy, S. Numerical models of ionic diffusion in one and three dimensions: application to dehydration of mantle olivine. *Physics and Chemistry of Minerals* **41**, 709–723. (2014).

Tiepolo, M., Oberti, R., Zanetti, A., Vannucci, R., Foley, S.F. Trace-Element Partitioning Between Amphibole and Silicate Melt. *Reviews in Mineralogy and Geochemistry* **67**, 417–452. (2007).

Toramaru, A. & Fujii, N. Connectivity of melt phase in a partially molten peridotite. *Journal of Geophysical Research* **91,** 9239–9252 (1986).

Touron, S., Renac, C., O'Reilly, S.Y., Cottin, J.-Y., Griffin, W.L. Characterization of the metasomatic agent in mantle xenoliths from Deves, Massif Central (France) using coupled in situ trace-element and O, Sr and Nd isotopic compositions. Geological Society, London, Special Publications **293**, 177–196. (2008).

V

Van Achterberg, E., Ryan, C. G., Jackson, S. E. & Griffin, W. Data reduction software for LA-ICP-MS. In: Sylvester, P. (Ed.), Laser Ablation ICP-MS in the Earth Science. *Mineralogical Association of Canada* 239–243 (2001).

Van der Waal, D. & Bodinier, J.-L. Origin of the recrystallisation front in the Ronda peridotite by km-scale pervasive porous melt flow. *Contributions to Mineralogy and Petrology* **122**, 387–405 (1996).

Van Orman, J. A. V., Grove, T. L. & Shimizu, N. Rare earth element diffusion in diopside: influence of temperature, pressure, and ionic radius, and an elastic model for diffusion in silicates. *Contributions to Mineralogy and Petrology* **141**, 687–703 (2001).

Vannucci, R., Piccardo, G.B., Rivalenti, G., Zanetti, A., Rampone, E., Ottolini, L., Oberti, R., Mazzucchelli, M., Bottazzi, P. Origin of LREE-depleted amphiboles in the subcontinental mantle. *Geochimica et Cosmochimica Acta* **59**, 1763–1771. (1995).

Vasseur, G., Vernieres, J., & Bodiner, J. L. Modelling of trace element transfer between mantle melt and heterogranular peridotite matrix. *Journal of Petrology*, **2**, 41-54. (1991).

Vernières, J., Godard, M. & Bodinier, J.-L. A plate model for the simulation of trace element fractionation during partial melting and magma transport in the Earth's upper mantle. *Journal of Geophysical Research* **102,** 24771–24784 (1997).

Von Bargen, N. & Waff, H. S. Wetting of enstatite by basaltic melt at 1350°C and 1.0- to 2.5-Gpa Pressure. *Journal of Geophysical Research* **93,** 1153–1158 (1988).

W

Wallace, P. J. & Anderson, A. T. Effects of eruption and lava drainback on the H2O contents of basaltic magmas at Kilauea Volcano. *Bulletin of Volcanology* **59**, 327–344 (1998).

Walter, M. J., Sisson, T. W. & Presnall, D. C. A mass proportion method for calculating melting reactions and application to melting of model upper mantle lherzolite. *Earth and Planetary Science Letters* **135,** 77–90 (1995).

Wang, Z., Hiraga, T. & Kohlstedt, D. L. Effect of H+ on Fe–Mg interdiffusion in olivine, (Fe,Mg)2SiO4. *Applied Physics Letters* **85,** 209–211 (2004).

Watson, B. E. & Brenan, J. M. Fluids in the lithosphere, 1. Experimentally-determined wetting characteristics of CO2H2O fluids and their implications for fluid transport, host-rock physical properties, and fluid inclusion formation. *Earth and Planetary Science Letters* **85,** 497–515 (1987).

Wilshire, H. G., Nielson, J. E., Meyer, C. E. & Schwarzman, E. C. Amphibole-rich veins in lherzolite xenoliths, Dish Hill and Deadman Lake, California. *American Journal of Science* **280**-A, 576–593 (1980).

Wilshire, H. G. & Shervais, J. W. Al-augite and Cr-diopside ultramafic xenoliths in basaltic rocks from western United States. *Physics and Chemistry of the Earth* **9**, 257–272 (1975).

Wilson, M. and Downes,. Tertiary Quaternary extension-related alkaline magmatism in werstern and central-Europe *Journal of Petrology*. **32**, 4, 811-849. (1991).

Withers, A.C., 2013. On the use of unpolarized infrared spectroscopy for quantitative analysis of absorbing species in birefringent crystals. *American Mineralogist* **98**, 689–697. ().

Withers, A.C., Bureau, H., Raepsaet, C., Hirschmann, M.M. Calibration of infrared spectroscopy by elastic recoil detection analysis of H in synthetic olivine. *Chemical Geology* **334**, 92–98. (2012).

Witt-Eickschen G; Seck HA; Mezger K. Lithospheric mantle evolution beneath the Eifel (Germany): Constraints from Sr-Nd-Pb isotopes and trace element abundances in spinel peridotite and pyroxenite xenoliths *Journal of Petrology*, **44**, 6, 1077-1095 (2003a).

Witt-Eickschen, G., Kramm, U. Evidence for the multiple stage evolution of the subcontinental lithospheric mantle beneath the Eifel (Germany) from pyroxenite and composite pyroxenite/peridotite xenoliths. *Contributions to Mineralogy and Petrology* **131**, 258–272. (1998).

Wittig, N., Baker, J.A., Downes, H. U–Th–Pb and Lu–Hf isotopic constraints on the evolution of sub-continental lithospheric mantle, French Massif Central. *Geochimica et Cosmochimica Acta* **71**, 1290–1311. (2007).

Wood, B. J. The Effect of H2O on the 410-Kilometer Seismic Discontinuity. *Science* **268,** 74–76 (1995).

Woods S.C. Mackwell, S. and Dyar, D. Hydrogen in diopside: diffusion profile. *American Mineralogist*. **85**, 480-487. 2000 ( ).

Woolley, A. R. & Kjarsgaard, B. A. Paragenetic Types of Carbonatite as Indicated by the Diversity and Relative Abundances of Associated Silicate Rocks: Evidence from a Global Database. *The Canadian Mineralogist* **46,** 741–752 (2008).

Wulff-Pedersen, E., Neumann, E.-R. & Jensen, B. B. The upper mantle under La Palma, Canary Islands: formation of Si−K−Na-rich melt and its importance as a metasomatic agent. *Contributions to Mineralogy and Petrology* **125,** 113–139 (1996).

Wulff-Pedersen, E., Neumann, E.-R., Vannucci, R., Bottazzi, P. & Ottolini, L. Silicic melts produced by reaction between peridotite and infiltrating basaltic melts: ion probe data on glasses and

minerals in veined xenoliths from La Palma, Canary Islands. *Contributions to Mineralogy and Petrology* **137,** 59–82 (1999).

Wyllie, P.J., Ryabchikov, I.D. Volatile Components, Magmas, and Critical Fluids in Upwelling Mantle. *Journal of Petrology* **41**, 1195–1206. (2000).

X-Y-Z

Xia, Q.-K., Hao, Y., Li, P., Deloule, E., Coltorti, M., Dallai, L., Yang, X., Feng, M. Low water content of the Cenozoic lithospheric mantle beneath the eastern part of the North China Craton. *Journal of Geophysical Research* **115**, B07207. (2010).

Xia, Q.-K., Hao, Y.-T., Liu, S.-C., Gu, X.-Y., Feng, M. Water contents of the Cenozoic lithospheric mantle beneath the western part of the North China Craton: Peridotite xenolith constraints. *Gondwana Research* **23**, 108–118. (2013).

Xu, Y.-G., Menzies, M.A., Bodinier, J.-L., Bedini, R.M., Vroon, P., Mercier, J.-C.C. Melt percolation and reaction atop a plume: evidence from the poikiloblastic peridotite xenoliths from Borée (Massif Central, France). *Contributions to Mineralogy and Petrology* 132, 65–84. (1998).

Yang, A. Y. *et al.* Chalcophile elemental compositions of MORBs from the ultraslow-spreading Southwest Indian Ridge and controls of lithospheric structure on S-saturated differentiation. *Chemical Geology* **382,** 1–13 (2014).

Yang, X.-Z., Xia, Q.-K., Deloule, E., Dallai, L., Fan, Q.-C., Feng, M. Water in minerals of the continental lithospheric mantle and overlying lower crust: A comparative study of peridotite and granulite xenoliths from the North China Craton. *Chemical Geology* **256**, 33–45. (2008).

Yaxley, G., Kamenetsky, V., Green, D. & Falloon, T. Glasses in mantle xenoliths from western Victoria, Australia, and their relevance to mantle processes. *Earth and Planetary Science Letters* **148**, 433–446 (1997).

Yaxley, G. M., Crawford, A. J. & Green, D. H. Evidence for carbonatite metasomatism in spinel peridotite xenoliths from western Victoria, Australia. *Earth and Planetary Science Letters* **107,** 305–317 (1991).

Yaxley, G.M., Green, D.H., Kamenetsky, V. Carbonatite Metasomatism in the Southeastern Australian Lithosphere. *Journal of Petrology* **39**, 1917–1930. (1998).

Yoshino, T., Matsuzaki, T., Yamashita, S. & Katsura, T. Hydrous olivine unable to account for conductivity anomaly at the top of the asthenosphere. *Nature* **443,** 973–976 (2006).

Yoshino, T., Shimojuku, A., Shan, S., Guo, X., Yamazaki, D., Ito, E., Higo, Y and Funakoshi, K. Effect of temperature, pressure and iron content on the electrical conductivity of olivine and its high-pressure polymorphs, *Journal of Geophysical Research*, **117**, B08205. (2012).

Yu, Y., Xu, X.-S., Griffin, W.L., O'Reilly, S.Y., Xia, Q.-K. H_2O contents and their modification in the Cenozoic subcontinental lithospheric mantle beneath the Cathaysia block, SE China. *Lithos* **126**, 182–197. (2011).

Zangana, N., Downes, H., Thirlwall, M., Marriner, G., Bea, F. Geochemical variation in peridotite xenoliths and their constituent clinopyroxenes from Ray Pic (French Massif Central): implications for the composition of the shallow lithospheric mantle. *Chemical Geology* **153**, 11–35. (1999).

Zangana, N.A., Downes, H., Thirlwall, M.F., Hegner, E. Relationship between deformation, equilibration temperatures, REE and radiogenic isotopes in mantle xenoliths (Ray Pic, Massif Central, France): an example of plume-lithosphere interaction? *Contributions to Mineralogy and Petrology* **127**, 187–203. (1997).

Zhang, Y. Diffusion in minerals and melt: Theoretical background. In: Y. Zhang & D. J. Cherniak (Editors), Diffusion in minerals and melts. *Review in Mineralogy and geochemistry*. **72**. American Mineralogical & Society Geochemical Society, Chantilly (Vir.), pp. 5-59. (2011).

Zinngrebe, E. and Foley, S.F. Metasomatism in mantle xenoliths from gees, west eifel, germany - evidence for the genesis of calc-alkaline glasses and metasomatic ca-enrichment. *Contributions to Mineralogy and Petrology* **122**, 79-96 (1995).

Zolitschka, B., Negendank, J.F.W. and Lottermoser, B.G. Sedimentological proof and dating of the early holocene volcanic-eruption of Ulmener Maar (Vulkaneifel, Germany). Geologische Rundschau **8**, 213-219. (1995).

ANNEXES

Annexe 1 : Notation de Kröger-Vink

Annexe 2 : Fiches filons

Annexe 1 – Notation de Kröger-Vink

La notation de Kröger-vink (Kröger & Vink, 1956) permet de décrire les défauts ponctuels dans un structure cristalline.

On note : A_S^c

A, l'occupation du site :

Le site peut être occupé par un élément chimique ; on note alors le symbole de l'élément (ex : un atome de silice : Si). Le site peut ne pas être occupé (il est vacant), il est alors noté « V » (de l'anglais « vacancie »)

Note : Si un atome de Vanadium « V » occupe le site, la charge du site ne sera pas celle du site vide.

s, le type de site occupé, noté en indice.

c, la charge relative du site ainsi occupé est indiquée en exposant.

Elle représente la différence de charge entre ce qui est dans le site et ce qui devrait y être.

En cas d'excès de charge on place un « • » en exposant. Une charge nulle est exprimée par un « × » et une charge relative négative par un « ' ».

Ex. :

Un atome de d'aluminium (Al^{3+}) occupe le site d'un atome de silice (Si^{4+}). Il manque une charge au site. On note donc : Al'_{Si} .

Un atome de fer ferreux (Fe^{2+}) occupe le site d'un atome de magnésium (Mg^{2+}). La différence de charge est nulle, on indique donc : $Fe^{\times}_{Mg}$.

Un site d'oxygène (O^{2+}) vacant est noté : $V_O^{\bullet\bullet}$.

Note : un site interstitiel a une charge nulle.

Pour écrire les équations de défauts ponctuels, les règles sont :

- la conservation de la matière. On doit retrouver de chaque côté de l'équation le même nombre d'atomes/moles.
- l'électroneutralité : on doit retrouver la même charge totale de chaque côté de l'équation.
- la conservation des sites atomiques : on doit retrouver le même nombre de site atomique de chaque côté de l'équation, de façon à ce qu'il n'y ait ni création, ni destruction de sites atomiques.

Annexe 2 – Fiches récapitulatives de l'étude « Filons »

Pour chaque xénolite composite, on retrouve :

(1) un récapitulatif des caractéristiques de l'échantillon et une photo de la lame épaisse où sont reportées les points d'analyses d'EPMA, de LA-ICP-MS, et de spectroscopie IRTF, selon la légende suivante :

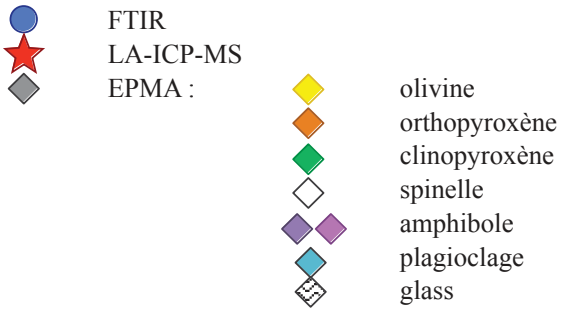

(2) Les spectres de terres rares normalisés aux chondrites et les spectres d'éléments en traces normalisés au manteau primitif (PM) (valeurs d'après McDonough & Sun, 1995).

(3) Les variations notables des éléments majeurs de chaque phase minérale en fonction de la distance au contact.

(4) Les variations notables des éléments en traces de chaque phase minérale en fonction de la distance au contact.

14V81 : Lherzolite and basaltic patch

(1) Locality : Victoria State, Australia

	ol	opx	cpx	spl	plagio.	verre	T°
Lherzolite	64	31	5	<0.2	-	-	942 ± 71 °C
Patch basaltique	44	15	24	-	1	15	979 ± 23 °C

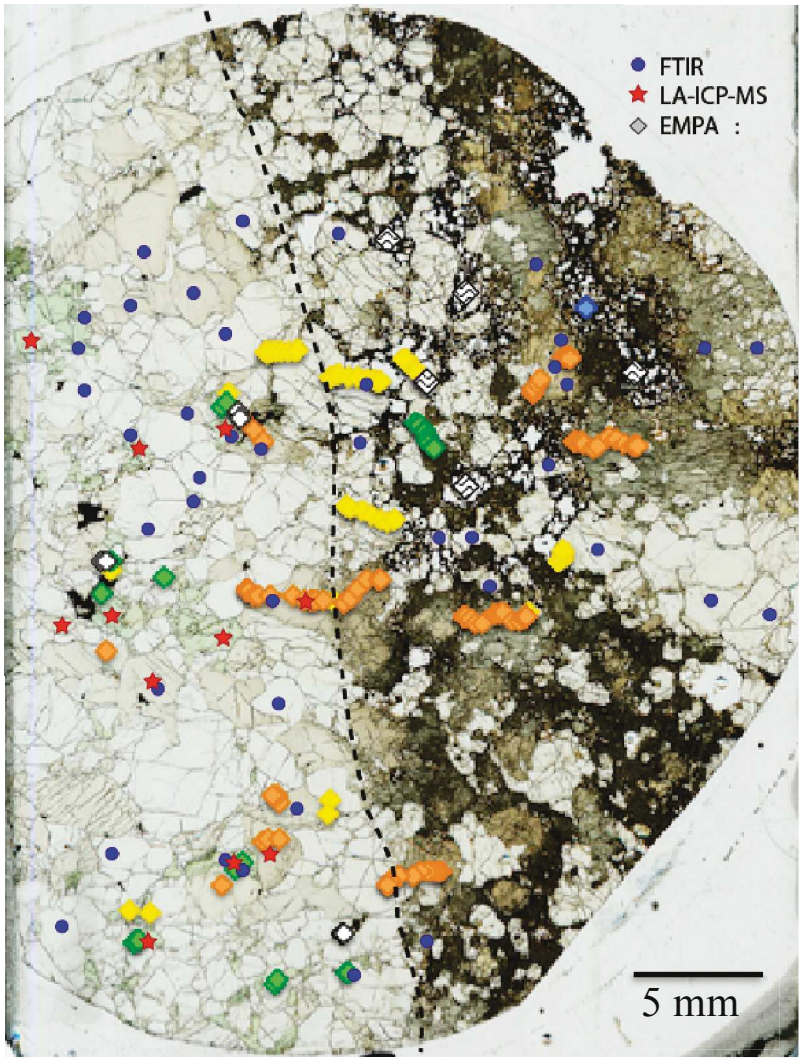

FTIR
LA-ICP-MS
EPMA :

olivine
orthopyroxène
clinopyroxène
spinelle
amphibole
plagioclage
glass

(2)

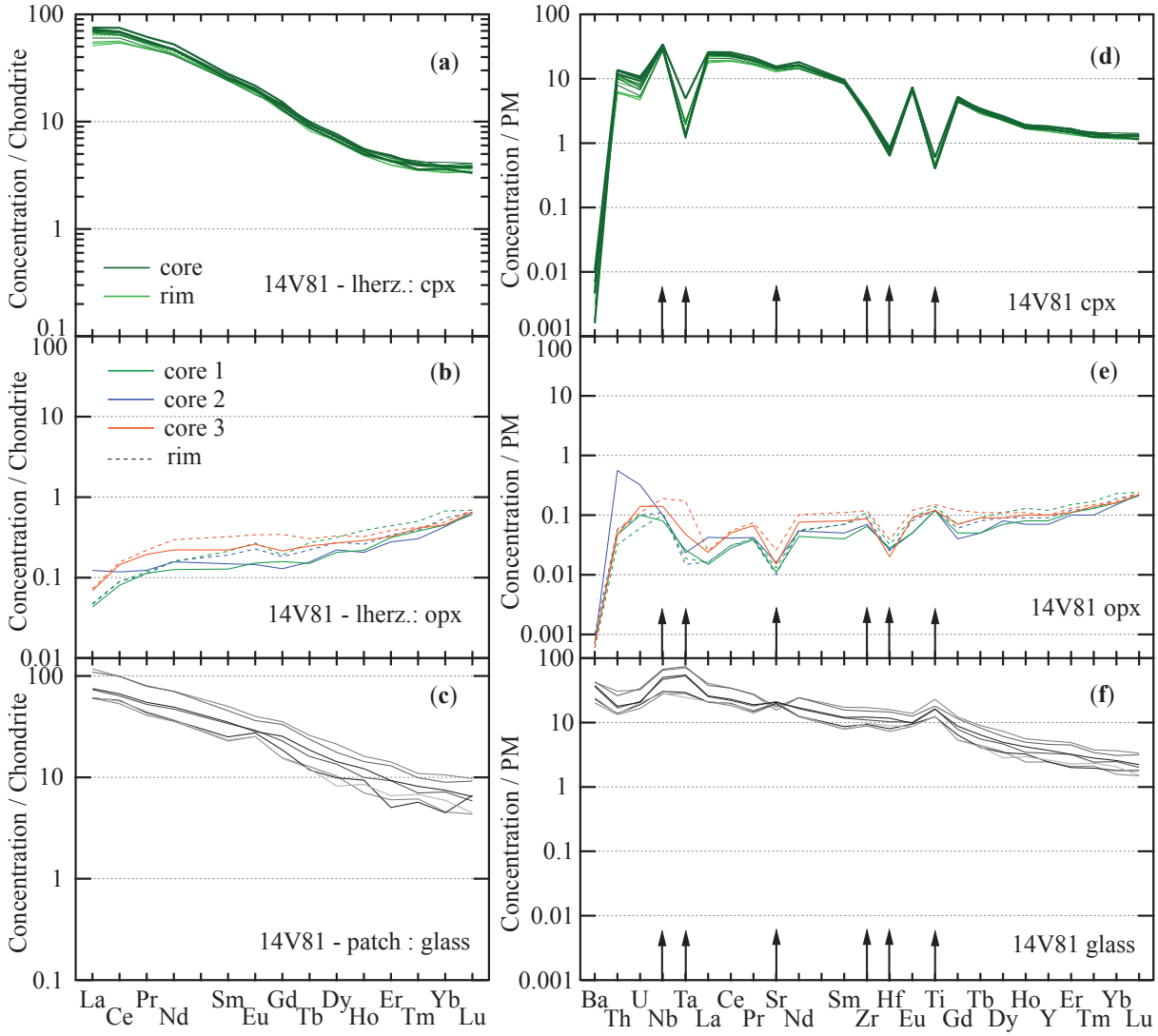

(2) a-c : Spectres de terres rares normalisés aux chondrites ; d-f :les spectres d'éléments en traces normalisés au manteau primitif (PM) (valeurs d'après McDonough & Sun, 1995). Lherz.: lherzolite; cpx: clinopyroxène; opx: orthopyroxène ; glass: verre.

(3)

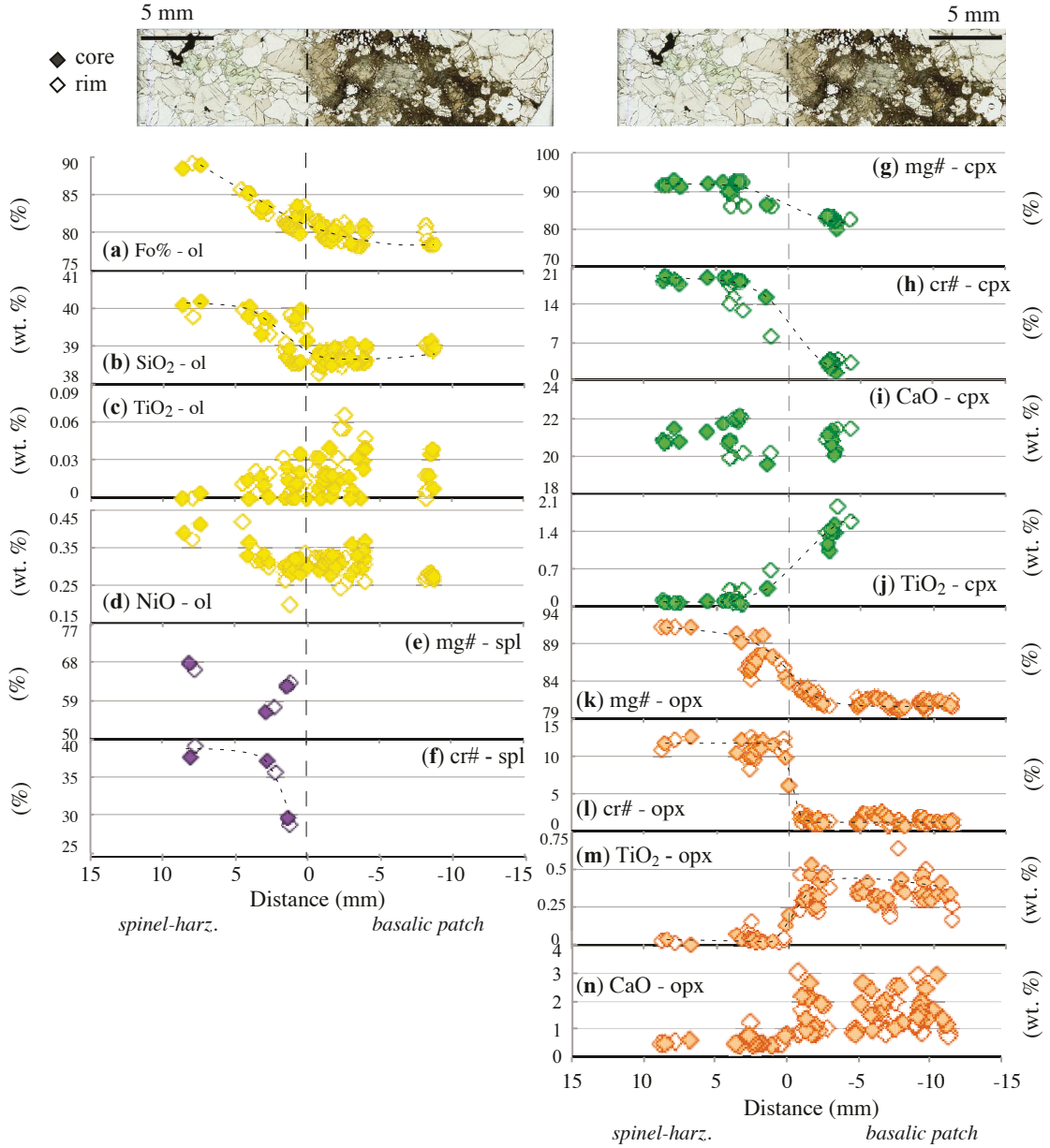

(3) Variations de concentration en éléments majeurs de chaque phase minérale en fonction de la distance au contact. ol : olivine ; spl : spinelle ; cpx : clinopyroxène ; opx : orthopyroxène. Fo% = 100* (Mg / (Mg + Mn+ Fe_{tot})) ; mg# = 100* (Mg / (Mg + Fe_{tot})) ; cr# = 100* (Cr / (Cr+Al_{tot})).

(4)

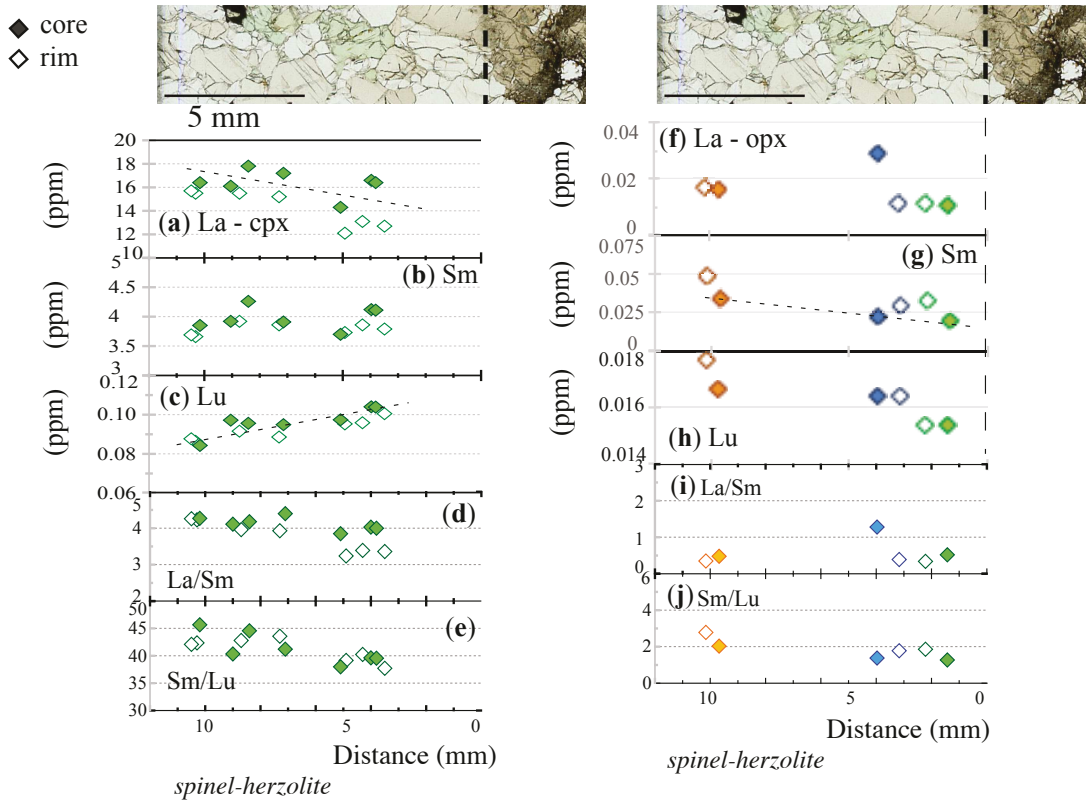

(4) Variations de concentrations en éléments en traces pour **(a-e)** les clinopyroxènes (cpx) et **(f-j)** les orthopyroxènes (opx) en fonction de la distance au contact.

13RP16 : Lherzolite and pyroxenite vein

(1) Locality : Ray Pic, French Massif Central, France

	ol	opx	cpx	spl	am	T°
lherzolite	68	25	5	<1	1	1048 ± 4 °C
pyroxenite	16	22	40	9	14	1043 ± 11 °C

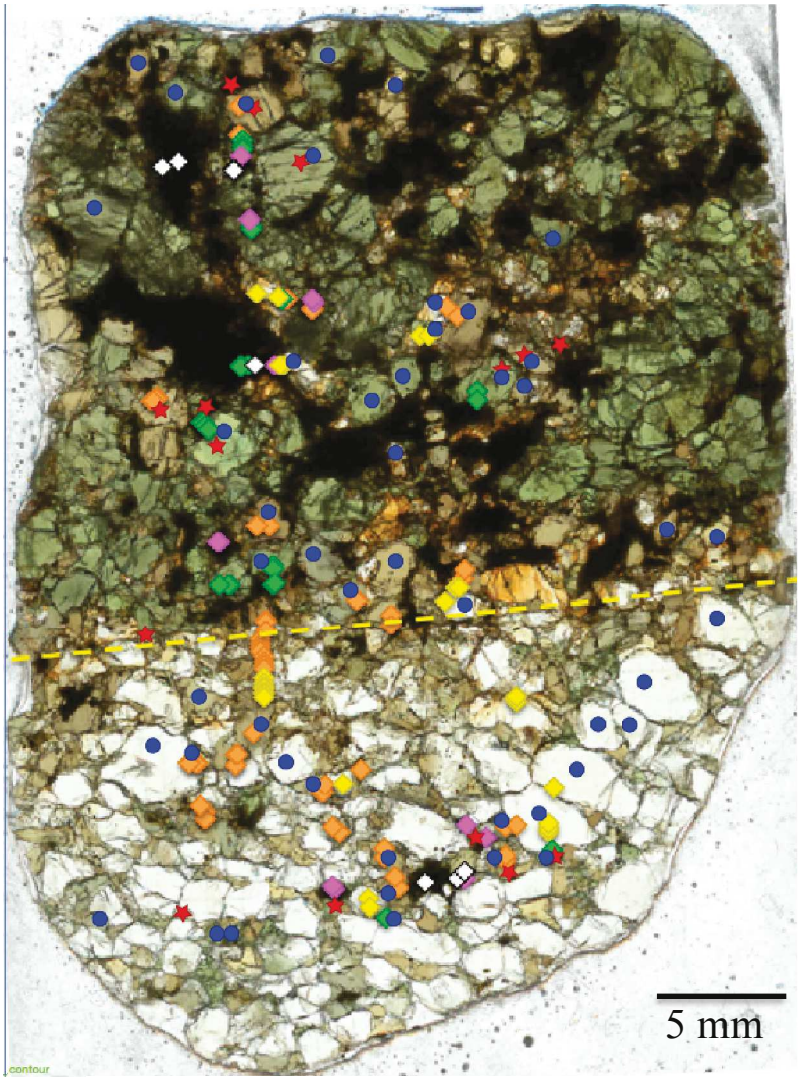

FTIR
LA-ICP-MS
EPMA :

olivine
orthopyroxène
clinopyroxène
spinelle
amphibole
plagioclage
glass

(2)

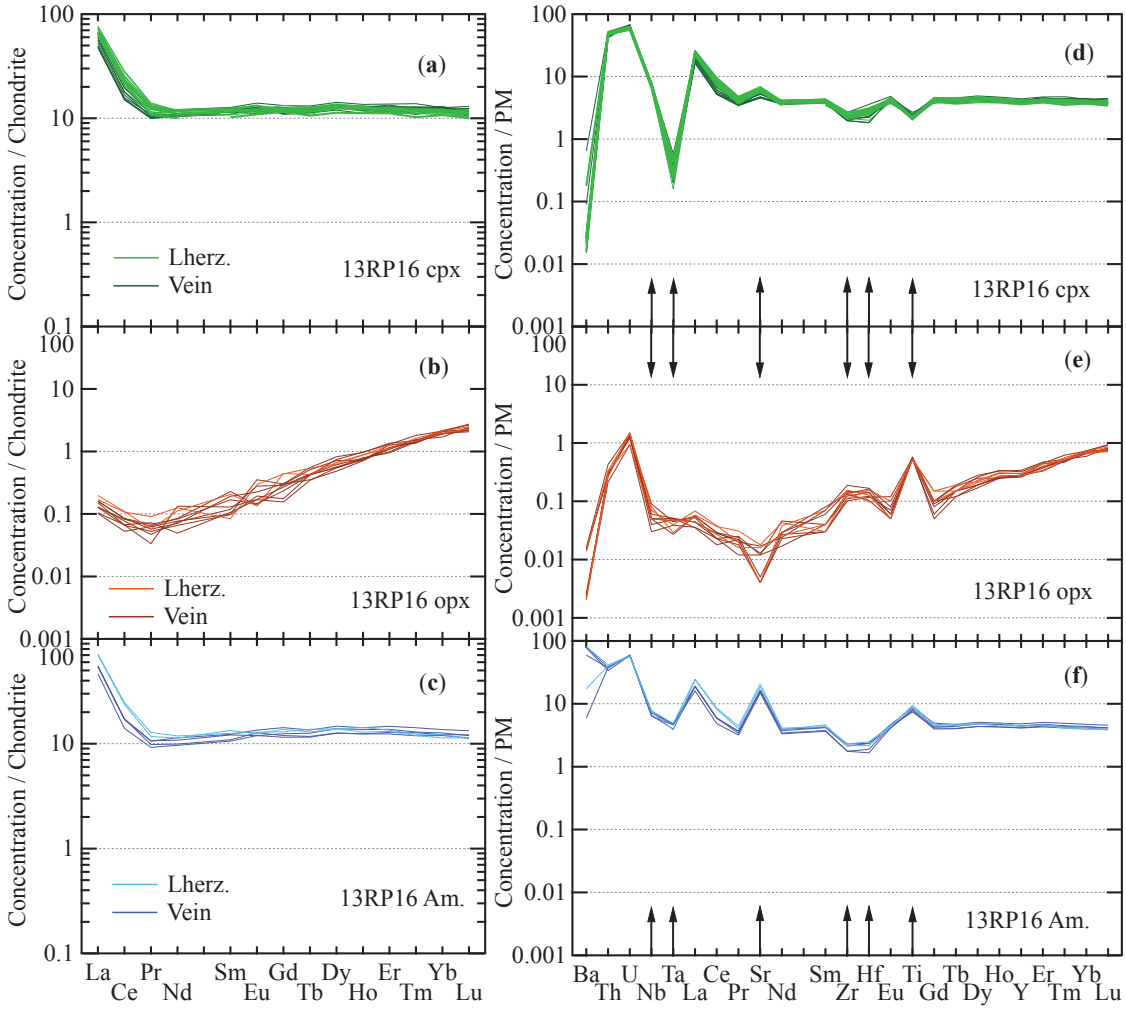

(2) a-c : Spectres de terres rares normalisés aux chondrites ; d-f :les spectres d'éléments en traces normalisés au manteau primitif (PM) (valeurs d'après McDonough & Sun, 1995). Lherz.: lherzolite; Vein: filon ; cpx: clinopyroxène; opx: orthopyroxène ; am.: amphibole.

(3)

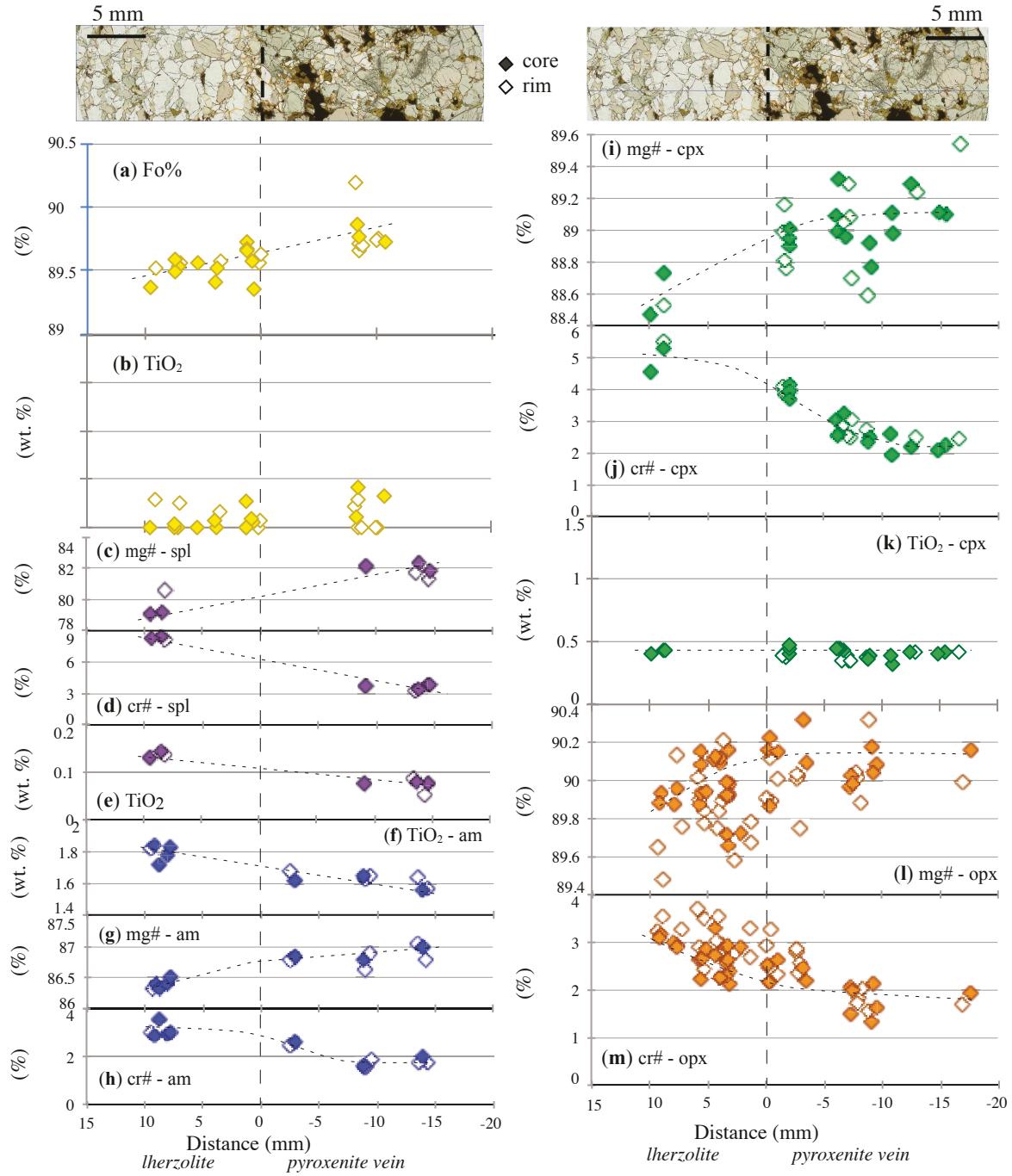

(3) Variations de concentration en éléments majeurs de chaque phase minérale en fonction de la distance au contact. ol : olivine ; spl : spinelle ; cpx : clinopyroxène ; opx : orthopyroxène ; am : amphibole. Fo% = 100* (Mg / (Mg + Mn+ Fe_{tot})) ; mg# = 100* (Mg / (Mg + Fe_{tot})) ; cr# = 100* (Cr / (Cr+Al_{tot})).

(4)

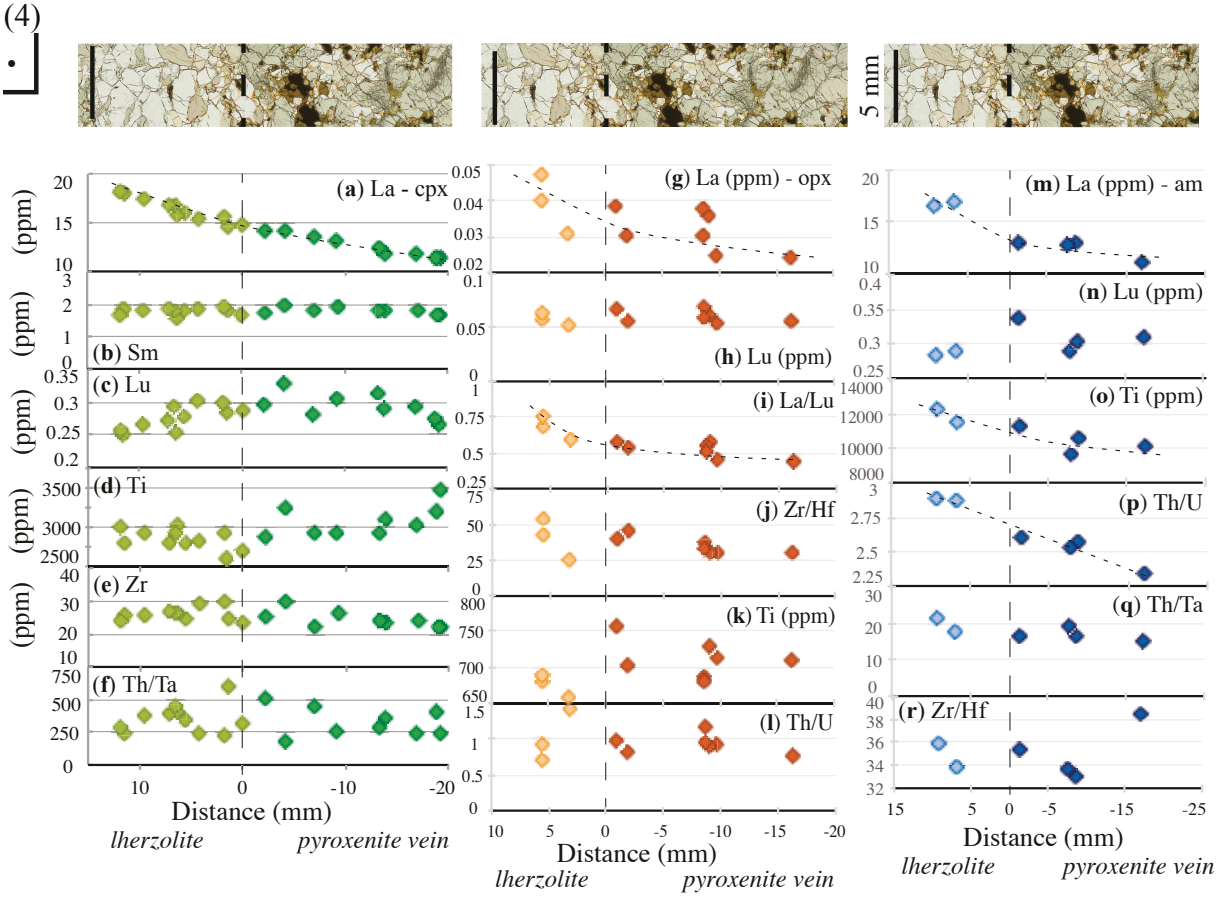

(4) Variations de concentrations en éléments en traces pour **(a-f)** les clinopyroxènes (cpx) ; **(g-l)** les orthopyroxènes (opx) et **(m-r)** des amphiboles (am) en fonction de la distance au contact.

13RP15 : Lherzolite and clinopyroxenite vein

(1) Locality : Ray Pic, French Massif Central, France

	ol	opx	cpx	spl	am	T°
lherzolite	58	29	8	4	<0.6	825 ± 30 °C
Pyroxenite center	<0.4	4	62	6	27	748 ± 11 °C
Pyroxenite border	2	5	86	2	5	

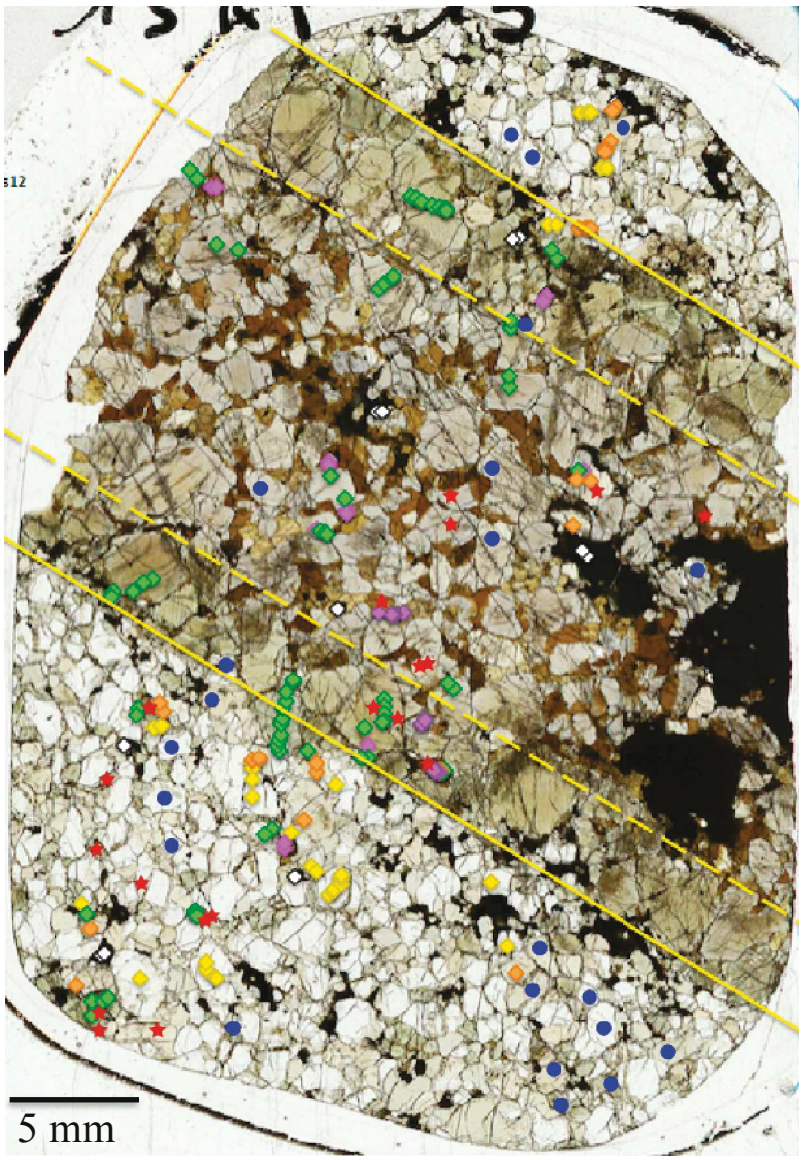

(2)

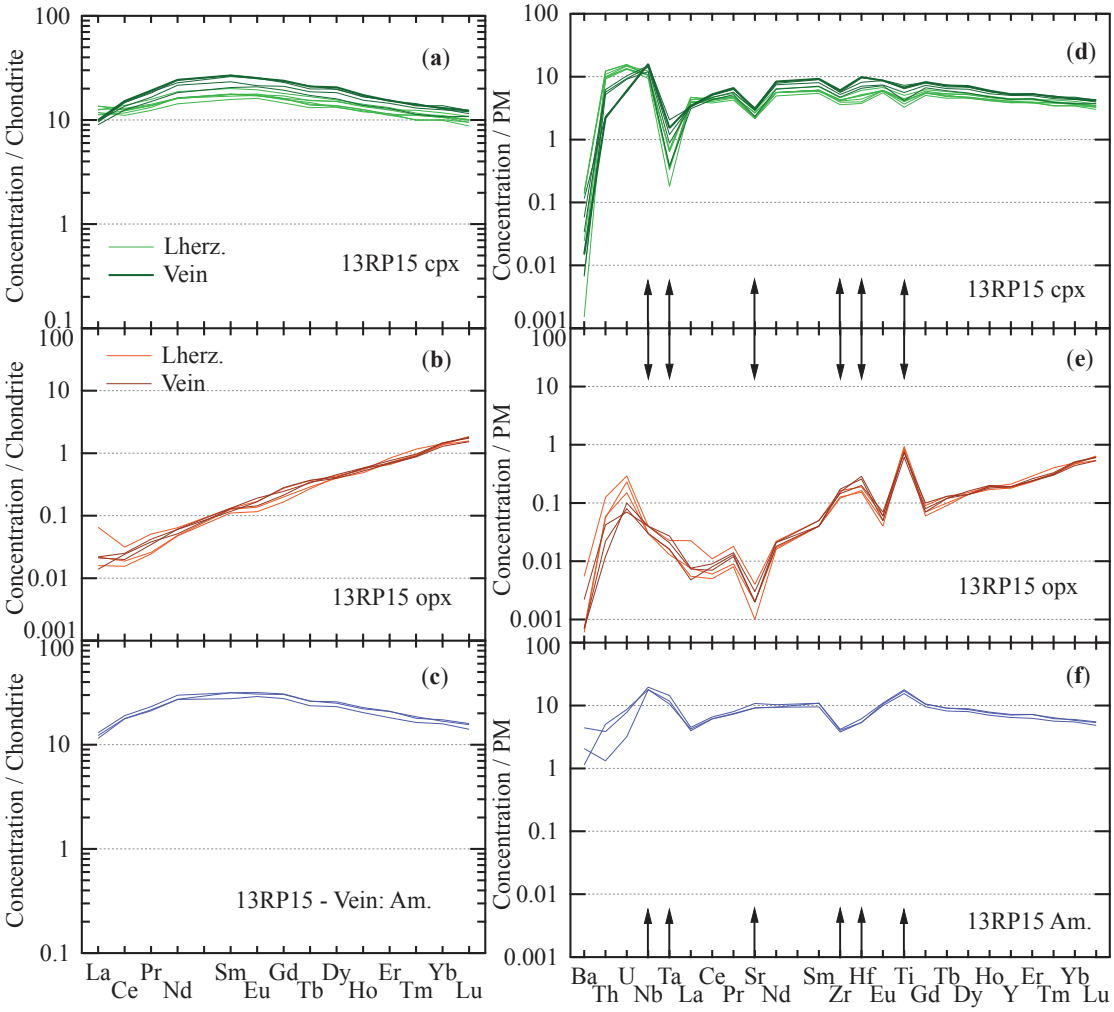

(2) a-c : Spectres de terres rares normalisés aux chondrites ; d-f :les spectres d'éléments en traces normalisés au manteau primitif (PM) (valeurs d'après McDonough & Sun, 1995). Lherz.: lherzolite; Vein: filon ; cpx: clinopyroxène; opx: orthopyroxène ; am.: amphibole.

(3)

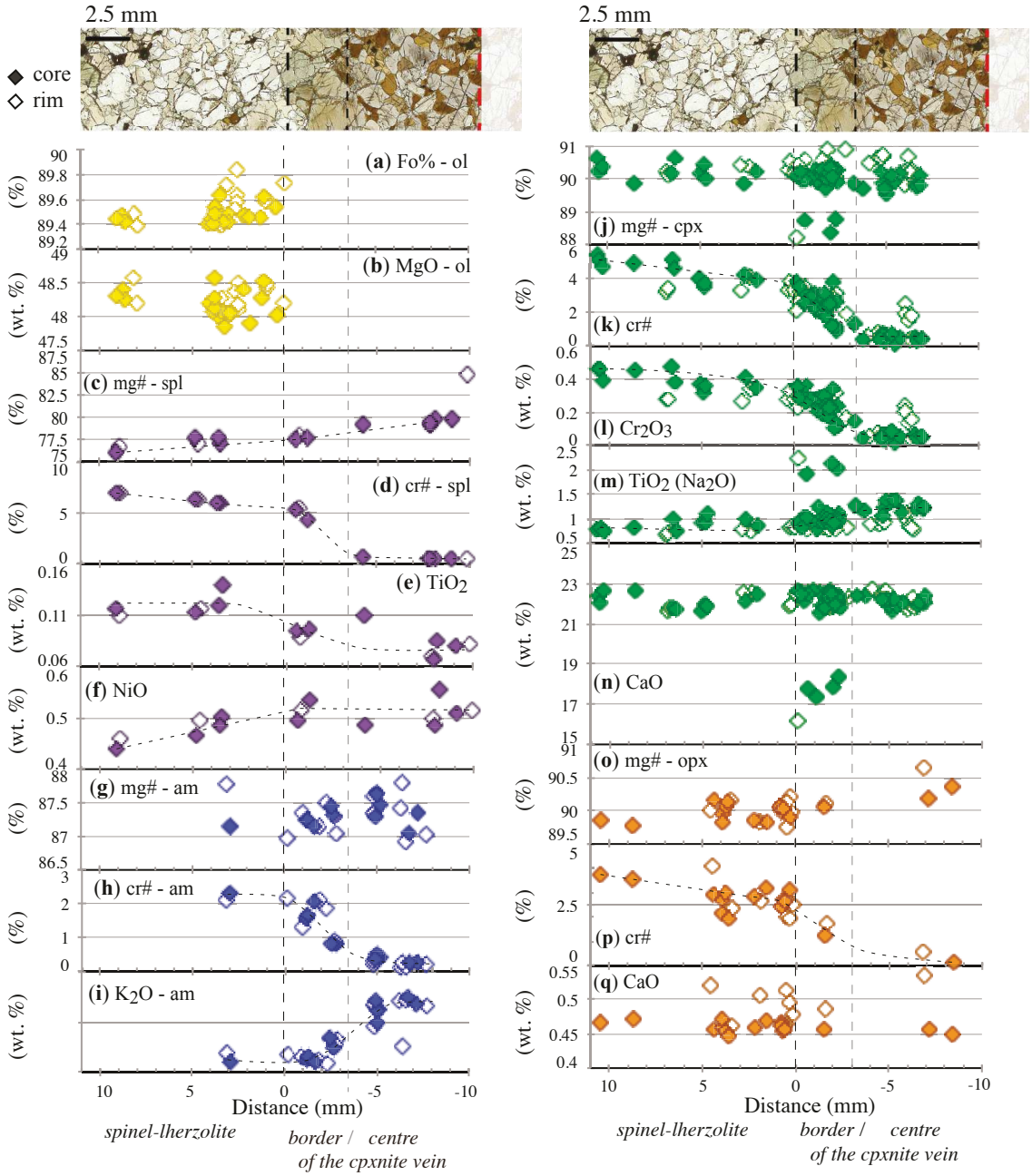

(3) Variations de concentration en éléments majeurs de chaque phase minérale en fonction de la distance au contact. ol : olivine ; spl : spinelle ; cpx : clinopyroxène ; opx : orthopyroxène ; am : amphibole. Fo% = 100* (Mg / (Mg + Mn+ Fe_{tot})) ; mg# = 100* (Mg / (Mg + Fe_{tot})) ; cr# = 100* (Cr / (Cr+Al_{tot})).

(4)

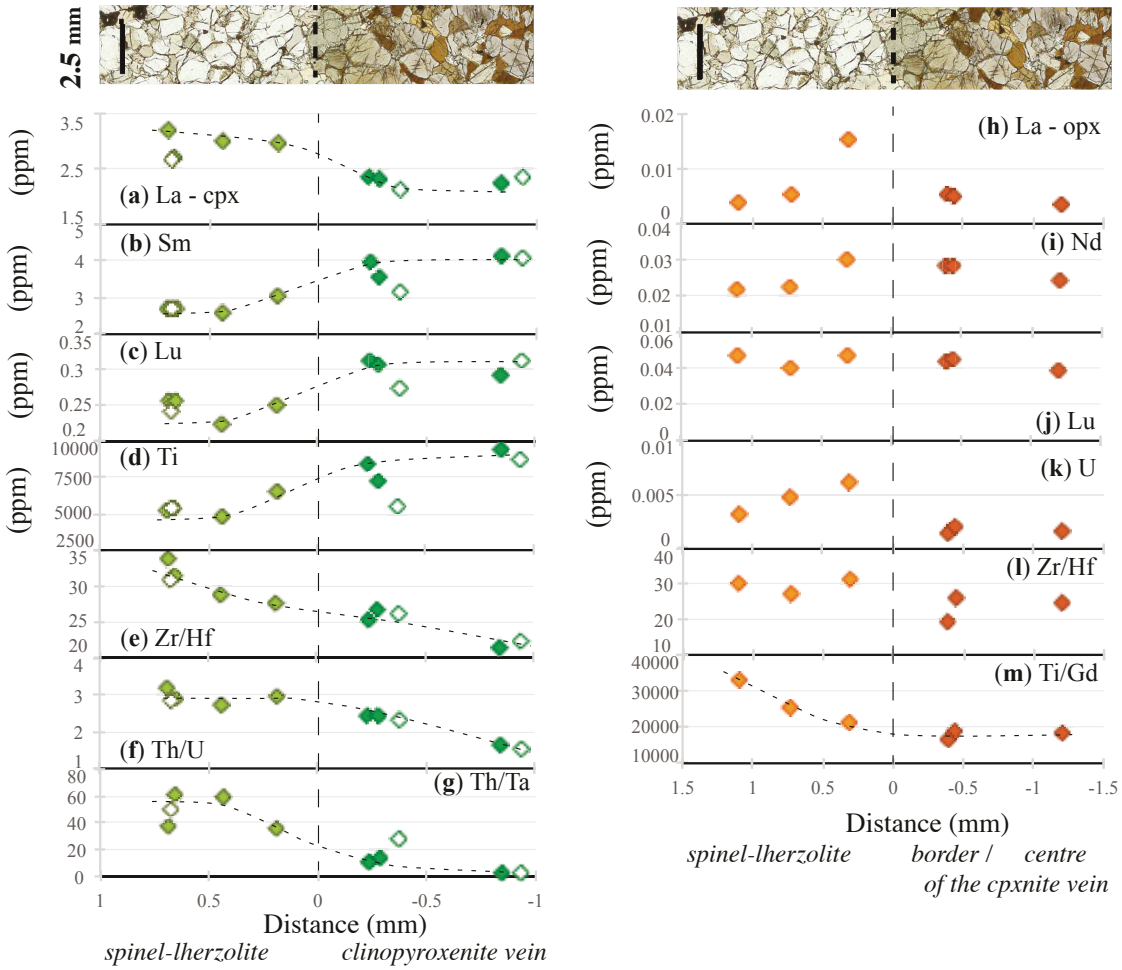

(4) Variations de concentrations en éléments en traces pour **(a-g)** les clinopyroxènes (cpx) et **(h-m)** les orthopyroxènes (opx) en fonction de la distance au contact.

TAH276-35 : Lherzolite and amphibolite vein

(1) Locality : Tahalra, Hoggar, Algeria

	ol	opx	cpx	spl	am	T°
lherzolite	68	16	14	2	1	977 ± 15 °C
amphibolite	2	-	-	-	98	-

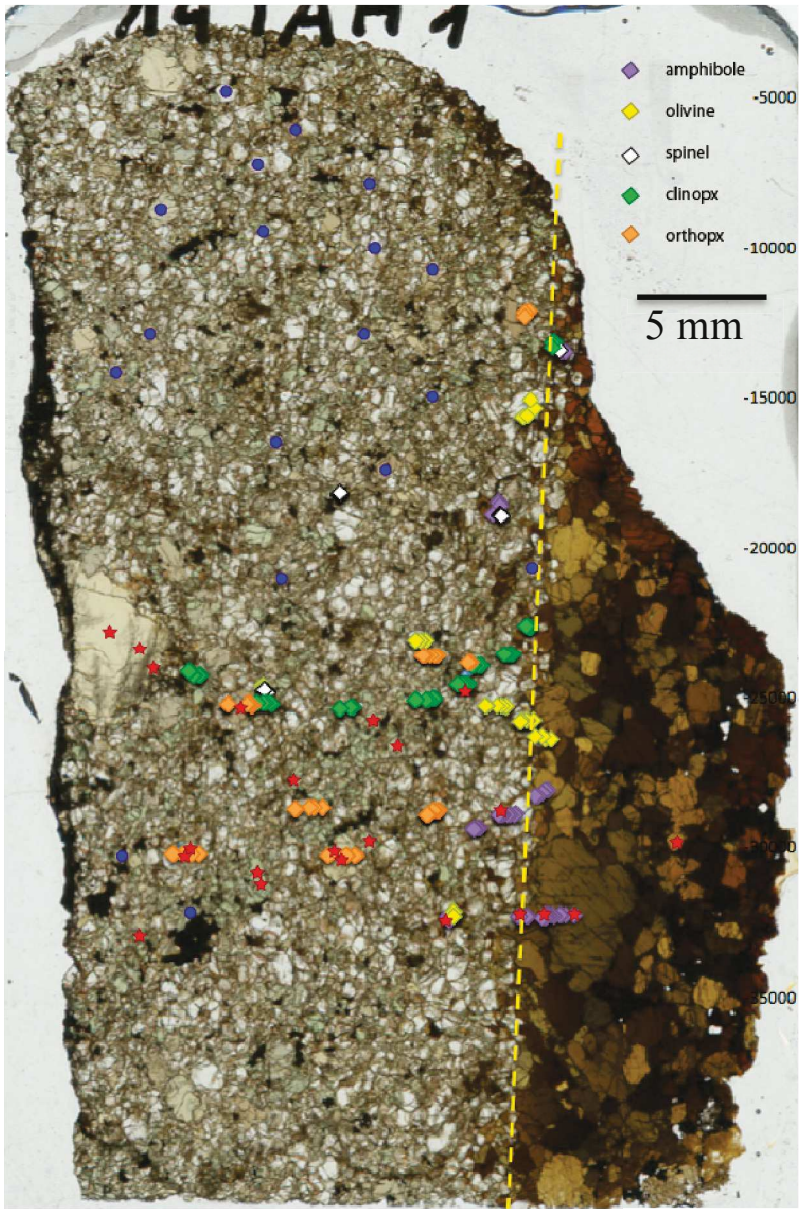

FTIR
LA-ICP-MS
EPMA :

olivine
orthopyroxène
clinopyroxène
spinelle
amphibole
plagioclage
glass

(2)

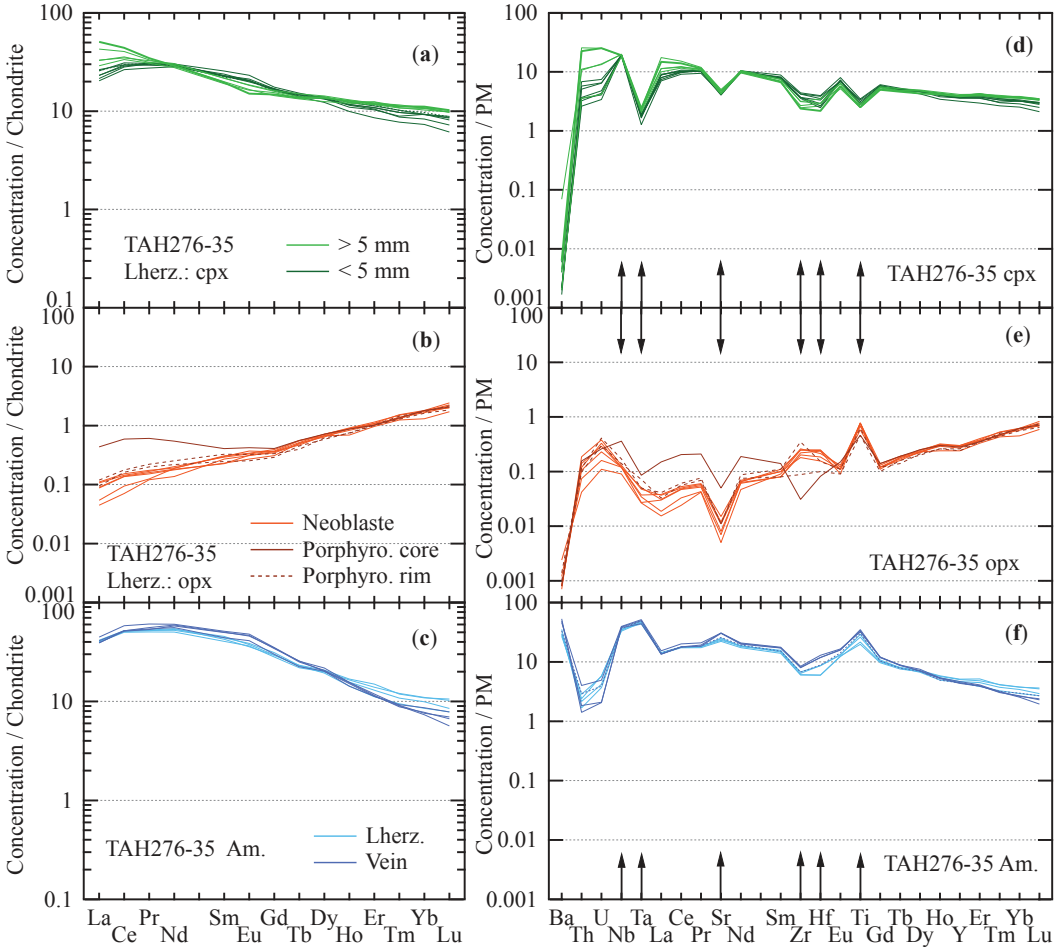

(2) a-c : Spectres de terres rares normalisés aux chondrites ; d-f :les spectres d'éléments en traces normalisés au manteau primitif (PM) (valeurs d'après McDonough & Sun, 1995). Lherz.: lherzolite; Vein: filon ; cpx: clinopyroxène; opx: orthopyroxène ; am.: amphibole.

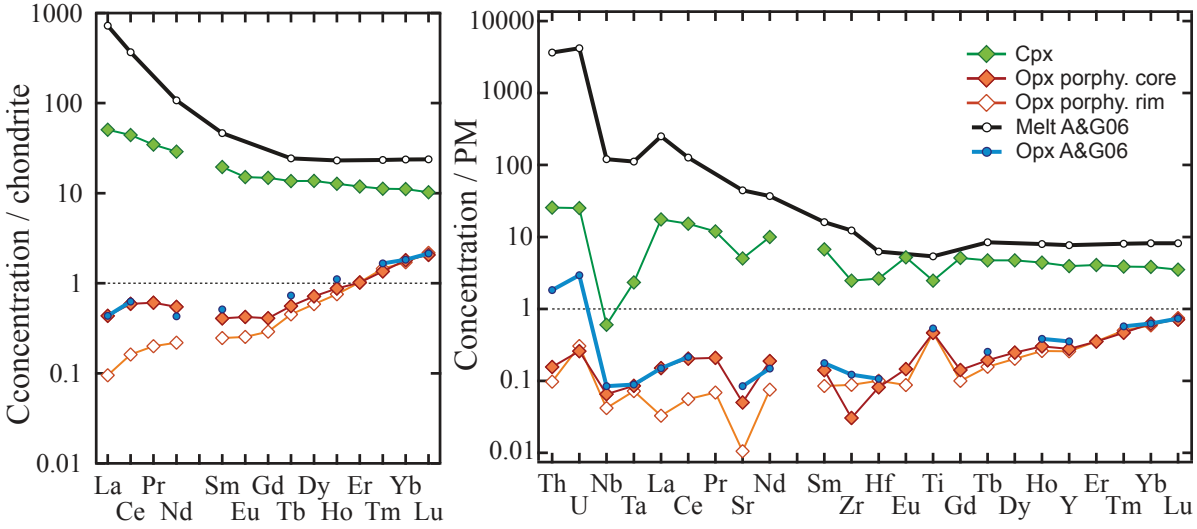

– Calculated composition of an orthopyroxene (opx) in equilibrium (blue) with a clinopyroxene (cpx) (green) of sample TAH 276-35 at 13 mm of the contact between the lherzolite and the amphibolite using the partition coefficients given by Adam and Green, 2006 (A&G06). Calculated composition of a melt (black).

(3)

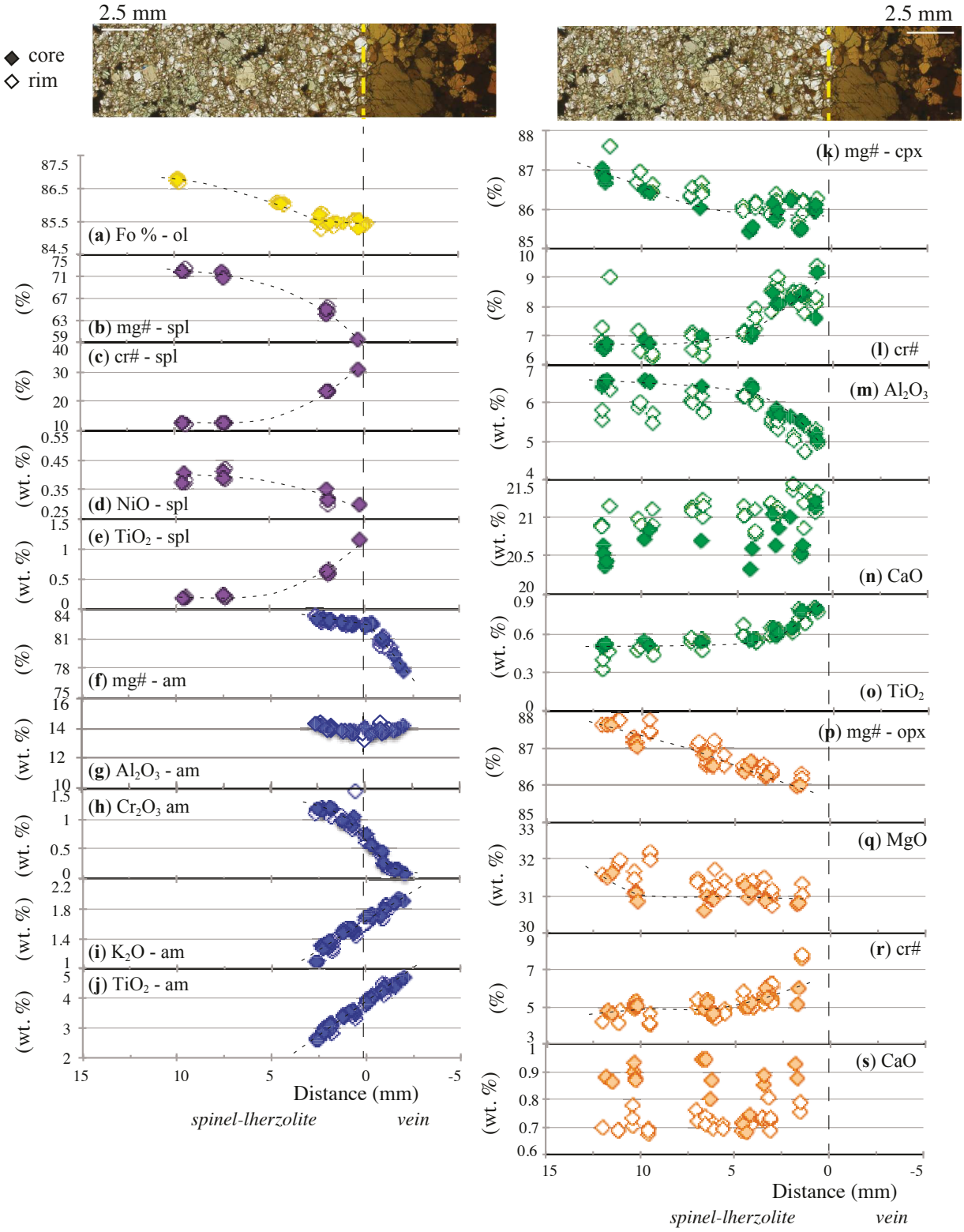

(3) Variations notables de concentration en éléments majeurs de chaque phase minérale en fonction de la distance au contact. ol : olivine ; spl : spinelle ; cpx : clinopyroxène ; opx : orthopyroxène ; am : amphibole. Fo% = 100* (Mg / (Mg + Mn+ Fe_{tot})) ; mg# = 100* (Mg / (Mg + Fe_{tot})) ; cr# = 100* (Cr / (Cr+Al_{tot})).

(4)

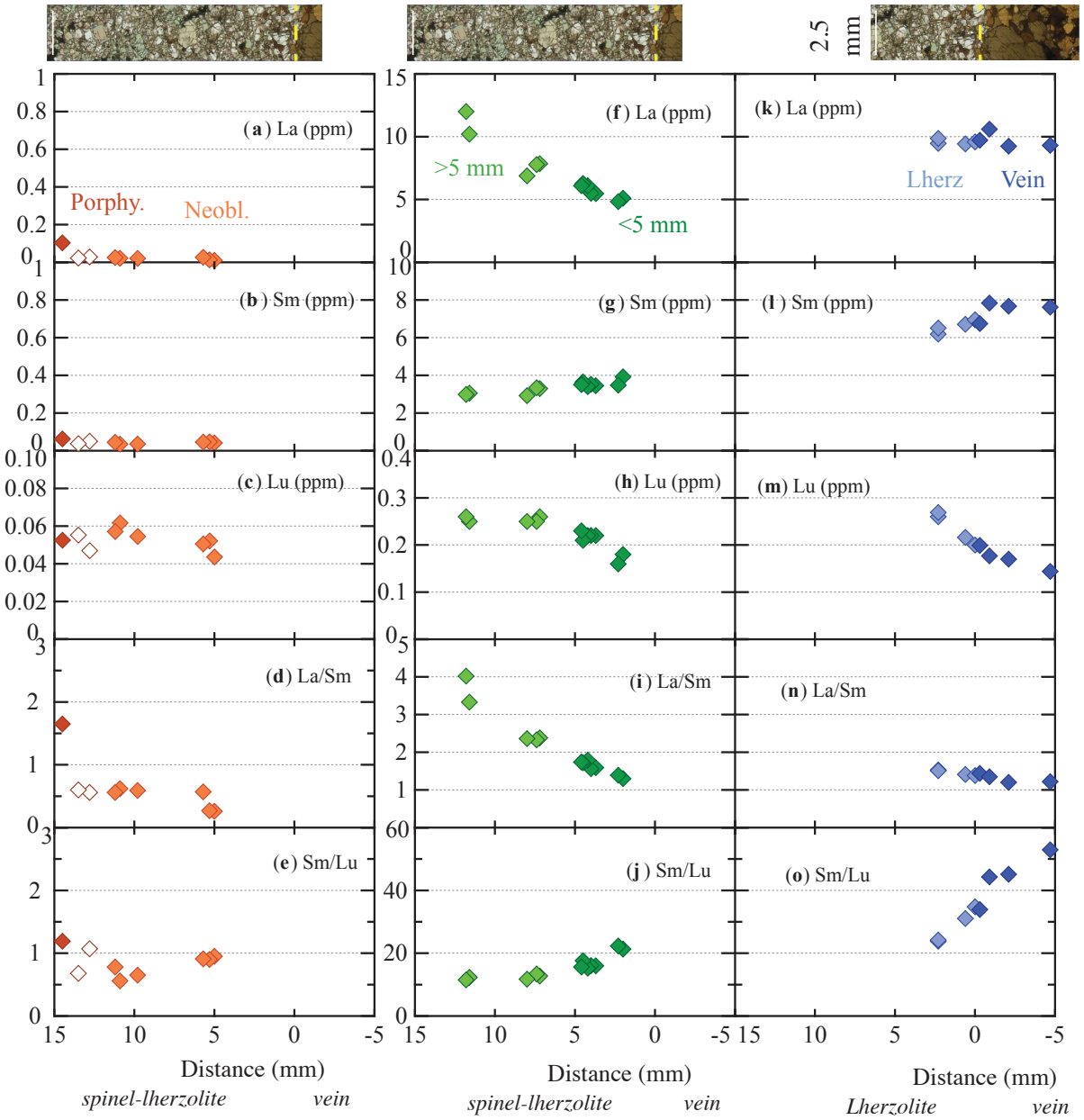

(4) Variations de concentrations en éléments en traces pour **(a-e)** les orthopyroxènes (opx); **(f-j)** les clinopyroxènes (cpx) et **(k-o)** les amphiboles (am) en fonction de la distance au contact. Porphy. :porphyroclaste ; Neobl. : Néoblastes ; Lherz : lherzolite.

COMPORTEMENT DE L'HYDROGÈNE LORS DES PROCESSUS MANTELLIQUES

Carole M.M. DENIS

Ces travaux de thèse apportent de nouvelles contraintes sur la concentration et le comportement de l'H dans le manteau lithosphérique. Ils reposent sur l'étude pétro-géochimique de trois séries de xénolites de péridotites à spinelle, associant les concentrations en élément majeurs et en traces y compris l'H dans les minéraux dits anhydres (les NAMs, ici, olivine, pyroxènes) et hydratés (amphibole).

Les effets de la remontée des xénolites dans du magma hôte sur les concentrations en H des NAMs ont été étudiés sur une série de xénolites de péridotite du champ volcanique d'Eifel (Allemagne). Une variation intracristalline de concentration en H a été identifiée dans l'olivine et non dans les pyroxènes coexistant. Ces profils de concentration en H peuvent être utilisés pour estimer des vitesses de remontées des magmas. Dans le cas des volcans étudiés, ces vitesses sont estimées entre 3.5 et 12 $m.s^{-1}$. Ces résultats suggèrent que les pyroxènes sont de meilleurs proxy que l'olivine pour quantifier la concentration mantellique de l'H.

Les xénolites de Ray Pic (Massif Central, France) ont permis de discuter de l'effet de la fusion partielle et du métasomatisme à grande échelle sur les concentrations en H des NAMs. Les concentrations en H des minéraux ne suggèrent pas de lien clair avec le métasomatisme subit, qu'il soit modal (amphibole) ou cryptique (métasomatisme par de faibles fractions de liquides enrichis en volatils et éléments incompatibles). Cependant, en comparant les concentrations en H avec un marqueur de la fusion partielle (Yb du cpx), l'H semble avoir un comportement similaire à une MREE (*e.g.*, Sm ; D(cpx/liquide) ~0.29).

L'interaction peridotite-basalte hôte a été étudiée et montre, dans le cas des olivines, des variations chimiques couplées entre éléments majeurs et les concentrations en H en fonction de leur proximité au filon. Plus l'olivine se rééquilibre avec le liquide moins elle contient d'H. Bien que partiellement rééquilibrés avec la lave hôte, les pyroxènes ne montrent pas le même comportement. Enfin, des xénolites composites (filons et veines traversant/jouxtant une péridotite) ont permis l'étude à l'échelle millimétrique à pluri-centimétrique du comportement de l'H lors du métasomatisme d'éponte. Chaque échantillon présente des concentrations en H homogènes pour chacune des phases minérales. Cependant plus les filons contiennent d'amphibole moins il y a d'H dans les NAMs. D'autre part, une nouvelle fois, la corrélation positive entre les concentrations en H des NAMs et le Sm(cpx) en tant que marqueur de métasomatisme suggère que l'H se comporte comme une MREE.

En conclusion, les minéraux des spl-harzburgites contiennent en moyenne un peu plus d'H que ceux des spl-lherzolites. Les concentrations en H des olivines sont sensibles à la dévolatilisation lors de la remontée dans le système magmatique et le rééquilibrage avec le magma. Au contraire, les concentrations en H des pyroxènes, spécialement l'opx, sont très homogènes suggérant que les concentrations mantelliques sont préservées. La présence d'amphibole n'implique pas un enrichissement en H des NAMs coexistant. Le comportement de l'H lors de la fusion partielle et du métasomatisme reste complexe ; nos données suggèrent que l'H suit les MREE tel que le Sm.

Mots clefs : péridotites, métasomatisme, fusion, pyroxénites, hydrogène, minéraux anhydres